University of Liège
Faculty of Sciences
Department of Geography

PhD Thesis
submitted in partial fulfillment of the requirements for the degree of
Doctor of Sciences in Geography

Impact of bathymetric thresholds on the hydrodynamic circulation in a micro-tidal setting and on the sedimentary processes in a semi-enclosed basin: case of the Corinth Gulf (Greece)

Basile CATERINA

Under the supervision of Aurélia HUBERT (SPHERES, ULiège, Belgium)
And the co-supervision of Jean-Marie BECKERS (GHER, ULiège, Belgium)

2021-2025

Members of the Jury

Prof. Brice NOEL (Chair, Université de Liège)

Prof. Aurélia HUBERT (Supervisor, Secretary, Université de Liège)

Prof. Jean-Marie BECKERS (Co-Supervisor, Université de Liège)

Dr. Evgeny IVANOV (Member, Université de Liège)

Prof. George PAPATHEODOROU (Member, University of Patras)

Dr. Nikolaos SKLIRIS (Member, University of Southampton)

Remerciements - Acknowledgements

Après 4 ans, cette thèse arrive à son terme. La finalisation de ce manuscrit marque la fin de ce chapitre de vie pour lequel des remerciements sont de rigueur.

En premier lieu, je tiens à remercier ma promotrice, Aurélia Ferrari. Tu m'as permis non seulement d'entreprendre cette thèse en me laissant une opportunité de travail sur un sujet qui me correspondait au mieux. Bien que ça n'ait pas toujours été évident, on trouvait toujours une solution à nos problèmes. Merci pour tes encouragements et nombreuses relectures sans lesquels ce travail aurait été plus compliqué.

Je tiens aussi à remercier Romain Rubi, qui en plus de m'avoir accompagné dans le comité de thèse, a été présent dès le début pour me lancer sur cette recherche et pour s'être inquiété de mon avancement à des moments clés de cette thèse.

Je remercie aussi les deux membres restant de mon comité : Jean-Marie Beckers et Alexander Barth. Merci d'avoir pris le soin de m'écouter, d'avoir répondu à mes questions et de m'avoir aiguillé vers certains aspects plus optimaux de la modélisation océanographique toujours avec la plus grande bienveillance.

Merci au FRIA-FNRS de m'avoir financé pour me permettre de réaliser cette thèse dans les meilleures conditions.

Special thanks go to the UPatras Oceanus-Lab team. Thanks to Gearge Papatheodorou and Maria Geraga for your warm welcome every time I came to visit you. Thanks to Dimitris Christodoulou and Xenophon Dimas for their help with data collection and treatment during our on-boat missions.

To my colleagues, thank you for being there, so joyful and helpful when I needed it. Many thanks to Evgeny, without whom this thesis would have been stuck with no optimized ROMS model.

Cécile, merci d'avoir été une collègue exceptionnelle et une super amie. Merci d'avoir été ma vieweuse n°1 puisqu'on a glandouillé bien assez dans la réalité pour qu'on puisse se permettre d'optimiser le fictionnel.

De très grands remerciements vont à ma famille proche et étendue. Merci à vous m'avoir soutenu et aidé ; et/ou de vous être occupés de Zartan et Élé qui m'ont eux aussi aidé à leur façon.

Norine, plus de milles mercis sont nécessaires pour te remercier de ton soutien et de ta bonne humeur. Tu as vécu les étapes de cette thèse avec moi et j'espère que tu resteras près de moi pour le reste de notre vie. Je t'aime.

Abstract

The Gulf of Corinth (Greece) is a semi-enclosed basin connected to the Ionian Sea through the Gulf of Patras and the Rio-Antirio Strait. The latter, with an average depth of about 70 m and a width of 2 km, acts as a major bathymetric threshold controlling the hydrodynamic circulation between the two gulfs. Despite the microtidal context typical of the Mediterranean Sea, tidal currents in the strait can reach up to 1.5 m s^{-1}, significantly influencing both regional ocean dynamics and local sedimentary morphology.

In the first phase, satellite data were used to assess variations in sea surface temperature (SST) and surface hydrodynamics. These data revealed: (1) a west–east SST gradient across the Gulf of Corinth, with a mean SST increase of 1.5°C over 14 years; (2) a succession of surface gyres influenced by the strait in its vicinity and by wind forcing in the wider basin; and (3) similarities between the Gulf of Corinth and the Mediterranean Sea hydrodynamics, both of which are largely controlled by their respective straits (Rio-Antirio and Gibraltar).

In a second phase, ROMS numerical simulations, validated by ADCP measurements, confirmed the combined influence of tidal and wind forcing. The models reveal strong bottom currents within the strait (up to 1.5 m s^{-1}), generating shear stress reaching 3 N m^{-2}. These conditions account for the formation of erosional features in the central part of the Rio-Antirio Strait and for the development of contourite deposits to the east, particularly in the Mornos delta area. Sedimentological analyses and age constraints demonstrate a direct relationship between bottom currents and tidal dynamics, whose influence extends approximately 15 km eastward from the Strait. In contrast, the deep basin of the Gulf of Corinth, less affected by currents, exhibits sediment accumulation—about 200 m since the beginning of the Holocene.

Finally, paleogeographic simulations tested several bathymetric configurations. Scenarios of sea-level lowering show that the Rio-Antirio Strait strongly amplifies bottom currents. Moreover, a simultaneous connection of the Gulf of Corinth to both the Aegean Sea via the Isthmus of Corinth and the Ionian Sea via the Rio-Antirio Strait appears necessary to reproduce the tidal conditions responsible for the herringbone sedimentary structures observed in the Corinth Canal, which are a proof of the existence of a former active tidal strait.

Keywords: Tidal Strait, Erosion, Gulf of Corinth, Rio-Antirio, Hydrodynamic Circulation, Sedimentation.

Résumé

Le Golfe de Corinthe (Grèce) est un bassin semi-fermé relié à la mer Ionienne par le Golfe de Patras et le détroit de Rio-Antirio. Ce dernier, d'une profondeur moyenne d'environ 70 m pour une largeur de 2 km, agit comme un seuil bathymétrique majeur qui contrôle la circulation hydrodynamique entre les deux golfes. En dépit du contexte micro-tidal typique de la Méditerranée, les courants de marée y atteignent jusqu'à 1,5 m s^{-1}, influençant significativement la dynamique océanique régionale et la morphologie sédimentaire locale.

Dans un premier temps, l'utilisation de données satellite a permis d'évaluer les variations de température de surface (SST) ainsi que l'hydrodynamique de surface. Ces données ont permis d'observer : (1) une variation ouest-est de la SST dans le Golfe de Corinthe, avec une augmentation moyenne de la SST de1,5°C en 14 ans ; (2) une succession de gyres à la surface, influencés par le détroit dans la vicinité de celui-ci et par les vents lorsque le bassin devient plus large ; (3) des similarités entre le Golfe de Corinthe et la Mer Méditerranée pour lesquels leurs détroits respectifs (Rio-Antirio et Gibraltar) contrôlent leur circulation hydrodynamique.

En second temps, les simulations numériques ROMS, validées par des mesures ADCP, confirment l'importance combinée du forçage de marée et du vent. Ces modèles révèlent la présence de forts courants de fond au niveau du détroit (jusqu'à 1,5 m s^{-1}) générant un cisaillement atteignant 3 N m^{-2}. Ces conditions expliquent la formation de structures érosives au centre du détroit et le développement de dépôts sédimentaires de type contourites à l'est, notamment dans la zone du delta du Mornos. Les analyses sédimentologiques et les datations associées démontrent un lien direct entre les courants de fond et la dynamique tidale, dont l'influence se prolonge sur environ 15 km à l'est du détroit. En revanche, le bassin profond du Golfe de Corinthe, moins soumis aux courants, présente une accumulation sédimentaire importante (environ 200 m depuis le début de l'Holocène).

Des simulations paléogéographiques complètent l'étude en testant diverses configurations bathymétriques. Les scénarios de baisse du niveau marin montrent que le détroit de Rio-Antirio amplifie fortement les courants de fond. De plus, une connexion simultanée du Golfe de Corinthe avec la mer Égée via l'isthme de Corinthe et la mer Ionienne via le détroit de Rio-Antirio apparaît nécessaire pour reproduire les conditions tidales à l'origine des structures en chevron observées dans le Canal de Corinthe, témoignant d'un ancien détroit tidale actif.

Mots-clés : Détroit tidal, Érosion, Golfe de Corinthe, Rio-Antirio, Circulation hydrodynamique, Sédimentation.

Contents

List of abbreviations

ADCP	Acoustic Doppler Current Profiler
BP	Before Present
CHL	Chlorophyll
CMEMS	Copernicus Marine Service
CRS	Constant Rate of Supply
CT	Computed Tomography
CTD	Conductivity Temperature Depth
DINEOF	Data Interpolating Empirical Orthogonal Function
ECMWF	European Centre for Medium-Range Weather Forecasts
FA	Facies Association
GEBCO	General Bathymetric Chart of the Oceans
HCMR	Hellenic Center for Marine Research
MBES	Multi-Beam Echosounder
MIS	Marine Isotopic Stage
MS	Magnetic Susceptibility
MSCL	Multi-Sensor Core Logger
MTD	Mass Transport Deposit
NETCDF	Network Common Data Form
ROMS	Regional Oceanographic Modelling System
SST	Sea Surface Temperature
WOD	World Ocean Database
XRF	X-Ray Fluorescence

Chapter 1: General Introduction: Concepts, Study Area and Objectives

1. Tidal straits

Bathymetric thresholds, or bathymetric sills, are shallower areas that restricts the water flow and sediment exchange between deeper parts of the basin. If they connect two different basins they are referred to as straits. The term "tidal strait" characterizes a strait, i.e. a narrow passage of water between two larger bodies, which is dominated and influenced by tidal amplification in its central part (Longhitano & Chiarella 2020). Several modern tidal straits have been studied and are well defined: the *Golden Gate Strait* (San Francisco Bay), the *Palk Strait* (India), the *Cook Strait* (New Zealand) and the *Messina Strait* (Italy) among others (Keller & Richards 1967; Barnard *et al*. 2006; Lamarche *et al*. 2011; Bouilloux *et al*. 2013; Longhitano 2018; Longhitano & Chiarella 2020). These strait systems share general aspects such as (1) a more independent tidal dynamic than the surrounding waters (Baines & Garnek 1990); (2) a topography induced by the proportional amount of water flowing through the strait (Bryden & Nurser 2003); (3) a possible internal wave phenomenon due to water stratification (Shanmugam 2013); (4) more distinct large scale bedforms (sand waves, tidal dunes, banks, etc. Longhitano & Chiarella, 2020); (5) a continuum of facies distribution widespread along the strait morphology (Longhitano 2013).

In terms of sedimentary dynamics, tidal straits are governed by tidal currents. These currents are seen to be bidirectional in the straits, which leads to the differentiation between ebb and flood deposits, marked by tidal asymmetry and velocity (Stow *et al*. 2009; Reynaud & Dalrymple 2012). Even if there are exceptions, anomalies and variance, a conceptual model of tidal straits depositional zones was proposed by Longhitano (2013) to describe the sedimentology of the tidal straits (**Figure 1.1**). In this model, the relative sea-level with respect to the structures is ignored as well as the yet unknown effects of the water-mass stratification over the tidal asymmetry (Longhitano & Chiarella 2020).

In tidal straits, the concepts of "flood" and "ebb" are harder to define because the flow does not move towards or away from the coast but is roughly parallel to the strait margins. However, the flood is suggested to be the tidal phase directed towards the smaller or more enclosed basin. The ebb will then flow in opposite direction (Defant 1958). These tidal currents depict also a tidal asymmetry in the straits leading to a diversity of directions and repartition of the sedimentary beds (Reynaud & Dalrymple 2012). This tidal asymmetry seems to always be marked by the same current, the strongest one; the one flowing in the opposite direction is poorly marked in the sediments.

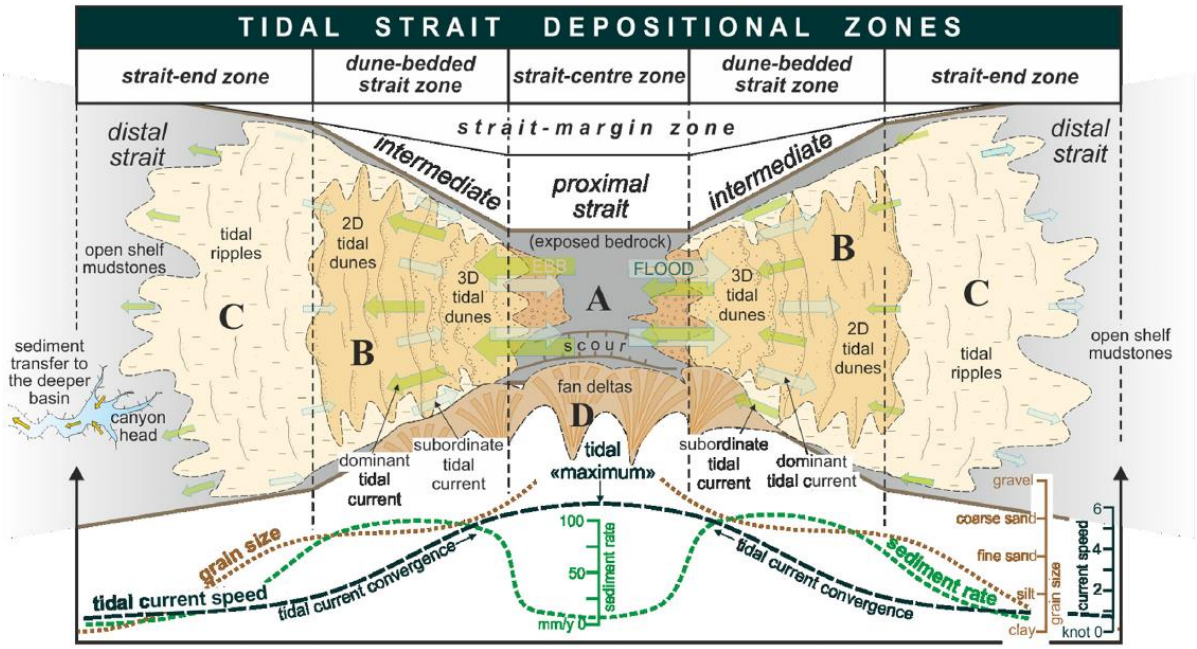

Figure 1.1: Depositional model for tidal straits and relative subdivision into zones characterized by different velocities of the tidal currents, corresponding bed-shear stress and resulting grain-size sediment distribution. From Longhitano & Chiarella (2020), modified after Longhitano (2013).

Overall, straits are very sensitive to climate and sea-level variations and allow a control on the paleoenvironment regarding paleoecology, sedimentology and stratigraphy. This is, for instance, the case of the Dover Strait which controls the origin of island Britain (Gupta *et al.* 2017). Since there are ephemeral environments, they would fade during the related basin evolution and are thus difficult to study. Tidal straits are the less understood tidal environments since there are only a few general models for these straits. In an actual societal context, straits are often used for navigation and installation of plumbing or wiring for technical uses. Therefore, the understanding of the depositional model and the associated oceanographic dynamics is needed for such complex systems. For their study, oceanographic data and models on present day tidal straits (Longhitano & Chiarella 2020) make key observations on the dynamics of the currents and their relatives morpho bathymetries, but an understanding based on sub-surface (seismic) and outcrop analogues are mandatory to get rid of the human timescale constrain. Both approaches are complementary for understanding the present and the evolution of the straits.

2. Bottom currents and deposits

2.1. Physics of the current

The term “bottom current” designate water current that happens at the bottom of the basin. They are crucial for the understanding of the circulation or the sedimentation that take place in a given basin (Rebesco *et al.* 2014). These currents can have several sources as synthetized by Shanmugam (2008). (1) They can be induced by the thermohaline circulation and the density differences between the water masses. In this scenario, they

can reach between 0.2 m s^{-1} and 1 m s^{-1} (Heezen *et al.* 1966). (2) Bottom currents can be wind induced and reach between 0.2 m s^{-1} to 2 m s^{-1} with less strength the deeper they are (Cooper *et al.* 1990). (3) Deep-marine tidal bottom currents, induced by tides, are slower (0..2 m s^{-1} to 0.5 m s^{-1}) and present a shift in their direction (due to the tide) (Petruncio *et al.* 1998). (4) Internal waves can generate strong bottom currents. These occur in shallow regions and can be associated to upwelling or downwelling movements (Alford *et al.* 2011; Morozov *et al.* 2017; Longhitano 2018). These currents can be generated by an internal tide when the wave matches the tide frequency (Rubi *et al.* 2022).

2.2. Contouritic deposits

By their velocity they apply shear stress on the bottom and are thus able to shape the morphology of the seafloor and to transport sediments (Canals *et al.* 2006; Trincardi *et al.* 2007). Sediments transported and deposited by these currents are known as contourite deposits (Faugères & Stow 2008; Rebesco *et al.* 2008; Stow *et al.* 2009). The morphology of the contouritic deposits depends on the granulometry of the sediments and on the flow velocity (**Figure 1.2**) (Stow *et al.* 2009; Rebesco *et al.* 2014). Depending on the orientation of the current deposits can be divided into two categories. Parallel to the flow contouritic deposits vary from surface lineations, grooves and ridges (or longitudinal triangular ripples), sours and cornet sours (erosion features) or ribbon marks (mostly sandy) (Flood 1983; Masson *et al.* 2004; Viana & Rebesco 2007). Transversal to the flow, ripples, hydraulic dunes or sediment waves can be formed (Wynn & Stow 2002; Wynn *et al.* 2002; Stow *et al.* 2009). Thus, depending on the form of the deposits, the velocity of the flow can be deduced if referred to **Figure 1.2**.

Associated to bottom currents, there is also an erosional factor creating contouritic erosion features (Hernández-Molina *et al.* 2008). Eroded surfaces can be observed as terraces along the slopes and at the interface of different water masses. Surfaces can also be abraded by the bottom currents, usually in association with sediment-waves or dunes. Linear erosional features can display several forms (Hernández-Molina *et al.* 2008; García *et al.* 2009): (1) Contourite channels are elongated depressions created by bottom currents. (2) Moats are parallel to the slope channels associated with giant elongated mounted contourite drifts. (3) Marginal valleys are formed by the interaction of bottom currents with bathymetric obstacles.

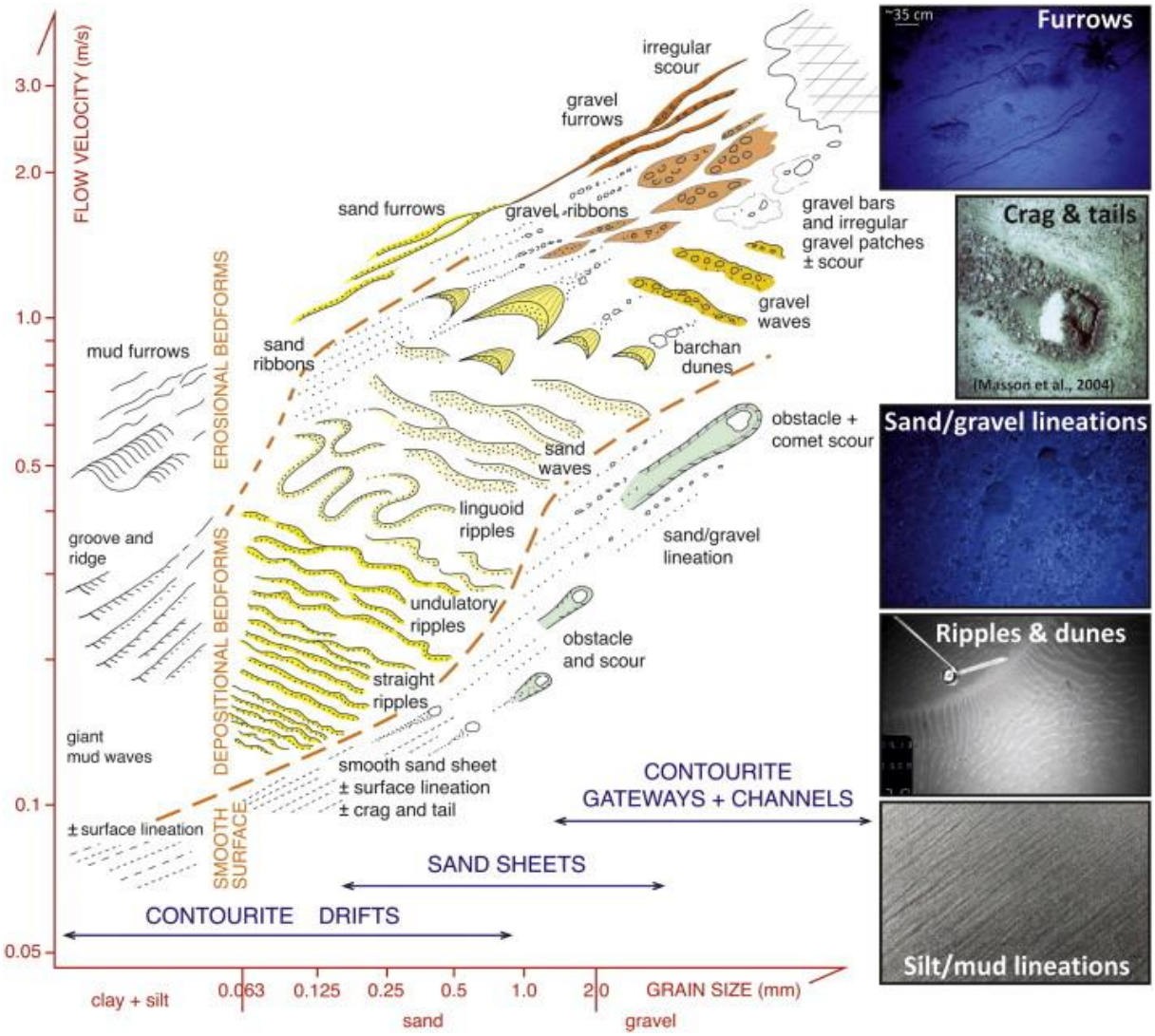

Figure 1.2: Bedform morphologies depending on the grain size and the flow velocity. Modified from Rebesco *et al.* (2014), originally published in Stow *et al.* (2009).

3. Corinth Gulf: an enclosed basin

3.1. Geography and connections

The Gulf of Corinth, also known as Corinth Gulf or Corinthian Gulf is the water mass that separates the continental Greece from the Peloponnesus. This Gulf is a basin of approximately ~900 m deep, 130 km long and 40 km wide. This elongated basin is connected to the Patras Gulf at its western end. The Patras Gulf, an almost circular shallower basin (150 m deep) of 20 to 25 km wide, connects the Corinth Gulf to the Ionian Sea in the Mediterranean Sea. This western end of the Corinth Gulf is the only actual oceanographic connection to the open sea (**Figure 1.3**).

Figure 1.3: Localisation of the Corinth and Patras Gulfs, separating the continental Greece from the Peloponnesus as part of the Mediterranean Sea.

The connection between the Patras and Corinth Gulfs is made by the Rio-Antirio Strait, which is one of the key features of this whole study. The Rio-Antirio Strait displays three sills. From West to East: the Patras sill (50 m depth), the Rio sill (68 m depth), and the Nafpaktos-Mornos sill (98 m depth). The Rio-Antirio bridge connects the north part of the Gulf to the south part and lies close to the Rio sill where the strait is the smallest (2 km wide).

On the south-eastern end of the Corinth Gulf, there is a manmade connection with the Aegean Sea through the Corinth Canal. This canal of 6.5 km long, 21 m wide and 10 m deep cannot, due to its size, be considered as an oceanographic connection to the Aegean Sea (Caterina *et al.* 2022). Its presence is there to allow the passage of boats and/or marine species from the Ionian Sea or the Corinth Gulf to the Aegean Sea without them having to go around the Peloponnesus.

3.2. Physiography of the Gulfs

The study area can be divided into 7 different regions based on their distinct physiographic characteristics (**Figure 1.4**). From west to east, there are the Ionian Sea, Patras Gulf, the Strait & Corinth Entrance, the West Corinth, the East Corinth, the Alkyonides Gulf and the Aegean Sea Regions. The difference in physiography of these regions is strongly related to varying tectonic deformations, sediment supply and hydrodynamics processes which have shaped the seafloor morphology (A. Beckers *et al*. 2016).

The shallow waters west of Cape Araxos were designated as the Ionian Sea Region. This area is a 6 km wide shallow water zone, where the large Achelos River discharges.

The Patras Gulf Region is an extensional and slowly subsiding tectonic basin, with an opening rate of 7 mm yr^{-1} (Briole *et al*. 2021) filled with Plio- Quaternary sediments (Stathopoulou *et al*. 2023). This wide, round-shaped basin has a mean depth of 56 m and a ~138 m deep central depocenter controlled by normal faulting (Ferentinos *et al*. 1985). On its northeastern side, the deformation pattern changes with a dominant right-lateral deformation along its southeast coastline (Rion- Patras Strike-slip fault; (Briole *et al*. 2021)). The gulf narrows sharply and ends at the Rion Strait sensu stricto. The first ~50 m deep Patras Sill occurs, 3 km west of the Rion Strait, and marks the eastern boundary of our defined Patras Gulf Region. Several relatively large rivers flow to the Patras Gulf, the Evinos River (from the north), and the Glafkos and the Piros (from the south).

To the east of the Patras Gulf, the Strait & Corinth Entrance Region is a complex physiographic zone characterized by an eastward deepening of its seafloor, which is the fastest present-day deforming area (11 mm yr^{-1}; (Briole *et al*. 2021)). The western part includes the Rio-Antirio Strait area that comprises in its center the ~115 m deep fault-bounded Nafpaktos Bay. The eastern part shows first a widening and a deepening to ~430 m over a length of ~3 km, and then the occurrence of a plateau. This part of the Corinth Gulf is bordered to the south by steep slopes with an absent or a very narrow shelf and active normal faults near the coastline, while the northern subsiding side has a much wider shelf with bays. The boundary between the Strait & Corinth Entrance and the West Corinth Regions is marked on the seafloor by a ~600 m deep tectonic horst bounded to the east by a canyon (**Figure 1.4**).

The West Corinth Region is characterized by an eastward seafloor widening and deepening to ~870 m depth. The central part of the West Corinth Region is a 9 km wide, ~850 m deep, WNW-ESW elongated flat area. Like in the eastern part of the Strait & Corinth Entrance, the southern coastline is straight and faulted; it is immediately followed by a steep slope without shelf ending in the ~850 m deep flat bottom basin. The northern subsiding shoreline is more convoluted and marked by the SSE-oriented, ~10 km wide, ~20 km long and 0-300 m deep Itea Bay, hanging above the ~850 m deep basin bottom to

the south. Its eastern boundary with the Eastern Corinth Region is marked by a north-south oriented, 15 km long Cape Pangalos.

East Corinth exhibits many similarities with West Corinth. It features the same 12 km wide, ~850 m deep flat central area and similar southern steep slopes and faulted coastlines without shelves. Its northern shore shows a gently southward sloping, 7.5 km wide, 15 km long and 0-300 m Antikyra bay hanging above the ~850 m deep flat depocenter and bordered to the east by a canyon. At the southeastern extremity of this region lies the Lechaio bay ending with the Corinth Canal. East Corinth is limited to the east by an abrupt shallowing of the bathymetry, marked by the Zoodochos Island and by the shallow bay of Lechaio in the south-east.

The Alkyonides Gulf Region, east of Zoodochos Island, is 13 km wide, 22 km long and has a maximum depth of 360 m. Its northern edge is convoluted and marked by small bays, whereas its southern edge is fault bounded, straight, and steep.

The Aegean Sea Region consists of the northwestern end of the Saronic Gulf. This sea is separated from the Corinth Gulf through the presence of the Corinth Isthmus. A navigable connection, the Corinth Canal, crosses the Isthmus but is not considered as an oceanographic connection since the canal is too narrow and very shallow.

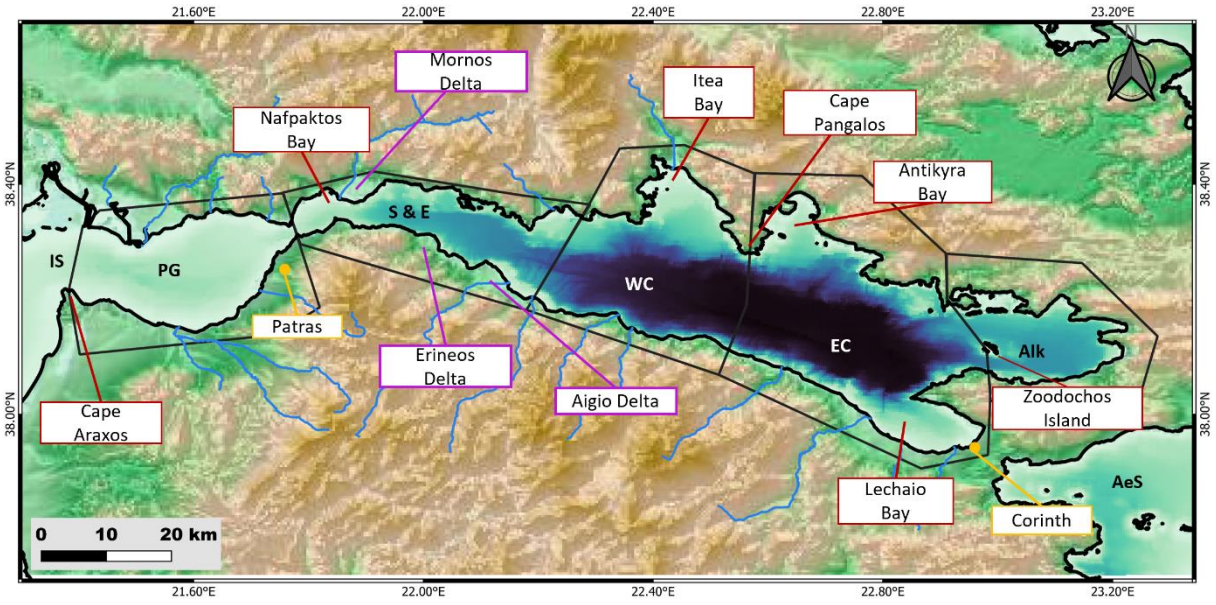

Figure 1.4: Bathymetrical map (GEBCO 2024) of the different regions of the study area: Ionian Sea (IS), Patras Gulf (PG), Strait & Entrance (S & E; also called Western Corinth), West Corinth (WC), East Corinth (EC), Alkyonides (Alk), Aegean Sea (AeS) (from West to East). The bays and capes are in red; the main deltas are in purple, and the cities of Patras and Corinth are represented in yellow

3.3. The Corinth Rift

The Corinth Gulf is observed to be one of the most active rift in the world with an extension of 1.5 cm yr^{-1} (Briole *et al.* 2000). The central part of the rift is subsiding at the rate of 0.7 mm yr^{-1} to 1 mm yr^{-1} since the last 250 ka (Lykousis *et al.* 2007). The rifting in the Gulf

is linked tot its high seismicity and active faulting systems (Brooks & Ferentinos 1984; Armijo *et al.* 1996; Stefatos *et al.* 2002).

The opening of the Corinth Rift is documented as progressive from east to west based on the Moho depth at these location (20 km to 40 km respectively) but no data on the oldest syn-rift deposits can confirm this theory (Sakellariou *et al.* 2001; Lykousis *et al.* 2007). The initiation of the rifting started around the Upper Miocene according to Kelletat *et al.* (1976). The oldest syn-rift sediments are mid-Pliocene volcanics located in the northern part of the Corinth Isthmus (Collier & Dart 1991). The oldest sediment infill for the Proto-Gulf of Corinth consists of Middle to Late Pliocene lacustrine and fluvial sands (Frydas 1987; Zelilidis *et al.* 1988; Lykousis *et al.* 2007).

The syn-rift sedimentation and evolution of the Corinth basin has been heavily studied (Ori 1989; Taylor *et al.* 2011; Ford *et al.* 2013, 2017; Nixon *et al.* 2016; Rohais & Moretti 2017; Gawthorpe *et al.* 2018). The syn-rift evolution of the Gulf of Corinth is divided into three major stratigraphic units: Lower Group (5–3.2 Ma), Middle Group (3.2–0.8 Ma), and Upper Group (0.8–0 Ma) (Rohais *et al.* 2007, 2008).

The rift initiated in the Lower Group between 5 and 3.6 Ma (Ori 1989; Collier & Dart 1991), with Miocene sediments corresponding to a "proto-Gulf of Corinth", initially continental to lacustrine. This Lower Group is subdivided into three formations: (1) Exochi, with massive alluvial deposits evolving into braided river conglomerates. (2) Valimi with gravels and conglomerates in lenticular beds, associated with silts and clays with pedogenetic traces and brackish fauna. (3) Aiges with fine deposits (bioturbated silts and clays) interbedded with sandy gravity-flow beds and tabular conglomerates (debris flows) including lacustrine and marine faunas. These formations reflect alternations between lacustrine and marine conditions, with E-NE oriented fluvial inputs (Ford *et al.* 2017; Gawthorpe *et al.* 2018; Rubi 2018).

The Middle Group (3.2–0.8 Ma) represents the "Rift Climax", marked by a deepening of the basin (3.2–2.6 Ma) and significant sediment supply through progradationnal Gilbert-deltas along the southern margin (Rohais *et al.* 2007, 2008). Sedimentation was concentrated in asymmetric turbiditic systems (Rohais & Moretti 2017), with flow axes progressively shifting from south to north (Ford *et al.* 2017), probably linked to regional tilting.

The Upper Group (0.8–0 Ma) represents the uplift of the Peloponnesus and the filling of the basin during the end of the Pleistocene. From 0.8–0.7 Ma onwards, uplift of the Peloponnese and increased subsidence led to a narrower rift and shorter depositional systems (Rohais *et al.* 2007, 2008). The Gulf opened to the sea through the Isthmus of Corinth and later the Rio Strait (0.6–0.4 Ma, during highstand). Sediment supply came mainly from the southern Peloponnese. In the east (Corinth Bay, Perachora Peninsula), carbonate deposits record sea-level variations and lacustrine/marine transitions. The

area was no longer significantly supplied with sediments; most inputs being trapped further west (Rubi 2018).

Seismic studies of the present Gulf of Corinth reveal Plio-Pleistocene syn-rift sediments that can accumulate up to 2.2 km in the basin (Myrianthis 1984). During this late and ongoing stage, the basin was filled with gravity deposits (turbidites, debris flow, mudflows, etc.) (Brooks & Ferentinos 1984; Piper *et al*. 1990; Poulos *et al*. 1996; Moretti *et al*. 2004; Lykousis *et al*. 2007; McNeill, Shillington, Carter, Everest, Le Ber, *et al*. 2019a; b). These deposits are mostly associated to seismically induced movements, slope failure, storms or extended hyperpycnal discharges (Perissoratis *et al*. 1984; Ferentinos *et al*. 1988; Piper *et al*. 1990; Poulos *et al*. 1996; De Gelder *et al*. 2022; Gawthorpe *et al*. 2022).

During the late Pleistocene, the Corinth basin experienced several disconnections with the Ionian Sea due to the shallow depth of the Rio-Antirio Strait and the sea level fluctuations. Lacustrine sedimentation has been evidenced in the Gulf at several locations (Perissoratis *et al*. 2000; Sergiou *et al*. 2024). During the MIS 5 it is possible that the Rio-Antirio strait was 10 m shallower, leading to less connection with the Ionian Sea (Sergiou *et al*. 2024) Moreover, connections through the Corinth Isthmus to the Aegean Sea might have been possible during higher sea level stages. A shallow water connection during the MIS 5 highstand at this location cannot be neglected ((Piper *et al*. 1990; Collier *et al*. 1992; Caterina *et al*. 2022).

3.4. Oceanography

The hydrological properties of both gulfs (Patras and Corinth) cannot be analyzed separately. These gulfs exhibit typical seasonal stratification in summer and mixing in winter (Friglios *et al*. 1985; Poulos *et al*. 1996). In the Corinth Gulf, the Sea Surface Temperature (SST) is approximately 25 °C in summer and 13.6 °C in winter (Poulos *et al*. 1996). At 200 m depth, temperatures are around 13.3°C in summer and 12.8°C in winter, based on the 1970 dataset (Anderson & Carmack 1973). In the Patras Gulf, central waters reach around 25 °C in summer while waters near the Rio-Antirio Strait are cooler, about 23 °C (Friglios *et al*. 1985). Salinity in the Patras Gulf is slightly higher due to the mixing between the salty waters from the Ionian Sea (38.6-38.7) and the less salty waters from the Gulf of Corinth (38.3-38.5) (Anderson & Carmack 1973; Friglios *et al*. 1985).

Two major hydrodynamic processes have already been identified in the two gulfs. The first type are gyres mainly driven by the winds that were described in the two gulfs. The prevailing winds are mostly E or WSW oriented and are funneled by the surrounding mountain ranges (Poulos *et al*. 1996; Koletsis *et al*. 2014). Cyclonic gyres have been observed in surface waters in the eastern Corinth Gulf in front of Antikyra Bay and in the Patras Gulf using satellites data (Lascaratos *et al*. 1989). In Patras, the hydrodynamic models show (Fourniotis & Horsch 2010, 2015) that the wind-induced cyclonic gyre affects the entire Gulf with colder waters in its center. The second type of hydrodynamic

processes are wind-induced upwellings. These have been evidenced on the northern shoreline of the Corinth Gulf and in the northeast part of Nafpaktos Bay between the two gulfs by using satellite data (Lascaratos *et al*. 1989). An upwelling was evidenced by modelling in front of the city of Patras (Horsch & Fourniotis 2017).

Between the two gulfs, the hydrodynamic circulation is controlled by the tides (Rubi *et al*. 2022). Even if the Corinth and Patras Gulfs are characterized by a microtidal environment with an average tidal amplitude variation of 15 cm, the constriction at the location of the Rio-Antirio strait area generates a strong amplification of the tidal currents. Surface current velocity can reach up to 1 m s^{-1} and bottom currents up to 3 m s^{-1}, as evidenced by ADCP data (Rubi *et al*. 2022). High-velocity surface currents in the Rio-Antirio Strait area have also been observed in a hydrodynamic model (Fourniotis & Horsch 2010) which focused on the Patras Gulf. This model highlights the funneling of waters at the Rio-Antirio strait sensu stricto. The effects of the tides are the following: during ebb tide, the surface waters are rising from Corinth (considered as the closed basin) towards Patras (open basin); while during flood tide, the surface waters flow from Patras to Corinth (Rubi *et al*. 2022; Caterina *et al*. 2025). The very high-velocity bottom currents are associated with a strong internal tide. The Corinth internal tide operates differently from the surface oceanic tides. Since the internal tide frequency is twice the one from the oceanic tide, during ebb tide, if the phases of both tides align some deep water from Corinth can overflow the bathymetric step of the strait and cross it to reach Patras Gulf from the bottom. In other situations, bottom waters flow should be reflected to the Corinth basin, not crossing the strait (Rubi *et al*. 2022).

4. Objectives

This thesis has several objectives.

First, the hydrodynamics of the Gulf of Corinth will be analyzed first at the surface with satellite data, then in the whole water column by using Regional Oceanographic Modelling System (ROMS). This redefinition of the circulation and of the oceanographic features is needed since technologies and even the dynamics have evolved since the last studies in the 90's (Lascaratos *et al*. 1989; Poulos *et al*. 1996).

Studying hydrodynamics with a focus on the Rio-Antirio strait will allow us to observe, constrain and define the important parameters that control and that are impacted by this bathymetric constriction. The hydrodynamics of the Rio-Antirio strait will support the observations previously made on the seafloor geomorphology (Rubi *et al*. 2022).

Then, once the hydrodynamics, particularly the situation at the bottom, are understood and well defined, the interaction with the sediments will be observed. This is mainly to get the complete overview over previous assumptions and hypotheses made by the observation of seismic lines and cores across the Corinth Gulf (A. Beckers *et al*. 2016; Gawthorpe *et al*. 2022; Sergiou *et al*. 2024).

Finally, to assess the connection and disconnections the Corinth Gulf has supposedly seen through its evolution, modelling of paleogeographic conditions will be operated. This modelling will offer answers to questions related to diverse dynamics that might have happened in the Corinth Gulf. This will be done by the test of 4 hypotheses: (1) Shallowing the Rio-Antirio strait by 10 m (Sergiou *et al*. 2024). (2) Shallowing the Rio-Antirio Strait by 25 m. (3) Have a connection only with the Aegean Sea with a closed Rio-Antirio Strait. (4) Opening the Corinth Gulf at the Rio-Antirio Strait and at the Corinth Canal location (to connect to the Aegean Sea) (Collier & Dart 1991; Caterina *et al*. 2022).

Chapter 2: Tidal straits in the Gulf of Corinth

This chapter will resume the starting point of the thesis with the focus on the straits of the Corinth Gulf. The dynamics of the actual strait (Rio-Antirio) have been observed and detailed in Rubi *et al.* (2022). The outlines of the paper and the questions it raised will be developed in this chapter.

Regarding the other end of the Corinth Gulf, in 2022, we supposed the presence of a past strait at the Corinth Canal location (Caterina *et al.* 2022). These observations were based on geological clues and led to diverse hypothesis concerning the connections between the Gulf and the Aegean Sea. These findings and hypothesis will be summarized in this chapter.

1. Rio-Antirio, the actual strait

1.1. Settings

The Rio-Antirio strait consists of 3 sills: from West to East, the Patras sill (50 m depth), the Rio sill (68 m depth), and the Nafpaktos-Mornos sill (98 m depth). These sills happen to be relevant since they shape the bathymetry of the strait and therefore influence the bottom currents that circle through the strait. The Rio sill marks the maximal constriction of the strait with a 2 km width. The enlargement of the strait is in the Patras Gulf that widens next to the strait and in the Corinth Gulf with the Nafpaktos Bay **(Figure 2.1**). The end of the strait area is limited by the Drepano spit and the Mornos Delta (Nafpaktos-Mornos sill). The bathymetry of the strait appears to be shaped by the currents and by faults (Briole *et al.* 2000; A. Beckers *et al.* 2016).

The few oceanographic information available for the strait area reveals that there is a mixing of the Patras and Corinth waters in the strait. In summer, the water of the straits are registered to be at 26 °C at the surface and at 21 °C at 60 m depth (Anderson & Carmack 1973; Lascaratos *et al.* 1989; Poulos *et al.* 1996). In winter, the temperature seems to homogenize around 13 °C to 14 °C.

Modelling through the Patras and Corinth Gulf revealed the presence of an internal wave and the dominance of tides in the strait (Fourniotis & Horsch 2015; Horsch & Fourniotis 2017; Fourniotis 2024). The tidal amplitude of in the strait is around 20 cm (Flanders Marine Institute (VLIZ) 2025). The tide amplifies the currents in the strait up to 2 m s^{-1} and generates an internal wave with a 20 m to 25 m amplitude (Fourniotis & Horsch 2015; Fourniotis 2024). The winds, able to reach a maximal speed of 15 m s^{-1}, appear to also affect the dynamics in the strait with a deepening of the thermocline of 60 m in the Patras Gulf (Fourniotis & Horsch 2010; Koletsis *et al.* 2014).

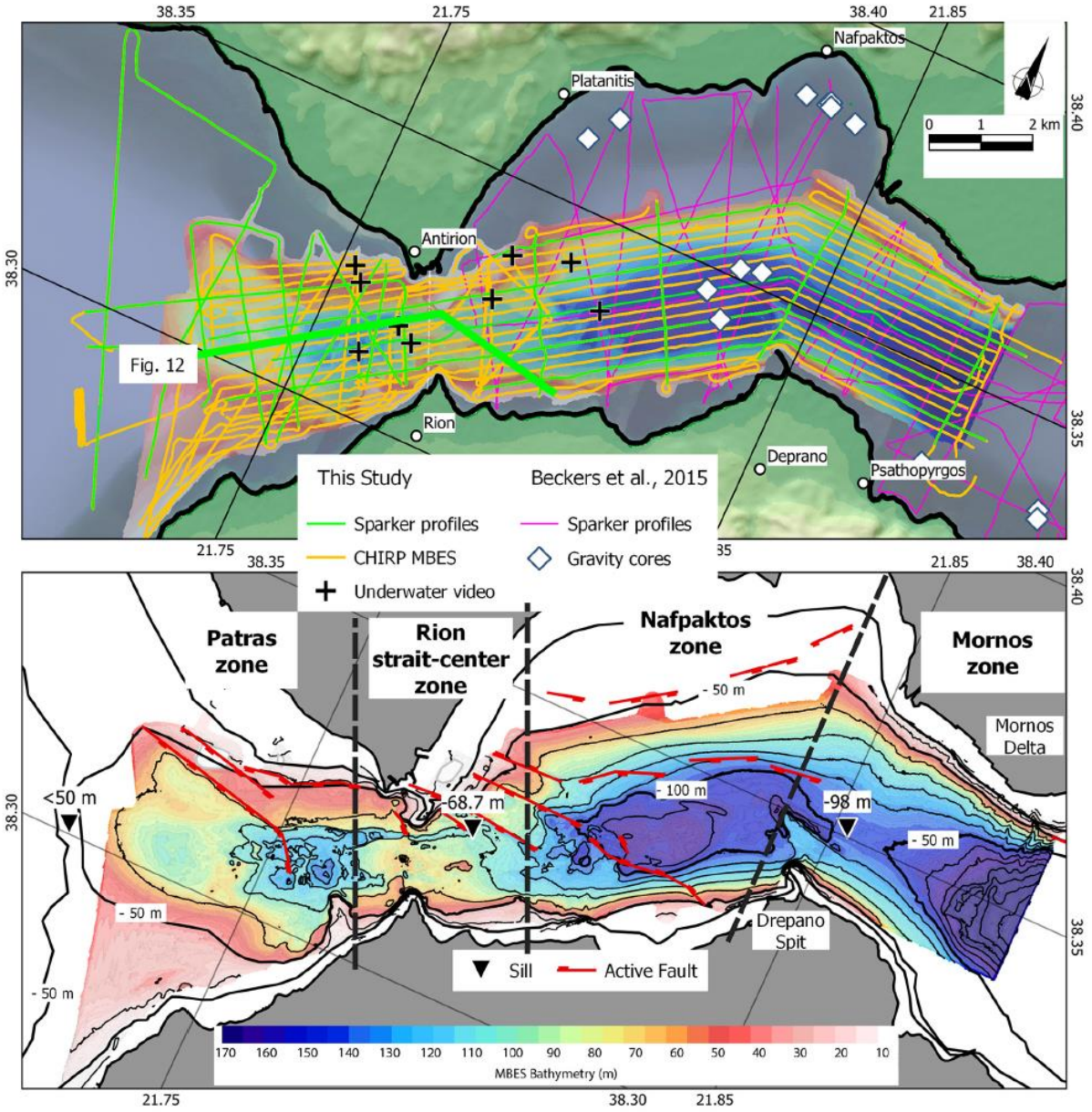

Figure 2.1: A. Data map with the location of seismic profiles and ADCP tracks. B. Detailed multibeam bathymetry and strait areas. Fig. 2 in (Rubi *et al.* 2022).

1.2. Data acquired

The strait was analyzed through several angles. Below the seafloor, a chirp Sub-Bottom Profiler and high-resolution seismic reflection sparker were used. For the sea floor itself, a multibeam echosounder (MBES) has been used. The water column was analyzed through an Acoustic Doppler Current Profiler (ADCP) and a Conductivity Temperature and Depth sensor (CTD) (Rubi *et al.* 2022). Details for the methodology can be found in Rubi *et al*. (2022).

The MBES data were acquired through Hypack 2016, while Elac's HydroStar software was used as the inertial beam forming navigation and attitude system. A Real Time Kinematics (RTK) GPS was used to obtain a 10 cm lateral positioning accuracy. The MBES survey was

performed with a dual-head MBES Elac Nautic Seabeam 1185, transmitting at 180 kHz. Geocoder tool (Hypack 2016 suite software) was used to identify and correct radiometric and geometric MBES backscatter artifacts. The MBES time series were also corrected for the tidal effects based on Patras tidal curves (data from www.worldtides.info). The MBES data covered an area of 211 km2 and provided a 5 m × 5 m lateral resolution bathymetric map.

The ADCP and MBES data were calibrated with CTD and sound velocity profiles on the water column using a Valeport MiniSVS-P. The ADCP times series were tied with the Patras tidal curves. The ADCP and CTD data were analyzed with Ocean Data View software (Schlitzer 2021). The MBES morphologies were displayed with QGIS software and with the extraction of bathymetric swath profiles across curved geomorphic features such as channels (Hergarten *et al*. 2014).

Sea Surface Temperature (SST) was studied by using L3 level data from CMEMS (Buongiorno Nardelli *et al*. 2013; CMEMS 2025) that were processed with Julia language as NETCDF files (Barth 2024). This product has a 0.02 x 0.02 degree resolution and was used to calculate SST average from 1st January 2019 to 1st January 2020. The area studied for the SST satellite coverage was extended to the whole Corinth Gulf and the divisions in sub-areas are as follows: Ionian region, Patras Gulf, Nafpaktos area and Corinth Gulf.

Lately, during the analysis of this thesis results, Regional Oceanographic Modelling System (ROMS) results were used to calibrate the tides for the ADCP Data. This manipulation has been done to correct what was described in Rubi et al. (2022). ROMS was used following the methodology described in detail in Caterina et al. (2025) over the month of May 2019 to fit the dates of the marine campaign previously done. From the ROMS output, zeta was used to get the tidal amplitude and slopes in the Strait. These data were validated for the building of ROMS from May 2023 through tidal gauge (Flanders Marine Institute (VLIZ) 2025) but no in-situ data from 2019 was found to validate it for the 2019 period.

1.3. Observations

1.3.1. Sea Surface Temperature

Having a “recent” overview of the SST in the Patras and Corinth Gulfs over a complete year allow to observe monthly SST depending on the selected areas (**Figure 2.2**). Overall, summer SST can reach up to 26°C and winter SST does not go below 13°C. Nevertheless, regional differences appear as the Ionian waters are always hotter than the Patras and Corinth ones. The Nafpaktos area remains the coldest area all year long. The Corinth Gulf is colder at the surface than the Patras Gulf except during some summer months. The SST boundary between the two gulfs was observed in the strait and the “cold spot” of the Nafpaktos area was attributed to an upwelling from the Corinth Gulf as outlined by Lascaratos et al. (1989).

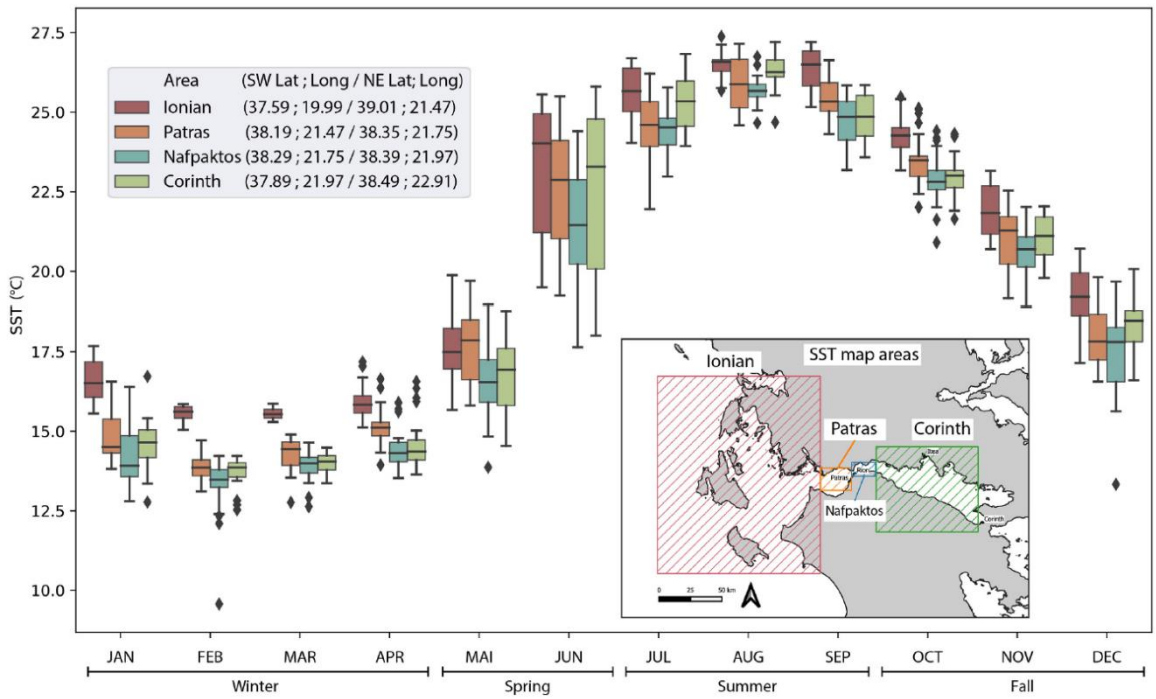

Figure 2.2: Monthly Sea Surface Temperature for the year 2019 with colors representing each area (Ionian, Patras, Nafpaktos and Corinth). Fig. 3 in Rubi et al. (2022).

1.3.2. Currents

The currents circulation was based on the ADCP data correlated with the tides. Here, reviews have been made after the analysis of the ROMS output validated for May 2023 (Caterina *et al.* 2025) and adapted to May 2019. The main outbreak is the inversion of the tidal phases compared to what was initially published in Rubi et al. 2022. Therefore, in this chapter, the results from the 2022 study will be interpreted with the flood tide matching the waters going from Patras to Corinth and the ebb tide with waters flowing from Corinth to Patras (**Figure 2.3**). Although it can be confusing due to the basins characteristics, the "new" phases of the tides are following what was established by Defant (1958) with the flood going towards the enclosed basin. This modification only affects the direction of the currents during the newly established phases but does not affect their intensity nor their interactions with the bottom and the bathymetry of the strait.

During flood tide, surface currents go from Patras to Corinth and can reach up to 1 m s^{-1} at the surface. This is common in straits due to tidal amplification induced by a restricted bathymetry (Gibbard 1995). These stronger currents can reach the Drepano spit, the Nafpaktos Bay and the Corinth Gulf. At the bottom, the current was observed to go in the other direction and to be significantly faster (up to 3 m s^{-1}) and more turbulent (**Figure 2.4**). After reaching the stage of high tide where currents appear slower, their velocity is increased at the start of the ebb tide. During this period, the currents are observed to be oriented in both directions and towards the southwest during the middle of the ebb tide (**Figure 2.3**).

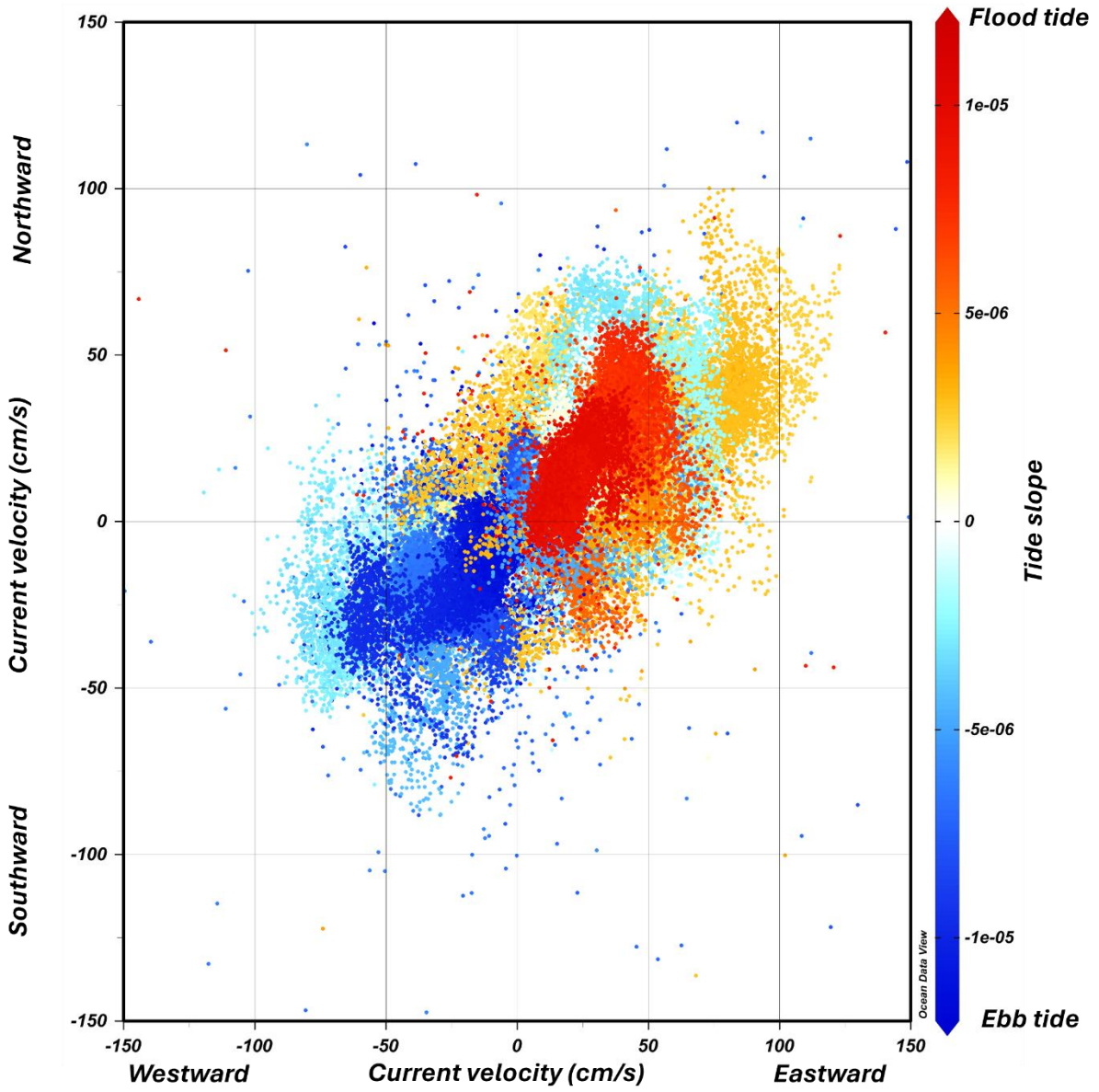

Figure 2.3: Current direction vs tide slope based on ADCP data in the strait area. The slope tide is extracted from the ROMS output for May 2019. Modified from Fig. 5 in Rubi et al. (2022).

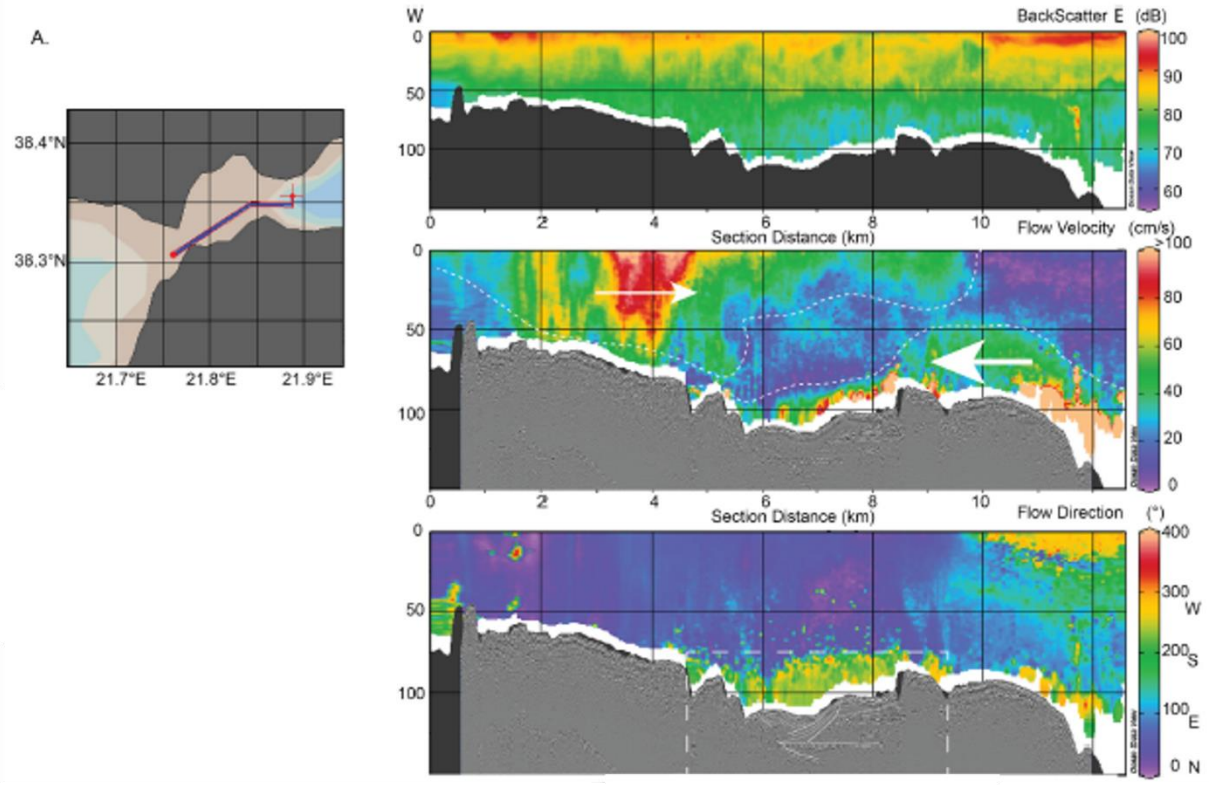

Figure 2.4: (A) Sections of the strait with the backscatter, current velocity and direction of the flow from the ADCP data.

1.3.3. Bathymetry and morphologies

The center of the strait consists of a plateau bounded by steep northern and southern slopes (**Figure 2.5**). This plateau is cut by a moat (a wide channel) forming a U-shaped valley parallel to the coastline. This moat, not associated with any river, might be due to the bottom currents at this location. These bottom currents were observed to cascade from the plateau to the Patras Gulf. The presence of pools can be referred to super-critical flows generating hydraulic jumps (Cartigny *et al.* 2014). This moat and the presence of the plateau with a small terrace in the western part of the strait lead to the water cascading in the Patras Gulf entrance. The association of turbulent currents and the lack of deposition in these locations create and maintain pool and crest (erosional features) in place. These deep pools have a diameter ranging from 100 m to 340 m (**Figure 2.6**).

In the eastern part of the strait, a channel is observed and is to be associated with the faulting in the area. This channel widens at the bottom of the deeper area that is in front of the Nafpaktos Bay. In the Nafpaktos Bay, sediments are observed plastered by the bottom currents on the northern slope of the strait (A. Beckers *et al.* 2016). The rest of the area is a giant pool (~120 m depth) reaching the Drepano Spit and marking the erosion in this area (**Figure 2.7**). The erosion is due to the bottom currents that alternate directions due to the internal tide.

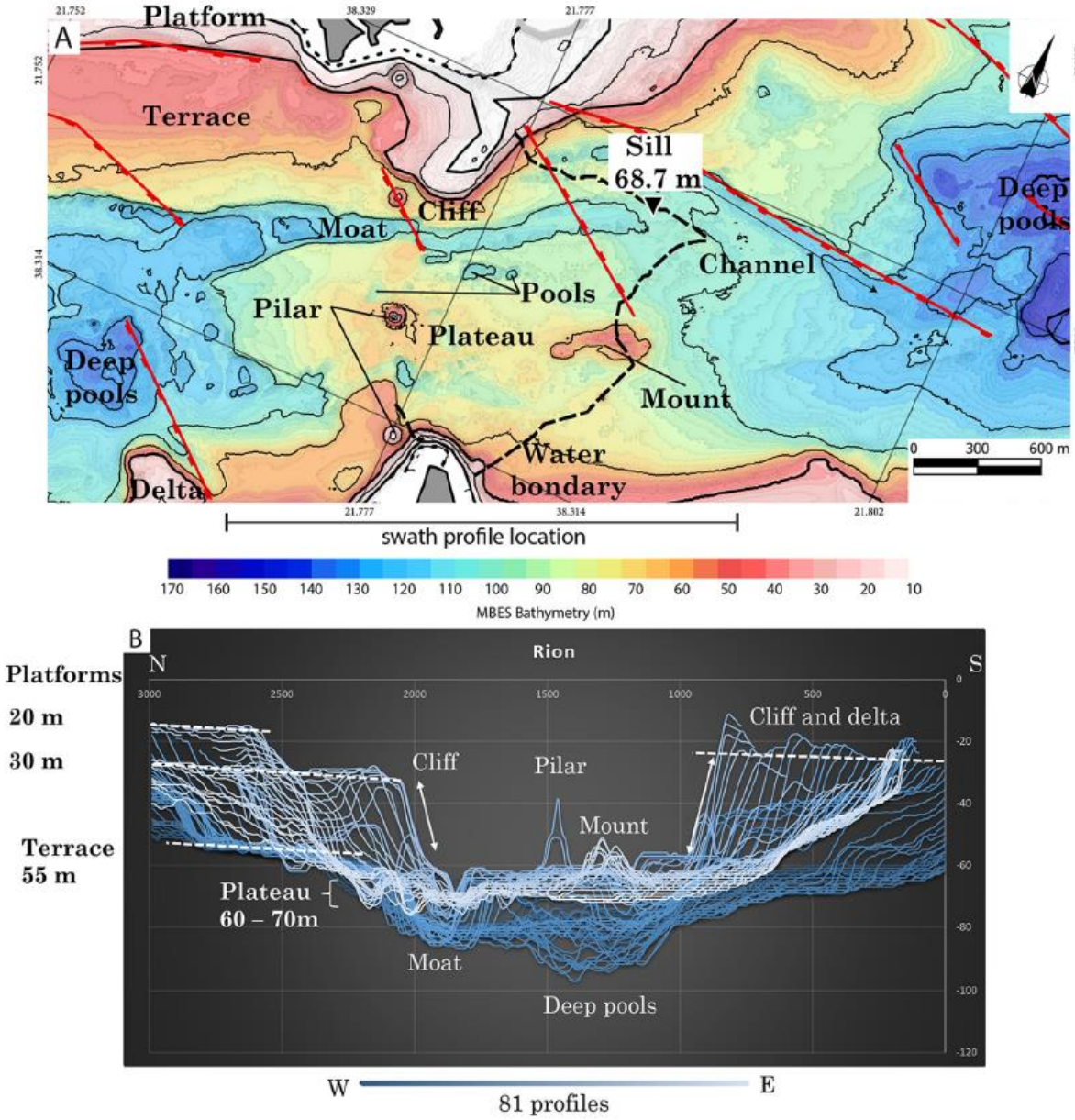

Figure 2.5: (A) Morpho bathymetry of the Rio Strait sensu stricto. (B) N-S swath profiles with dark blue for western profiles and light blue for eastern profiles (modified from Rubi et al. (2014)).

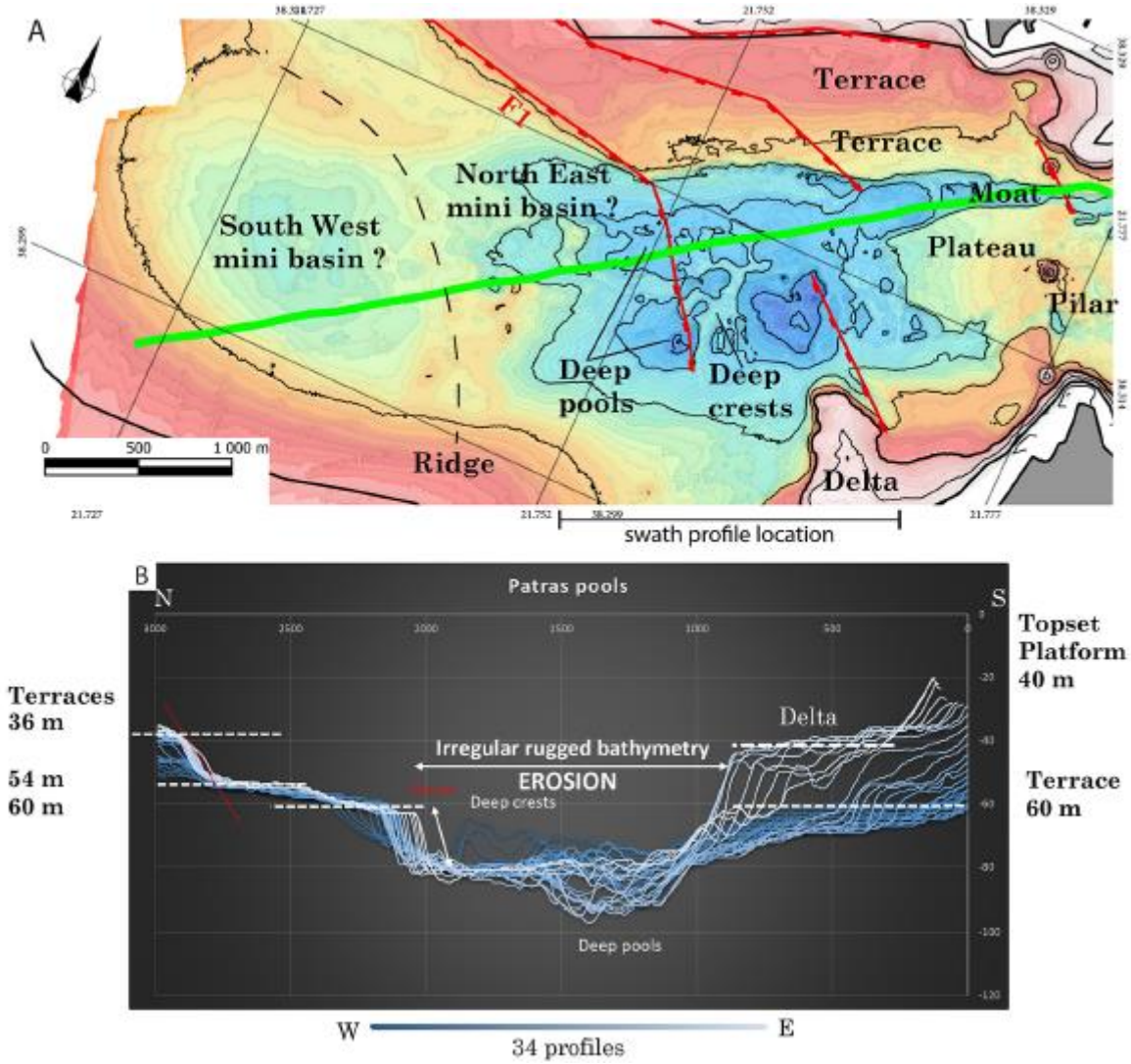

Figure 2.6: (A) Morpho bathymetry of the Patras Gulf near the strait. (B) N-S swath profiles with dark blue for western profiles and light blue for eastern profiles (modified from Rubi et al. (2014)).

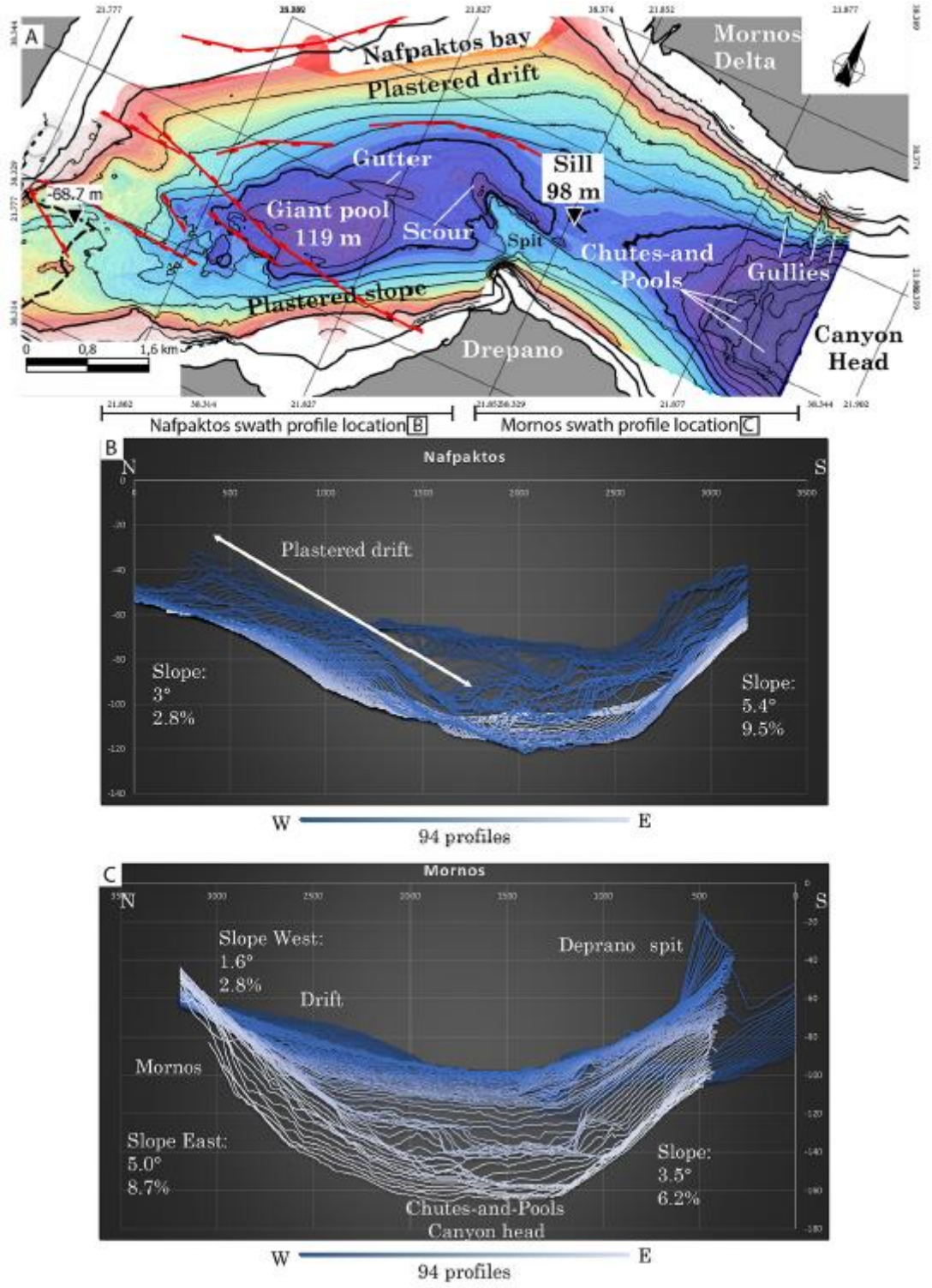

Figure 2.7: (A) Morpho bathymetry of the Nafpaktos/Mornos area. (B, C) N-S swath profiles with dark blue for western profiles and light blue for eastern profiles (modified from Rubi et al. (2014)).

1.4. Impact of tidal currents

The features observed in Rio-Antirio strait are shaped by an asymmetric hydro-sedimentary system dominated by tides and internal tides. The strait presents some differences with the depositional model for tidal straits proposed by Longhitano (2013). Indeed, the lack of dunes and more generally the lack of tidal deposits is not observed.

Instead of the dune-bedded strait zone with 3D and 2D tidal dunes, deep pools with steep borders were observed and interpreted as erosional areas with coarse-grained sediments, pebbles and sand carried by turbulent bottom currents, which digs the seafloor by analogy with the stream pothole. The present study raises the possibility that the usual dune-bedded strait zones can be dominated by pool-and-crest morphology in relation to seafloor erosion on each side of the sill by the internal tides. We suppose that turbulent flowing plays a key role in this case.

Added to the turbulent flow, the internal waves are also restricted or empowered by the bathymetry and the tidal cycle. With the observations it appeared that the internal tide has a frequency that is higher than the surface tide (**Figure 2.8**). This frequency difference can lead to a strait overflow from the bottom currents to the Patras Gulf during ebb tide. On the other hand, the bottom waters from the Corinth Gulf can stay enclosed when the surface tide is not going towards the Patras Gulf (flood tide where the flow is directed to Corinth).

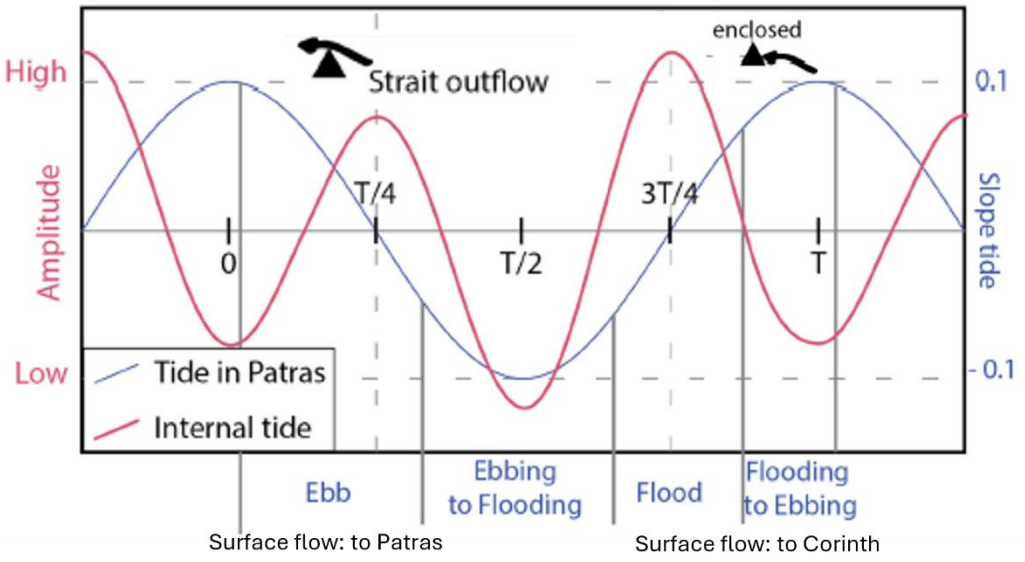

Figure 2.8: Amplitude of the surface tide and internal tide in the Patras Gulf. Modified from Rubi et al. (2014) with observations from Caterina et al. (2025).

2. Corinth Canal

2.1. Settings

The Corinth Isthmus is a ~10 km wide corridor located at the southeastern end of the Corinth Gulf. The isthmus is bounded by the Loutraki fault to the north and the Kechriaie fault to the south **(Figure 2.9**). On the north of the Loutraki fault, the basement is made of

flysch, chert limestones and ophiolites while on the south of Kechriaie fault, there is the presence of a limestone horst. Splitting the isthmus in half is the Canal of Corinth.

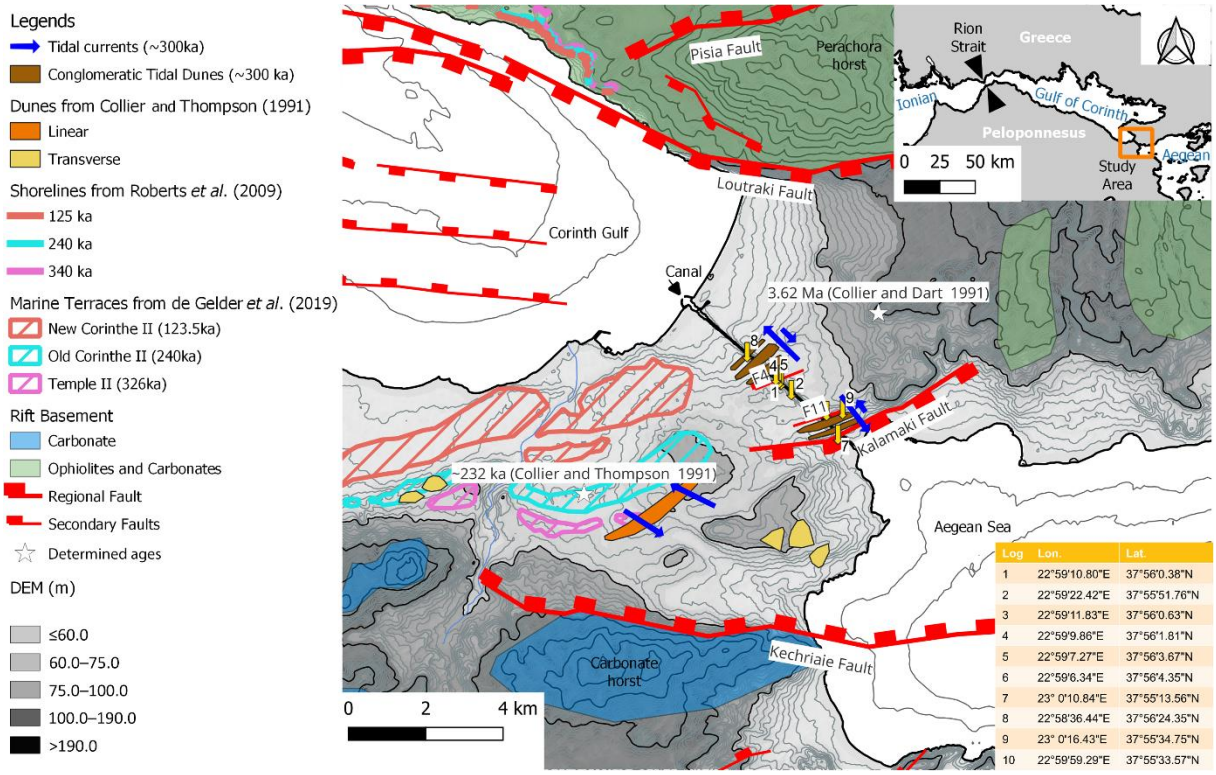

Figure 2.9: Map of the Corinth Isthmus and the position of the logged sections along the Corinth Canal (Caterina *et al.* 2022). The basement and faults are compiled from Pallikarakis (2018) and Fernández-Blanco *et al.* (2020) and the marine terraces from de Gelder *et al.* (2019).

This manmade canal represents a basin-scale outcrop of 6.4 km long and up to 80 m high to study the connections between the Corinth Gulf and the Aegean Sea. Due to the uplift of the area at an average rate of 0.3 m/ka over the last 205 ka (Collier 1990) the Canal presents a central horst and an adjacent graben (Isthmia Graben) (**Figure 2.10**) separated by the Kalamaki-Isthmia fault.

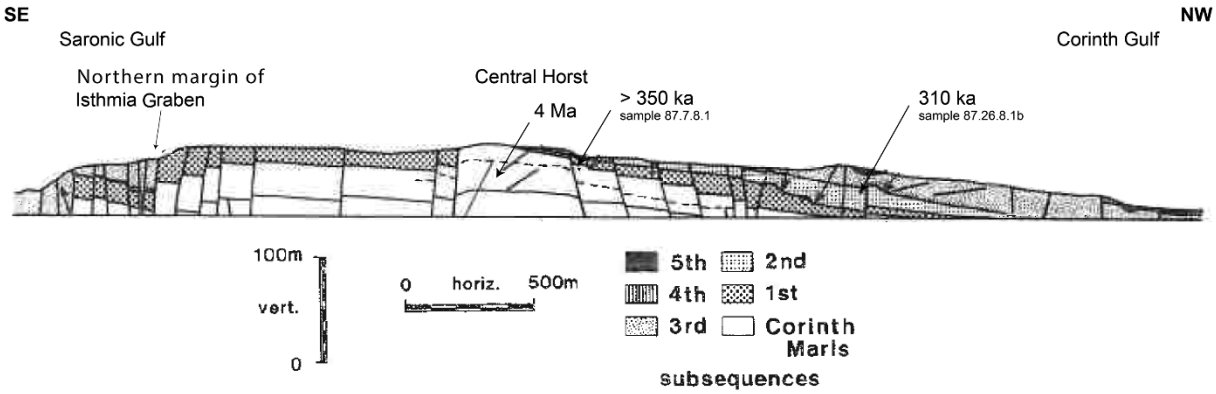

Figure 2.10: Modified section proposed by Collier (1990). The section presents the central horst with the Corinth Marls and the five transgressive subsequences. All the sample numbers refer to the study by Collier (1990) and the ages to the one of Collier and Dart (1991).

The sedimentary evolution of the canal section is revealed by sequences that comprise lower Pleistocene lacustrine Corinth Marls at the base (sensu Collier 1990) that are overlain by marine tidal sediments (von Freyberg 1973). These middle–upper Pleistocene marine sediments have been interpreted and subdivided into five transgressive subsequences: wave-reworked conglomerates (first) and beach–shoreface sandstones (second and third); oolitic calcarenites (fourth); and fluvial deposits and soils (fifth). These five subsequences have been tied to major eustatic sea-level fluctuations with a periodicity of c. 100 kyr (Collier 1990). In the SE part of the canal (i.e. in the Isthmia Graben), boreholes studies have highlighted conglomeratic sands that can be associated with a fluvial environment (Papanikolaou *et al.* 2015). In these boreholes, foraminifera assemblages indicate a shallow-marine environment between a lagoon and a more coastal environment at c. 175 ka (Papanikolaou *et al.* 2015).

2.2. Data acquired

During a field campaign (20 to 27 August 2020), sedimentological descriptions and drone photogrammetry study were made. Ten high resolutions millimeter-scale vertical sedimentological sections were described to document the facies and facies associations. The sedimentological data included: grain size, grain type, sedimentary structures, color, texture, and fossil types and bioturbation. Although originally indicated for fluvial deposits, the Miall facies codes (Miall 2006) were applied to describe the textural facies features of the marine deposits. This choice was based on their very similar attributes when compared to fluvial facies. The complete facies and facies association list can be found in the Tables 1 and 2 from Caterina et al. (2022). For this summary, only the facies associated with the FA6 (Conglomerate tidal dunes) in Caterina et al (2022) will be detailed (**Table 2.1**).

The drone survey consisted of 24 flights that gave a total of 15 497 photographs to compute the photogrammetric model of the canal, including both of its walls. The model was constructed using Context-Capture from the Bentley suite of software. The model interpretation was performed using IFPEN's Virtuoso software, which enabled work to be carried out on an adaptive zoom mesh model (Schmitz *et al.* 2014). The geometries were constrained and quantified in 3D. Sequences based on major unconformity surfaces that are continuous for more than 1 km were mapped. The drone acquisition and the building of the photogrammetric model led to the creation of a schematic section for the Corinth Canal (**Figure 2.11**).

Table 2.1: Facies

Facies	Description	Geometry	Interpretation
Silt			
Fc: Silt with floating granules	White silt with floating granules levels. Granules are matrix supported and mainly aligned. Some bivalve's phantoms are observed.	Beds are 1 cm to 30 cm thick.	Settling deposits reworked by bottom currents. The granules are interpreted as lag deposits (Rebesco *et al*. 2014; Rubi *et al*. 2018).
Sand			
Sm: Fine- to medium-grained massive sand	Massive to crude inverse- to normal-grading with: - Few shells (whole and debris) - Bioturbations. Poorly lithified	Beds are 0.5 to 1.5 m thick.	Grain-flow (Donald R. Lowe 1982)
Sp: sand with planar cross-stratification	Medium-grained sandstone with planar cross stratifications. Alternative direction of the planar oblique stratifications is leading to herringbone cross bedding.	Beds are cm thick.	The planar cross stratifications indicate a tractive current (Rubin & Carter 1987; J. G. Venditti *et al*. 2005). The herringbone cross bedding highlights a tidal current (Hutchison 2005) by the migration of straight-crested dunes under lower bed-shear stress values (Rubin & Carter 1987; J. G. Venditti *et al*. 2005).
St: sand with trough cross-stratification	Fine- to medium-grained sandstone with trough cross-stratifications.	Beds are cm thick with large dunes and anti-dunes geometries.	The trough cross stratifications indicate a tractive current by the migration of sinusoidal-crested dunes under high bed-shear stress values (Rubin & Carter 1987; J. G. Venditti *et al*. 2005).

Conglomerates			
Gmg: conglomerates with mudclats	Massive, matrix-supported conglomerate with: - Clasts: granules to pebbles - Matrix: silt to medium-grained sand; carbonated - Erosive base with mudclasts - Crude normal grading - Bioturbated at top	Beds are ~1.5 m thick.	Sub-aqueous mass transport deposit (Nemec 2009; Nugraha *et al.* 2020).
Gcm: Massive clast-supported granules with pebbles	Massive clast-supported granules and pebbles beds, erosive at base.	Beds are ~1 m thick.	High-energy tractive currents (Martín *et al.* 2001, 2009, 2014).
Gh: horizontal granules	Horizontal beds of coarse-grained sand to granules with aligned pebbles on surface. Well-sorted and well-bedded	Beds are ~10 cm to 20 cm thick. Stacked in unit of 3 m thick.	Gravel lag indicates bypass and erosion by high velocity tractive currents (granules to pebbles; in strait-centre (Sergio G. Longhitano, 2013)).

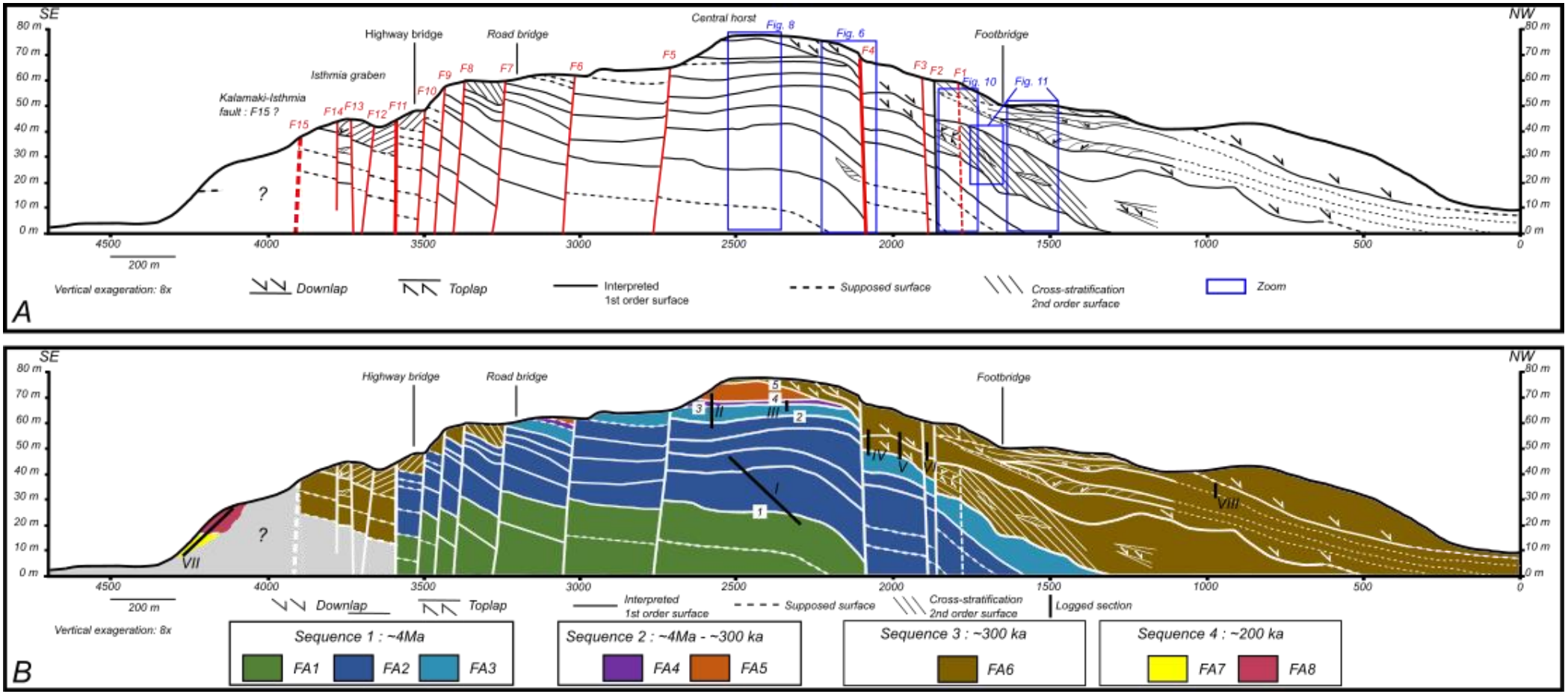

Figure 2.11: Sections of the SW wall of the Corinth Canal. (A) Structural section displaying all the features identified in the field or the model. The faults are numbered from NW to SE, and the location of the Isthmia Graben and the horst are based on the section by Collier (1990). (B) Section showing the facies associations (FAs), the logged sections and identification of the numbered unconformity surfaces that define the sequences associated with their age, based on Collier (1990) and Collier and Dart (1991).

2.3. Results

2.3.1. Facies and Facies association

From the 21 facies recorded along the Corinth Canal, only 8 are present in the FA6 (strait conglomerate tidal dunes). These facies are Gp, St, Sp, Gh, Gmg, Fc, Sm and Gcm (**Table 2.1)**.

FA6 consists mainly of planar and trough cross-stratified sands, granules and conglomerates interbedded with herringbone cross-bedding in a partially reddish matrix. FA6 is thicker on both ends of the canal section (20 m thick in the SE and 40 m thick in the NW) and eroded or undeposited in its central part (**Figure 2.11**).

The base of FA6 is erosive, and the first-order surfaces are erosive, as evidenced by both toplap and downlap stratal terminations and undulated surfaces. The planar and trough cross-stratifications that downlap in two opposite directions (NW and SE) are delimited by the F10 fault: they dip towards the NW to the NW of the F10 fault, and towards the SE to the SE of the F10 fault (**Figure 2.11**).

On the NW end of the canal section, we observed second-order surfaces that consist of large-scale asymmetrical herringbone cross-bedding with lower and thicker (c. 7 m) foreset bedding with a low angle (c. 10°) to the NW, and upper thinner (c. 1.5 m) foreset bedding with a higher angle (20°) to the SE (**Figure 2.12**).

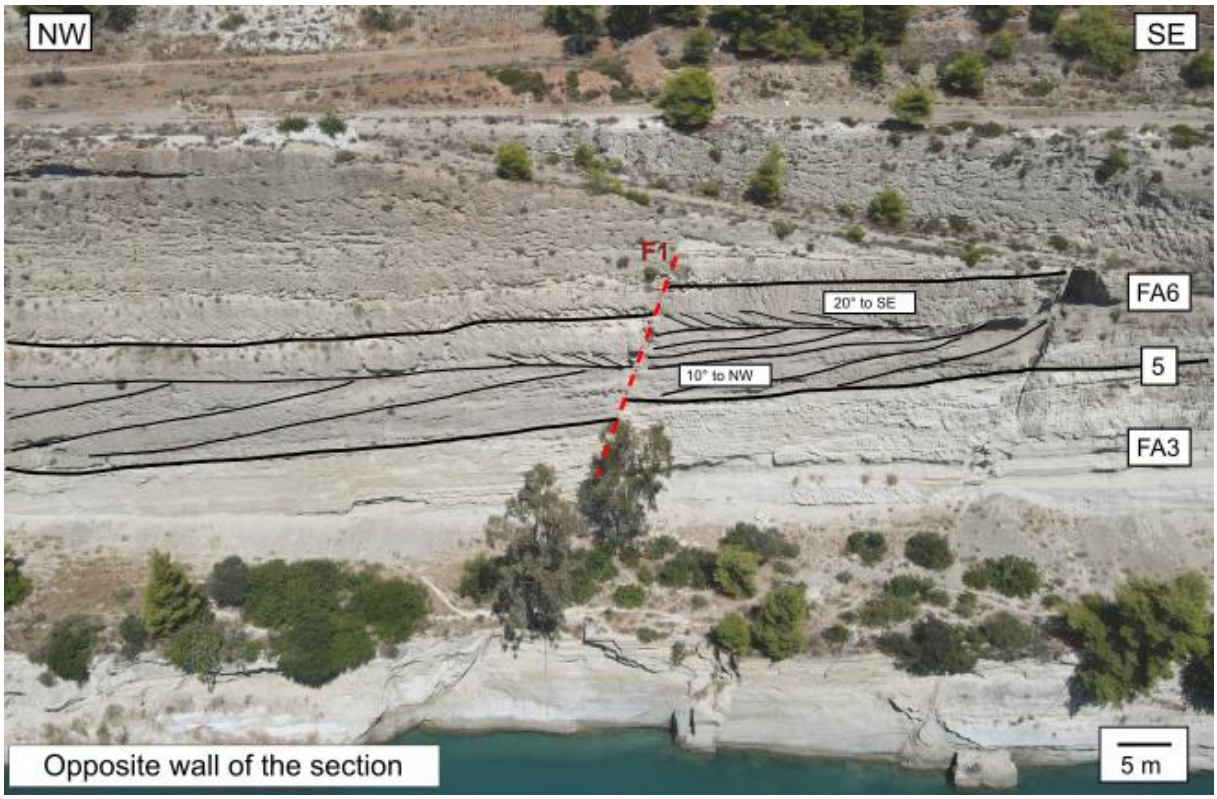

Figure 2.12: Close-up of the asymmetrical herringbone cross-stratification with the main migration direction towards the NW (FA6). The thicker lines represent the first-order surfaces, the medium lines represent the second-order surfaces and the thinner lines are the third-order surfaces.

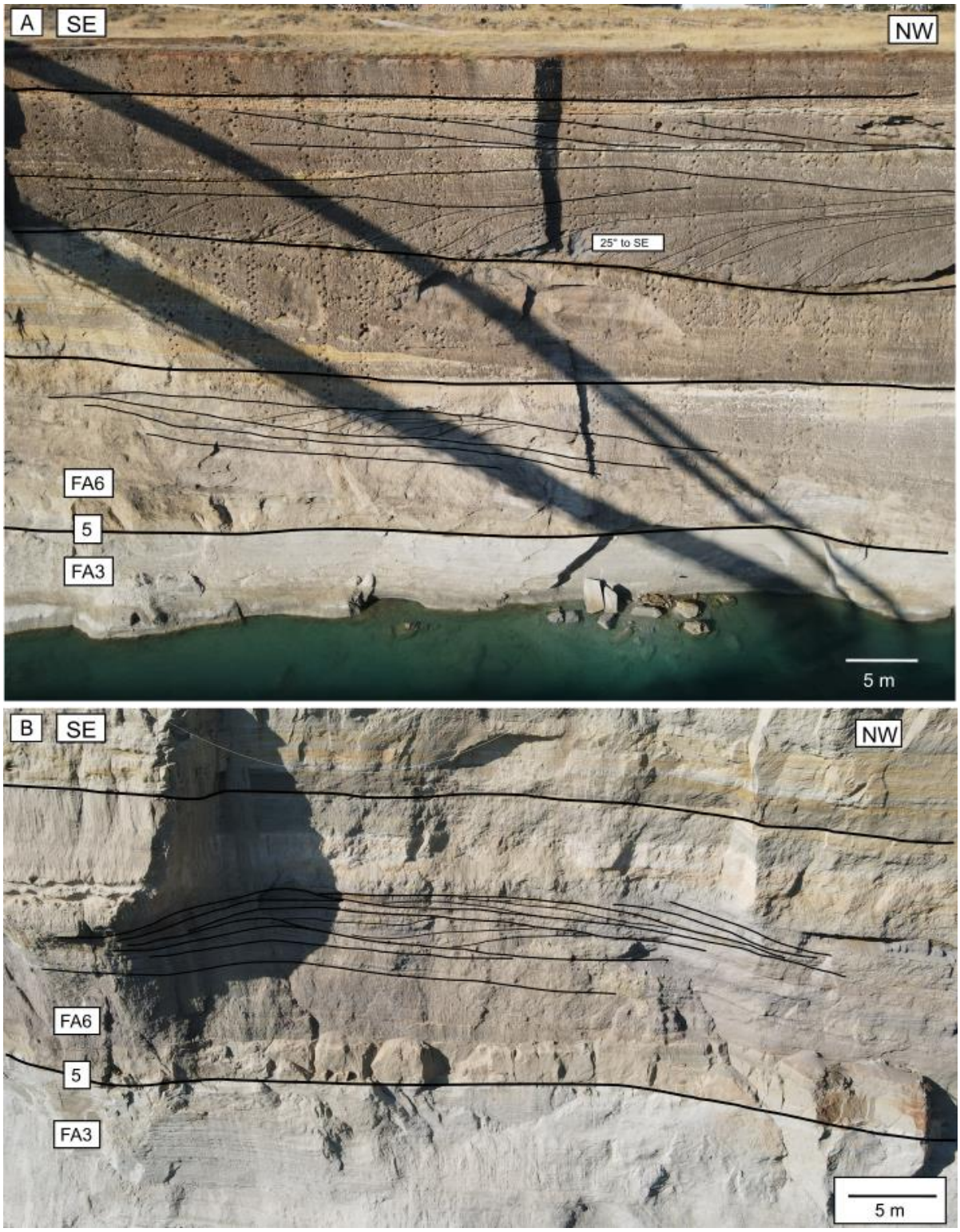

Figure 2.13: Close-up of some of the compound-dune features cropping out in the FA6 conglomeratic beds with the migration direction towards the NW and the secondary reverse foreset direction towards the SE. (A) Second-order surfaces (medium thickness lines) are observed to be downlapping onto first-order surfaces (thickest lines; to the NW). The third-order surfaces (thinner lines) downlap in the opposite direction (to SE) on both the first- and second-order surfaces, forming dune structures. The dip angle is larger for the surfaces downlapping towards the SE than for the surface downlapping to the NW. (B) Similar features to those shown in (A).

At the third order, we document compound-dune formations with dominant foreset deposition towards the NW and a subordinate reverse foreset direction towards the SE (**Figure 2.13**).

At the facies scale, FA6 is dominated by oblique cross-stratified conglomerates (facies Gp), and trough (facies St) and planar (facies Sp) oblique cross-stratified sandstones. These oblique cross-stratified deposits can be overlain by horizontal clast-supported conglomerates (facies Gh, Gcg and Gcm), gravel lags (facies Fc) and massive sandstones (facies Sm). The oblique cross-stratification (facies Gp, St and Sp) is outlined by meter-thick beds internally organized into centimeter- to decimeter-thick foresets based on erosional surface and are normally graded (**Figures 2.14; 2.15**); the tops of the beds can be either eroded or preserved. The facies grain-size sorting shows a high variability from very poorly sorted to well sorted clasts (**Figure 2.15 A, B**). We report occurrences of herringbone cross-bedding in medium-grained sandstones (facies Sp) interbedded with horizontal conglomerates (facies Gh: **Figure 2.15 C**). Along the logged section, no evidence of mud is observed.

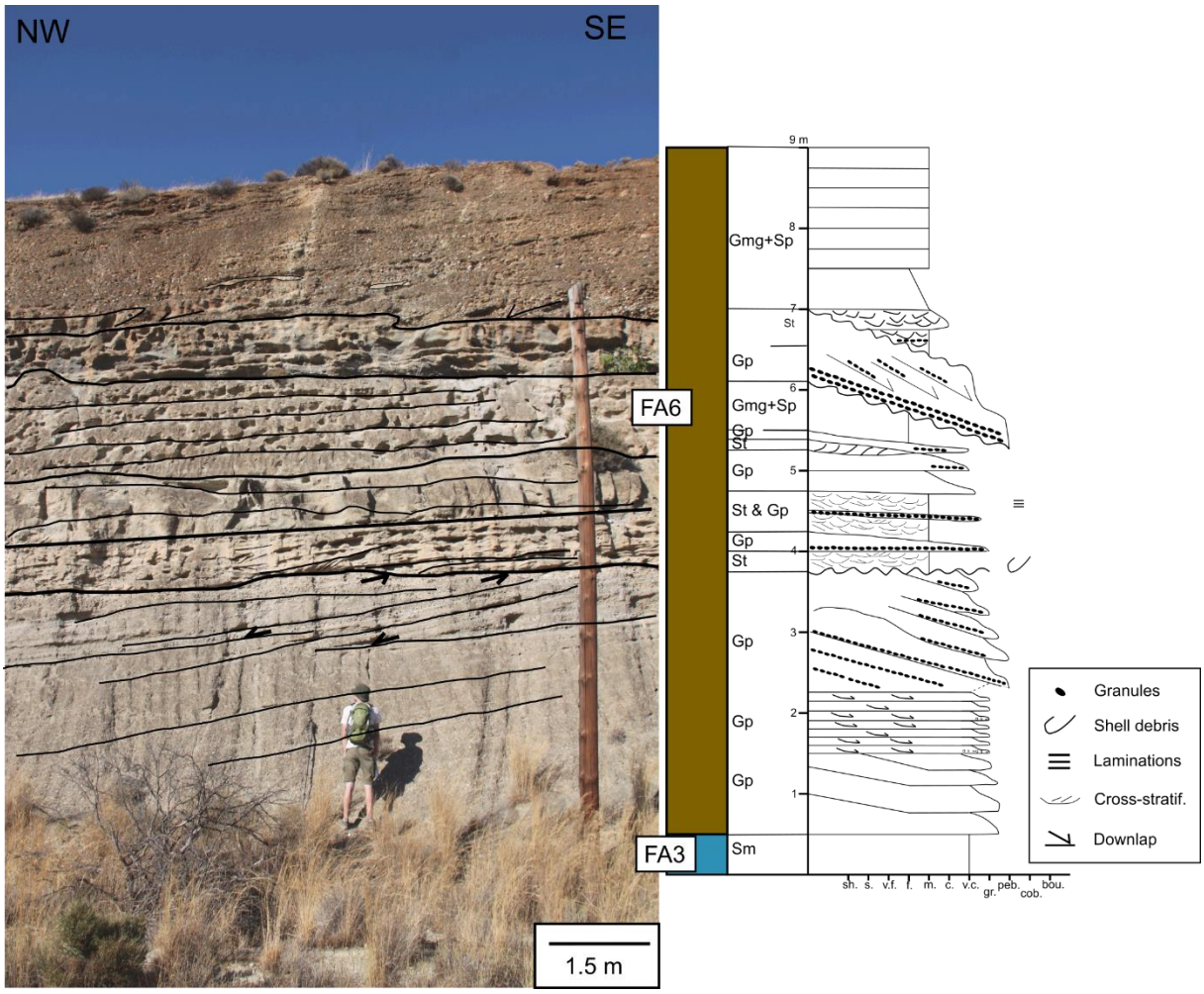

Figure 2.14: Outcrop and sedimentological logged section of FA6.

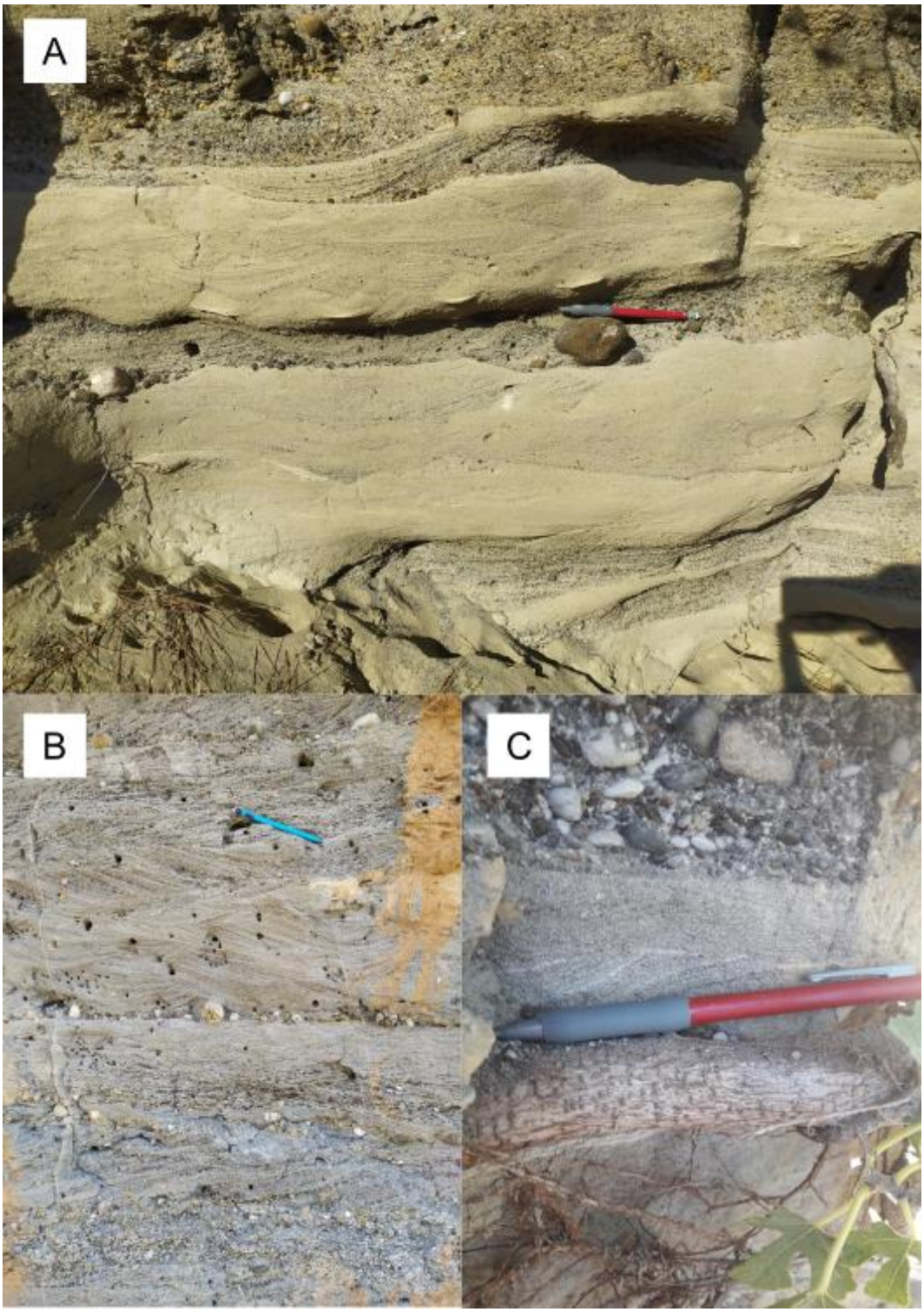

Figure 2.15: FA6 facies variability. (a) Variability in the St facies from very poorly sorted with heterogeneous granulometry to well sorted with similar granulometry. (b) Variability in the St facies with more granular elements. (c) Herringbone cross-bedding in the Sp facies.

2.3.2. Complex tidal dunes

Based on the criteria proposed by Longhitano and Chiarella (2020), we interpret FA6 as a sandy conglomeratic tidal dune complex accumulated in a strait. Evidence for this interpretation includes planar and trough cross-stratification of sands, granules and

conglomerates showing two opposite downlapping directions towards the NW and SE that vary from facies to large scale. In consequence, at both ends of the central horst, FA6 dips preferentially in two main opposite directions away from the central height.

Based on the last generalized model for tidal straits proposed by Longhitano and Chiarella (2020), we interpret the horst as the location of a bedload parting (i.e. zone 'A', strait-center zone) that forms the constriction and the sill here of the strait. In this area, sediments produced by erosion and bypass were transported outwards to both the SE and NW strait exits and formed the dune-bedded strait zone (i.e. zone 'B') that is mainly characterized by large-scale cross-bedding (Longhitano and Chiarella 2020). A complementary interpretation is proposed by Dalrymple (2023): the two oppositely directed cross-bedded deposits could represent the two 'constriction-related deltas' (CRDs) that develop in the strait areas of flow expansion as the sediment is transported away from the bedload parting/ constriction. Moreover, the tabular cross-stratification is interpreted as having formed by migration of straight crested dunes under lower bed-shear-stress values (facies Sp) (Costello & Southard 1981; Harms *et al.* 1982; Rubin & Carter 1987; Ashley 1990; J. G. Venditti *et al.* 2005). The trough cross stratification reflects the migration of sinusoidal crested dunes under high bed-shear-stress values (facies St) (Rubin & Carter 1987; J. G. Venditti *et al.* 2005). To create such dune-bedded structures, the depositional current velocity is estimated to range from 1 m s^{-1} to 2 m s^{-1} (Ashley 1990; Stow *et al.* 2009; Reynaud & Dalrymple 2012).

Second, we identified herringbone cross stratification with a strong asymmetry. The NW-dipping foresets are thicker with a lower angle than the SE reverse foresets. We interpret this structure to be the result of asymmetrical tidal currents with a dominant flow towards the NW and a reverse secondary flow towards the SE (Dalrymple 1992; Reynaud & Dalrymple 2012). Asymmetrical tidal currents are preferentially reported in straits due to the cyclical amplification of one tidal phase over the opposite phase induced by passage through the central constriction (Reynaud & Dalrymple 2012; Longhitano 2013).

Third, the mud-free facies association (FA6) is another criterion used to recognize a dune-bedded strait from other tidal environments due to its high energy setting (Longhitano & Nemec 2005). Here, the sediment sources are very close to the canal; like the Perachora horst to the north, which is made up of ophiolitic rocks. Hence, the lack of mud in FA6 is probably due to energetic tidal currents transporting mud in suspension away from this depositional area of the strait.

Fourth, compared to other tidal environments, the thickness of FA6 (at least 40 m thick) also argues for a tidal strait environment (Longhitano & Chiarella 2020).

Fifth, we observe compound foreset architectures (**Figure 2.13**), which are interpreted as dunes derived from the superimposition of smaller simple dunes on top of large dunes by tidal reverse flows. These dune architectures are reported in inshore tidal environments, as well as in tidal estuaries, tidal deltas and tidal straits (Dalrymple 1992; Reynaud &

Dalrymple 2012; Longhitano & Chiarella 2020). In micro-tidal settings, such as in the Mediterranean Sea, tidal deltas and tidal estuaries are unusual depositional systems (Longhitano & Colella 2007) and are probably not strong enough to generate large-scale coarse grained dunes. However, tidal dunes of medium- to coarse-grained sand up to gravel, which can be up to 10 m in height, are documented in the center of the Messina Strait (Longhitano 2018) with associated current velocities that vary between 1 m s^{-1} and 3 m s^{-1} (Santoro *et al.* 2002).

2.4. Connections with the Aegean Sea

2.4.1. Paleogeographic sequence

Sequence 1 (**Figure 2.11**) records a transition from deep lacustrine to shallow marine water during a 'transgression': from a lacustrine to a marine environment. This setting requires two conditions: (1) a fault-related opening of the marine connection when (2) the lake level was above the sea level, which is common. If these conditions are met, the active faulting connection can reduce the bathymetry of the basin and establish a marine environment. This opening may be associated at the rift scale with the c. 1.8 Ma marine transgression and migration of the Gilbert type deltas towards the north (Ford *et al.* 2017) and the regression of the southern coast (Rohais & Moretti 2017). This stage corresponds with the transition from Lower/Phase 1 to Middle/Phase 2 of the rift evolution (Nixon *et al.* 2016; Ford *et al.* 2017; Gawthorpe *et al.* 2018).

Sequence 2 (**Figure 2.11**) is associated with MTDs and soil formations. The dating of conglomerates above (FA6 in sequence 3) at c. 300 ka (Collier 1990) implies a large time gap in the sedimentary section. This time gap is locally represented in the geological record by the observed paleosol (FA5). Regionally, this period corresponds to the beginning of the Peloponnesus uplift. Since c. 600 ka, regular (~100 ka) eustatic reconnections to the sea have also been recorded by marine terraces (de Gelder *et al.* 2019) and in deep International Ocean Discovery Program (IODP) cores (McNeill, Shillington, Carter, Everest, Gawthorpe, *et al.* 2019) but are not preserved in the study area.

The syntectonic Sequence 3 (**Figure 2.11**) was built by the tidal strait (FA6) during MIS 9–MIS 8 (337–300 ka: Collier 1990), and records the connection between the Gulf and the Sea in the canal area. Previously, Collier and Thompson (1991) proposed that this connection was located southwards and that the canal area was a strait margin characterized by beach to shoreface deposits. They based their interpretations on the NW-dipping sets of conglomerates, associated with climbing dunes that were interpreted as storm berms. Collier's interpretation implied SW and NE longshore currents, perpendicular to the canal section. These current directions are quite unusual when the NW– SE-orientated gateway that connected the Corinth Gulf and the Aegean Sea is considered (**Figure 2.9**). Along this gateway, the tidal currents are expected to be parallel to, or close to, its NW–SE orientation but not perpendicular to it (due to the orientation of

the dunes). In addition, their interpretation of the canal area as a strait margin contradicts the fact that it is the lowest topographical region connecting the Gulf of Corinth and the Aegean Sea (0 m - 70 m).

The FA6 strait deposits may also record the reduction in and last connection between the Corinth Gulf and the Aegean Sea. Indeed, the marine Sequence 4 is restricted to the hanging wall of the Kalamaki–Isthmia Fault and is dated at 205 ka (Collier 1990). Likewise, other marine deposits associated with this c. 240 ka transgression are localized near the shores of the Corinth Bay and the Aegean Sea (marine terraces and transverse dunes) (Collier & Thompson 1991; Hayward 1996) but not in the center of Corinth Isthmus (**Figure 2.9**). These findings suggest that during highstands the Gulf of Corinth has been connected to the Ionian Sea to the west at least since 240 ka.

2.4.2. Double opening

The FA6 tidal dune architecture records the presence of a strait during MIS 9 - MIS 8 (c. 300 ka) and attests for strong tidal currents. Within the Mediterranean micro-tidal context, straits can amplify tidal currents by up to 1 m s^{-1}, such as, for example, in the strait center of the present-day Rio–Antirio Strait located west of the Corinth Gulf (Fourniotis & Horsch 2015; Rubi *et al.* 2022). To reach velocities high enough to build the observed dunes (1 m s^{-1} to 2 m s^{-1} would have been needed), our hypothesis is that the Corinth Gulf was open both to the west and to the east with an effective connection between the Ionian Sea and the Aegean Sea through the gulf.

This double opening could have enhanced the tidal amplification due to the time difference between the tides in the two mentioned seas. Due to the distance separating the two open seas and the usual spread of the tides, a time difference of around 1-2 h can be supposed (Tsimplis 1994). If the Gulf of Corinth had had a double connection, the amplification of tidal currents at the Corinth Strait would have been marked by an increase in the current velocity coming from the Aegean Sea around 1-2 h before the high tide of the Ionian Sea. This hypothesis fits the observation of the tide asymmetry registered by the herringbone crossbedding in FA6 (**Figure 2.12**). The dominant current coming from the Aegean Sea (SE of the canal section) was probably responsible for the deposition of the larger and flatter foresets, dipping to the NW, whereas the subordinate weaker current deposited the smaller foresets, dipping to the SE, preserved at the top of the herringbone cross-bedding.

An alternative explanation for the asymmetry is that it could have been generated by the superposition of a unidirectional current on the reversing tidal currents, such as in the Messina Strait (Longhitano 2018). The unidirectional current in the Messina Strait is density driven because of the west-to-east increase in aridity, which generates a west-to-east increase in salinity in Mediterranean Sea (Robinson *et al.* 2001; Schroeder *et al.* 2012). The salinity-driven south-to-north current helps to cause an asymmetry in the sediment transport through the strait (Longhitano 2018).

Chapter 3: Using 14 years of Satellite Data to Describe the Hydrodynamic Circulation of the Patras and Corinth Gulfs

In the previous chapter, the importance and the details of the straits of Corinth were described. Analyzing these straits, in particular the Rio-Antirio strait led to several questions related to the water circulation on the Gulfs of Patras and Corinth. But due to the paucity of information regarding the water dynamics in these gulfs, the first goal of the PhD Thesis was to assess this hydrodynamic circulation. With this chapter, the focus was on the surface circulation by using satellite data as they were the only available data to start this part of the research at this large scale.

This chapter is written in a "paper" format since it was published during the PhD: (Caterina & Hubert-Ferrari 2025); Caterina, B. & Hubert-Ferrari, A., 2025. Using 14 Years of Satellite Data to Describe the Hydrodynamic Circulation of the Patras and Corinth Gulfs. *J. Mar. Sci. Eng.*, **13**, 623. doi:10.3390/jmse13030623.

1. Introduction

Understanding the hydrodynamics of a coastal area is crucial for several applications. It is for example essential for unravelling the sedimentary deposit distribution including general pollutants, and nutrient availability, such as chlorophyll, which forms the base of the marine food chain. Nowadays, the oceanography of most regions around the world is quite well understood, particularly thanks to oceanographic databases such as the World Ocean Database (WOD), and Copernicus, as well as satellite data (Buongiorno Nardelli *et al.* 2013; Boyer *et al.* 2018). However, there remain several important but poorly understood regions, such as the Patras and Corinth Gulfs, where significant oceanographic phenomena occur but are not well comprehended.

Since the last comprehensive oceanographic study of the Corinth and Patras Gulfs by Lascaratos et al. in 1989 (Lascaratos *et al.* 1989), there has been a significant gap in published information on the oceanography of these regions. This previous general study lacked some of the technologies we have today. Also, in their study, Lascaratos et al. (1989) used only 12 images over 152 available at the time, covering only 1 year and 5 month (June 1981 to November 1982; (Lascaratos *et al.* 1989)). Having access to a higher resolution dataset over 14 years will allow us to observe events that were maybe missing from Lascaratos et al. study (Lascaratos *et al.* 1989). Over the past 35 years, advancements in methods and knowledge have greatly enhanced our ability to characterize hydrodynamic phenomena. Despite these improvements, the availability of oceanographic data remains limited. In-situ data databases from the Gulf of Corinth are often scarce and insufficient to infer general hydrodynamic patterns. While modelling

efforts, such as those by Fourniotis & Horsh (2010, 2015) (Fourniotis & Horsch 2010, 2015), have been conducted for the Patras Gulf, the Gulf of Corinth remains largely unstudied. Hence, like Lascaratos's approach in the 1980s, leveraging available satellite data presents a valuable method for studying the general hydrodynamics of the Corinth Gulf. Present time satellite data offer a better resolution and better coverage than in the 1980s while computers can also manage bigger datasets with ease.

Despite the lack of oceanographic knowledge over the main processes in the Gulf of Corinth, this area has been studied from a geological point of view. Regarding the sediment dynamics, it is still unclear what are the origins of all the patterns that are observed. Even determining which configuration caused which sediment deposition, having an idea of the actual hydrodynamic conditions will help to limit the hypotheses (A. Beckers *et al.* 2016; Rubi *et al.* 2022). Indeed, information over the hydrodynamics can be expected from the geological data such as the orientation of the depositional currents in some areas (Iatrou 2013; A. Beckers *et al.* 2016), the strength of some currents depending on the location (Rubi *et al.* 2022) or even the paucity in chlorophyll (CHL) in some regions informing about potential poor CHL currents (McNeill, Shillington, Carter, Everest, Le Ber, *et al.* 2019a; Sergiou *et al.* 2024). But these hints alone can never fully explain what is happening at the scale of the Corinth Gulf in terms of hydrodynamics.

Therefore, the goal of this study is to better assess the major hydrodynamic processes occurring in the Patras and Corinth Gulfs. This will primarily be achieved by analyzing Sea Surface Temperature (SST) maps derived from satellite data over a 14-year period. Additionally, Chlorophyll (CHL) satellite data will be utilized to complement the information obtained from SST observations. Once the hydrodynamic structures are identified and described, the observed phenomena will be contextualized within the general hydrodynamic framework of the Patras and Corinth Gulfs. Subsequently, a Data Interpolating Empirical Orthogonal Functions (DINEOF) analysis will be conducted as defined in (J.-M. Beckers *et al.* 2006; Alvera-Azcárate *et al.* 2009). This analysis, which involves interpolating missing data in a manner similar to Principal Component Analysis (PCA), will provide insights into the temporal and spatial variations of the identified phenomena. Through this comprehensive analysis, an overview of the entire dataset will be achieved, enhancing our understanding of the hydrodynamic processes in these regions.

2. Physiography and Oceanography of the Gulfs

The Gulf of Corinth is the active rift basin separating mainland Greece from the Peloponnesus. This basin, approximately ~900 m deep, 130 km long and 40 km wide, is connected to the smaller, almost circular, shallow Gulf of Patras, which is only 120 m deep and 20-25 km wide. The Patras basin is connected to the Ionian Sea in the West. The connection between the two Gulfs is made by the Rio-Antirio Strait, which plays an important role in the hydrodynamic circulation of the water masses (Rubi *et al.* 2022). This

strait is about 2 km wide and 70 m deep. At the eastern end of the Corinth Gulf, the connection with the Aegean Sea is made by the Corinth Canal. This 6.5 km long and 21 m wide man-made canal, with an average depth of only 8 meters, cannot be considered as an actual substantial oceanic connection (Caterina *et al.* 2022).

2.1. Physiography of the study area

The study area extends from 21.3°E to 23.3°E and comprises the Patras and Corinth Gulfs, which are separated by a 12 km long Rio-Antirio strait area. The Rion strait sensu-stricto is defined by the narrowest 2 km wide opening at the location of the Rio-Antirio bridge, near the ~70 m deep Rion Sill (Rubi *et al.* 2022).

We have divided the study area into 6 different regions based on their distinct physiographic characteristics (**Figure 3.1**). From west to east, there are the Ionian Sea, Patras Gulf, the Strait & Corinth Entrance, the West Corinth, the East Corinth, and the Alkyonides Gulf Regions. The difference in physiography of these regions is strongly related to varying tectonic deformations, sediment supply and hydrodynamics processes which have shaped the seafloor morphology (A. Beckers *et al.* 2016).

We designated the shallow waters west of Cape Araxos, as the Ionian Sea Region. This area is a 6 km wide shallow water zone, where the large Achelos River discharges.

The Patras Gulf Region is an extensional and slowly subsiding tectonic basin, with an opening rate of 7 mm yr^{-1} (Briole *et al.* 2021) filled with Plio- Quaternary sediments (Stathopoulou *et al.* 2023). This wide, round-shaped basin has a mean depth of 56 m and a ~138 m deep central depocenter controlled by normal faulting (Ferentinos *et al.* 1985). On its northeastern side, the deformation pattern changes with a dominant right-lateral deformation along its southeast coastline (Rion- Patras Strike-slip fault; (Briole *et al.* 2021)). The gulf narrows sharply and ends at the Rion Strait sensu stricto. The first ~50 m deep Patras Sill occurs, 3 km west of the Rion Strait, and marks the eastern boundary of our defined Patras Gulf Region. Several relatively large rivers flow to the Patras Gulf, the Evinos River (from the north), and the Glafkos and the Piros (from the south).

To the east of the Patras Gulf, the Strait & Corinth Entrance Region is a complex physiographic zone characterized by an eastward deepening of its seafloor, which is the fastest present-day deforming area (11 mm yr^{-1}; (Briole *et al.* 2021)). The western part includes the Rio-Antirio Strait area that comprises in its center the ~115 m deep fault-bounded Nafpaktos Bay. The eastern part shows first a widening and a deepening to ~430 m over a length of ~3 km, and then the occurrence of a plateau. This part of the Corinth Gulf is bordered to the south by steep slopes with an absent or a very narrow shelf and active normal faults near the coastline, while the northern subsiding side has a much wider shelf with bays. The boundary between the Strait & Corinth Entrance and the West Corinth Regions is marked on the seafloor by a ~600 m deep tectonic horst bounded to the east by a canyon (**Figure 3.1**).

The West Corinth Region is characterized by an eastward seafloor widening and deepening to ~870 m depth. The central part of the West Corinth Region is a 9 km wide, ~850 m deep, WNW-ESW elongated flat area. Like in the eastern part of the Strait & Corinth Entrance, the southern coastline is straight and faulted; it is immediately followed by a steep slope without shelf ending in the ~850 m deep flat bottom basin. The northern subsiding shoreline is more convoluted and marked by the SSE-oriented, ~10 km wide, ~20 km long and 0-300 m deep Itea Bay, hanging above the ~850 m deep basin bottom to the south. Its eastern boundary with the Eastern Corinth Region is marked by a north-south oriented, 15 km long Cape Pangalos.

East Corinth exhibits many similarities with West Corinth. It features the same 12 km wide, ~850 m deep flat central area and similar southern steep slopes and faulted coastlines without shelves. Its northern shore shows a gently southward sloping, 7.5 km wide, 15 km long and 0-300 m Antikyra bay hanging above the ~850 m deep flat depocenter and bordered to the east by a canyon. At the southeastern extremity of this region lies the Lechaio bay ending with the Corinth Canal. East Corinth is limited to the east by an abrupt shallowing of the bathymetry, marked by the Zoodochos Island and by the shallow bay of Lechaio in the south-east.

The Alkyonides Gulf Region, east of Zoodochos Island, is 13 km wide, 22 km long and has a maximum depth of 360 m. Its northern edge is convoluted and marked by small bays, whereas its southern edge is fault bounded, straight, and steep.

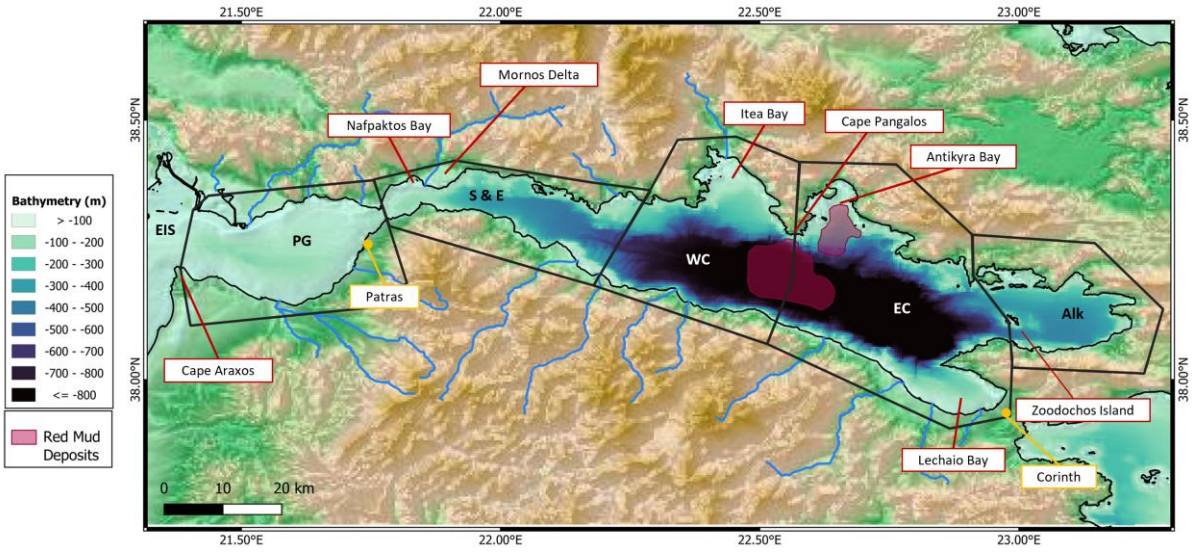

Figure 3.1: Bathymetry (in meters) map (GEBCO 2024) of the 6 different regions of the study area: Eastern Ionian Sea (EIS), Patras Gulf (PG), Strait & Entrance (S & E), West Corinth (WC), East Corinth (EC), Alkyonides (Alk) (from West to East). The smaller locations are in red and the cities of Patras and Corinth are represented in yellow. The red mud deposits locations are positioned according to Iatrou et al., 2010.

2.2. Oceanography of Patras and Corinth Gulfs

The hydrological properties of both gulfs exhibit typical seasonal stratification in summer and mixing in winter (Friglios *et al*. 1985; Poulos *et al*. 1996). In the Corinth Gulf, the SST is approximately 25°C in summer and 13.6°C in winter (Poulos *et al*. 1996). At 200 m depth, temperatures are around 13.3°C in summer and 12.8°C in winter, based on the 1970 dataset (Anderson & Carmack 1973). In the Patras Gulf, central waters reach around 25°C in summer while waters near the Rio-Antirio Strait are cooler, about 23°C (Friglios *et al*. 1985). Salinity in the Patras Gulf is slightly higher due to the mixing between the salty waters from the Ionian Sea (38.6-38.7) and the less salty waters from the Gulf of Corinth (38.3-38.5) (Anderson & Carmack 1973; Friglios *et al*. 1985).

Two major hydrodynamic processes have already been identified in the two gulfs. The first type are gyres mainly driven by the winds that were described in the two gulfs. The prevailing winds are mostly E or WSW oriented and are funneled by the surrounding mountain ranges (Poulos *et al*. 1996; Koletsis *et al*. 2014). Cyclonic gyres have been observed in surface waters in the eastern Corinth Gulf in front of Antikyra Bay and in the Patras Gulf using satellites data (Lascaratos *et al*. 1989). In Patras, the hydrodynamic models show (Fourniotis & Horsch 2010, 2015) that the wind-induced cyclonic gyre affects the entire Gulf with colder waters in its center. The second type of hydrodynamic processes are wind-induced upwellings. These have been evidenced on the northern shoreline of the Corinth Gulf and in the northeast part of Nafpaktos Bay between the two gulfs by using satellite data (Lascaratos *et al*. 1989). An upwelling was evidenced by modelling in front of the city of Patras (Horsch & Fourniotis 2017).

Between the two gulfs, the hydrodynamic circulation is controlled by the tides (Rubi *et al*. 2022). Even if the Corinth and Patras Gulfs are characterized by a microtidal environment with an average tidal amplitude variation of 15 cm, the constriction at the location of the Rion-Antirion strait area generates a strong amplification of the tidal currents. Surface current velocity can reach up to 1 m s^{-1} and bottom currents up to 3 m s^{-1} to 6 m s^{-1}, as evidenced by ADCP data (Rubi *et al*. 2022). High-velocity surface currents in the Rio-Antirio Strait area have also been observed in a hydrodynamic model (Fourniotis & Horsch 2010) which focused on the Patras Gulf. This model highlights the funneling of waters at the Rio-Antirio strait sensu stricto. The effects of the tides are the following: during ebb tide, the surface waters are rising from Corinth towards Patras; while during flood tide, the surface waters flow from Patras to Corinth (Rubi *et al*. 2022). The very high-velocity bottom currents are associated with a strong internal tide. The Corinth internal tide operates differently from the surface oceanic tides. Since the internal tide frequency is twice the one from the oceanic tide, during ebb tide, if the phases of both tides align some deep water from Corinth can overflow the bathymetric step of the strait and cross it to reach Patras Gulf from the bottom. In other situations, bottom waters flow should be reflected back to the Corinth basin, not crossing the strait.

3. Materials and Methods

3.1. Data acquisition

All the SST data (**Table 1**) were downloaded from the CMEMS catalogue (Buongiorno Nardelli *et al*. 2013) as NETCDF datasets (CMEMS 2025). The L3 level sea surface temperature data in high resolution (0.01 x 0.01 degree) were used since the studied area is quite small (120 km x 40 km). Data from January 1, 2008, to January 20, 2022, were downloaded and utilized for this study.

3.2. Data Preprocessing and Filtering

After downloading and reading the data, they were pre-processed by creating a mask for SST outliers and land pixels. This step eliminated the days with excessive missing data (> 95 %) over the studied period. With this step, the number of available days went from 5127 to 3838, which represents a loss of 25% of the initial dataset. Despite this basic treatment the quality of the dataset often remains poor depending on the days. The filter was set to 95% to keep a good amount of data but also to eliminate the days when there were only few pixels of information.

In addition to the SST, chlorophyll (CHL; **Table 3.1**; (Copernicus Marine Service 2025)) data from satellite datasets over the same 2008-2022 period were observed. The selection and refinement process for CHL data were the same as for the SST data. For this dataset, the restriction of the 95% maximum missing data made us go from 5154 days to 3093 days.

3.3. Selection of Key Hydrodynamic Events

The mean SST was then calculated across the entire region, first by longitude, then by latitude, to obtain an overview over its temporal evolution. Regional SST means and standard deviations were calculated to compare each region (**Figure 3.1**). A temporal examination of SST maps was conducted and 64 daily maps showing significant spatial changes in SST related to major and regional hydrodynamic processes in the Patras and Corinth Gulfs were manually selected. This initial review allowed us to visually identify days with notable oceanographic events. We also examined SST maps 2 days before and 2 days after the 64 selected dates to understand the temporal evolution of the observed SST variations and confirm the hydrodynamics processes responsible for the changes. Manual selection of these dates allowed us to identify images where spatially continuous events occurred even if the map was not totally covered by the data.

Only L3 CHL data maps were analyzed to confirm hydrodynamics processes in the selected SST maps and to identify other possible hydrodynamics phenomena. Some of the selected maps were kept to illustrate key hydrodynamics features.

3.4. DINEOF Reconstruction and Statistical Analysis

To complement this initial analysis based on selected SST and CHL maps, a statistical analysis of the entire SST dataset was performed. No statistical analysis was conducted on the CHL data due to their poor quality, despite the valuable information provided by the raw maps. The statistical analysis of the pre-processed SST data was conducted using Data Interpolating Empirical Orthogonal Functions (DINEOF; (J.-M. Beckers *et al*. 2006; Alvera-Azcárate *et al*. 2009)). DINEOF is a data analysis technique used to reconstruct missing satellite data and perform statistical analysis. It is especially suited to oceanographic datasets. Here, it was used to fill in missing data caused by clouds and other factors in the pre-processed data and to quantify the spatial and temporal variability of the SST.

There are four steps in DINEOF analysis. It begins by decomposing the signal into Empirical Orthogonal Functions (EOFs) that represent the dominant modes of variability in the dataset. These modes capture the most significant spatial structures and variations in the data. Then, using the determined EOFs, the missing data are reconstructed. To reduce noise in the EOFs, a Laplacian filter was applied within the iterations of the DINEOF analysis. The strength of this filter ensures a realistic calculation of the SST while reducing gradient and some local information loss (Alvera-Azcárate *et al*. 2009). The third step of DINEOF analysis is an iterative process to adjust the EOFs and the estimated missing data values until the reconstruction converges to a stable solution. This process results in an optimized reconstruction that preserves the statistical properties and variability of the original dataset as closely as possible (J.-M. Beckers *et al*. 2006; Alvera-Azcárate *et al*. 2009).

For the DINEOF analysis performed, the parameters were set as follows: α (strength of the filter) is set to 0.1, number of iterations (“numit”) for the filter is 3 and at most 50 EOF modes are asked. Other parameters were set by default. Since the studied area is quite small, DINEOF was able to run successfully for the entire 14-year period, rather than requiring year-by-year interpolation as used in larger oceanic areas (Alvera-Azcárate *et al*. 2009). The results of the DINEOF analysis were exported as a new NETCDF file and read by using Julia programming language (Barth 2024). From this newly interpolated dataset, the same dates as in the initial SST dataset were saved as maps to examine the same phenomena and their SST variations with fully filled maps.

Table 3.1: Datasets information and treatments used in this study

Name	Resolution	Time Coverage	Source	Treatment
SST	0.01° × 0.01°	From 1 January 2008 to 20 January 2022	CMEMS [24]	- Elimination of days with >95% missing data - Manual selection of maps showing key events - DINEOF Analysis
CHL	1 × 1 km	From 1 January 2008 to 20 January 2022	CMEMS [25]	- Elimination of days with >95% missing data - Manual selection of maps showing key events

4. Results

4.1. SST and CHL data in Patras and Corinth Gulfs

4.1.1. Mean SST changes

Over the 14 years covered by the SST data (**Figure 3.2**), mean SSTs ranged between 13.1°C and 28.2°C. A major seasonal variability was evidenced with a temperature drop of around 12 °C between summer and winter. Examining the different regions defined in **Figure 3.1**, the Ionian Sea Region is consistently warmer than the Patras Gulf, particularly in winter and slightly less so in summer. This pattern was previously noted by Lascaratos et al. (1989) (Lascaratos *et al*. 1989). Between the Patras and Corinth Gulfs, the differences in temperature differences are minimal if the Strait & Entrance Region is not considered. The most significant difference between regions is that the Strait & Entrance Region is always the coldest (**Table 3.2**). This was also observed by Rubi et al. (2022) (Rubi *et al*. 2022) for the entire year 2019. The temperature difference is more pronounced in summer, with a 0.9°C of difference in the mean SST compared to the far east of the Corinth Gulf, the Alkyonides Gulf Region (**Table 3.2**). When both Gulfs are observed as a whole, clear evidence of the increase of the SST is observed, showing a ~1.4°C increase of the mean in 14 years (0.0977°C yr^{-1}). This increase of temperature is two to three times higher than what is commonly observed for the Mediterranean Sea (~0.026°C yr^{-1} to 0.042°C yr^{-1}) (Skliris *et al*. 2012; García-Monteiro *et al*. 2022; Kubin *et al*. 2023; Androulidakis *et al*. 2024).

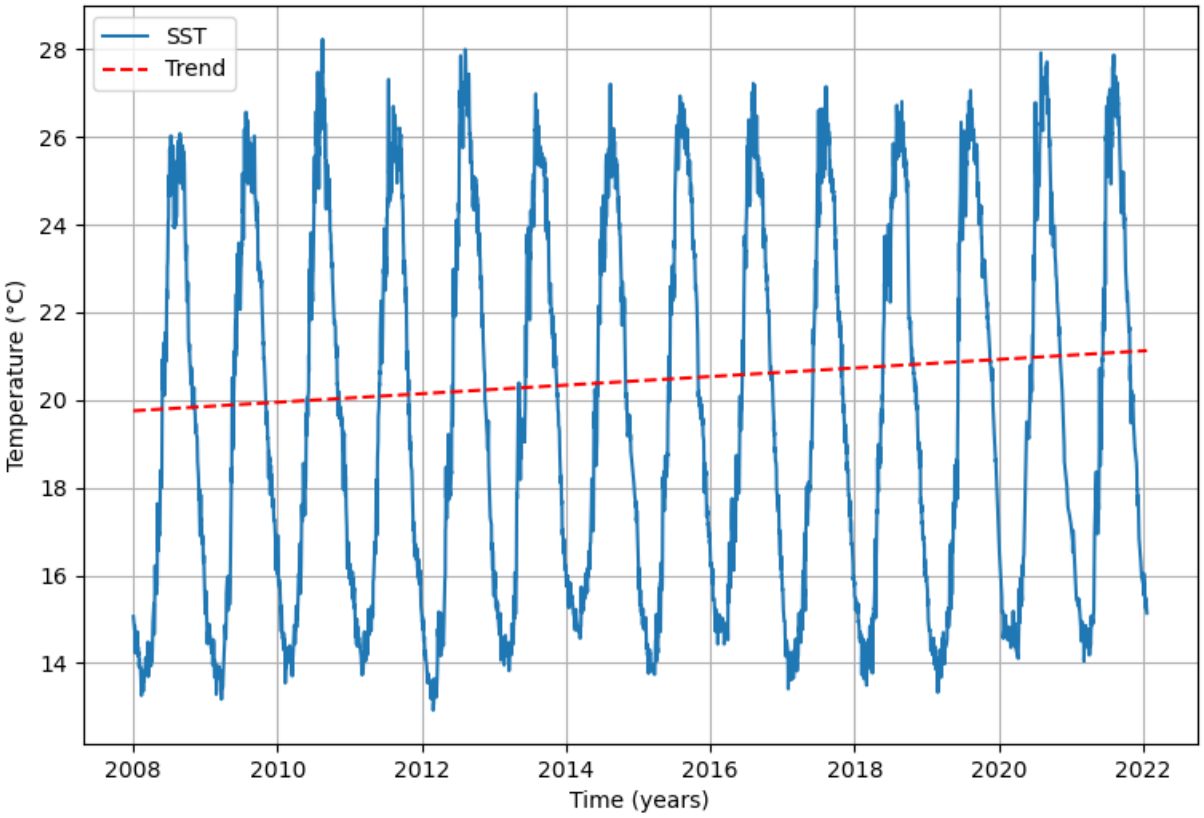

Figure 3.2: Mean SST evolution over the Patras and Corinth Gulfs between 2008 and 2022. The temperature is in °C.

Table 3.2: Mean SST and standard deviation (STD) for the six regions, over all the 2008-2022 period and with difference between winter (November to April) and summer (May to November). Region boundaries according to Figure 1.

SST °C	Mean			STD		
	Year	Winter	Summer	Year	Winter	Summer
Eastern Ionian Sea	21.11	16.77	23.87	7.21	6.29	5.55
Patras Gulf	20.55	16.01	23.42	7.61	6.30	6.34
Strait and Entrance	20.03	15.86	22.81	7.03	5.56	6.28
West Corinth	20.30	16.03	23.17	7.19	5.56	6.54
East Corinth	20.56	16.08	23.57	6.43	4.93	5.07
Alkyonides Gulf	20.85	16.06	23.70	8.47	7.03	7.14

4.1.2. General circulation patterns

Our examination of the selected 64 daily SST maps evidenced varied patterns. First, a gradient exists in the Corinth Gulf, with the warmest waters in the East Corinth Region. The temperature gradient can reach up to 3°C between the two ends of the Corinth Gulf, leading to the formation of an oceanic front between the East and West Corinth Regions. Second, SST variations in the Corinth and Patras Gulfs are significantly different, suggesting dissimilar circulation patterns in the two gulfs. In the Patras Gulf, the main observed SST phenomenon is a cyclonic gyre affecting the entirety Patras water mass. In Corinth, hydrodynamics is more complex, particularly the cold temperature anomaly in the Strait & Entrance Region.

The occurrence of the cold spot (0.6°C difference on average with East Corinth Region over a whole year) in Rio-Antirio already evidenced (**Table 3.2**) is also displayed in SST maps. This lower surface temperature can be explained by an upwelling. This upwelling involved dense and cold Corinth bottom waters reaching the surface in Rio-Antirio due to bathymetric shallowing. Another mechanism responsible for the local cold spot in the SST in the Strait & Entrance Region could be the strong internal tides dominating the strait hydrodynamics and Corinth waters not always reaching the Patras Gulf at each tide (Rubi *et al*. 2022). When the internal tides do not rise simultaneously with the surface tides, the upwelled Corinth waters seem to not cross the strait and are trapped in the Strait & Entrance Region. Consequently, this flow restriction contributes to the local cold spot in the SST in Rio-Antirio Strait. Finally, upwelled deep waters from Corinth that manage to cross the sill of the strait contribute to lowering the SST in the Patras Gulf compared to the Eastern Ionian Sea (0.6°C difference on average over a whole year; **Table 3.2**), and to its gyre's strong contrast in SST.

4.2. Patras Gulf

Details about the Patras hydrodynamic circulation were uncovered through some of the 64 daily SST maps and complementary CHL maps (**Figure 3.3** and **Figure 3.4**). The Patras cyclonic gyre is observable year-round in SST and CHL maps. In this cyclonic circulation affecting the entire Patras Gulf, warmer waters are located along the southern border of the Gulf (**Figure 3.3**), and the temperature difference between colder waters at the gyre center and along its external borders can reach up to 2°C (**Figure 3.3B**).

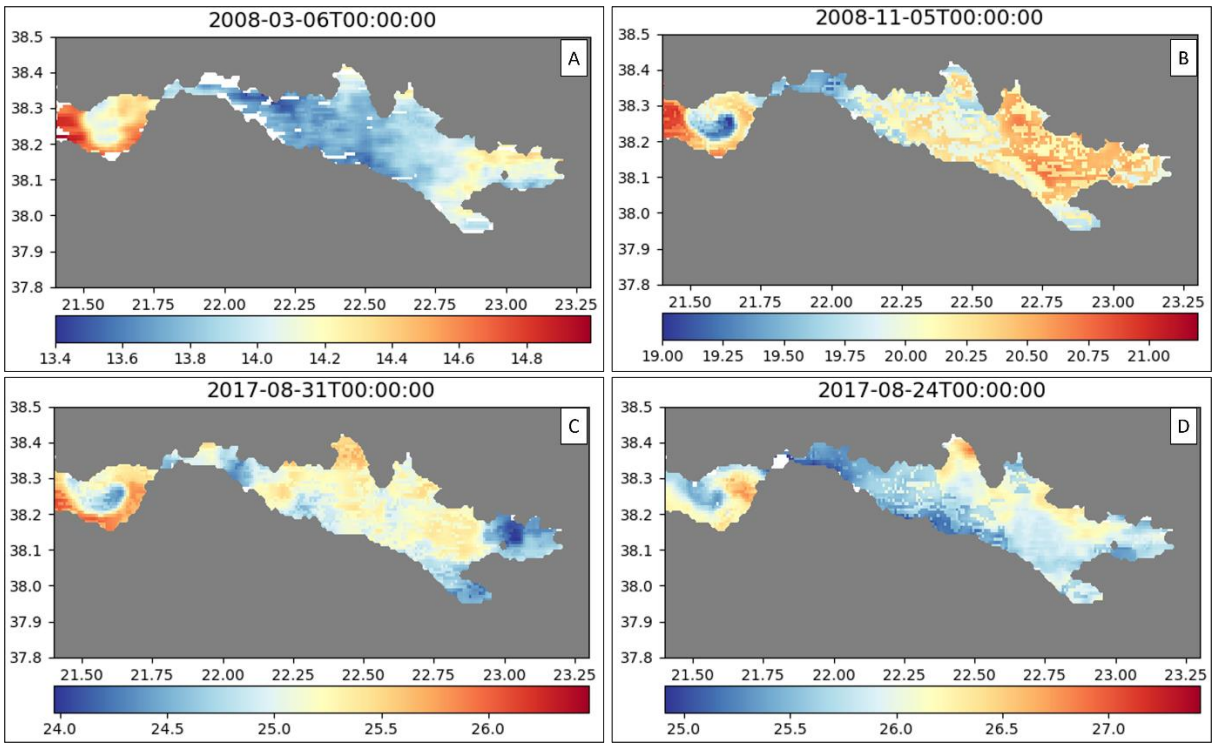

Figure 3.3: SST maps evidencing phenomenon in the Patras Gulf. The color scales are in °C

In this eddy, warm water comes from the Eastern Ionian Sea Region. Two hypotheses exist regarding the source of colder waters within the eddy. One hypothesis is that the observed colder waters correspond to the general Patras waters, and the warm waters are from the incoming Eastern Ionian waters. This hypothesis is not supported by the water temperature difference within the eddy, as the SST variation is generally larger than the mean water temperature difference between the Ionian Sea and Patras Gulf Regions (**Table 3.2**). Additionally, the Ionian/Patras temperature difference is smallest in summer (**Table 3.2**), whereas the SST gradient in the gyre is the lowest in winter (compare **Figure 3.3A** with **Figure 3.3B** to **D**). Therefore, we infer that the cold waters are deep Corinth waters upwelled in the Strait & Entrance Region that cross the sill and reach the Patras Gulf. The cold waters likely do not come from the Patras Gulf, as the pool of cold water in Patras is too restricted. In Patras, the thermocline is around 60 m, with deep waters at ~14°C covering only 190 km^2, whereas the deep Corinth water pool covers a 1960 km^2 and is at ~13°C. The arrival of the upwelled Corinth deep water in Patras is well evidenced on the 24 August 2017 map, showing a cold SST spot at the extreme east of the Patras gyre, exiting the strait, and being included in the gyre (**Figure 3.3D**). This map, along with others (**Figure 3.3B, C**), also shows a slight decrease in hot SST of the Patras gyre near the strait, interpreted as dilution with colder Strait & Entrance waters. Fourniotis and Horsh (2015) (Fourniotis & Horsch 2015) identified another upwelling in front of the Patras harbor that is not evidenced in the SST data, possibly due to the resolution of the satellite data or the non-inclusion of the internal wave from Corinth Gulf in their model.

The CHL maps show that the shallow Gulf of Patras (**Figure 3.4 B, C, D**) have the one of the highest chlorophyll concentrations in the study area. Various factors can explain these high CHL concentrations. Firstly, the tributaries of large rivers in both areas can bring diverse nutrients that support phytoplankton growth. **Figure 3.4 B, C** and **D** illustrate strong CHL concentrations along the southern coast of Patras, suggesting the riverine inputs at these locations (**Figure 3.1**). Secondly, the waters of Patras being shallower compared to the ones of the Corinth Gulf may affect the dilution of the CHL content with less space available for dilution. However, these two factors alone cannot explain the higher CHL concentration in the Patras Gulf compared to the Eastern Ionian Sea Region, which is also shallow and compared to the site of the Achelos river delta, the largest in the study area. We infer that the high concentrations in the Patras gyre result from a combination of in situ CHL production and CHL-rich Ionian waters. This also explains why the central part of the Patras eddy has the lowest CHL concentration in the Patras Gulf Region.

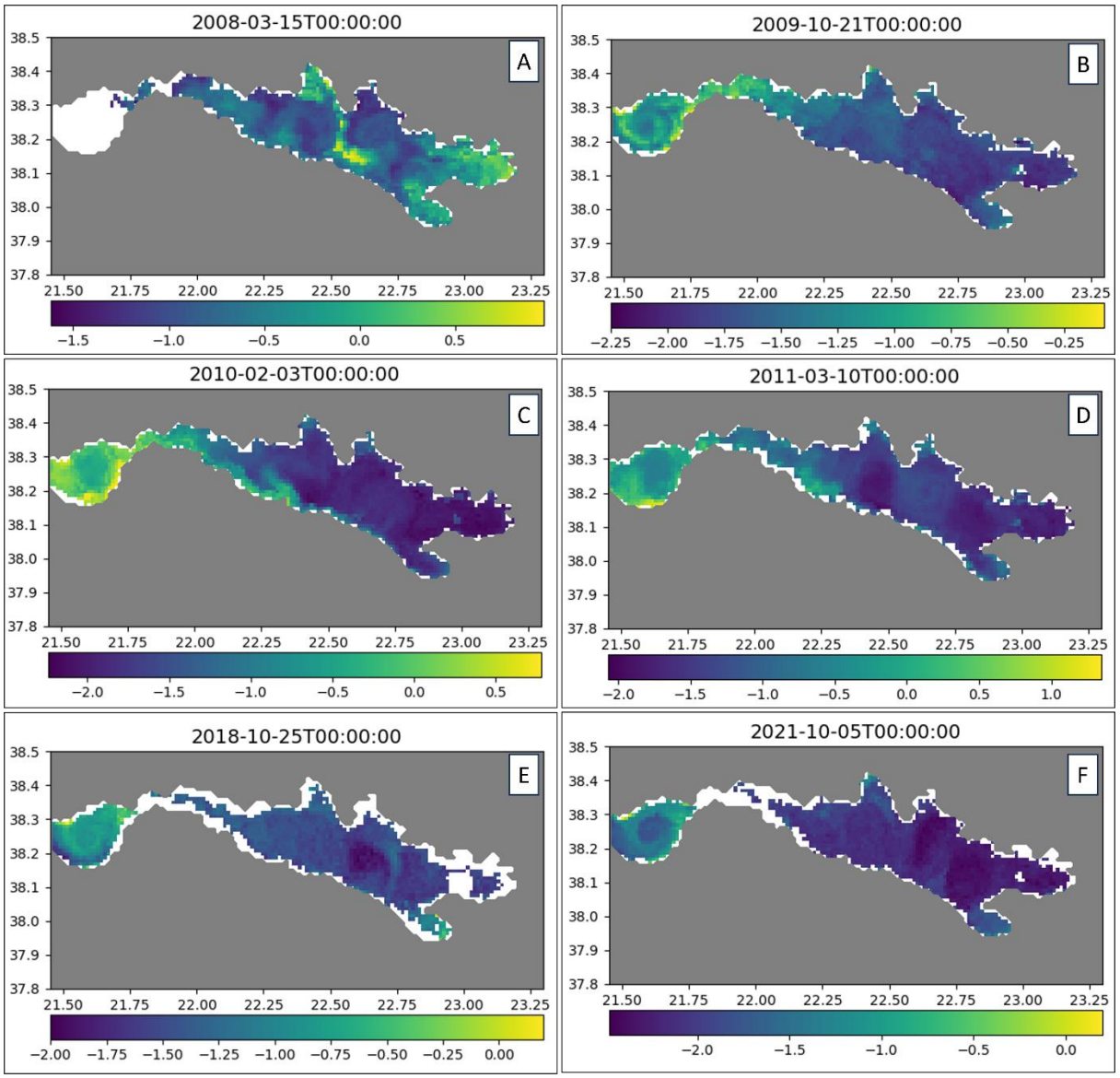

Figure 3.4: CHL concentration over several days in the study area. The scale is a logarithmic scale (log10 mg/m^3) for a better view of the concentrations.

4.3. Rio Strait, the Nafpaktos Bay and the westernmost Corinth Gulf

In the Strait & Entrance Region, we can track surface water flows with two methods. First, the 64 SST daily maps and observations over 5 days provide insights and these findings are confirmed with CHL daily maps. This is feasible because the strait waters have the coldest SSTs. CHL maps can also help in tracking water flow, as the Patras Gulf Region and the western part of Strait & Entrance Region are CHL-rich, while the Corinth Gulf is mostly depleted. The high CHL content in this region is linked to the high nutrient supply brought mostly by the Mornos River (i.e. annual suspended sediment flux: 160–325 x10^3 m^3 yr^{-1}; (Watkins *et al.* 2019)) and its low dilution in the Nafpaktos Bay, west of the Mornos Delta.

The daily images provide detailed patterns of cold SST in the region and the associated hydrodynamics. The first pattern is associated with the upwelled deep cold-water flow in

this region. The coldest water hotspot is found in front of the Mornos Delta (**Figure 3.5**, right), where a bathymetry steeply rises in direct continuity with the 900m deep cold-water pool, ~50km further SSE. This cold spot is related to wind induced upwellings (Lascaratos *et al.* 1989) and the shallowing of the internal wave (Rubi *et al.* 2022). The surface arrival of the deep cold Corinth waters can be observed year around. Other relatively cold hotspots appear in the daily maps, always near the northern side of the Corinth Gulf, indicating that the deep-water flow follows this margin. The CHL maps confirm the inferred water flow direction. The Mornos River, the largest one flowing into the Patras and Corinth Gulfs, supplies nutrients to the Nafpaktos Bay to the west. Just east of the Mornos Delta, the northern margin of Corinth Gulf is often less rich in CHL, indicating the lack of eastward surface water flow along this margin.

In the daily map, another anomaly is the eastward moving cold SST anomaly along the southern margin of the Corinth Gulf. The hydrodynamic evidence suggests a surface water flow from the Rio-Antirio strait sensu stricto towards the Corinth Gulf, following the southern margin (**Figure 3.5**). Occasionally, this incoming cold-water volume is too large to follow the south coast only, filling nearly the entire 50 km long Strait & Entrance Region. This cold flow typically dissipates itself at the beginning of the West Corinth Region, rarely reaching the East Corinth Region. This hydrodynamic feature is also evidenced in the CHL daily maps. Although most of the high CHL area is confined to the Nafpaktos area, west of the Mornos Delta, a trail of high CHL can be found in the Corinth southern margin, evidencing the surface flow. Again, this hydrodynamic feature can be interpreted in relation to the internal waves from Corinth Gulf and the restricted flow through the Rio-Antirio Strait (Rubi *et al.* 2022). Because the strait acts as a barrier for the tidal currents, some of the upwelled cold waters coming from Corinth cannot cross the strait and therefore return towards Corinth as colder surface waters. This backwash of cold water occurs regardless of the season. In conclusion, the daily maps reveal the following hydrodynamics along the Corinth margins: an eastward surface-water flow along the southern margin and a deep-water flow along the northern margin in the opposite direction.

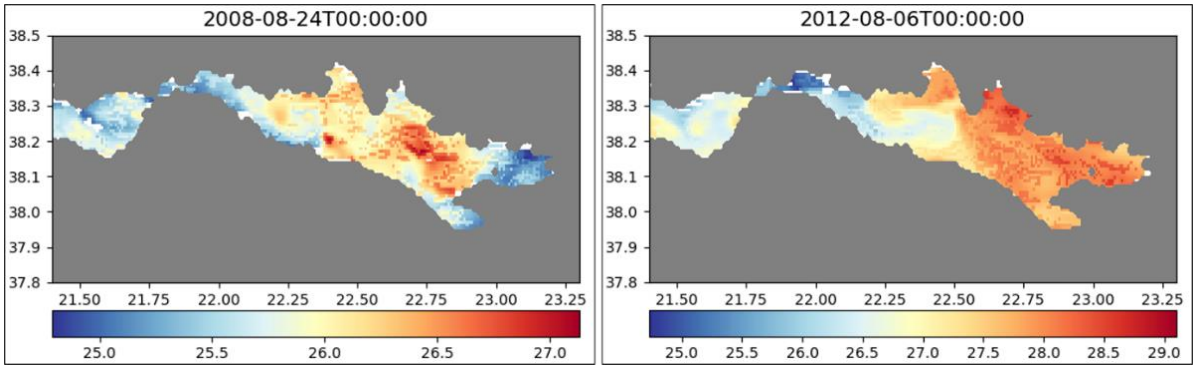

Figure 3.5: SST maps of cold waters entering the Corinth Strait through the Rio-Antirio strait. The color scales are in °C.

4.4. Itea Bay and West Corinth

In the West Corinth Region, the Itea Bay plays an important role. This N-S bay, covering a 51km^2 area shallower than 300m deep, is protected from winds and has warmer waters than the waters of the central part of the Gulf. This temperature difference can be linked to the bay's enclosure and shallowing, allowing a more significant stratification. Stratification is enhanced by the reduced effects of the dominant winds, as the dominant west winds cannot reach the bay, protected by the 2500m high N-S oriented Hellenides range. Rivers draining these mountain ranges provide high levels of nutrients to the bay, resulting in high CHL concentrations.

The hydrodynamics of this region can be evidenced by the subtle SST contrast between the warm Itea waters and the cool surface waters coming from the Strait & Entrance Region following the southern coast. These cool waters are pushed into the West Corinth Region by the wind. As the gulf widens, the SST anomaly extends along the southern coast and then makes a subtle clockwise trail in front of the Itea Bay (**Figure 3.6A** to **F**). We infer that the eastward surface water flowing along the southern coast is mobilized into a wind-induced anticyclonic gyre (**Figure 3.6**). This is coherent with the fact that waters in the central part of the gyre, being the West Corinth waters, are warmer than the surrounding waters from the Strait & Entrance Region, remobilized by the gyre. The Itea's warmer waters are mobilized southward by the anticyclonic eddy and bought to the central part of the Western Corinth Region. In the SST maps, the gyre has a radius of ~10 km and can occupy the entire West Corinth Region. It is often limited to the east by a ~N-S trending oceanic front bounding the West Corinth Region, generally aligned with the Cape Pangalos located between the Itea and Antikyra Bays (**Figure 3.1**).

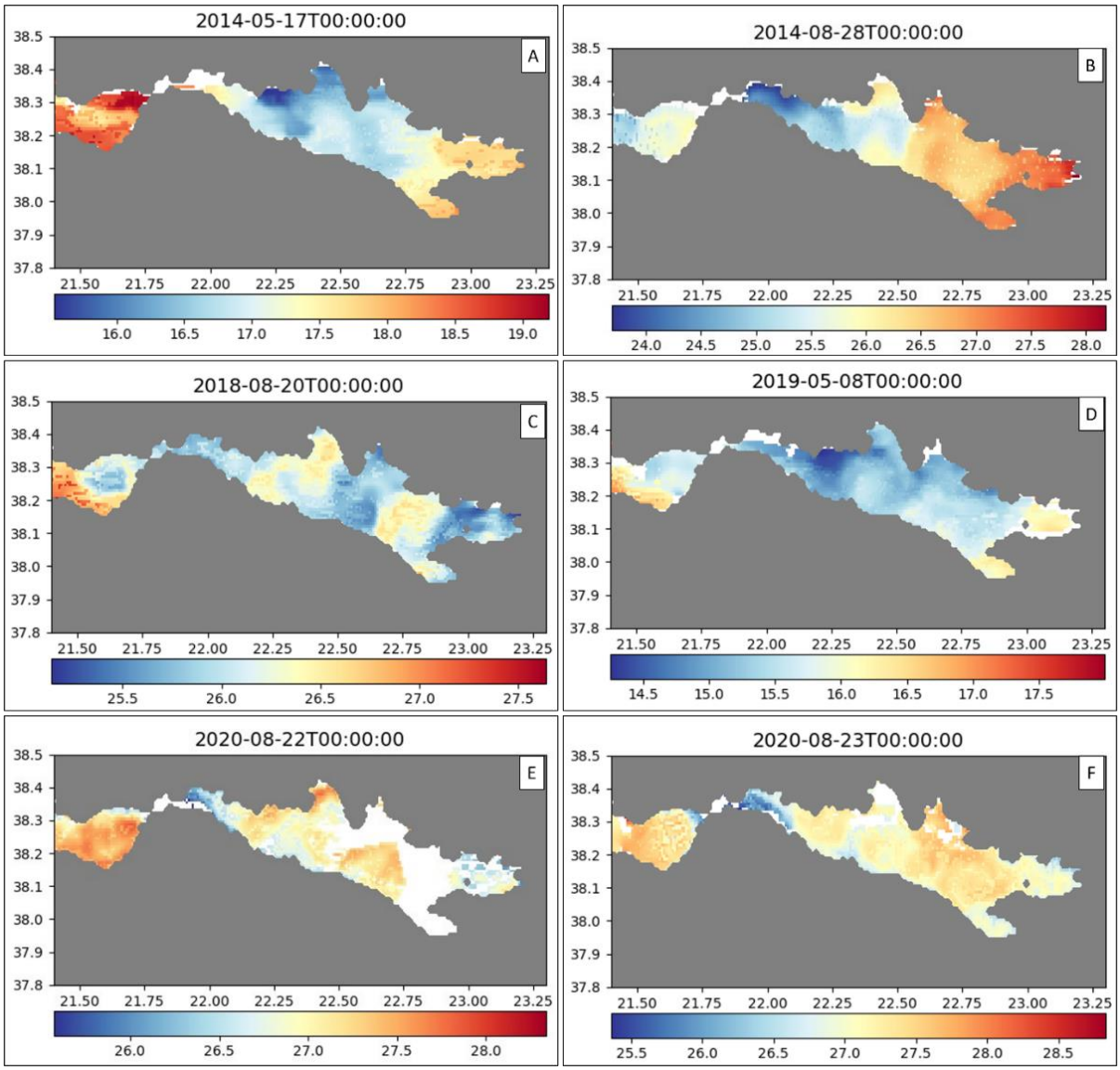

Figure 3.6: Evidence through SST data of the hydrodynamic circulation that takes place in front of the Itea Bay. The color scales are in °C.

The chlorophyll data (**Figure 3.4A, F**) provides additional information about hydrodynamics in the West Corinth Region. High CHL concentrations are found along the southern coast, where the CHL-rich flow from the Strait & Entrance Region is trapped in the anticyclonic gyre, and where further nutrient supply is provided by rivers draining the mountainous southern part of the Corinth Basin. The highest CHL concentrations are still found in Itea Bay. This hotspot for CHL is due to the bay's shallow bathymetry and the high amount of riverine nutrients. The depleted central part of the gyre is related to anticyclonic movement, which mobilizes the two CHL sources at its borders. The maps indicate that Itea's CHL- rich waters can be driven southward by the eddy and reach the deep basin in the central part of the Gulf. This flux of CHL-rich water can even reach the East Corinth Region when the eddy waters reach the southern margin of the Corinth Gulf.

4.5. Antikyra Bay and East Corinth

The East Corinth Region can be separated from the West Corinth Region by a sharp SST gradient, creating an oceanic front. This front can display a ~1°C change in SST over ~5km (**Figure 3.7A, E, F**) and is most often located in front of the Pangalos Cape between the Itea and Antikyra Bays. This marks the boundary separating the West Corinth water body from the East Corinth water body. We infer that this front is nearly stable because the East Corinth waters are consistently the warmest in the Corinth Gulf expect in summer where the waters from the Alkyonides Gulf are hotter. In winter, there is no significant SST difference between the West and East Corinth Region (**Table 3.2**), and the occurrence of an oceanic front is less likely to be observed (**Figure 3.3A**).

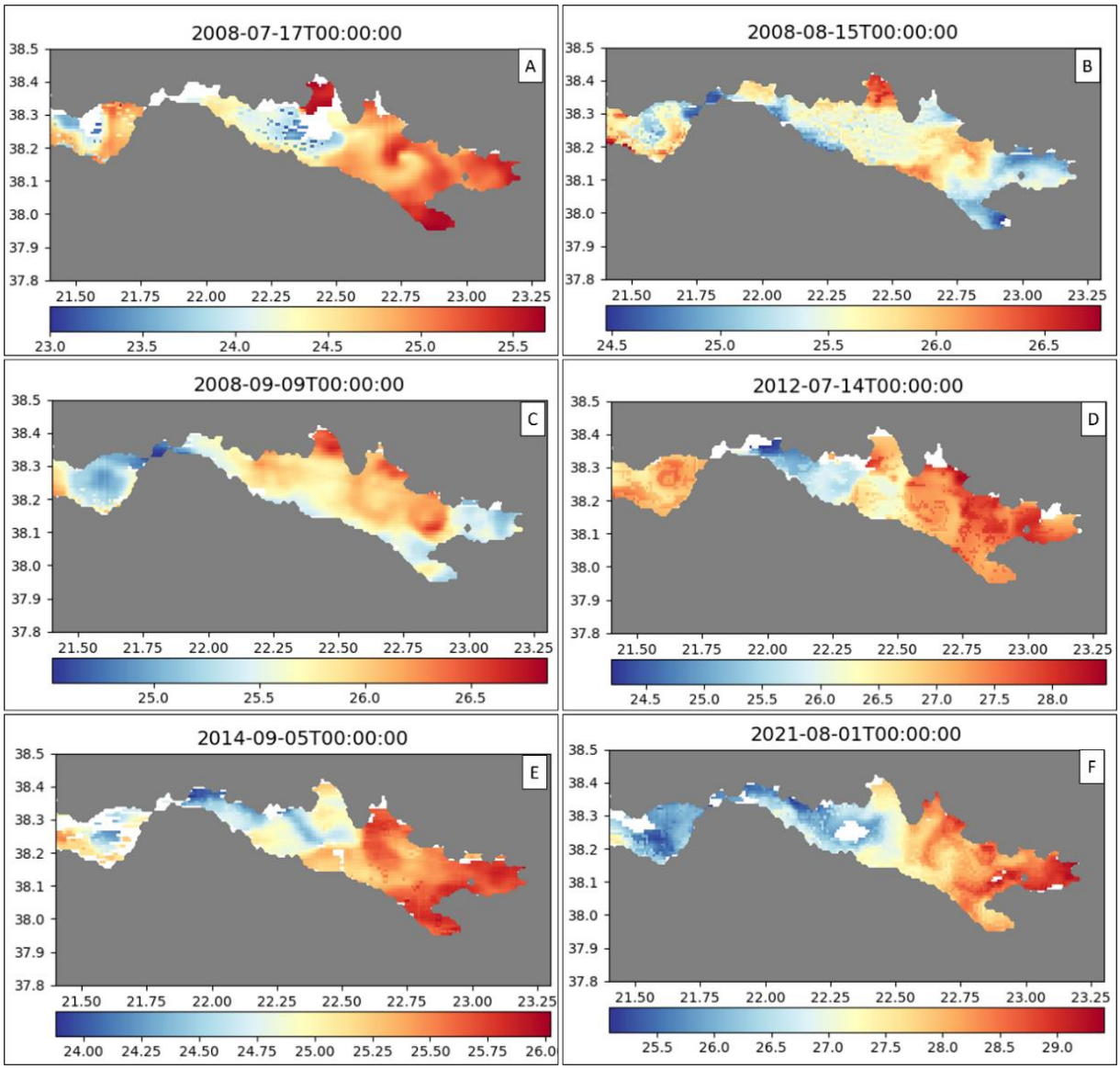

Figure 3.7: SST maps of the Corinth Gulf evidencing phenomena located in front of Antikyra Bay. The color scales are in °C.

The presence of the oceanic front between the West and East Corinth Regions limit surface water exchange between the two regions and explain the low standard deviation

of the SSTs in East Corinth (**Table 3.2**). The temporal examination of SST maps shows that the oceanic front does not completely impede surface water exchange between the two regions. Warm, chlorophyll-rich waters from Itea Bay, mobilized by the anticyclonic gyre, flow southeastward and can enter the East Corinth Region (**Figure 3.4A**). When they reach the southern margin of the Gulf, CHL-rich waters are carried by the eastward coastal current, likely driven by the dominant winds coming from the W to NW (**Figure 3.8**, (Koletsis *et al.* 2014)).

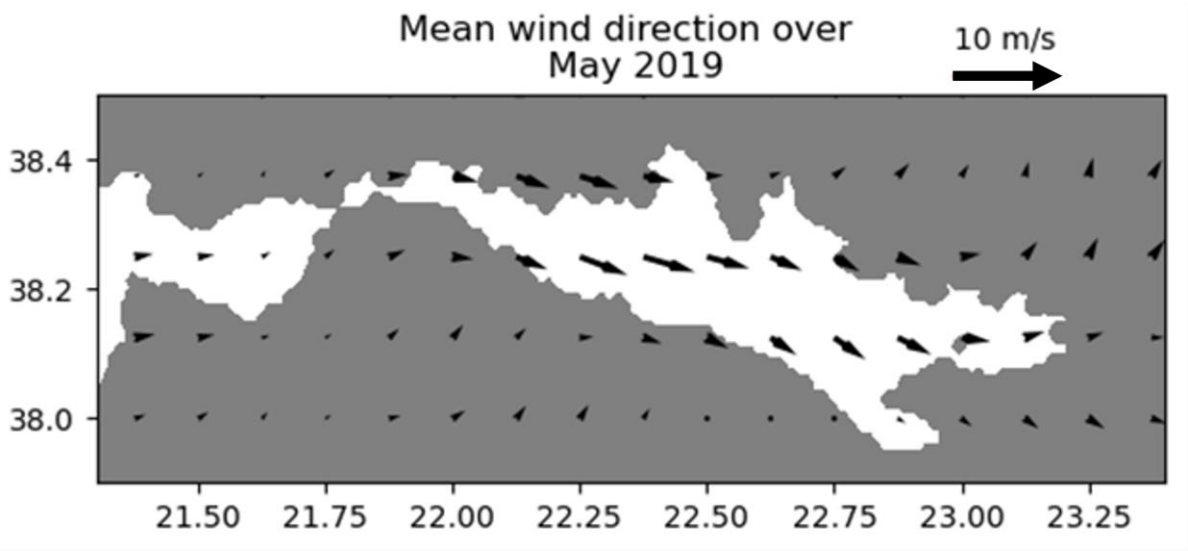

Figure 3.8: Flow direction and velocity of the mean winds over the month of May 2019 based on the ECMWF dataset.

In the East Corinth Region, the hydrodynamic features are more diverse than in the West Corinth Region. Most of the time, a large cyclonic gyre is observed with a radius of ~10 km, and colder waters usually located on its southern edge (**Figure 3.7A, D, E, F**). Even though CHL concentrations are low in this region, their geographical disposition supports the presence of a cyclonic gyre. Occasionally, smaller structures such as smaller anti-cyclonic and cyclonic eddies are observed, for example, on the 15th August 2008 or on the 9th September 2008 (**Figure 3.7B, C**).

The impact of the Antikyra Bay over the hydrodynamic circulation of the Corinth Gulf is not as strong as the Itea Bay. Antikyra Bay is half the size of Itea Bay, less protected from winds by mountains, and lack large mountainous river outlets. This results in lower CHL content in Antikyra Bay compared to Itea Bay. Across the entire Eastern Corinth Region, the only CHL-rich waters are found in the Antikyra Bay (**Figure 3.3C, D**). However, daily images evidence that Antikyra Bay does not supply CHL to the central deep basin of the Corinth Gulf: instead, CHL presence in the central part of the Eastern Corinth Region is due to Itea waters exported from the West Corinth Region by its gyre and caught by the Eastern Corinth Gyre (**Figure 3.3A**).

Also in this region, Lechaios Bay (in the south) exhibits a high SST (**Figure 3.7A, E**). CHL concentrations are higher here than in the rest of the East Corinth Region (**Figure 3.3A, E**),

likely due to stronger riverine nutrient inputs and shallow bathymetry (100m to 200m deep; **Figure 3.1**), which reduces CHL dilution.

4.6. Alkyonides Gulf

The Alkyonides Gulf is located at the eastern end of the Corinth Gulf. This 13km wide and 22km long small gulf is separated from the East Corinth Region by the Zoodochos island constriction and is characterized by the steep decrease in bathymetry, from ~800m deep west of the island to 300m deep to the east. The island and the associated constriction (geographical and bathymetrical wise) likely disrupt hydrodynamic circulation and partially block the connection with the East Corinth waters. This region is observed to be the hottest in the whole Corinth Gulf in summer. The high SST in this area can be explained by its location at the extremity of the Corinth Gulf where hot surface waters of the East Corinth Region are pushed by the westerly winds (**Figure 3.8**). This difference of temperature can also be linked to the shallowing of the Alkyonides Gulf, and the reducing of water circulation linked to the Zoodochos island which allows for greater stratification. This stratification is further enhanced by the reduced impact of the dominant winds.

In the Alkyonides Gulf, the most interesting phenomenon is related to SST values that are sometimes smaller than the local average near the northern coast (**Figure 3.9**), interpreted as an upwelling. The occurrence of upwelling would explain the high standard deviation of the SST in this region, which is usually warm (**Table 3.2**). When an upwelling happens, there is a ~1°C to ~2°C difference between these waters and the East Corinth Region waters. Since there are no major rivers found in the area, an upwelling, bringing to the surface the cold deep waters from the Corinth Basin, is an explanation for these SST reductions. Like the Strait & Entrance Region, the strong bathymetric rise from the deep Corinth basin to the shallower Alkyonides Gulf can facilitate upwelling. Also, this upwelling might be an expression of the internal tide observed in the Strait which would be mirrored here due to the closure of the basin and the rising bathymetry. This phenomenon occurs mainly in the northern part of the Alkyonides due to the presence in the south of the Zoodochos island which acts as a barrier to most high dimension hydrodynamic events. Furthermore, the bathymetric shallowing between the northern Alkyonides Gulf and Eastern Corinth is more pronounced than in the south, where there is a faulted sub-marine canyon separating the Zoodochos island from the Perachora peninsula.

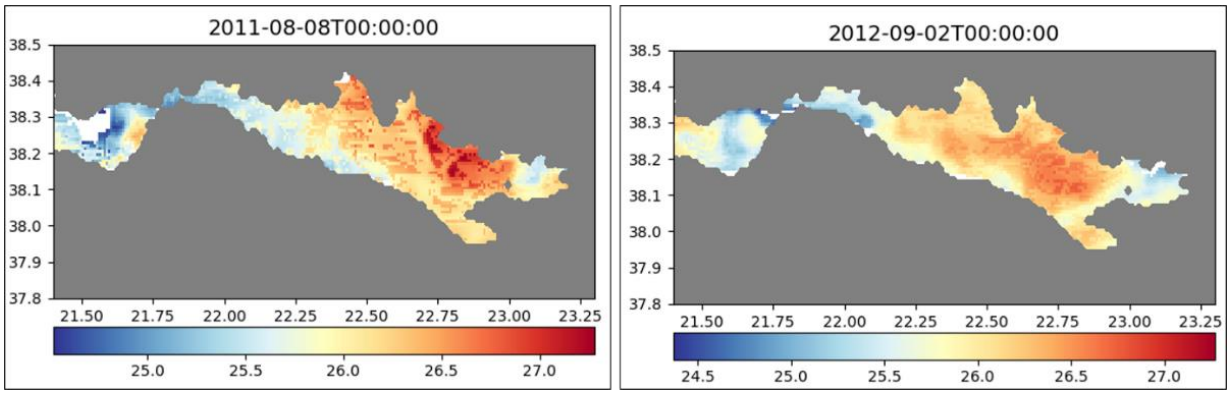

Figure 3.9: SST maps of the Corinth Gulf evidencing the relatively cold waters of the Alkyonides Gulf in the warmer waters from the east Corinth region. The color scales are in °C.

In terms of CHL concentrations, the Alkyonides Gulf appears depleted unless upwelling events allow an increase in the concentrations (**Figure 3.4C, D**). This low CHL concentration can be attributed to the absence of major rivers supplying nutrients to the sea, while upwellings can bring nutrients from the deep Corinth basin.

4.7. EOF modes

The DINEOF interpolation identified three major modes to explain the SST variation over the study period. The first and dominant one explains 98% of the SST variability, while modes 2 and 3 explain 1.1% (0.73%, 0.37%, respectively). Since there are no field measurements, the EOF spatial patterns are not cross validated.

The first EOF mode is the dominant one, representing seasonality. **Figure 3.10A** shows the temporal variability of this mode, indicating that the seasonal factor is dominant, with one positive peak during winter and one negative peak during summer. The spatial variability of this mode, depicted in the corresponding maps, indicates that the strait area is less prone to variability due to the seasonal changes, whereas the Itea Bay, Antikyra Bay and East Corinth are the most sensitive to the winter and summer cycles. Due to the dominant winds towards the E-SE (Koletsis *et al*. 2014), waters accumulate in the eastern part of Corinth and since the basin is closed, the waters can "stagnate" there and become more sensitive to seasonal temperature variations. In addition, East Corinth is separated from West Corinth by an oceanic front, which limits surface water exchanges, in particular the cool waters coming from the Strait and Entrance Region. The EOF map also evidences the upwelling zone in the Alkyonides Gulf, as a small reduction in the seasonal variability. The Strait & Entrance Region is the least sensitive to the seasonal dominant mode. In this region, the dynamics are higher in relation with the narrowing and shallowing of the Gulf and the internal tides, which causes greater water motion and mixing with less time to "adapt" to the atmosphere temperature. Additionally, the year-round upwelling near the Mornos Delta or on the Patras side of the Rio Strait sensu stricto makes these areas less sensitive to the seasonal variability like for the northern Alkyonides Gulf.

When looking at the second EOF mode, the spatial and temporal variability are both interesting. First, spatially, the variation of the SST is stronger in the Strait & Entrance

Region (in the negative values) especially in the upwelling area in front of Nafpaktos. The variability is also strong (in the positive values) in the Patras Gulf. There is thus a strong difference in variability between these two areas suggesting an impact of the upwelling and the strait action over the variability of the SST. Looking at the temporal disposition of the second mode, the variability seems to be stronger in summer. This would suggest that the stratification may play an important role in the area. Combining these two observations allows evidence that the Rio-Antirio Strait dynamics plays an important role. Indeed, when there is a stratification, in summer, in the Strait sensu stricto, the internal waves might be stronger and therefore the upwelling they induce might occur more often leading to a more relevant cooling of the surface waters of the Strait & Entrance Region. Since the temporal peak over winter indicates less variability, we can deduce that upwellings occur also during winter but are less strongly represented in the SST variations. The lesser variability of time can also be associated with a complete mixing of the water column, leading to no stratification whereas stratification should enhance the internal waves and the upwellings around the Strait.

The third EOF mode shows less consistency in its temporal variation, with an enhancement of the variability in winter. The geographical repartition for this mode indicates that the variability is linked to a W-E phenomenon. We thus interpret this mode in relation to the dominant winds coming from the west to northwest and pushing the waters towards the enclosure of the basin. The temporal variation supports this interpretation, as in winter, the wind strength is enhanced.

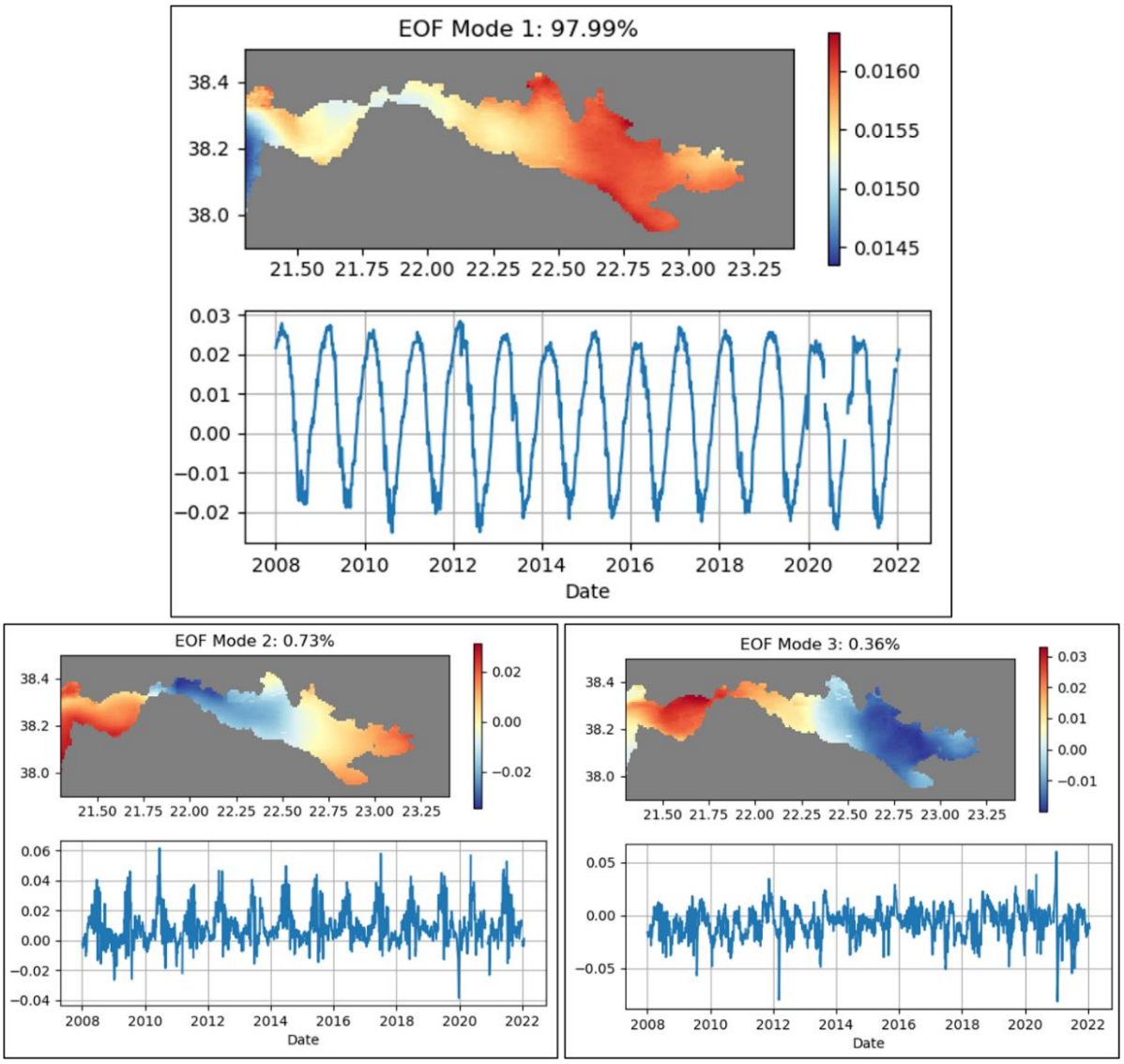

Figure 3.10: Display of the spatial and temporal variability given by the EOF analysis. The color scale indicates a variability factor, and the graph displays the temporal evolution of this variability.

5. Discussion

5.1. Circulation from the Ionian Sea to the Alkyonides Gulf

Regarding regional dynamics of the regions, a west-to-east continuity is observed (**Figure 3.11**). In the Patras Gulf, the cyclonic gyre appears due to the winds and the inflow of the upwelled deep cold Corinth waters over the strait. This gyre is restricted to the Patras Gulf since it is too big to cross the 2km wide Rio-Antirio strait and it doesn't seem to extend towards the Ionian Sea, probably due to the circular shape of the Patras Gulf and the presence of the Araxos Cape, forming a shallow sill (-50m) separating the Patras Gulf from the Ionian Sea. In the Strait & Entrance Region, when the deep waters from the Corinth Basin reach the surface and do not cross the strait, they flow back into the Corinth Gulf along the steep fault-bounded southern coast. Most of the time, these cold and nutrient-rich waters continue along the southern coast up to the oceanic front in the

middle of the Gulf. These waters can then be trapped in the West Corinth anticyclonic gyre, but the coastal flow path can sometimes continue to the East Corinth Region. There, these waters can be influenced by the East Corinth cyclonic gyre in front of the Antikyra Bay. The two opposite eddies are more likely to appear in front of the Itea and Antikyra Bays. This is because the most available space exists in front of these two bays and the water flow can be influenced by winds (Koletsis *et al.* 2014).

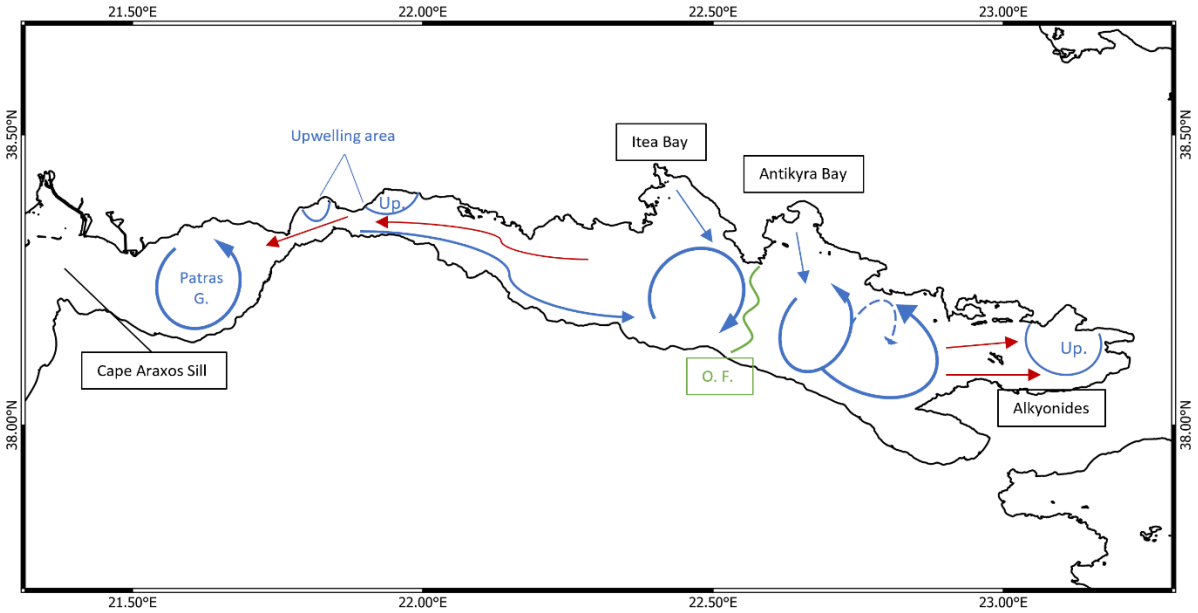

Figure 3.11: Synthetic map of the main dynamics in the Gulfs of Patras and Corinth. In blue there are the surface phenomena and in red the inferred bottom dynamics. "Up." Stands for upwelling and "O.F." for Oceanic Front.

Compared to the previous overview study on the general hydrodynamic circulation of the Corinth Gulf proposed by Lascaratos et al. (1989) (Lascaratos *et al.* 1989), this study provides more detailed information (**Figure 3.11**). While the positions of the cyclonic gyres in the Patras Gulf and in front of the Antikyra Bay were already identified, more precision is now provided on their dynamics and origins. The upwellings along the northern coast of the Strait & Entrance Region were also evidenced by Lascaratos et al. in 1989 (Lascaratos *et al.* 1989). However, their impacts and dynamics are detailed only in this work, with potential link to the internal wave at the Rio-Antirio Strait influencing the redistribution of the currents (Rubi *et al.* 2022). Other differences this study include are the observation of an anticyclonic gyre in front of the Itea Bay, the cool surface current along the southern coast, details of the gyre in front of the Antikyra Bay, sometimes cyclonic sometimes anticyclonic, and the presence of upwelling in the Alkyonides Gulf.

In terms of general circulation, the Corinth Gulf can be compared to the Mediterranean Sea on a smaller scale due to the presence of the Rio-Antirio Strait acting like the Gibraltar strait. Like the larger scale in the Mediterranean Sea, there is a strong temperature gradient from West to East in the Gulf of Corinth. Another similarity is that the dominant

north-westerly winds (Pinardi & Masetti 2000; Koletsis *et al*. 2014) push surface waters towards the closed eastern end of the basin (**Figure 3.9**), while its bottom waters would flow in the opposite direction (Pinardi & Masetti 2000; Rubi *et al*. 2022). The straits (Gibraltar and Rio-Antirio), both regulate exchanges between an open basin and a closed one. Due to their shape and specific bathymetric settings, combined with water stratification, internal tides would be created, amplifying the currents and the exchanges in both straits (Morozov *et al*. 2002; Rubi *et al*. 2022).

5.2. Impacts of the circulation on sediment routing

Several studies have shown that certain areas of the Corinth Gulf exhibit diverse dynamics in terms of sediment transport (Iatrou 2013; A. Beckers *et al*. 2016; Rubi *et al*. 2022). Our study, exploiting satellite data, allows to directly infer water motion at the sea-ocean interface using contrast in SST between water masses. Although only surface components are observed, we can still infer dynamics extending to the sea bottom. Particularly, in shallow or coastal areas where coupling with the surface is stronger. Therefore, we propose the following new insights about the sediment routing and deposition in the Gulf of Corinth.

The Strait & Entrance Region is the most dynamic region of the Gulf. Strong currents in the region result in a distinctive pattern of sediment disposition. This was already evidenced by A. Beckers et al. (2016) and supported by Rubi et al. (2022) (A. Beckers *et al*. 2016; Rubi *et al*. 2022). A. Beckers et al. (2016)(A. Beckers *et al*. 2016) show the near absence of sediments in the central part of Strait sensu stricto and the Nafpaktos Bay, sediment plastered drift on the slopes at the eastern exit of the strait in the Nafpaktos Bay, and thicker sediment plastering on the southern slopes of the Strait and Entrance Region east of the Mornos Delta. Such plastered drift on slopes occurs in the presence of a strong bottom current (Faugères & Stow 2008). This kind of current has been evidenced through the satellite data of our study by the observation of the upwellings happening near the Rio-Antirio strait. Moreover, the surface currents following the southern coast indicate that the bottom currents might follow the northern coast of the Strait & Entrance Region. This disposition of the currents would explain the sedimentary pattern already evidenced (A. Beckers *et al*. 2016). A strong surface current also facilitates the discharge of sediments eroded from the strait (Rubi *et al*. 2022) towards the center of the Corinth Gulf where they could be deposited or could be trapped in other hydrodynamic patterns.

Another area impacted by sediment discharge is the Antikyra Bay. There is an Aluminum processing plant treating bauxite since more than 50 years. The red muds rejected by the plant are discharged on the shelf and sink up to 120m depth (Iatrou *et al*. 2010; Iatrou 2013). During their descent, the mud flow can be trapped in the cyclonic eddy that can reach the center of the Antikyra Bay. In that way, some bauxite muds could be routed towards the center of the Corinth Gulf to the southwest of the Antikyra Bay. This is confirmed by the mapping of the red mud deposits (**Figure 3.1**) (Papatheodorou *et al*.

1999; Iatrou *et al*. 2010; Iatrou 2013; G. Bearzi *et al*. 2016) that reach the 850 m deep basin floor mainly in front of the Pangalos Cape to the west of the Antikyra Bay. The red mud deposits do not extend farther west, evidencing the importance of the oceanic front separating the two main eddies of Western and Eastern Corinth Regions. The hydrodynamics at depth can be inferred to be like the surface one. The relatively limited spreading (Iatrou *et al*. 2010; Iatrou 2013) of the red mud in the deep basin is also probably linked with the low velocity of the flow at that location.

Getting information about the general circulation patterns in the Corinth/Patras Gulfs might also help with the actual concerns about the dispersion of plastic pollution (Stefatos *et al*. 1999). Since Patras is the third more populated city of Greece, the Strait & Entrance area can be a spot for redistribution of anthropogenic pollutants over both Gulfs. The Patras Gulf seems to be sensitive to land-based plastics being degraded and sinking with the sediments (Koutsodendris *et al*. 2008). These plastics can be remobilized by the strong currents leaving the Strait & Entrance area towards the Gulf of Corinth. Due to its geographical disposition and its current patterns, the Strait & Entrance Region might be the most sensitive area in terms of land-based pollution going to the sea.

5.3. Chlorophyll in the Corinth Gulf

The paucity of the CHL concentration in the center of the Corinth Gulf has been evidenced in the present study. The CHL pattern displayed in **Figure 3.4** shows that the CHL-rich waters are present in the Patras Gulf, the Strait & Entrance Region, and the Itea Bay. In the three cases, this is due to the local enrichment and nutrient input from rivers in shallower areas which results in a less diluted CHL concentration. In the Patras Gulf and mostly in the Strait & Entrance area, upwellings play an important role for CHL concentrations. One main reason might be that, before the Nafpaktos Bay and in front of the Mornos area, the internal wave and the upwelling are the strongest (Rubi *et al*. 2022). This would create strong bottom currents that will resuspend the sedimentary litter. Therefore, the upwelled waters will be enriched in clastic particles that might serve as nutrient for algal blooms and therefore increase the CHL concentrations in this area.

Occasional local enrichment of the center of the Corinth Gulf in CHL may have two origins. First, CHL-rich waters from the Strait & Entrance Region can reach the center of the Corinth Gulf by following the southern coast and then getting trapped in the gyres in front of the Itea Bay. Second, the gyre in the West Corinth Region can affect CHL-rich waters from Itea Bay and export some towards the center of the Corinth Gulf. These patterns were already observed with the positive trend in CHL concentration along the southern coast of the Corinth Gulf while the northern parts appear with a negative trend, except for Itea Bay (Colella *et al*. 2016). This trend of decreasing CHL from West to East in the Corinth Gulf can be similar to the trend of the increasing oligotrophy in the Mediterranean Sea where eastern waters are poorer in CHL than the western ones (Turley

et al. 2000; Siokou-Frangou *et al*. 2002; D'Ortenzio & Ribera d'Alcalà 2009; Belgacem *et al*. 2021).

These CHL concentrations seem to influence the movements of dolphins present in the Gulf of Corinth (Issaris *et al*. 2012). The mapping of Bearzi et al., (2016) (G. Bearzi *et al*. 2016) evidenced the presence of *Tursiops truncates* remaining mostly in the Itea Bay, even if they used to occupy the whole northern coastal waters. While this dolphin species is commonly found in coastal water areas, its presence preferentially in the 0-300m Itea Bay (Giovanni Bearzi *et al*. 2011; G. Bearzi *et al*. 2016), is probably related to its high CHL concentrations or the presence of an aquacultural farm at the south-west edge of the Itea Bay. Phytoplankton is the base of the marine food chain, and their abundance can significantly influence the entire trophic chain, leading to the occurrence of higher trophic level species like *Tursiops truncates*. The other dolphin species *Stenella coeruleoalba* is found mostly in the deeper environment (G. Bearzi *et al*. 2016) in the center of the Gulf at the location where the anticyclonic eddy would export CHL from the Itea Bay towards the center of the Gulf (**Figure 3.4A**). It suggests again an influence of the bay over the Gulf.

The low CHL concentration levels at the center of the Corinth Gulf are recurrent through geological times. In the sedimentary cores retrieved during the IODP Expedition n°381 (McNeill, Shillington, Carter, Everest, Le Ber, *et al*. 2019a; b; Shillington *et al*. 2019), few sedimentary units were found rich in planktonic foraminifera. These cores were drilled in the East Corinth Region. The latest occurrence of foraminifera rich levels date from 70ka at the location of the IODP Core n°M0078 (McNeill, Shillington, Carter, Everest, Le Ber, *et al*. 2019a), when sea-level was lower than the present one, close to a lake setting. A well-developed Deep Chlorophyll Maximum was identified in the Corinth Basin (IODP Core n°M0079) dating from 106 to 104ka (McNeill, Shillington, Carter, Everest, Le Ber, *et al*. 2019b; Sergiou *et al*. 2024). The pattern of the actual ocean dynamics explaining the paucity of CHL in the center of the Corinth Gulf could have, sometimes, been similar since the last 100ka. If during the last 100ka, the oceanic configuration of the Corinth Gulf was similar to the present one (Sergiou *et al*. 2024), the proposed hydrodynamism would explain the low CHL concentration of planktonic species found in the cores (McNeill, Shillington, Carter, Everest, Le Ber, *et al*. 2019a; b; Sergiou *et al*. 2024). Concerning the rare foraminifera rich level, they may be related to other oceanographic configurations of the Gulf of Corinth with different connections or due to increased riverine inputs (Sergiou *et al*. 2024). Due to the oligotrophy of the surrounding waters (Mediterranean Sea; (Turley *et al*. 2000; Siokou-Frangou *et al*. 2002; D'Ortenzio & Ribera d'Alcalà 2009; Belgacem *et al*. 2021)), it is indeed expected to have low CHL concentrations in the Corinth Gulf and it should not be surprising that it was the case through the last 100ka, even with minor changes in the Gulf's paleogeography (Sergiou *et al*. 2024).

6. Conclusions

While no relevant in-situ data exist to study the overall dynamics over the Corinth and Patras Gulfs, satellite data proved to be extremely relevant in describing the oceanography of these gulfs. We were able to identify several gyres, one in Patras and two major ones in the Corinth Gulf while also evidencing diverse upwelling areas and steady currents along the south coast of the Strait & Entrance Region. Using a dataset with 14 years of records allowed us to observe seasonal variations in SST and in CHL concentrations. With this amount of data, we were able to get a rough idea of the evolution of the SST over more than a decade and the computed SST means evidenced the key regions regarding the evolution and the disparity of the temperatures in the Gulfs.

Advances in remote sensing technologies have enabled us to delve deeper and analyze a comprehensive dataset spanning 14 years of data. The datasets we used were limited by their resolution (0.01°x0.01°) and by the cloud cover. Removing the days in which more than 95% of the data were missing due to clouds eliminated 25% of the initial dataset. Nonetheless, we were able to sort this dataset to evidence key events for the hydrodynamics of the Gulfs. To strengthen this, the use of DINEOF was effective in gaining insights into the variability of the phenomena and filling in gaps where data pixels were missing. This statistical approach has led to better understanding of an overall unstudied oceanographic region. Thus, we were able to interpolate missing pixels in the maps and get an overview of the main patterns that are dictating the variability of the SST in the Gulfs. To further this analysis, modelling could be used to gain a more comprehensive understanding of the entire water column dynamics, as satellite data can only provide information about surface behavior.

Nonetheless, satellite data are very useful for this kind of study, where the goal is to observe large scale phenomena, both spatially and temporally. Consequently, with its description of the oceanographic dynamics, this work could serve as an up-to-date reference for future studies. By redefining the key features of the hydrodynamic circulation of the Gulfs of Patras and Corinth, further studies will have a strong basis to analyze any data linked to this oceanographic circulation. Understanding the currents and the main SST variations inside a basin is a key for any ocean related study. Also, understanding the sedimentary dynamics or chlorophyll patterns of the Corinth Gulf will be easier when considering the various features presented by the oceanography of this gulf. The general dynamics of the Corinth Gulf appear to be driven in a west-to-east pattern with the Strait & Entrance Region playing a major role in the distribution of the variability of the studied patterns. Due to the importance of this region, understanding the dynamics of the Rio-Antirio Strait seems to be crucial in the understanding of the ocean dynamics of the Corinth Gulf.

Chapter 4: Modelling of the Present Oceanographic Situation of the Gulfs of Patras and Corinth

One goal of the thesis was to fully understand the hydrodynamics of the Corinth Gulf. After looking at the surface dynamics through satellite data, questions about the dynamics in depth emerged. In order to get the complete understanding of the oceanographic context in Corinth, modelling was used to calculate important oceanographic parameters.

This chapter is written in a "paper" format since it was published during the PhD: (Caterina *et al.* 2025): Caterina, B., Hubert-Ferrari, A., Barth, A. & Beckers, J.-M., 2025. Modelling of the Present Oceanographic Situation of the Gulfs of Patras and Corinth. *J. Mar. Sci. Eng.*, **13**, 1827. doi: doi.org/10.3390/jmse13091827.

1. Introduction

The ocean dynamics in the Patras and Corinth Gulf are important since they affect their environmental impacts. These two gulfs are separating the continental Greece from the Peloponnesus. Even if they are considered as gulfs they display a very enclosed morphology that plays an important control over their oceanographic dynamics (Lascaratos *et al.* 1989; Fourniotis 2024; Caterina & Hubert-Ferrari 2025). For a long time, the Gulf of Corinth has been studied by geologists due to its fault network and active seismicity (Ori 1989; Rohais *et al.* 2007; A. Beckers *et al.* 2015, 2016; Nixon *et al.* 2016; McNeill, Shillington, Carter, Everest, Gawthorpe, *et al.* 2019). Despite Corinth Gulf's geology being studied, its oceanography is not yet fully understood and well described. Old studies over this peculiar oceanography were made by Lascaratos et al. in 1989 (Lascaratos *et al.* 1989) or by Poulos et al. in 1996 (Poulos *et al.* 1996) featuring early stages of satellite images in the first and in-situ CTD data from 1983 for the second. The techniques and the methodology have evolved since then and having a new look over this important area might bring light over key features of the dynamics in the Gulf.

Since the year 2000, no publicly available in-situ data has been evidencing the whole oceanographic circulation of the Gulfs of Patras and Corinth. To counter this lack of in-situ data, a recent study has been published by analyzing satellite data over a 14 year period by Caterina & Hubert-Ferrari in 2025 (Caterina & Hubert-Ferrari 2025). This study was useful to describe the surface dynamics and only hypothesis for the bottom circulation. The use of modeling, that would give information over the whole water column for any given time, is therefore a great interest in understanding the dynamics. Modelling effort has already been done over the Gulf of Patras (Fourniotis & Horsch 2010, 2015), over the Rio-Antirio Strait (Fourniotis 2024) which connects the two gulfs or even over the Gulf of Corinth itself (Aspioti & Fourniotis 2025) but they were more focused on

the causes of the dynamics rather than the description of the circulation and its 3D complexity.

Getting to understand the complexity of the hydrodynamics over the whole water column with an emphasis over the surface and the bottom phenomena appears to be the key to assessing any geomorphological or geological interpretation made in the Corinth Gulf. Moreover, it has already been assessed that the Rio-Antirio Strait plays a crucial role over the control of the dynamics (Rubi *et al.* 2022; Fourniotis 2024; Caterina & Hubert-Ferrari 2025) and the impact over the geomorphologies and the biodiversity (Rubi *et al.* 2022; Paramana *et al.* 2023; Titri *et al.* 2025). Being able to see its impact over the whole Corinth Gulf is one of the reasons that modelling this area is important.

In this paper, we aim to model the hydrodynamic circulation of the Gulfs of Patras and Corinth to address the current lack of understanding regarding the circulation of the water at depth but also the consequences of the seasonality or the winds over these basins. This will be achieved mainly using ROMS modelling completed by scarce in-situ data and satellite imagery.

2. Settings of the Corinth Gulf

The Gulf of Corinth separates the continental Greece from the Peloponnesus. Its western connection to the Patras Gulf is made by the Rio-Antirio Strait while at the east, the connection with the Aegean Sea is a small, manmade one through the Corinth Canal. The Gulf of Corinth is considered as elongated since it is 120 km long and 40 km wide at maximum (**Figure 4.1**). Its deepest point lies at around 900 m deep, and the gulf presents steep slopes, particularly in the south. The Patras Gulf is smaller, almost circular, since it is 20-25 km wide. This Gulf is also shallower (120 m deep). The connection between these two gulfs is done by the 18 km Rio-Antirio Strait area which plays a very important role in the hydrodynamic of the basins. The strait's bathymetry deepens from West to East from ~50 m depth to ~100 m depth (Ferentinos *et al.* 1985; Rubi *et al.* 2022).

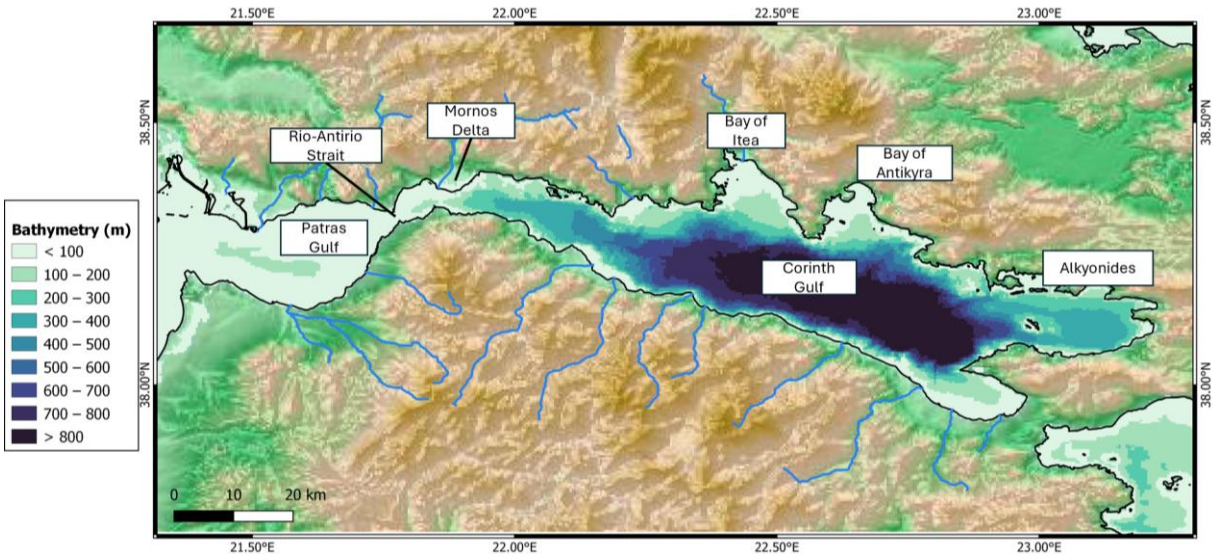

Figure 4.1: Bathymetry map of the Patras and Corinth Gulfs with the identification of the specific locations of the area

Previous studies about the general oceanographic phenomena in the Gulfs of Patras and Corinth evidenced surface dynamics with the presence of several eddies and upwellings based on Sea Surface Temperature (SST) (Lascaratos *et al.* 1989; Caterina & Hubert-Ferrari 2025). The main eddies are a cyclonic gyre in the Patras Gulf and for the Corinth Gulf, an anticyclonic gyre in front of the Bay of Itea and a cyclonic gyre in front of the Bay of Antikyra (locations on **Figure 4.1**; (Caterina & Hubert-Ferrari 2025)). The main inferred upwellings are located at the exit of the Rio-Antirio Strait in the Corinth Gulf and in the smaller Gulf of Alkyonides. These upwellings appear on the northern coast of the Gulf of Corinth while the main surface flow seems to travel close to its southern coast from the Strait towards Corinth center.

Regarding the winds over the Gulf of Corinth, they appear to be mostly easterly 70% of the time and stronger in winter (Koletsis *et al.* 2014). The Rio strait area is dominated by stronger eastern winds while the dominant wind direction near the eastern end of the Corinth Gulf is from northwest (Koletsis *et al.* 2014). Winds are considered as a key factor for the hydrodynamics of both the Patras and the Corinth Gulfs (Lascaratos *et al.* 1989; Fourniotis & Horsch 2010; Aspioti & Fourniotis 2025).

3. Materials and Methods

3.1. Regional Ocean Modeling System

The model Regional Ocean Modeling System (ROMS) was used to perform all the simulations (Moore *et al.* 2011). This model was used due to its strength regarding resolution of coastal areas since the Corinth Gulf is narrow enough to be considered as a coastal area in terms of modelling. Also, it seems ROMS performs well in strait areas and enclosed basins as already been shown by several studies (Nagy *et al.* 2019; Mujiasih *et al.* 2021).

One of the key features required for these simulations was the terrain-following approach (Moore *et al*. 2011) since the dynamics near the seabed were the focus of this study. ROMS's approach of vertical levels with σ-coordinates allows us to get less numerical errors than z or s grids near the bottom.

The horizontal spatial resolution of the model was, for this study, fixed by the bathymetry dataset from GEBCO with a resolution of ~450m (15 arc-second). The bathymetry was computed to build a ROMS initial grid with manual corrections for the low bathymetries before interpolating the initial conditions. First, a smoothing of the bathymetry was made (rmax = 0.8; strength of the smoothing) to conserve hydrostatic consistency and avoid large bottom gradient due to the sigma system construction of the model (Shchepetkin & McWilliams 2005; Barth 2025). Then the manual corrections were mainly focused on low bathymetries over the whole domain. They consisted in the addition of +5 m for each point between 0 m and 10 m, +10 m for each point between 10 m and 30 m, and +5 m for each point between 30 and 35 m. Points deeper than 35 m were observed as correct in the shallower area of the Gulf. These variations were based on the high resolution bathymetry of the strait presented in Rubi et al. (2022).

For the borders, the grid was built to only consider one open connection, at the far west of the area, between the Ionian Sea and the Gulf of Patras. All other borders were considered closed, even the Corinth Canal opening since with its shallow depth and 30 m width it is not considered as a proper oceanographic connection (Caterina *et al*. 2022). The specific ROMS parameters of the grid were specified to be: Tcline (width (m) of surface or bottom boundary layer in which higher vertical resolution is required during stretching) = 50, θs = 5 (S-coordinate surface control parameter, 0<= θs <= 10), θb = 4 (S-coordinate bottom control parameter, 0 <= θb <= 4), nlevels = 32 (number of vertical adaptative layers). The equation chosen for the vertical transformation was the improved formulation of Shchepetkin (2005) (Eq. (2) in (WikiROMS 2019), extracted from (Shchepetkin & McWilliams 2005)) and the one for vertical stretching was the Shchepetkin (2009) improved double stretching function (Eq. 2.3 in (Shchepetkin & McWilliams 2009) for the surface and Eq. 2.4 in (Shchepetkin & McWilliams 2009) for the bottom).

Therefore, the vertical repartition of the levels is focused on the surface and the bottom. Preliminary tests indicated that surface and bottom refinement were necessary to achieve accurate simulations. Given that near-bottom dynamics are a focus of this study, maximum refinement (θb = 4) was applied for the bottom (Shchepetkin & McWilliams 2009). It translates to a repartition of the 32 levels as shown in **Figure 4.2** for the entirety of the modelled domain.

Finally, the preparation of the initial grid was made by using Julia scripts (Barth 2025) where all the inputs are retrieved from the CMEMS (Buongiorno Nardelli *et al*. 2013) or the ECMWF for the winds. From the CMEMS, we retrieved modelled data for the temperature, the salinity, the sea surface elevation and u end v movements. In order to force the tides

in the model, as we suspect them to have a strong influence over the dynamics (Rubi *et al.* 2022), we used data from the TPXO Tidal Model (Egbert *et al.* 1994; Egbert & Erofeeva 2002). From this model, parameters of the tides (velocity of the currents, amplitude and phases) were exported over the whole domain to serve as tidal boundary conditions. The open boundary conditions were set at the extremity of the grid between the Patras Gulf and the Ionian Sea; the rest of the boundaries were considered closed. This calibration was done by setting the West border of the model as open under "RadNud" conditions for the 3D velocity, the temperature and the salinity in the "roms.in" initiation script (Shchepetkin & McWilliams 2005; Barth 2025). "RadNud" implies radiation boundary condition with nudging (Shchepetkin & McWilliams 2005).

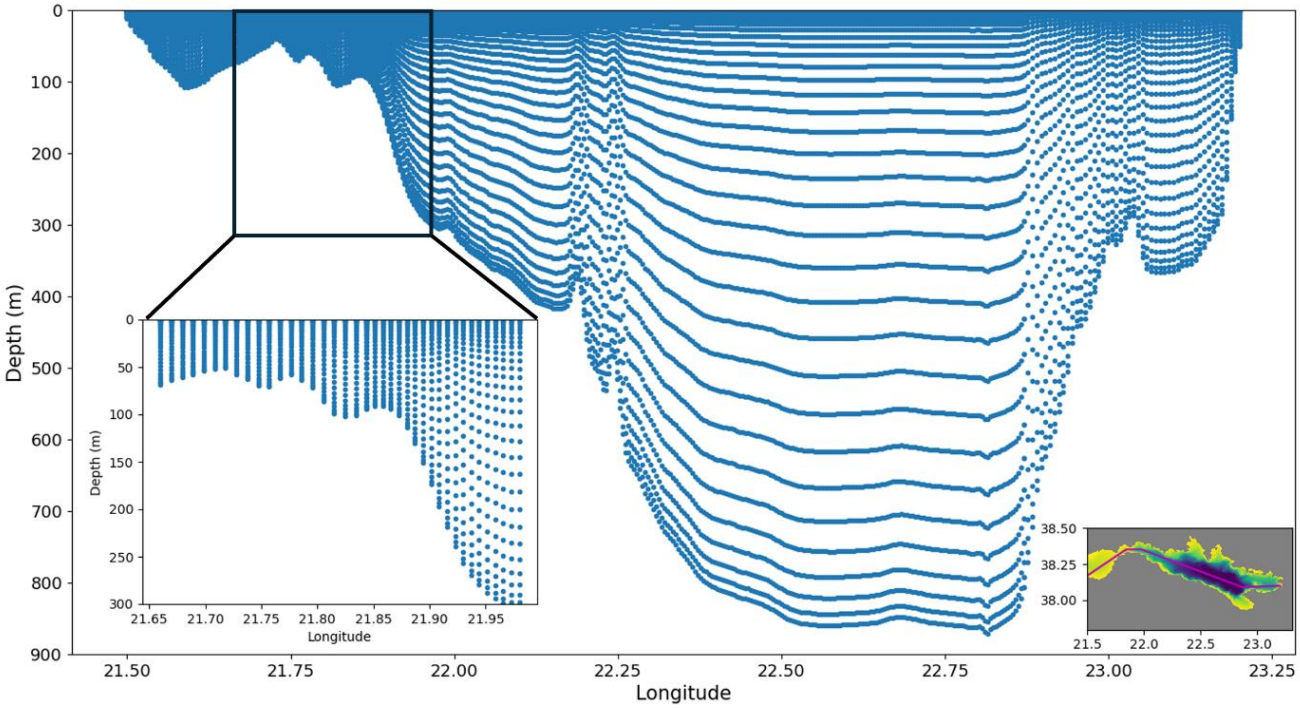

Figure 4.2: Repartition of the 32 vertical adaptive levels over a section cutting through the whole domain.

To analyze different outcomes, several setups were tested with different time periods or forcing fields. The final time periods were the months of January 2023 (winter case), May 2023 (reference time) and September 2023 (summer case). Each month was simulated separately due to model running time and available memory storage. Having three seasons modelled can allow us to see the different impacts of the stratification of the thermocline since we expect it to be stronger in summer than in spring and stronger than in winter. The initial conditions for the 3 different months were roughly the same: the bathymetry stayed identical in the 3 simulations; only the dates for the initial oceanographic conditions retrieved from CMEMS (Buongiorno Nardelli *et al.* 2013), the winds from ECMWF and the initial date for the TPXO Tidal Model (Egbert *et al.* 1994; Egbert & Erofeeva 2002) changed according to the month simulated (01 January to 31 January 2023, 01 May to 31 May 2023 and 01 September to 01 October 2023).

May 2023 was selected and after used as reference for this study since we collected in-situ data that could help us with the validation of the model.

To assess the impact of the wind on the hydrodynamic circulation, three cases were considered for different simulations of the month of May 2023. First the baseline case where the winds are not modified from the ECMWF model. Second, the case where the wind was neglected by setting its velocity to 0. Third, a stronger-wind case where the wind velocity was multiplied by $\sqrt{3}$ (to increase shear-stress by 3), resulting in a threefold increase in surface shear stress. This increase is set to this value to not exaggerate the shear stress and to fit to maximal wind velocities observed by Koletsis et al. (2014) (Koletsis *et al*. 2014). This increase will also affect other parameters such as sensible heat and latent heat, like real atmospheric changes would.

For all these simulations, the spin-up time of ROMS with our external data as initial conditions was around 7 to 8 simulated days. Therefore, the output analysis started on the 9th day for the simulations. The main outputs on which the simulations focused were the temperature, the salinity, the currents (u and v) and the sea surface elevation. These outputs were chosen to have a good overview of the current dynamics at a very high resolution.

3.2. Data for the validation of the model

Acoustic Doppler Current Profiler (ADCP) data were collected in collaboration with the Oceanus-Lab (Oceanus-Lab 2025) from the University of Patras (Greece) during a marine campaign extending from 12 May 2023 to 19 May 2023. ADCP data were collected and calibrated with sound velocity profiles on the water column using a Valeport MiniSVS-P. Then the ADCP data were temporally linked with Patras tidal curves for the measured period (Tideschart 2025) and analyzed with Ocean Data View (ODV) software (Schlitzer 2021) to be displayed as “real-time” sections through area of interest to cross-validate the model. They provide direct in-situ measurements of currents throughout the water column, enabling validation of both surface and near-bottom circulation in the model.

In addition, model outputs were compared to L3 level satellite data coming from the CMEMS Database (Buongiorno Nardelli *et al*. 2013; CMEMS 2025). These data were downloaded for the month of May 2023 as NetCDF files and spatially analyzed through Julia language as daily maps. Their resolution is 0.01 degrees (36 arc-second) which is 2.4 coarser than the model output (GEBCO data source, 15 arc-second = ~450 m). This difference in resolution can provide inaccurate quantitative comparison of the dataset without using an interpolation tool. So, to overcome this resolution difference, only semi-qualitative general patterns and a mean of the SST satellite data were used to validate the model. Moreover, Sea Surface Temperature (SST) from L3 satellite data is our only available satellite dataset to compare it to the model since neither salinity nor water height are measured or calculated for the Corinth Gulf through CMEMS L3 or L4 levels database.

Tidal gauge data from the Flanders Institute of the Sea (VLIZ) (Flanders Marine Institute (VLIZ) 2025) were used to verify the Sea Surface Height (SSH) of the ROMS output model. These data were also used to be certain of the high and low tide periods to understand flow directions under the tide influence.

4. Results

4.1. Model Validation

Due to the section location, we were able to compare the westward current velocities from the ADCP data to the model output from the 17 May of 2023 between 8 a.m. and 9 a.m. (local time). When visually comparing the two sections, from the model and from the ADCP, the same dynamics can be observed (**Figure 4.3**). At the time and location of the section, a strong westward current (0.5 m s^{-1}) is observed at the middle of the water column and near the bottom. Eastwards currents are present in the north part of the section (on the right hand) with a smaller velocity (0.2 m s^{-1}). The velocity range computed by the model is the same as the one collected by the ADCP. On the ADCP section, there is a rough "jump" in the effective depth of the data regarding the high velocity westward currents "patch". Even with this kind of variation in the ADCP data, the model can be validated at least to the location of the section.

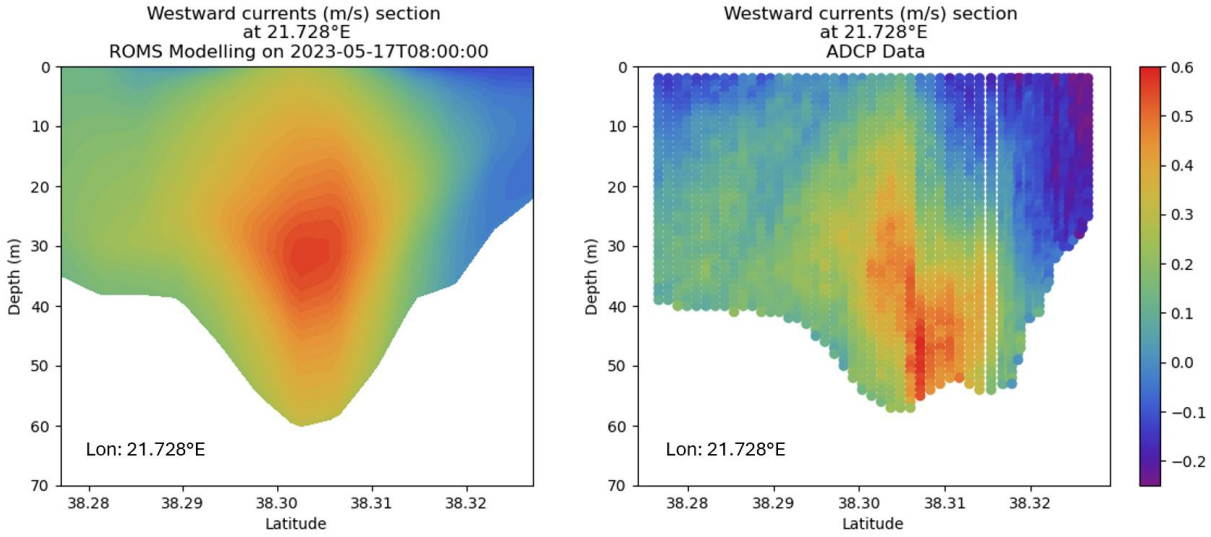

Figure 4.3: Qualitative comparison for the validation of the model with the ADCP Data from the 21.728°E South to North section at the entrance of the strait from the Patras Gulf.

In addition to the ADCP data, model results were compared to satellite-derived SST fields to evaluate surface temperature accuracy. By using a map of the temporal average SST from the satellite data we were able to compare it with an interpolated map for the temporal mean modelled temperature at the subsurface (1m below sea level) for the same month (**Figure 4.4**). To get to these averages, a mean over every time step was done for both datasets to get only one map for the mean. Differences in a few areas may be attributed to gaps in satellite data due to cloud cover, which limits the number of available

time steps contributing to the monthly average. Also, the model overestimates SST by approximatively 1°C in the central basin. Temperature discrepancies may also result from the difference in measurement methods: satellites retrieve sea surface temperature (SST), whereas the model provides bulk temperature, which can exhibit slight deviations even when sampled at approximately the same depth. Overall, modelled SST patterns are consistent with satellite observations.

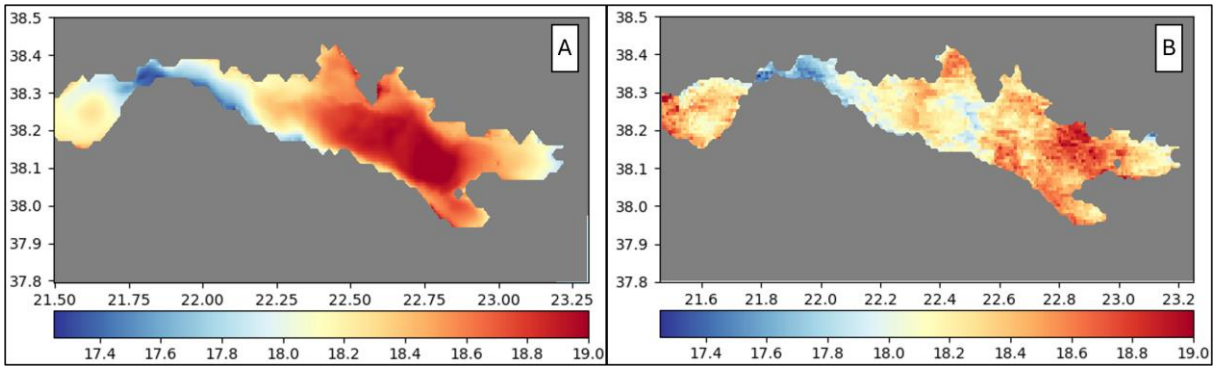

Figure 4.4: Mean temperature for the subsurface of May 2023 represented by (A) the ROMS output and (B) satellite data.

4.2. General circulation patterns

4.2.1. Patras Gulf

Using a model of the hydrodynamics allowed us to observe continuous events both in space and in time. By looking at the SST, the Patras gyre can be identified. According to the seasonal simulations, the Patras gyre varies in direction and intensity depending on the month of the year (**Figure 4.5**). On average for the month of May and September the gyres is cyclonic and with strong velocities like it was previously described (Lascaratos *et al.* 1989; Fourniotis & Horsch 2010, 2015; Aspioti & Fourniotis 2025; Caterina & Hubert-Ferrari 2025). During the month of January 2023, the gyre appears to be anticyclonic with stronger average velocities near the northern coast of the Patras Gulf.

The inflow of the warm Ionian waters in the gyre follows the south coast of the Patras Gulf while the cold waters are mainly along the northern coast (**Figure 4.4**). The northern part of the Gulf seems to be always dynamic, even in winter, possibly due to the influence of the Rio-Antirio Strait. Exchanges with the Rio-Antirio strait are also evidenced with alternate flow roughly every 6 hours according to the tides (**Figure 4.6**). Waters coming to Patras through the strait are often colder than the surface Patras waters. Corinth exiting's waters follow the north coast of the Patras Gulf, being captured by the gyre movement. Tidal amplification appear to be the strongest in the Rio-Antirio strait and this impacts the SSH of the Patras Gulf that rises according to the tides that are more evidenced in Corinth (**Figure 4.6**), suggesting another parameter controlling the high connectivity of the two Gulfs.

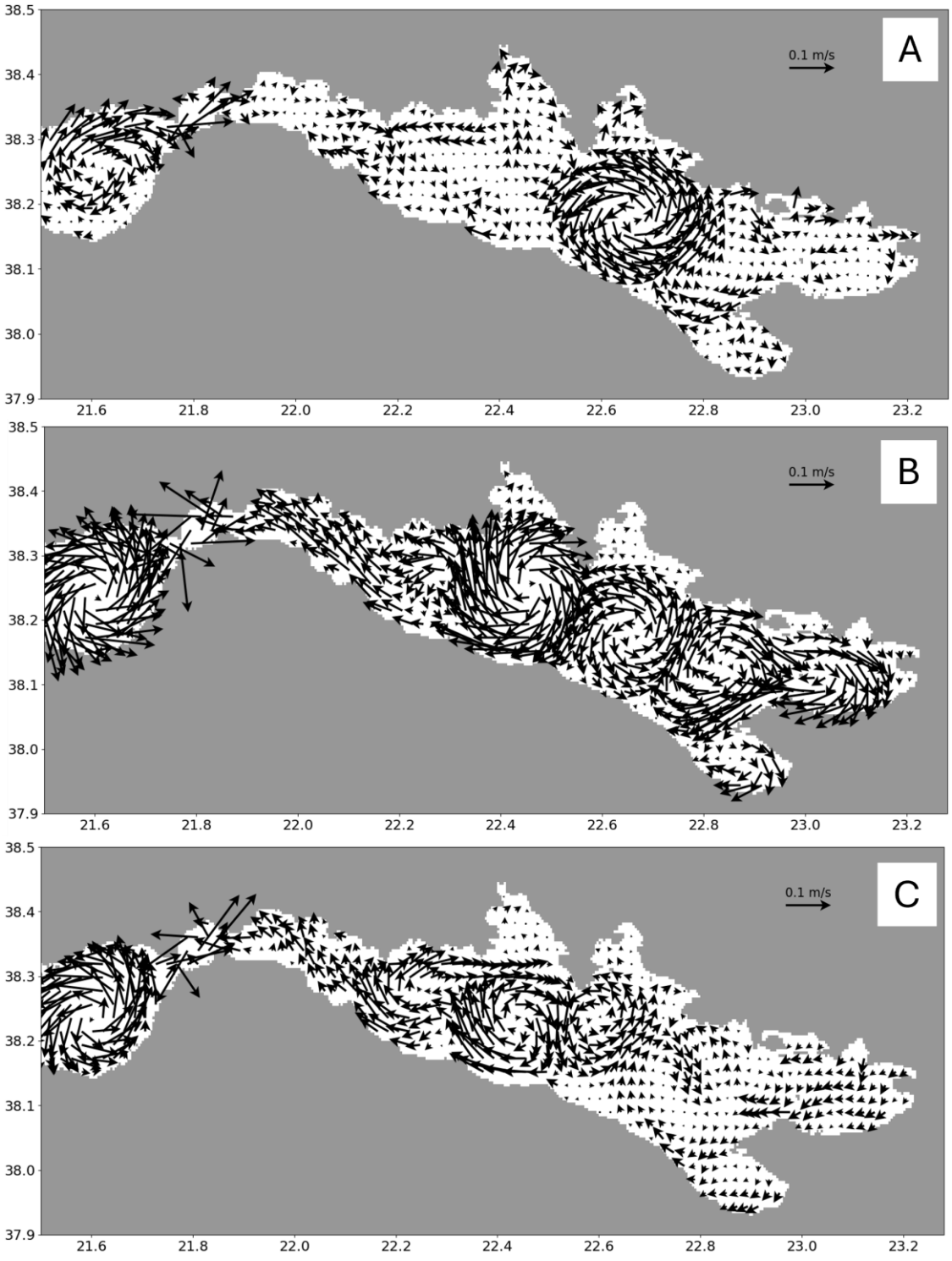

Figure 4.5: Mean velocities in m s^{-1} modelled at the surface. (A) January 2023 (B) May 2023 (C) September 2023.

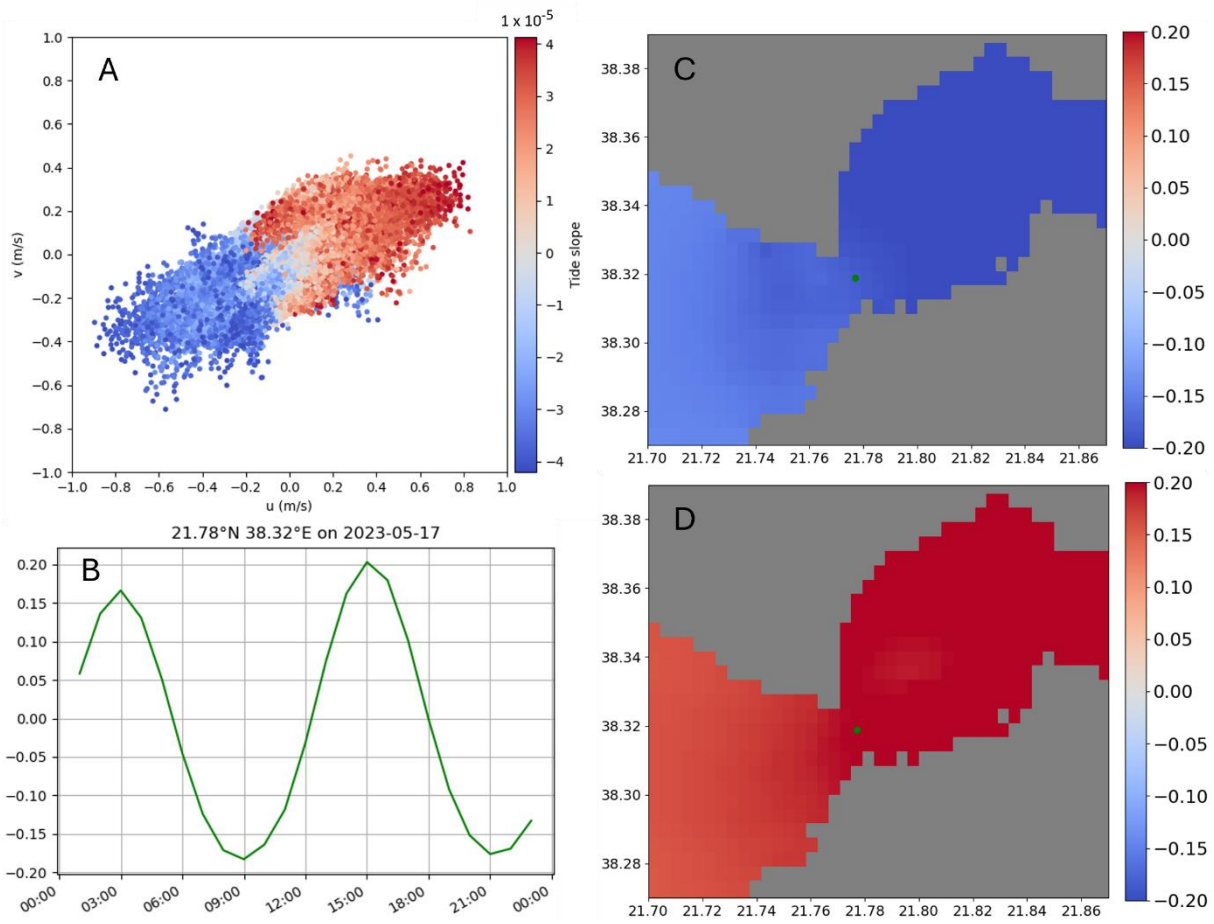

Figure 4.6: Impacts of the tides over the currents and the Sea Surface Height (SSH). (A) Distribution of u and v (m s^{-1}) at the bottom for the strait area according to tidal slope taken at Aigio (Flanders Marine Institute (VLIZ) 2025). (B) SSH (m) at the green dot location in the center of the strait showing the high and low tides for the 17th of May 2023 from ROMS output. (C) SSH (m) map at low tide (2023-05-17 at 9 am). (D) SSH (m) map at high tide (2023-05-17 at 3 pm).

4.2.2. Corinth Gulf

The gyre in front of the Bay of Itea, already observed through satellite data (Caterina & Hubert-Ferrari 2025) is also observable and consistent for the month of May 2023 (**Figure 4.5B**). A smaller cyclonic gyre is observed near the Cape of Akrata. This gyre might be formed due to the bathymetric influence of the cape that serves as a direction guide or a gutter for the water flow. The gyres in front of the Bay of Antikyra appears to be more complex in terms of position and amplitude that what was previously described using only satellite images (Caterina & Hubert-Ferrari 2025) . The main gyre in front of the Bay of Antikyra always appears cyclonic for the modelled periods. During the month of May, its extension is smaller than during winter or summer (**Figure 4.5**). Also, during the month of May, this gyre is less strong and is divided into smaller gyres. These patterns are validated trough satellite data as all of these features were already described (Lascaratos *et al.* 1989; Caterina & Hubert-Ferrari 2025). The circulation in the Alkyonides area seems to be still on average during winter and spring while in summer the surface circulation goes clockwise in the bay and seems to be an extension of the Antikyra gyre (**Figure 4.5C**).

The entrance of the Corinth Gulf (the Rio-Antirio strait area) remains the coldest area of the domain in terms of SST (**Figure 4.4**; Caterina & Hubert-Ferrari 2025). The modelled phenomenon occurring in this area explains what was deduced before (Rubi *et al*. 2022; Caterina & Hubert-Ferrari 2025). By doing a vertical section through the strait (**Figure 4.7**), it appears that, according to the phase of the tide (**Figure 4.6**), the deep and cold water coming from the Gulf of Corinth doesn't always cross the strait. With the upsloping due to the steep rise in bathymetry, the bottom currents reach the subsurface. If the surface current flows towards the Patras Gulf, which is the case during ebb tide (**Figure 4.6**), the whole water column can be displaced towards the west with strong bottom current entering the Patras Gulf. If the surface current is going towards the Corinth Gulf (during flood tide; **Figure 4.6**), the bottom currents are then brought to the surface and reflected to the Corinth Gulf. In this second case, cold water reaches the surface which lowers the SST near the East of the Rio-Antirio Strait.

The behavior of the internal wave generated by the density difference of the waters and the interaction between the surface and the bottom currents can be associated to the tides and their directions (**Figure 4.6**, **Figure 4.7**). This conclusion is supported by the observation of a shift in current direction every 6 hours (**Figure 4.6**, **Figure 4.7**), consistent with the tidal phases at this location(Tsimplis 1994; Rubi *et al*. 2022; Flanders Marine Institute (VLIZ) 2025). Since the Rio-Antirio Strait lie in a microtidal context (Tsimplis 1994; Horsch & Fourniotis 2017; Aspioti & Fourniotis 2024, 2025; Fourniotis 2024), as part of the Mediterranean Sea, the maximal tidal amplitude observed is less than 30 cm (**Figure 4.7**) (Flanders Marine Institute (VLIZ) 2025; Tideschart 2025) which appears irrelevant compared to the depth of the adjacent basins. In this case, the tide impact is more reflected by the presence of an internal tide due to the bathymetric variations of the strait (Rubi *et al*. 2022; Fourniotis 2024) rather than the small amplitude of the waves (**Figure 4.7**).

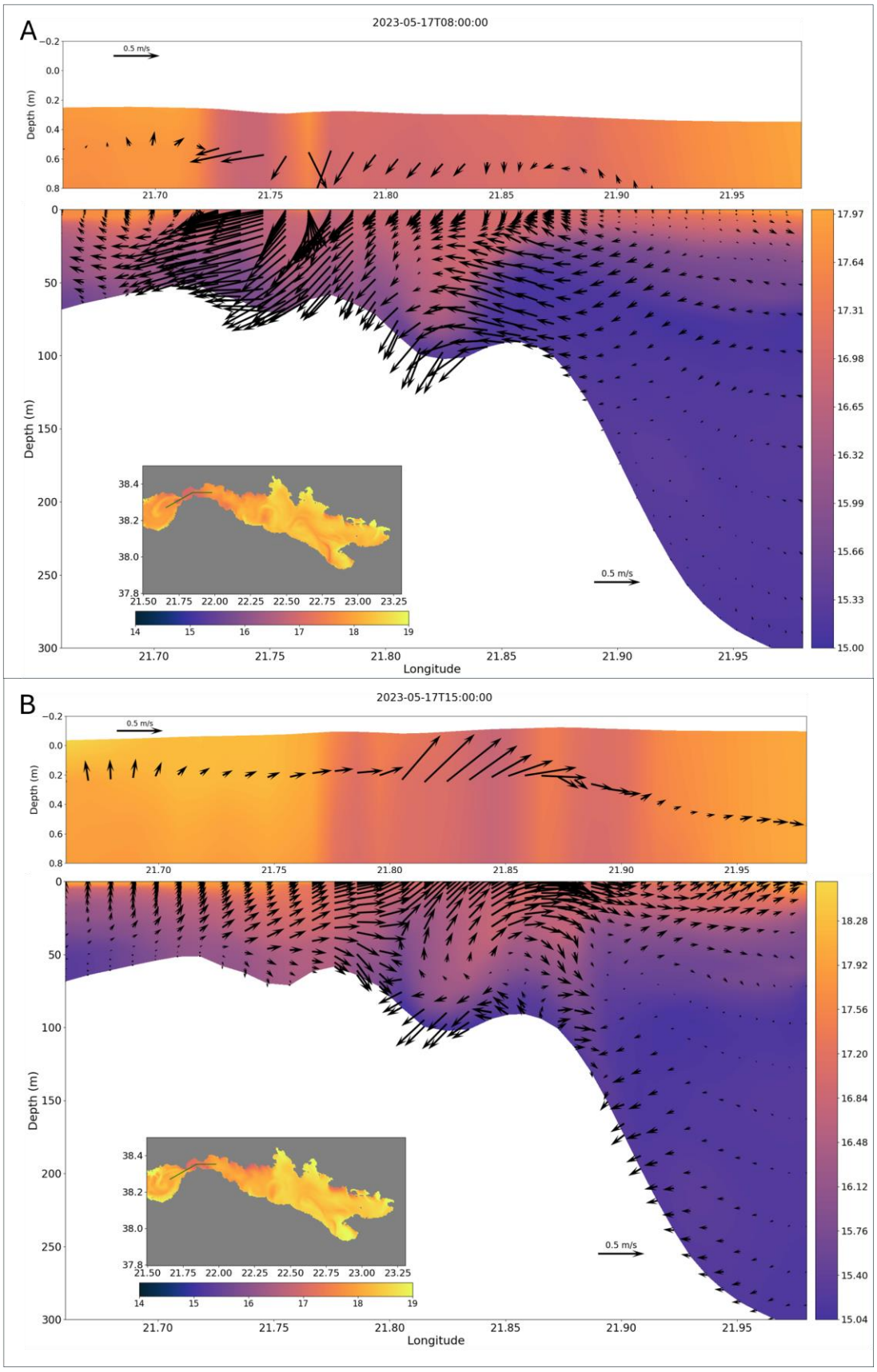

Figure 4.7: Section of the modelled strait displaying the temperature (°C, colors) of the water and the current direction and intensity (m s^{-1}, arrows) under two different tidal dynamics. A zoom on the SSH variation is displayed over each section. (A) Section during the low tide and (B) Section during the high tide according to SSH and tidal gauge data (Flanders Marine Institute (VLIZ) 2025).

4.3. Wind impact over the Patras and Corinth Gulf

To answer the question about the wind being one important factor over the surface dynamics in the Gulfs of Patras and Corinth we observed 3 situations.

For the Patras Gulf, the wind plays an important role as in the “no wind” situation, the waters along the northern coast stay still on average (**Figure 4.8**). Thus, when no easterly winds are present over the Gulf; easterly winds being present over the month of May 2023 (**Figure 4.9**); only the southern part of the Patras waters is dynamic overall. When the easterly winds are enhanced, the Patras gyre velocities are therefore enhanced. With these observations, the Patras gyre can be considered as wind driven since it disappears when there is no wind and is enhanced when the wind is enhanced. Regarding SST, increasing the wind will decrease the temperature by around 2°C on average. The “no-wind” case will result in a 2°C increase for the average SST of the Patras Gulf (**Figure 4.8**).

At the Rio-Antirio strait location, it appears that winds have few effects other than changing the water temperature (**Figure 4.8**). Water movement does not change despite the wind being absent or enhanced. This information is relevant to identify that the rising from the colder bottom waters from the Corinth Gulf is due to an upsloping or an upslope flow (**Figure 4.7**) rather than a wind-driven upwelling (Deleersnijder 1989). Indeed, the cold surface waters are still present even in a “no-wind” case.

In the Gulf of Corinth, the gyres have different behavior depending on the wind intensity. The gyre in front of the Bay of Itea appears less strong in the “no-wind” situation. This might be due to the general direction for the wind over the month of May 2023 that would have induced a movement of the surface waters towards the west. Despite not being a clear gyre movement, anticyclonic circulation can still be observed in front of the Bay of Itea (**Figure 4.8**). In the enhanced wind simulation, the gyre is larger, anticyclonic and has less interactions with the waters in front of the Bay of Antikyra.

Still in the enhanced wind simulation, the dynamic in front of the Bay of Antikyra appears on average less circular but still with a cyclonic movement. The cyclonic movement in a big and unique gyre is present in front of the Bay of Antikyra in the “no-wind” simulation (**Figure 4.8**).

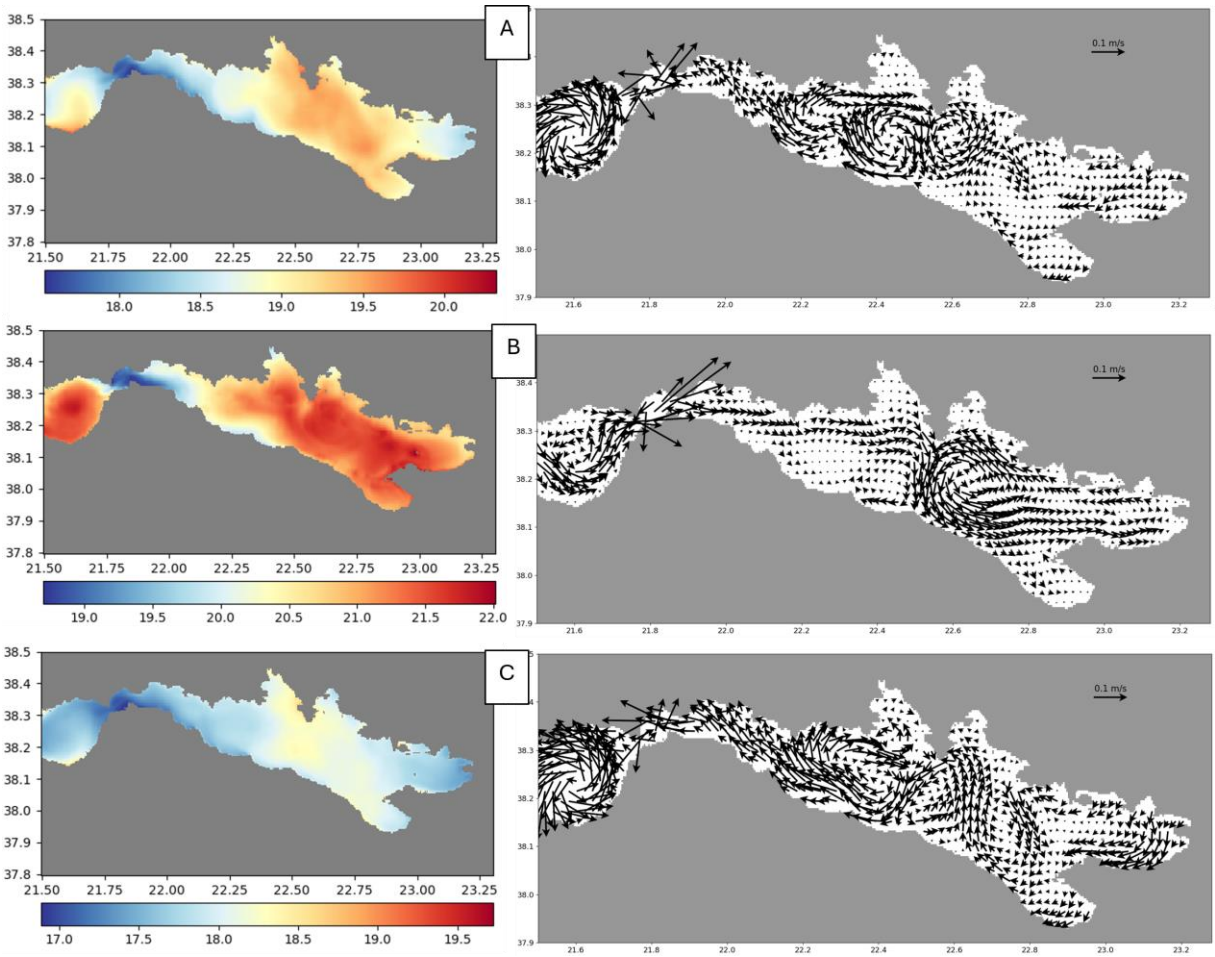

Figure 4.8: Comparison of the effects of the winds for the month of May 2023. On the left: mean SST maps (the scale is in °C), on the right: mean velocities at the surface (m s^{-1}). (A) Normal winds, (B) No winds (velocities set to 0), (C) Enhanced winds (shear stress multiplied by 3).

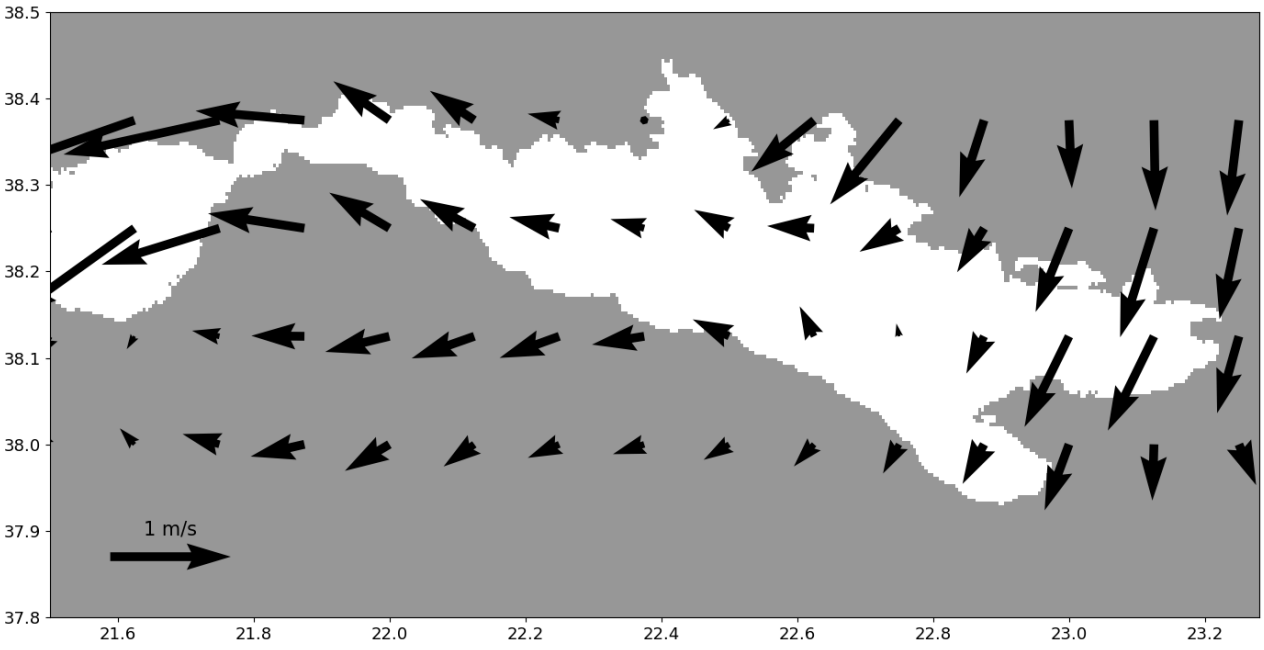

Figure 4.9: Mean wind direction and velocity for the month of May 2023

4.4. Dynamics at the bottom

While surface dynamics have been described several times for the Corinth Gulf (Lascaratos *et al.* 1989; Fourniotis & Horsch 2010; Aspioti & Fourniotis 2025; Caterina & Hubert-Ferrari 2025), evidence of bottom dynamics is sparse in the center of the Corinth Gulf (Poulos *et al.* 1996) or focused on the Rio-Antirio Strait (Rubi *et al.* 2022). ROMS simulations provide new insights into bottom dynamics. With an overview of the mean velocities at the bottom of the Corinth Gulf, three main regions can be observed: the Rio-Antirio strait, the deep Corinth Basin and the surroundings of the Zoodochos Island (**Figure 4.10**).

The Rio-Antirio strait is the most energetic area of the Gulf. The high-velocities bottom currents of the strait have already been investigated (Rubi *et al.* 2022) but the modelling offers a new perspective for their origins (**Figure 4.10D**). It seems the origin of these high velocities is the bathymetric constriction that the strait presents. Indeed, the bathymetric constriction between the deep Corinth Gulf and the Rio-Antirio Strait (350 m in 45 km; **Figure 4.2**) forces bottom waters to flow upslope, accelerating as they approach the narrower and shallower sections of the strait. The slope becomes steeper in front of the Mornos Delta where bottom velocities start reaching a maximum of 0.5 m s^{-1}. In the strait sensu-stricto, maximum velocities of 1.3 m s^{-1} are found near the most constricted area. The strongest currents, on average, are the ones that exit the Corinth Gulf through the bottom of the strait to reach the Patras Gulf (**Figure 4.10A**).

From the strait to the center of the Corinth Gulf, the velocities at the bottom decrease as the depth increases. Some higher local velocities can be found near the steep depth increases, mostly along the southern coast of the Gulf. In the center of the Corinth Gulf, the average speed for the bottom current velocity is close to 0.01 m s^{-1}. The maximum velocities in the area can reach up to 0.25 m s^{-1} but it seems that these velocities are located near the slopes of the basin. A near 0 m s^{-1} average velocity indicates that there are variations in the directions of the currents indicating the presence of different directions flow (**Figure 4.10C**). This observed shift in direction was already evidenced by in-situ data from Poulos et al., 1996 (Poulos *et al.* 1996) with a shift every 2 to 3 days. This flow seems to reach at maximum around 0.05 m s^{-1}, which is very slow compared to the strait area velocities. By looking at their directions during the month of May 2023 (**Figure 4.10B**), the bottom currents in the central part of the Corinth Gulf follow a cyclonic circulation with the stronger currents following the southern coast of the Gulf.

The bathymetric rise from the deep Corinth basin to the shallower Alkyonides basin presents an area where bottom currents are stronger than the average ones in other parts of the Gulf (except in the Rio-Antirio Strait; **Figure 4.10**). The currents near the Alkyonides are unidirectional as they are mainly going towards the west. They follow the bathymetric depression through the canyons in the area going towards the deep Corinth Basin, exiting the enclosed bay of the Alkyonides. Due to the presence of the Zoodochos Island and the

relatively steep bathymetric rise, the Alkyonides Gulf appears separated from the main Corinth Gulf body. The presence of the island creates a local dynamic with very low velocities on average (**Figure 4.11**). Also, the bottom waters from the Alkyonides appear to leave this gulf by cascading at the bottom, through the canyons, towards the Corinth Gulf

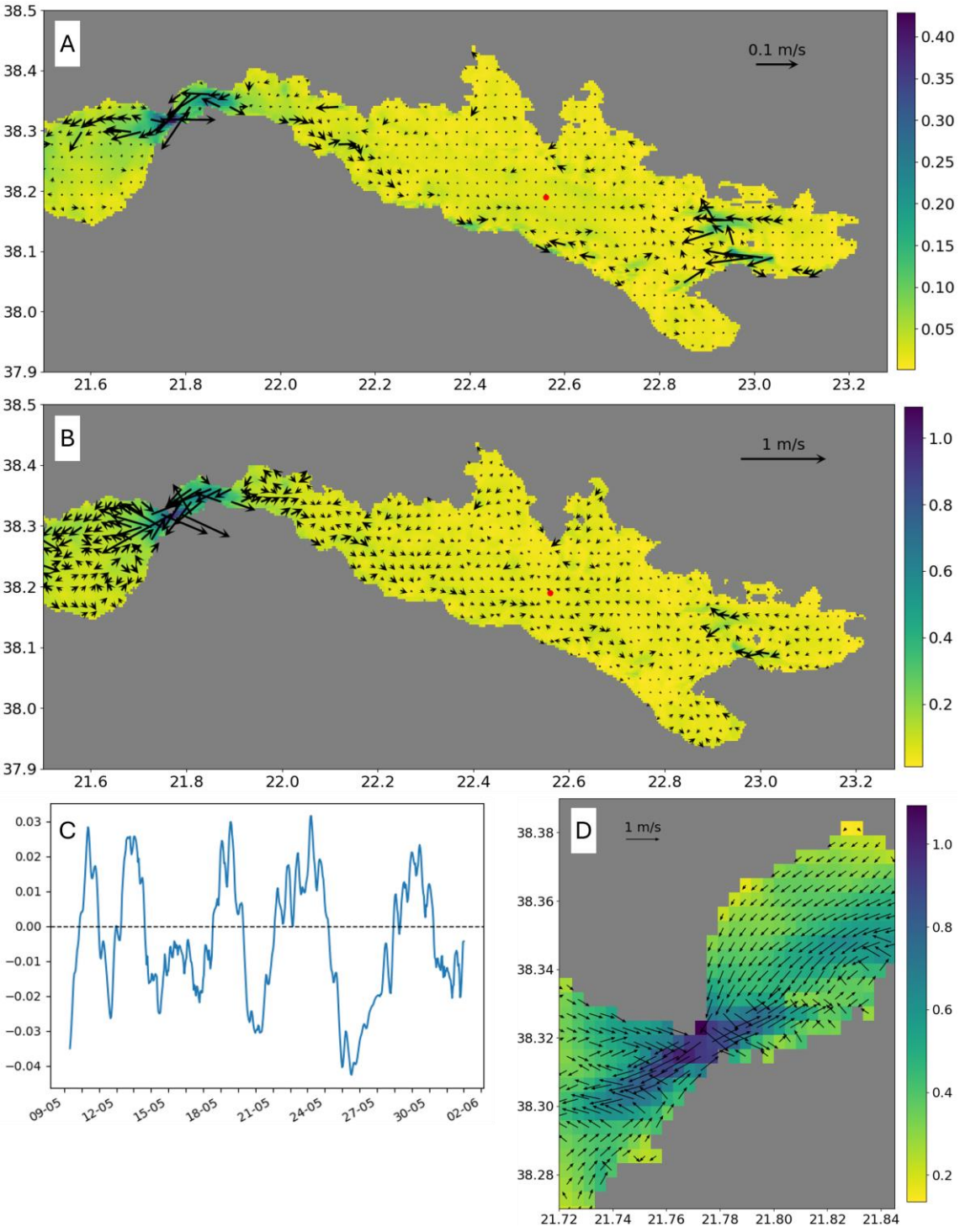

Figure 4.10: Maps of the bottom current magnitudes (colors; in m s^{-1}) and directions (arrows) over the month of May 2023. (A) Mean for May 2023, (B) Maxima for May 2023, (C) U-velocities at the red dot location over the simulated time, (D) Zoom on the maximal velocities at the bottom of the Rio-Antirio Strait.

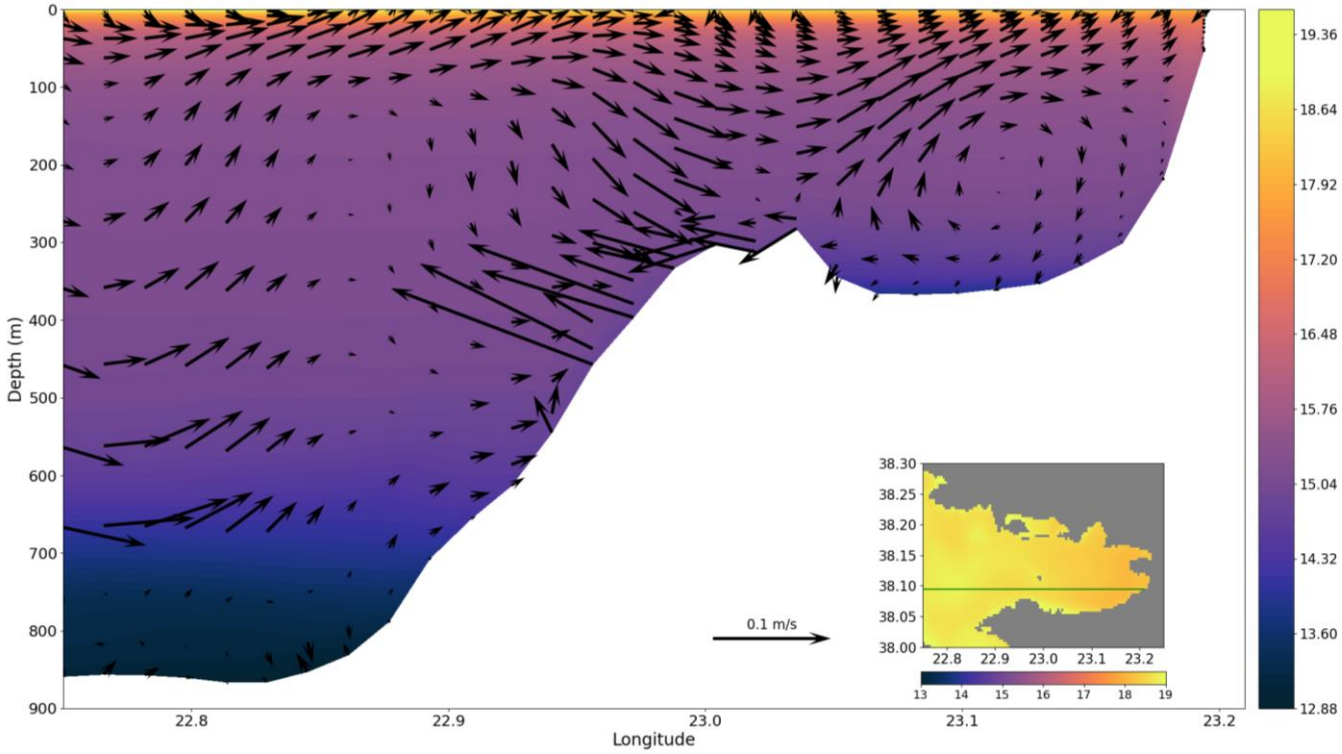

Figure 4.11: Vertical section over the Alkyonides Gulf of the average temperature (colors, °C) and currents (arrows, m s^{-1}) for the month of May 2023.

4.5. Influence of the tide

The influence of the wind previously discussed was mainly observable for the surface dynamics. For a specific simulation we did not use any tidal forcing to determine the importance of the tidal forcing compared to the wind forcing. On one hand, the enhancement or the negation of the wind mainly affected surface dynamics and not that much the bottom (**Figure 4.8**). On the other hand, negating the tides results in differences in the whole water column dynamics, particularly near the Rio-Antirio Strait (**Figure 4.12**). The Patras Gulf appears to be affected by the neglection of the tides but with a smaller range of modifications.

The fact that these areas are more sensitive to the tides might be linked to two factors. First, the tides are forced at the boundaries of the grid which in our case corresponds to the western part of the Patras Gulf. Second, these areas are the shallowest of the domain, particularly the Rio-Antirio Strait. Therefore, the tidal amplitude (even if it stays in the microtidal range; **Figure 4.6**, **Figure 4.7**) appears relatively stronger in those areas rather than in the deep Corinth Gulf. Nevertheless, not accounting the tide in the simulations does not provide velocities strong enough to be compared to what is observed through in-situ data near the Rio-Antirio Strait (**Figure 4.3**; Rubi *et al.* 2022). Due to its bathymetry, the deep Corinth Gulf is less affected by the tides (**Figure 4.12**); the differences between the two simulations being very close to 0. This also indicates that surface phenomenon in the center part of the Corinth Gulf is more wind driven than tide driven. The difference between the simulations resides in the fact that the Corinth Gulf is considered microtidal

(Tsimplis 1994; Horsch & Fourniotis 2017; Rubi *et al*. 2022; Aspioti & Fourniotis 2024; Fourniotis 2024), therefore tides have low impact over the general circulation. The only place where the impact is higher is in the Rio-Antirio strait due to the tidal amplification associated to straits (Keller & Richards 1967; Baines & Garnek 1990; Barnard *et al*. 2006; Lamarche *et al*. 2011; Bouilloux *et al*. 2013; Shanmugam 2013; Longhitano 2018; Longhitano & Chiarella 2020; Aspioti & Fourniotis 2024). There, even if the tidal amplitude is very low (less than 30 cm (Flanders Marine Institute (VLIZ) 2025; Tideschart 2025)) the tidal currents affect the whole water column and particularly the bottom due to the presence of an internal wave (**Figure 4.6**,**Figure 4.7**,**Figure 4.10**,**Figure 4.12**).

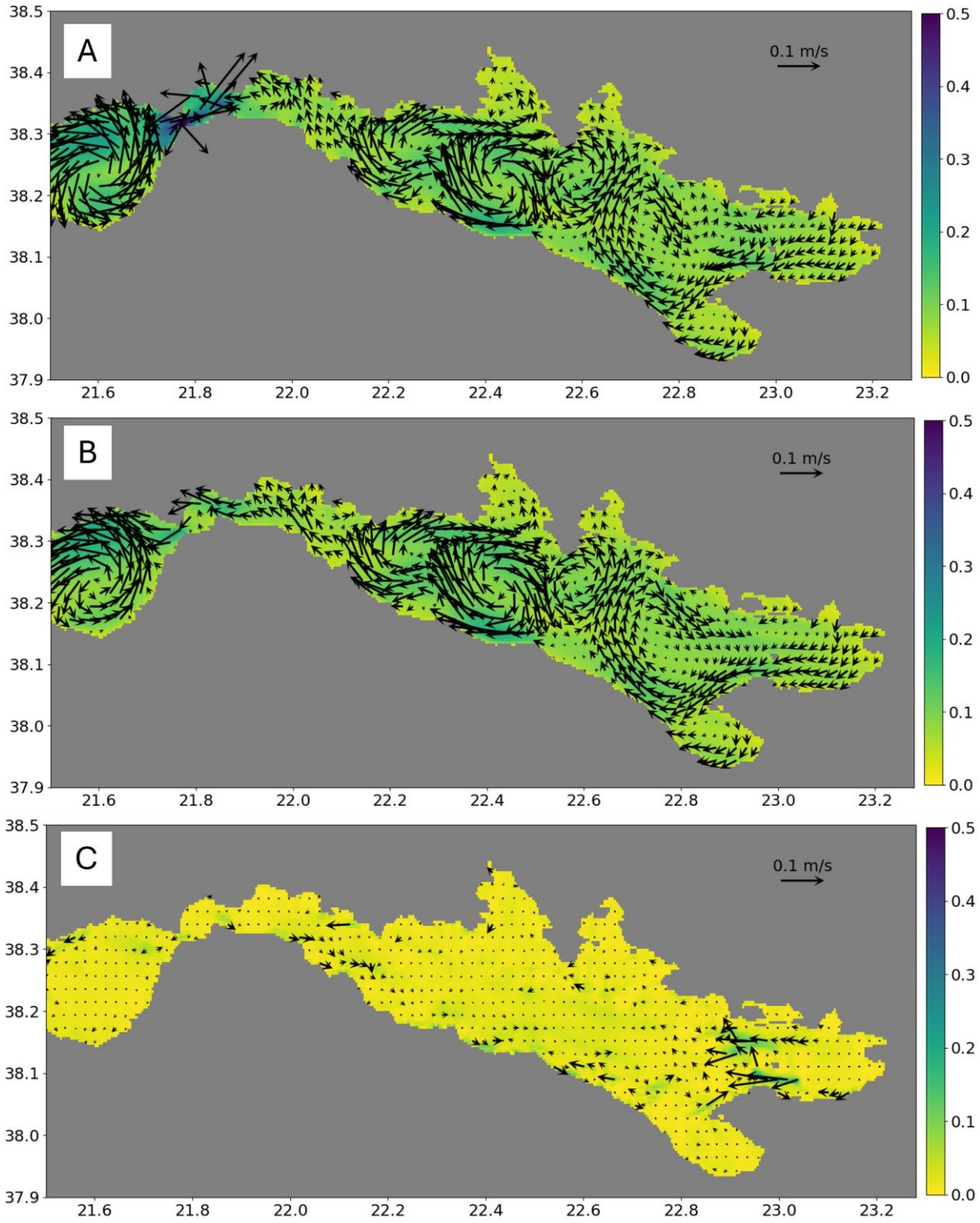

Figure 4.12: Comparison between (A) the direction and intensity (m s^{-1}) of the mean surface currents under the influence of the tidal forcing, (B) the direction and intensity (m s^{-1}) of the mean surface currents without tidal forcing and (C) the direction and intensity (m s^{-1}) of the mean bottom currents without tidal forcing.

5. Discussion

5.1. General circulation patterns

From West to East, the surface circulation is similarly modelled to what was already described (Lascaratos *et al*. 1989; Caterina & Hubert-Ferrari 2025). The Patras gyre is well represented, regardless of the season or the wind influence. New insights are for the Rio-Antirio straight area. The strait area still appears as the coldest of the region (**Figure 4.4**, **Figure 4.8**) and the vertical sections and the analysis of the currents at depth allow to understand the impacts of the circulation over the surface temperature. Near the strait, what was interpreted as upwellings (Lascaratos *et al*. 1989; Caterina & Hubert-Ferrari 2025) now appear more like upsloping. The water coming from the depth of the Corinth Basin is forced to move upwards due to the steep bathymetric rise from the center of the Gulf to the Mornos Delta. More variations of the bathymetry are located near the strait sensu-stricto, causing the colder waters to move faster near the bottom due to the shallowing of the bathymetry (**Figure 4.7**).

Going towards the center of the Gulf, the surface gyres previously described are also present in the numerical simulations. The intensity and location of the gyres change according to the wind intensity (**Figure 4.8**) and the seasons (**Figure 4.5**) but overall, they remain at the same location. Regarding the bottom circulation in the center of the Gulf, few descriptions were previously made by Poulos et al., 1996 (Poulos *et al*. 1996). With our model we were able to better understand the patterns of the bottom circulation. The center of the Corinth Gulf can be described as quiet with maximal velocities not exceeding 0.1 m s^{-1}. Also, it appears that the direction of the currents is shifting every 2 to 3 days (**Figure 4.10C**) like what was observed through in-situ data by Poulos et al. in 1996 (Poulos *et al*. 1996).

In the Alkyonides Gulf, the waters seem to be trapped in an enclosed basin due to the presence of the Zoodochos Island. During the months of May and September 2023 (**Figure 4.5**), an anticyclonic circulation is observable at the surface, allowing the waters to circulate back towards the Corinth Gulf. By observing the average behavior for the currents for the month of May 2023, high velocity flows are found at the bottom of the canyons from the Alkyonides to the Corinth Gulf (**Figure 4.11**). With the modelling no clear evidence of the suspected upwellings (Caterina & Hubert-Ferrari 2025) in the Alkyonides was found. The closest phenomenon to an upwelling can be the internal dynamics of the Alkyonides due to the presence of the Zoodochos Island increasing the local bathymetry, constraining the waters in the small gulf. Despite the presence of currents going upwards (**Figure 4.11**), no significative temperature flows can be observed to qualify this phenomenon as upwelling.

5.2. Main forcings for the hydrodynamic circulation

With our simulations we explored the effect of enhancing the winds as well as negating it and the tides. With the winds, mainly the surface circulation was affected (**Figure 4.8**). The Patras appears quite steady regardless of the wind intensity if this wind is blowing to the West, as it was the case for May 2023. The size, intensity or even direction of the gyres in the Corinth Gulf also depend on the wind.

For the tides, the center of the Corinth Gulf, at least at the bottom, is not affected by their presence or absence since the surface modification of the dynamics does not reach the deepest part of the Gulf. The Patras Gulf, by being shallower, seems to have its bottom dynamics affected by the non-inclusion of the tide forcing. The water still moves following a cyclonic circulation but with lower velocity (**Figure 4.12**).

The critical region under the influence of both winds and tide is the Rio-Antirio strait area and the waters in front of the Mornos Delta. In this area, tidal currents are needed to generate the observed velocities (**Figure 4.3**, **Figure 4.6**, **Figure 4.12**); (Rubi *et al*. 2022)). Without the tides, dynamics in the whole water column are observed to be quieter around the strait. In a "no wind" scenario, tidal dynamics overcomes the movement induced by the winds and dynamics are still present. Tidal dynamics are prevalent over the Rio-Antirio Strait, particularly when it regards the overflow of the strait from the deep Corinth waters. Under ebb tide, bottom waters are going towards the Patras Gulf (**Figure 4.6**), overflowing the strait (**Figure 4.7**). Under flood tide, the deep-water Corinth's flow is not crossing the strait and is then flowing back towards the Corinth Gulf (**Figure 4.6**, **Figure 4.7**). This dynamic related to the tide is observed to be the opposite of what was previously described (Rubi *et al*. 2022) but appears to be very consistent with the observed current direction and SSH (**Figure 4.6**, **Figure 4.7**) Our observations of the changes in the current direction at this location suggest a different origin from what was already observed by Aspioti and Fourniotis (2025) (Aspioti & Fourniotis 2025). In their study, the direction towards the Patras Gulf occurs under the influence of a 4 m s^{-1} NE wind and the flood tide, while the flow going to the Corinth Gulf was observed under ebb tide and 4 m s^{-1} SW wind conditions (Aspioti & Fourniotis 2025). In our study we associate these movements more likely to the tides rather than the winds, classifying the strait as a tidal strait in a microtidal context (Longhitano & Chiarella 2020; Rubi *et al*. 2022; Aspioti & Fourniotis 2024). Indeed, when the tides are negated, no evidence of strong movement are observed (**Figure 4.12**) and movement towards the Patras Gulf appear during ebb tide (**Figure 4.6**). The role of the tide or the winds could be investigated further to understand in which proportion they affect the current direction near the Rio-Antirio Strait.

6. Conclusions

Our study presented a description of a numerical point of view over the hydrodynamics circulation of the Patras and Corinth Gulfs. The combined forcing of the winds and the tide over the model proved that they both are needed to study the oceanographic dynamic. Both Patras and Corinth Gulfs are sensitive to the winds but are even more dependent on the tide, particularly for the bottom dynamics. Over all the seasons observed (January 2023, May 2023 and September 2023), the dynamics appear to be steady in time with the presence of surface gyres in the Patras and Corinth Gulfs.

The most sensitive location of the area in terms of dynamics is the Rio-Antirio strait where the most energetic sea area is observed. Very high bottom velocities, up to 1.3 m s^{-1} can be found and related to the tidal influence in a relatively shallow area. The tidal induced movement over the bottom water is controlling the exchanges between the two gulfs, allowing the overflow, or not, of the deep Corinth waters over the Rio-Antirio strait to the Patras Gulf. While in shallow waters the dynamics are strong, in the deep center of the Corinth Gulf, bottom velocities appear to be close to 0 m s^{-1}, making the central part of this basin very quiet.

Chapter 5: Influence of Present-Day Bottom Currents over the Sedimentation in the Corinth Gulf (Greece)

After modelling the entirety of the Corinth Gulf's hydrodynamics and evidencing the key patterns, the impacts over the sedimentary structures from the Rio-Antirio Strait to the Alkyonides Gulf needed to be investigated. This investigation involved a more geological approach, and this chapter will potentially be published after the thesis.

1. Introduction

In semi-enclosed basins, sedimentary architectures are generally interpreted within a source-to-sink framework (Allen 2017) in which the main controlling parameters are the accommodation space and the sediment supply (Schlager 1993). This approach typically assumes that sediment transfer within the basin is dominated by gravity-driven processes such as turbidity currents or mass wasting, with little consideration for the potential influence of bottom currents (Mutti & Normark 1987; Hernández-Molina *et al.* 2008; Rebesco *et al.* 2014; Stow & Smillie 2020). In deep-marine basins, however, it has long been recognized that persistent bottom currents can exert a major control on sediment transport and deposition, producing distinctive morphological and sedimentary features collectively known as contourites (Faugères & Stow 2008; Hernández-Molina *et al.* 2008; Rebesco *et al.* 2014). Consequently, contourite deposits have traditionally been associated with deep-water environments influenced by oceanic circulation. Yet, similar processes may also occur in shallower or semi-enclosed settings (Rebesco *et al.* 2014). Even in relatively confined basins, bottom currents can induce substantial sediment remobilization and redistribution, generating both erosional and depositional features analogous to those found in open-ocean contourite systems. Such systems often develop where intensified bottom currents are forced through narrow topographic constrictions, such as gateways or straits (Martorelli *et al.* 2010; Miramontes *et al.* 2019).

The Corinth Gulf represents an ideal natural laboratory to investigate these processes. This deep (~900 m), semi-enclosed syn-rift basin connects to the Mediterranean Sea through a narrow passage at its western end. The entrance area is affected by high-velocity bottom flows reaching 0.5–1 m s^{-1}, whereas much weaker currents prevail in the deeper and more enclosed parts of the basin (Poulos *et al.* 1996; Caterina & Hubert-Ferrari 2025; Caterina *et al.* 2025). Along the margins of the strait zone, contourite-like accumulations have been described (A. Beckers *et al.* 2016), while widespread erosion dominates the inner part of the strait sensu lato (Rubi *et al.* 2022).

Previous studies have therefore identified the sedimentary geomorphology controlled by bottom currents—namely, erosional features and contouritic or plastered drifts (A.

Beckers *et al.* 2016; Rubi *et al.* 2022)—as well as direct measurements of bottom-current velocities (Rubi *et al.* 2022). However, a comprehensive understanding of the spatial organization and variability of the near-bottom hydrodynamics was still lacking. Building on the hydrodynamic modelling developed in Chapter 4, we can now examine in greater detail how the present-day bottom-current pattern correlates with the sedimentary architecture of the Corinth Gulf. This approach is first applied to the strait domain, including the wider Nafpaktos Bay connecting the Gulfs of Patras and Corinth, and then extended to the entire Gulf. In doing so, we aim to evaluate how bottom-current activity contributes to the shaping and redistribution of sediments within this semi-enclosed rift basin—an aspect that has so far received little attention compared to gravity-driven remobilization processes such as turbidity currents.

2. Settings

Separating continental Greece and the Peloponnesus, the Corinth Gulf is considered as a deep basin (**Figure 5.1**). Its connection to the Mediterranean Sea occurs through the Patras Gulf and the Ionian Sea. Between the Patras and Corinth Gulfs lies the Rio-Antirio Strait, which represents the shallowest part of the Corinth Gulf, with its main sill located at about 68 m depth (Rubi *et al.* 2022). This shallow area is the most sensitive to oceanic variations, especially tidal currents (Rubi *et al.* 2022; Fourniotis 2024; Caterina & Hubert-Ferrari 2025) even through it lies within a microtidal context (Tsimplis 1994). It remains the coldest area throughout the year due to its particular bottom dynamics and the shallow bathymetry (Caterina & Hubert-Ferrari 2025). As a result of the mixing between bottom waters and surface waters, temperatures in the strait range between 15 °C at the bottom and 18°C at the surface for the month of May 2023 (satellite and modelled data; (Caterina & Hubert-Ferrari 2025; Caterina *et al.* 2025)).

The rift of Corinth is the most active European rift with present-day extension rate of 1.5 cm yr^{-1} (Briole *et al.* 2000). The Corinth rift evolution is rather well constrained (Ori 1989; Taylor *et al.* 2011; Ford *et al.* 2013; Nixon *et al.* 2016; Rohais & Moretti 2017; Gawthorpe *et al.* 2018; Shillington *et al.* 2019) and could be divided in three phases (Rohais *et al.* 2007): (1) an initiation phase dominated by small-extension continental and lacustrine sedimentation called “the Lower Group”; (2) an increase of the fault activity associated with a connection of the basins leading to a deep-water lacustrine to marine sedimentation referred to as “the Middle Group”; (3) the exhumation of the syn-rift deposits on the southern shore by the uplift of the Peloponnesus and the northward shift of the deltaic systems since 1 Ma.

The sedimentary basin of the Gulf results from its tectonic subsidence. This basin is affected by numerous active faults, located on the southern coastline, offshore and along the northern coast (Stefatos *et al.* 2002; Bell *et al.* 2008, 2009; Taylor *et al.* 2011; A. Beckers *et al.* 2015, 2016). The fault network controls the overall morphology of the Gulf and to a certain scale the one of its western tip (A. Beckers *et al.* 2016).

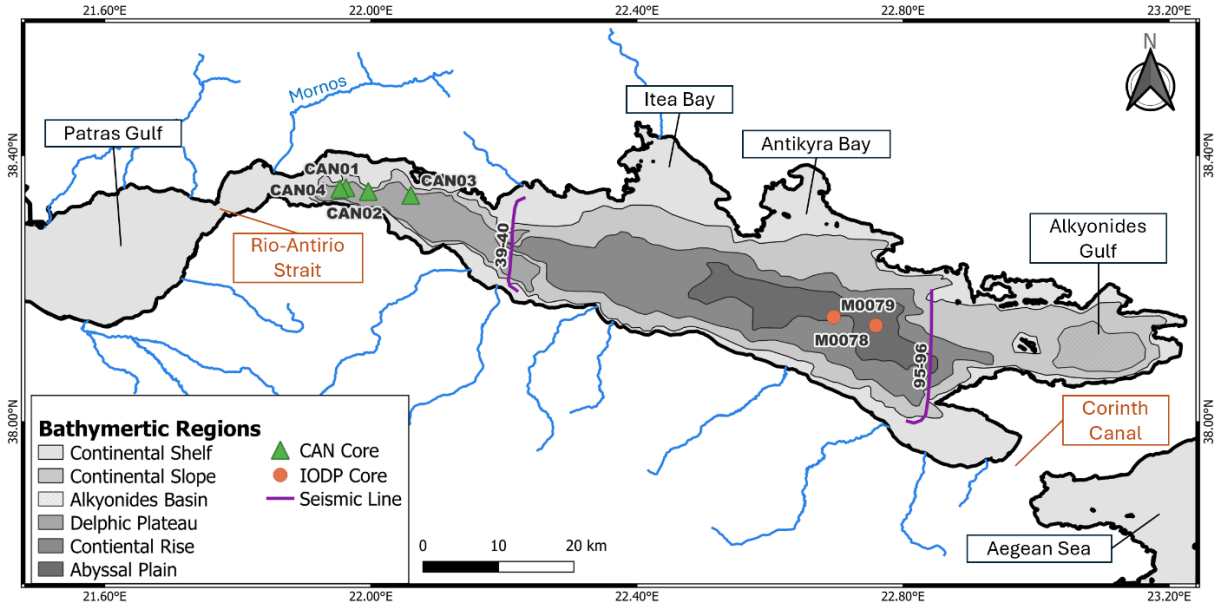

Figure 5.1: Bathymetric Map of the Gulf of Corinth with geological data used in the present study to discuss the importance of bottom current in shaping sediment deposition (seismic line's location and the key core locations).

3. Methodology

Several techniques were used to assess the interactions between the bottom currents and the associated sedimentology.

3.1. ROMS Model

For the modelling of the dynamics and the bottom currents, the Regional Oceanographic Modelling System (ROMS) was used (Moore *et al.* 2011). The resolution for the modelling was fixed by GEBCO Bathymetry at 450 m (GEBCO 2024). Initial conditions applied on the grid were extracted from CMEMS (Buongiorno Nardelli *et al.* 2013) for the oceanographic constituents, from ECMWF (ECMWF 2018) for the winds and from TPXO (Egbert *et al.* 1994; Egbert & Erofeeva 2002) for the tides. The month of May 2023 was selected since collected in-situ data were collected to validate the model outputs (Caterina *et al.* 2025; Oceanus-Lab 2025). The key parameters used to analyze the impact of the bottom currents over the sediments were the horizontal velocities (u and v) and the bottom shear-stress. More details over the specificity of the ROMS build can be found in Caterina et al. (2025).

3.2. Bathymetry

Multibeam echosounder (MBES) data were recovered during a survey conducted in May 2019 by the Laboratory of Marine Geology and Physical Oceanography of the University of Patras. The methodology and results of this campaign are more detailed in Fakiris et al. (2019) and Rubi et al. (2022). The MBES covered an area of 211 km^2 producing a bathymetric map with a lateral resolution of 5m x 5m. These data were collected using

Hypack 2016 and positioned with a Real Time Kinematics GPS (10 cm accuracy). The survey was carried out with a dual-head MBES Elac Nautic Seabeam 1185, transmitting at 180 kHz (Rubi *et al*. 2022).

3.3. Seismic Lines

The seismic lines in the central Corinth Basin used in this study were provided by the Hellenic Center for Marine Research (HCMR). They were acquired by the M. V. Vasilios in 1995 with a single-channel sparker with a 0.85s TWTT (Rubi 2018). The position of the lines is displayed on **Figure 5.1**.

High-resolution single-channel seismic reflection profiles were acquired in 2011 and 2012 using a Sparker and a 3.5 kHz subbottom profiler by the Renard Centre of Marine Geology (Ghent University) (A. Beckers *et al*. 2016). This seismic dataset also served to construct the isopach map of Holocene deposits shown in **Figure 5.9** (A. Beckers *et al*. 2016). A detailed bathymetric map of the study area was also used to define core locations and interpret sedimentary structures.

3.4. Core data

3.4.1. Materials

Four sediment cores (1.2–2.2 m long) were collected in 2014 using a BENTOS® gravity corer (Figure 1, Table 0.1). The cores are aligned along an approximately E–W transect extending eastward from the Rio–Antirio Strait into the deepest part of the western basin, within the depocenter. Frequent turbidity currents have been reported in this area from previous studies (Heezen *et al*. 1966; Piper *et al*. 1980; A. Beckers *et al*. 2017). These turbidity currents originate from several potential sources: the Mornos delta to the west, the Trizonia Fault scarp to the north, and the Erineos delta to the south. Furthermore, Beckers et al. (2016) described the Influence of bottom currents on the sedimentary processes at the western tip of the Gulf of Corinth. The aim here is to assess the extent to which bottom currents may rework turbiditic deposits away from the strait, forming potentially a mixed contouritic–turbiditic system similar to those described in the literature (Stow & Smillie 2020; Rodrigues *et al*. 2022).

Table 5.1: Positions of the CAN Cores with their length and seabed depth

Name	Lat. (°N)	Lon. (°E)	Water Depth (m)	Length
CAN01	38.3517	21.9627	292	202
CAN02	38.346	21.9962	310	181
CAN03	38.3402	22.0601	360	120
CAN04	38.3499	21.9535	283	209

3.4.2. Sedimentological and analytical methods

Sedimentological analyses were performed on each core to identify and characterize contouritic and event-related deposits. X-radiography was first conducted on one split

half of each core to reveal sedimentary structures, followed by high-resolution computed tomography (CT) scanning for detailed internal imaging. CT scans were acquired using a Siemens SOMATOM Definition Flash CT scanner (Siemens AG, Munich, Germany) at the Ghent University Hospital. The scanner was operated at 120 kV, 200 mAs, and a pitch of 0.45. Reconstructed voxel size was approximately 0.15 mm (X–Y) and 0.6 mm (Z). The resulting 3D images were visualized with VGStudio 2.2 and processed in ImageJ to extract Hounsfield Units (HU), a calibrated measure of X-ray attenuation related to material composition and density (Cnudde *et al.* 2006). Physical properties were measured every 0.5 cm using a GEOTEK Multi-Sensor Core Logger (MSCL) at RCMG (Ghent University). We focused on wet bulk density and magnetic susceptibility (MS) obtained with a Bartington MS2E point sensor (Bartington Instruments, Witney, UK). X-ray fluorescence (XRF) core scanning was conducted on CAN1, CAN2, and CAN3 using an Avaatech® XRF core scanner at the EDYTEM Laboratory (Université Savoie Mont Blanc, France). Measurements were performed at 10 kV (10 s) and 30 kV (45 s). Down-core resolution was 2 mm for the upper 100 cm and 5 mm below 100 cm, except for CAN3, which was fully scanned at 2 mm resolution.

Detailed core logging and facies descriptions were based primarily on CT-scan imagery, complemented by MSCL and XRF data (**Table 5.2**). Facies classification followed the contouritic framework of Rebesco et al. (2014). Event deposits were interpreted considering previously identified earthquake-triggered turbidites in the 65 cm-long PSP05 short core studied by Beckers et al. (2017), located very close to CAN2. Beckers et al. (2017) also described instantaneous sediment emplacement at this site related to slope failures on the southern Erineos delta.

3.4.3. Chronology

Age constraints were derived from short-lived radionuclides (^{210}Pb and ^{137}Cs) and AMS radiocarbon dating. Unsupported $^{210}Pb_{xs}$ and ^{137}Cs activities were measured in all cores (**Table 5.3**) using gamma spectrometry. Analyses were carried out at the LSCE's Modane Underground Laboratory (France) for CAN3 and at the University of Bordeaux for the other cores, using low-background, high-efficiency, well-shaped CANBERRA detectors. Supported ^{210}Pb was assumed to be in equilibrium with in-situ ^{226}Ra, and excess $^{210}Pb_{xs}$ was obtained by subtraction. Sedimentation rates were calculated using the Constant Rate of Supply (CRS) model (Appleby & Oldfield 1978, 1983; Binford *et al.* 1993).

In addition, AMS radiocarbon dating was performed on terrestrial or mixed organic matter from coarse-grained event layers (due to insufficient foraminifera or organic material in hemipelagic intervals) at the ARTEMIS facilities (France) and the KIK-IRPA laboratories (Royal Institute for Cultural Heritage, Belgium) (**Table 5.4**).

Table 5.2: Facies documented in CAN Sediment Cores forming the following facies associations : Mud (M= Mb, Mm), Mass-Transport Deposits (MTD= Md, S), Contourites (C= C1, C2, C3), and Turbidites (T= T(l), Tsd, Td).

Facies	Description	Interpretation
Mb = Mud bioturbated	Very fine sediment. Not finely laminated, but horizontal centimetric layers (cf. color changes on photo scan). With bioturbation. Non-erosive.	Deposits by bioturbated settling, no currents.
Mm = Mud massive	On CT-scan: uniform grey. Very fine and massive sediment. Grain size analysis suggests silt due to clay flocculation.	Fine grained deposit possibly in association with MTD (Mass-Transport Deposit) like in CAN1 at 0.6-0.8 m.
Md = Mud deformed	Fine sediment in between Mm and C1. Massive aspect but with some deformed structures.	Not hemipelagic sedimentation. Massive input of fine sediment from muddy MTD with sediment source on slopes
S = Slump	A single slump in CAN01 with some parts highly deformed and others retaining the initial structure.	Slump deposit.
C1= Type 1 Contourite, i.e. Ml= Mud laminated	3 types of laminated mud structured with: (A) discontinuous millimetric laminations; (B) continuous millimetric laminations (wavy, flat, or inclined); (C) small mm-scale lenses. Finely laminated background.	Laminated contourite sequence according to Rebesco et al. (2014).
C2 = Type 2 Contourite, i.e. Motsilt =Mottled silt	Mottled silt with irregular layers and silt lenses.	Mottled silt contourite sequence according to Rebesco et al. (2014).
C3 = Type 3 Contourite or i.e. Motsand = Mottled sand	Mottled sand: (A) massive, homogeneous bed with wavy top; (B) heterogeneous sand lenses with OM; (C) sometimes OM at the top giving an apparent fining-upward trend; (D) centimetric sand lenses.	Mottled sand contourite sequence according to Rebesco et al. (2014).
T(l) = Turbidite sometimes laminated	Erosive base. Horizontal. Normally graded. Sometimes internal laminations.	Turbidite: Td and Te terms of the Bouma sequence.
Tsd = Turbidite with soft deformation	Erosive base. Continuous, horizontal layer. Soft deformation (injection). No internal laminations.	Turbidite (primary depositional process) + soft deformation (diagenetic process).
Td= Turbidite deformed	Deformed graded layer. In some areas, erosive base preserved with internal laminations.	Deformed turbidite: erosive base and Td laminations no longer systematically preserved.

Table 5.3: Measurements for radionuclide dating using excess ^{210}Pb and ^{137}Cs . Isotopes are measured in mBq/g.

CAN01 - Prof. (cm)	^{210}Pb	^{226}Ra	^{228}Th	^{137}Cs	K %
0,5	64 ± 4	22 ± 1	30 ± 1	6,4 ± 0,4	10,2%
1,5	59 ± 6	22 ± 1	28 ± 1	7,1 ± 0,7	10,0%
2,5	50 ± 4	22 ± 1	31 ± 1	7,3 ± 0,5	10,6%
4,5	44 ± 3	23 ± 1	29 ± 1	7,4 ± 0,4	10,7%
6,5	32 ± 3	21 ± 1	31 ± 1	9,0 ± 0,4	10,7%
8,50	21 ± 3	26 ± 1	33 ± 1	1,5 ± 0,3	10,9%

CAN02- Prof. (cm)	^{210}Pb	^{226}Ra	^{228}Th	^{137}Cs	K%
0,5	91 ± 7	28 ± 1	33 ± 1	7,5 ± 0,7	9,7%
2,5	79 ± 5	25 ± 1	29 ± 1	8,9 ± 0,6	9,9%
4,5	44 ± 4	24 ± 1	31 ± 1	9,2 ± 0,6	11,3%
5,5	42 ± 3	24 ± 1	29 ± 1	9,1 ± 0,5	10,6%
6,5	32 ± 3	22 ± 1	29 ± 1	9,2 ± 0,5	10,5%
8,5	29 ± 2	21 ± 0	28 ± 1	6,6 ± 0,3	9,2%
10,5	33 ± 3	23 ± 1	29 ± 1	2,3 ± 0,3	10,2%
12,5	23 ± 3	22 ± 1	28 ± 1	0,3 ± 0,2	9,0%

CAN03- Prof. (cm)	^{210}Pb	^{226}Ra	^{228}Th	^{137}Cs	K %
0,5	176,9 ± 7,2	27 ± 0,9	36 ± 0,9	10,3 ± 0,6	1,95%
1,5	123,7 ± 6,2	27 ± 0,9	33 ± 0,9	13,7 ± 0,7	2,04%
2,5	114,2 ± 3,5	28 ± 0,5	32 ± 0,5	14,0 ± 0,4	2,01%
3,5	108,8 ± 6,2	25 ± 0,8	33 ± 0,9	13,9 ± 0,7	1,97%
3,5	90,7 ± 5,9	25 ± 0,8	33 ± 0,9	12,1 ± 0,6	2,03%
4,5	92,5 ± 3,4	28 ± 0,5	35 ± 0,5	12,3 ± 0,4	1,99%
5,5	73,4 ± 5,1	24 ± 0,8	30 ± 0,8	9,3 ± 0,6	1,68%
6,5	37,9 ± 3,5	16 ± 0,6	19 ± 0,6	3,0 ± 0,3	1,05%
7,5	12,8 ± 2,9	12 ± 0,5	14 ± 0,5	1 ± 0,2	0,90%
9,5	35,5 ± 4,8	30 ± 0,9	40 ± 1		2,13%
10,5	32,2 ± 4,1	28 ± 0,8	33 ± 0,8		1,83%
11,5	30,6 ± 2,4	27 ± 0,5	34 ± 0,5		1,86%
12,5	29,8 ± 2,7	30 ± 0,5	37 ± 0,5		2,09%
14,5	38,3 ± 4,9	28 ± 0,9	35 ± 0,9		2,04%

CAN04- Prof. (cm)	^{210}Pb	^{226}Ra	^{228}Th	^{137}Cs	K %
0,5	79,31 ± 4,4	29 ± 0,7	36 ± 0,8	5,7 ± 0,4	10,26%
2,5	78,88 ± 5,2	21 ± 0,8	27 ± 0,9	8,5 ± 0,6	9,90%
3,5	66,48 ± 6,5	22 ± 1	30 ± 1,2	7,6 ± 0,7	10,31%
4,5	52,61 ± 5,1	20 ± 0,8	30 ± 1	7,6 ± 0,6	9,17%
6,5	44,62 ± 2	21 ± 0,3	29 ± 0,4	8,7 ± 0,3	10,15%
7,5	38,60 ± 2,8	20 ± 0,5	30 ± 0,6	7,7 ± 0,3	0,00%
8,5	38,07 ± 2,8	23 ± 0,5	33 ± 0,6	7,9 ± 0,4	10,50%
10,5	24,60 ± 2,4	20 ± 0,4	30 ± 0,5	7,2 ± 0,3	10,31%
14,5	23,50 ± 2	21 ± 0	32 ± 0	7,7 ± 0,3	10,60%

Table 5.4: Radiocarbon dating from the CAN Cores

Core	Orig. depth (cm)	Corr. Depth (cm)	^{14}C age (yr BP)	2s error (yr)
CAN01	98,5	74,5	270	30
CAN01	121	95	2778	34
CAN01	164,5	128	425	28
CAN01	171,5	130	395	30
CAN02	84,5	73,5	310	30
CAN02	122	102	782	28
CAN03	38		1361	24
CAN03	55		392	23
CAN03	55		399	22
CAN03	89,5	71	953	28
CAN04	181,5	145,5	390	30

3.4.4. Core Correlation

The first criterion for core correlation was the chronological alignment of dated layers (**Figure 5.2**). In a second step, facies similarity and geophysical property patterns were used to refine correlations, assuming that deposits with comparable composition and provenance were synchronous. Finally, considering that most coarse-grained event layers correspond to sediment remobilization nearshore and downslope transport triggered by earthquake shaking (A. Beckers *et al.* 2017), these deposits are expected to have a broad lateral extent and to be recorded in multiple cores. Correlations were thus established by integrating the new analytical results with previously published stratigraphic constraints

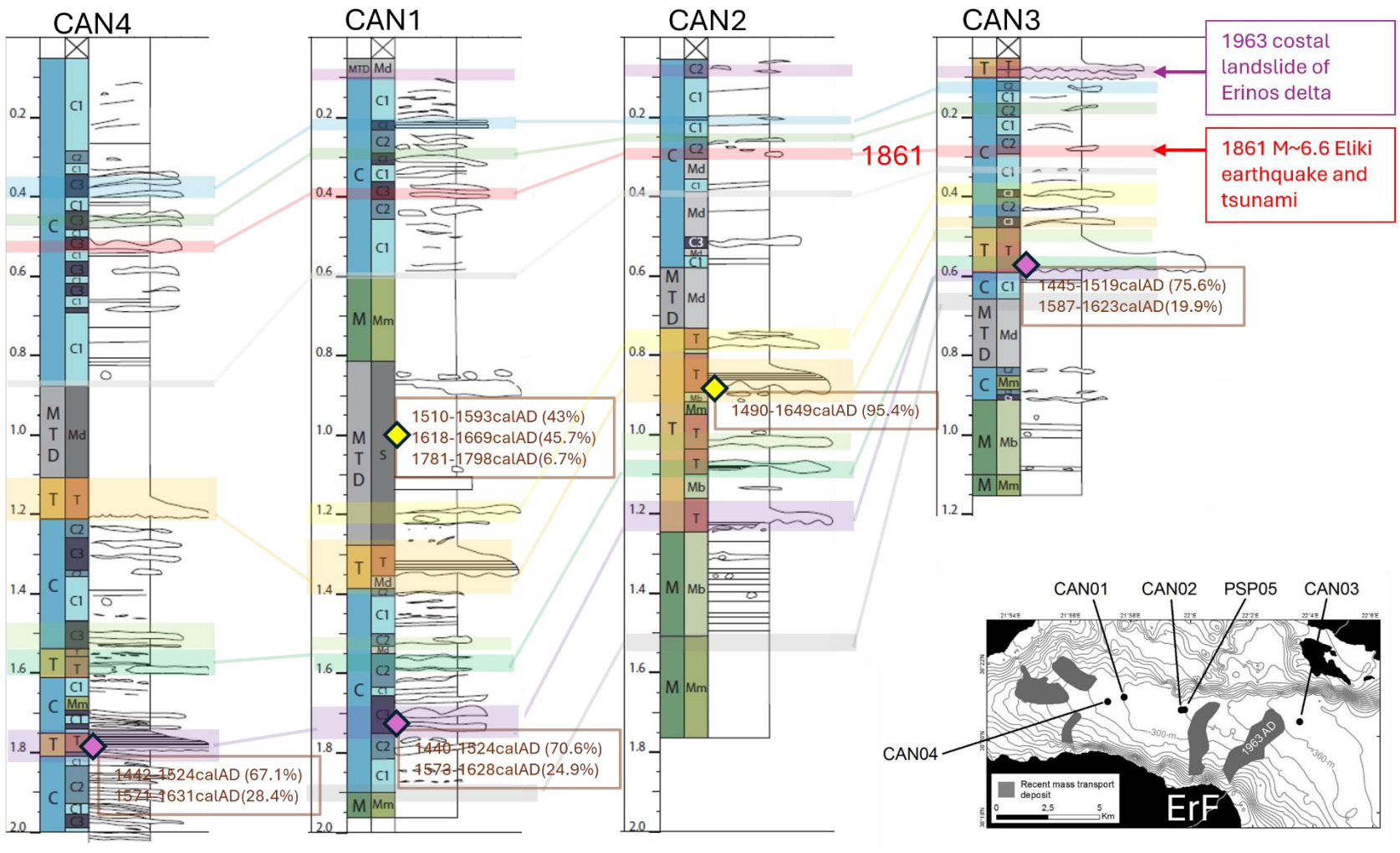

Figure 5.2: Display of the CAN Cores with log, facies and facies associations. Core correlations are evidenced in pale colors while date correlations are represented by the purple diamonds. Other consistent radiocarbon ages are indicated with yellow diamond. The radiocarbon ages are calibrated using Oxcal. In small insect on the bottom right, core locations, with bathymetry and recent MTD in gray. ErF = Erineos Fan.

4. Results: Bottom currents, Shear stress and Geomorphology

The direct interaction between bottom currents and sediments is expressed through bottom shear stress. This parameter is one of the key variables used in this study to link the hydrodynamic modelling results with the observed sedimentary architecture. In the following, we examine both the amplitude and direction of the simulated bottom shear stress, as these control the potential for sediment remobilization and the spatial variability of erosion and deposition across the Gulf.

4.1. Rio-Antirio Strait

In this section, we examine the pattern of bottom currents and the associated sedimentary architecture on both sides of the Rio–Antirio Strait, distinguishing between the eastern (Nafpaktos Bay and Drepano area) and western (Patras side) domains.

4.1.1. East of Rio-Antorio Strait: Nafpaktos Bay and Drepano Spit

The hydrodynamic modelling highlights several key features in the eastern domain of the Rio–Antirio area, (1) on its eastern side, near Drepano, (2) toward its western side, near the Rio–Antirio Strait sensu stricto, where the flow pattern is strongly influenced by tidal exchanges through the sill, and (3) on differences between the southern and northern coasts of Nafpaktos Bay

Regarding the first point, near the Drepano, a localized zone of strong bottom currents and high shear stress is observed (**Figure 5.3**). In front of the Drepano spit, the model calculated an average stress of 0.15 N m^{-2}, and a maximum of 1.5 N m^{-2}. This intensity of shear stress is enough to remobilize sediments up to sand grain size (Dey 1999; Peterson 1999). In addition, in front of the Drepano spit, due to the peculiar bathymetry, a small cyclonic gyre is observed through modelling (**Figure 5.3**). On average, the currents near the southern coast flow northeastward (**Figure 5.4**), whereas those in more open waters flow southwestward, with an average velocity of about 0.2 m s^{-1}. This change in the current direction forces the waters to rotate and enhances local stress through directional shifts. The gyre margins, where flow divergence and convergence occur, are areas of high stress,

Second, at the other extremity of this gyre, near the Rio-Antirio Strait sensu stricto, the shear stress is also high (0.15 N m^{-2} on average and 2 N m^{-2} at maximum), but the flow pattern is strongly influenced by tidal exchanges through the sill. At this location, the relatively steep bathymetric rise and the tidal oscillations create two possible scenarios. The first occurs during the ebb tide, when deep Corinth waters flow upslope the slope and cross the Rio-Antirio Strait toward the Patras Gulf. The second occurs during flood tide, when bottom currents are reflected back toward to the Corinth Gulf (Rubi *et al*. 2022; Caterina *et al*. 2025). This alternating flow depending on tidal phase generate bottom turbulence, which plays an important role in the local erosion.

Third, in Nafpaktos Bay, a strong south-to-north gradient of shear stress is observed with a marked asymmetry existing between the southern and northern coasts in terms of current intensity and thus potential sediment remobilization. Near the southern coast, in front of the Drepano spit, the area is exposed to the intermediate values of shear stress, with averages of 0.15 N m^{-2}. Near the northern coast, the stress values are lower averaging 0.05 N m^{-2} (**Figure 5.3**). In the central part of the bay, shear stress is much higher with average values ranging from 0.10 N m^{-2} to 0.15 N m^{-2} on average.

The effect of the modelled bottom currents is directly reflected in the seabed morphology. First, close to the Drepano spit, a gutter has been described by Rubi *et al*. (2022), corresponding to the area where the current direction shifts and where maximal shear stress occurs. Second, the gyre motion and its relatively high velocity create an important shear stress which creates a giant pool of erosion in the deep part of Nafpaktos Bay (**Figure 5.5**) (Rubi *et al*. 2022), where coarser gravelly sediments are found (A. Beckers *et al*. 2016). Third, the pool and crest morphologies observed in the western part of Nafpaktos Bay, closer to the strait sensu stricto (Rubi *et al*. 2022) would correspond to erosional depressions formed by tidal turbulences generated by the gyre and by the backflow of the Corinth waters. Finally, the south-to-north shear stress gradient can explain the presence of the sedimentological and depositional gradient. The contouritic deposits are developed along the north coast (plastered drift in Rubi et al (2022)), restricted on the southern coast (plastered slope in Rubi et al. (2022) and erosion occurs in-between (**Figure 5.6**) (A. Beckers *et al*. 2016).

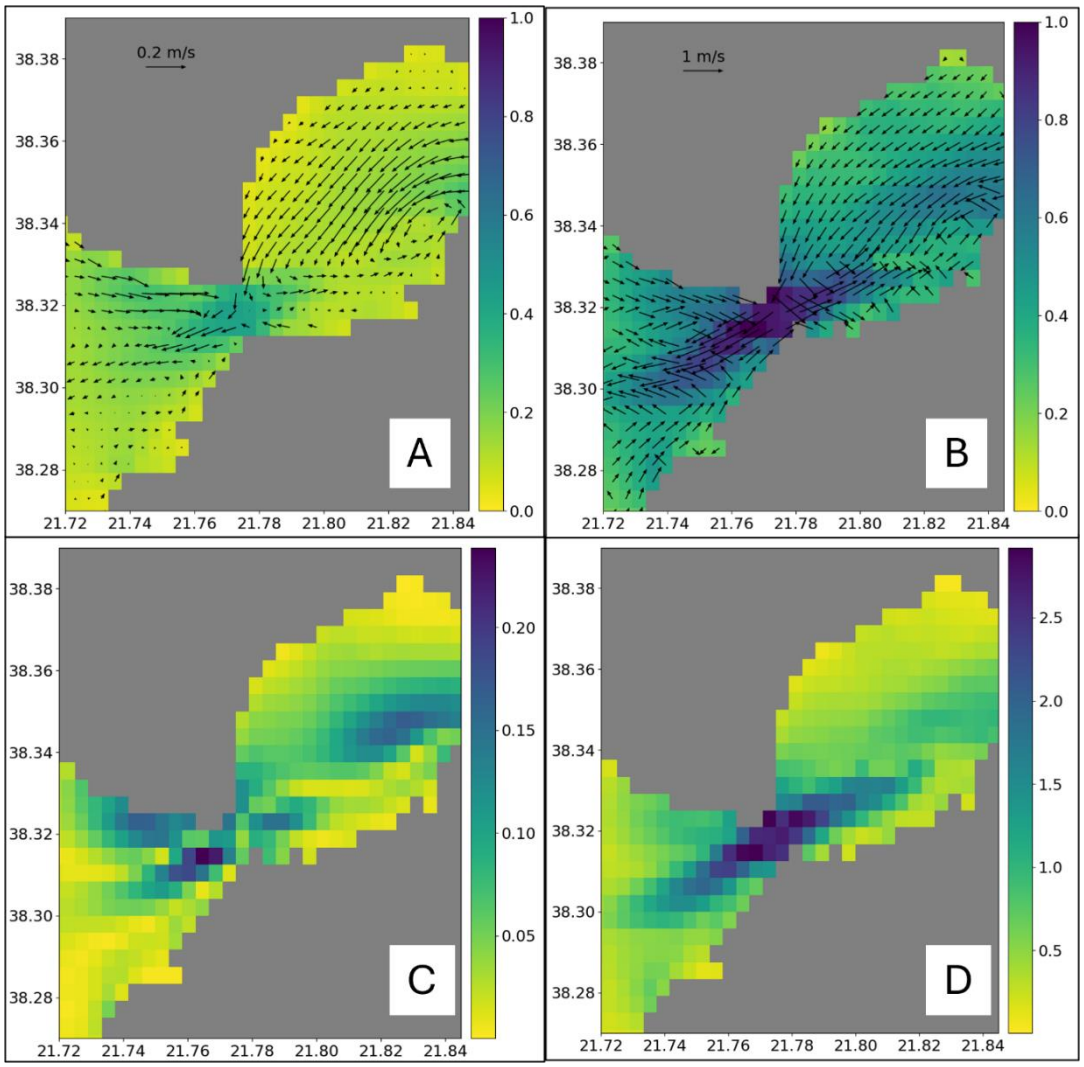

Figure 5.3: ROMS outputs for May 2023 focused on the bottom of the strait. (A) Mean velocities (m s^{-1}). (B) Maximal velocities (m s^{-1}). (C) Mean shear stress (N m^{-2}). (D) Maximal shear-stress (N m^{-2}).

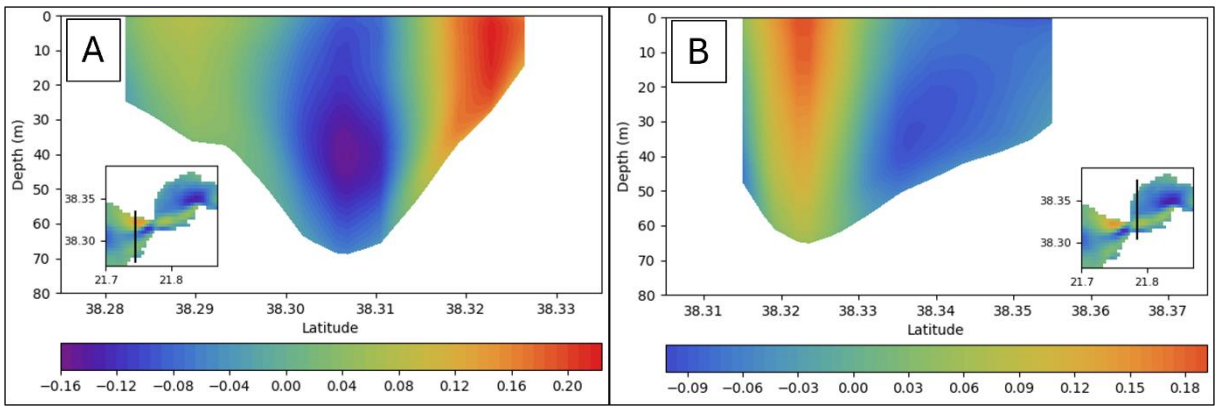

Figure 5.4: Sections of the modelled average eastward currents (m s^{-1}). (A) Section in the west basin of the strait. (B) Section in the east basin of the strait.

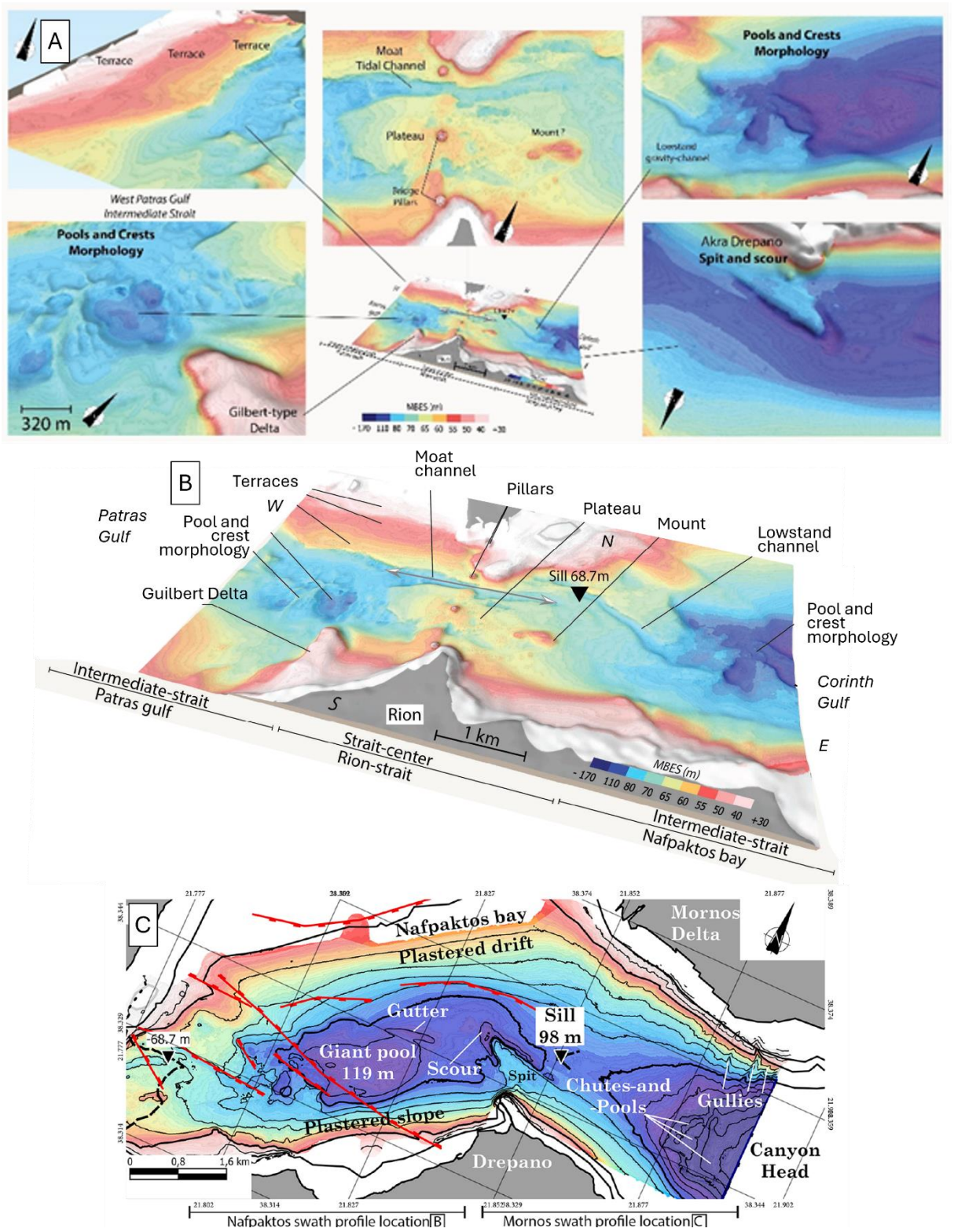

Figure 5.5: Panels presenting the erosion features near the Rio-Antirio Strait observed through high resolution MBES data, modified from Rubi et al., 2022. (A) Close up on individual features. (B) Zoom on the strait with relief perspective. (C) Zoom on the bathymetric map of the extended Nafpaktos Bay

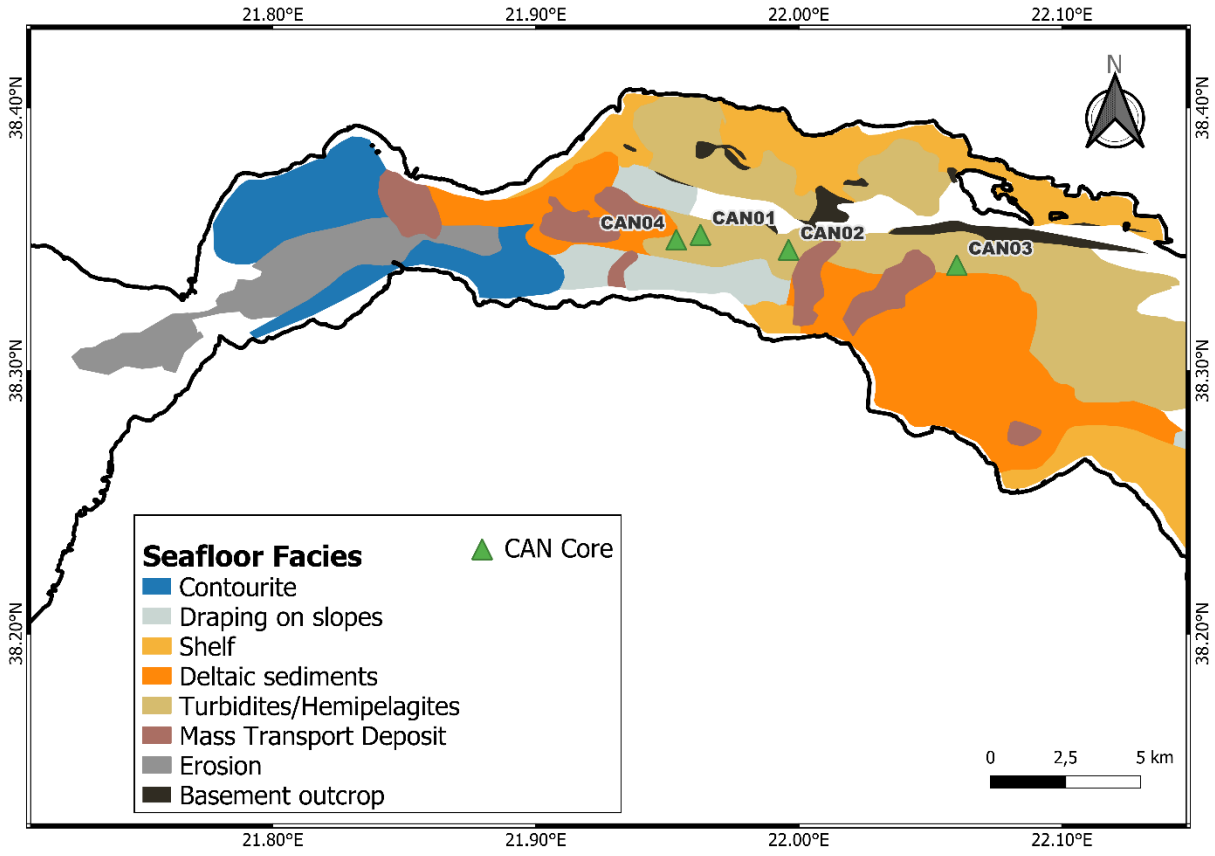

Figure 5.6: Facies map of the Rio-Antirio Strait and Western Corinth area, modified from Beckers et al. (2016).

4.1.2. Rio-Antorio strait sensu stricto and western domain

Moving westward, the hydrodynamic pattern becomes more intense due to the sill constriction and stronger tidal exchange. So, at the location of the Rio-Antirio strait sensu stricto, this translates into intense shear stress. On average, the stress values observed on the Patras side of the strait reach up to 0.2 N m^{-2}, with maximal shear stress around 3 N m^{-2}. These stress levels are enough to remobilize medium to coarse sand (Dey 1999; Peterson 1999).

Examination of bottom current direction maps (**Figure 5.3**) allows several observations. First, in this area, average currents display similar dynamics to those observed under maximal current conditions. Second, the dynamics differ on both sides of the strait. To the east, a small cyclonic gyre develops that we described earlier, while to the west, a mainly unidirectional central flow extends from the strait to the Patras Gulf. The intensity of the main flow decreases as it enters the Patras Gulf. On average, currents close to the center of the strait sensu stricto are flowing away from the middle of the strait (**Figure 5.4**). Third, both north and south of the main axis of this central flow, smaller currents move toward the Corinth Gulf. In the north, they are more intense than in the south and vary with the tidal phase, whereas in the south they are deflected/slowed against the bathymetric high formed by the remnant of a river delta. Shearing between these different flow masses generates bottom turbulence where waters are trapped in small gyres. These

turbulent zones are well represented in the model, as the shear stress in these locations ranges from 0.15 N m^{-2} to 0.2 N m^{-2} on average, and reaches 2 N m^{-2} to 3 N m^{-2} at maximum (**Figure 5.3**).

These dynamics can explain the geomorphological features observed by Rubi et al. (2022). The erosional and non-depositional areas near the strait are associated with the high modelled flow velocities. The only depositional zone in the area lies at the western end of the depressions created by the erosive flow. Sedimentation starts approximately 3 km west of the strait and first occurs along the southern basin margin, where currents are weakest. Flow energy progressively decreases westward from the strait, allowing sediment to be deposited following the sequence described by Piper et al. (1980), showing a progressive decrease in grain size (Piper & Panagos 1979; Piper *et al.* 1980; Rubi *et al.* 2022). We also observe that, close to the strait, the incision corresponding to the northern moat south of the terraces marks the area where currents and bottom shear stress are most intense, and where opposite flow directions coexist (**Figure 5.3**). We therefore infer a causal relationship between these high-stress zones and the observed erosional morphology. Finally, the smaller pools and crests found west of the center of the strait, forming a plateau (Rubi *et al.* 2022), are interpreted as being related to the intense overflow of deep Corinth waters crossing the strait. This overflow is observed as a cascading flow in the western part of the strait, leading to intense turbulence and high shear stress (up to 3 N m^{-2}; **Figure 5.3**). In this area, small gyres locally excavate the seafloor, creating the observed small pools. Some areas of the strait are more protected from high shear stress and may serve as potential refuges for cold-water corals (Titri *et al.* 2025).

Overall, the spatial variability of bottom shear stress explains the observed alternation between erosional and depositional zones across the Rio–Antirio Strait. The correspondence between high-stress areas and morphological depressions supports the role of bottom currents as a key control on sediment remobilization and the present-day sedimentary architecture of the Gulf.

4.2. Western Corinth (East of Mornos Delta)

East of the Rio–Antirio Strait Area and the Mornos Delta, the seafloor morphology in the central Corinth Gulf is dominated by a 3-km-wide, 300- to 430-m-deep canyon that widens and deepens eastward (A. Beckers *et al.* 2016). Further east, the canyon merges into the Delphic Plateau, that is bordered to the south by steep slopes formed by large delta (A. Beckers *et al.* 2016). Westward, the Delphic Plateau terminates in a tectonic high associated with a network of E–W-striking normal faults (Bell *et al.* 2008; A. Beckers *et al.* 2016). These fault-bounded horsts locally uplift the seafloor, forming a pronounced bathymetric high. South of this horst system and north of the Aigio Delta lies the Aigio canyon incised into the slope, forming a key morphological conduit between the southern

margin and the deep basin. This canyon system plays an important role in the present-day hydrodynamics and in the sediment transfer pathways described below.

In the following sections, we first analyze the pattern of near-bottom currents and sediment trajectories across this western sector (**Section 4.2.1**), then we examine the sedimentary record from the CAN cores to evaluate how these dynamics are archived in facies and stratigraphy (**Section 4.2.2**).

4.2.1. Currents and sediment trajectories

The presence of the canyon where the cores are located plays an important role for the bottom currents' dynamics. In front of the Mornos Delta, the high velocities originating from the strait area decrease sharply leading to the deposition of contourites deposits and deposition on the steep southern slopes without significant land sources (Figure 0.6; Beckers *et al*. 2016). Near the north coast, the velocities appear even slower (0.025 m s^{-1}; **Figure 5.7**), which lead to significant sediment draping on the Trizonia bathymetric scarp (**Figure 5.6**). A slight increase in velocity is observed globally, along the south coast, and in the Aigio canyon. The main "hotspots" of higher velocities are in front of the Erineos Delta and in front of the Aigio Delta. At this location, bottom waters cascade from the plateau (400 m) to the deep basin (700 m) in the east through the Aigio canyon.

Differences between the northern and southern part of the Western Corinth area concern both velocity's intensity and flow direction (**Figure 5.7**). Near the northern coast, the bottom shear stress is slower and, on average, directed towards the Rio-Antirio strait. Consequently, bottom shear stress is most significant in front of the Mornos Delta, where the southern flow move eastward and the northern flow moves westward.

In the western part of the canyon, close to the Mornos delta, tidal currents significantly influence bottom circulation. Tidal variations cause bottom currents to reverse direction and to temporarily increase in velocity, although their influence decreases with depth. The alternating ebb and flood movement are clearly visible in the model with a shift in the direction of the bottom currents every 6h (**Figure 5.8**). The tidal related motion extend over 14 km away from the Mornos Sill.

When simulating particle trajectories near the bottom of the Western Corinth area, several patterns related to sea-bed location are observed (**Figure 5.7C**). Near the northern slope, particles seem to be trapped there. Due to the stronger bidirectionality of the currents along the northern coast, particles are confined in circular motions, remaining mostly in the same location favoring sediment accumulation (**Figure 5.9**) on slopes forming drapes and drifts (**Figure 5.6**). Particles located within the central part of the plateau are exported to the deeper Corinth Basin. These particles generally follow a straight trajectory until they reach Aigio Delta and the associated tectonic canyon to the north. There they become more affected by multidirectional currents. There, the low velocities of the currents might be an indication for more favorable deposition settings.

Tidal forcing exerts a dominant influence near the Mornos Delta, where the local bathymetry and coastline geometry strongly modulate near-bottom current dynamics. This zone is particularly important, as the Mornos represents the largest drainage basin and the main sediment source of the Corinth Gulf. It therefore provides a key setting to examine how sediments delivered to the seabed—whether by gravity-driven processes or hyperpycnal flows—are subsequently redistributed by tidally influenced bottom currents.

Sediments delivered to the western part of the delta are exported toward Nafpaktos Bay and, if not deposited there in its northern drift, may continue toward the Strait. In contrast, sediments arriving from the eastern part of the delta can either be exported westward to Nafpaktos Bay or transported toward the southern coast, where they may become trapped (**Figure 5.7D**) or exported towards toward the central Corinth Gulf (**Figure 5.7C**). The "rapid" (every 6h) shift in current directions in front of the Mornos Delta (near the southern coast) explains why sediments are trapped and therefore deposited in this area. This is reflected in the Holocene thickness of sediments (**Figure 5.9**) that appear higher greater than in surroundings areas where the currents flow more unidirectionally.

In front of the Erineos River, the delta protrudes seaward and exerts a strong control on local bottom current dynamics. West of the delta, bottom currents show mean velocity of about 0.10 m s^{-1}, reaching up to 0.25 m s^{-1}, with a net eastward transport (**Figure 5.7**). This flow is diverted by the deltaic body of the Erineos Delta, which acts as a hydrodynamic obstacle. East of the delta, current velocities are much lower, forming a sheltered zone where sedimentation prevails. This area corresponds to the maximum Holocene sediment thickness observed in the study area (**Figure 5.9**), consistent with the isopach map. The relatively high fluvial sediment supply of the Erineos River (20–40 x 10^3 m^3 yr^{-1}; Watkins *et al.* 2019), combined with the low-energy hydrodynamic conditions east of the delta, favors local accumulation of fine-grained material. The pattern therefore reflects the combined influence of the delta morphology, the hydrodynamic field, and the sediment supply on deposition and redistribution.

A similar configuration is observed near the Aigio Delta, although the hydrodynamic effects are more pronounced. Here, the bottom flow is locally constricted by the tectonic horsts that close the plateau and is further accelerated within the Aigio Canyon due to the steep topographic gradient toward the ~700–800 m deep Corinth Basin (Figure 5.7). Despite a significantly higher fluvial sediment supply (80–160 x 10^3 m^3 yr^{-1}; Watkins *et al.* 2019), the Holocene sediment accumulation near the Aigio Delta is considerably lower than in front of the Erineos (**Figure 5.9**). This difference results from the enhanced current velocities and the canyon geometry, which together promote sediment bypass toward the deeper central basin of the Corinth Gulf, with only limited local deposition along the delta front.

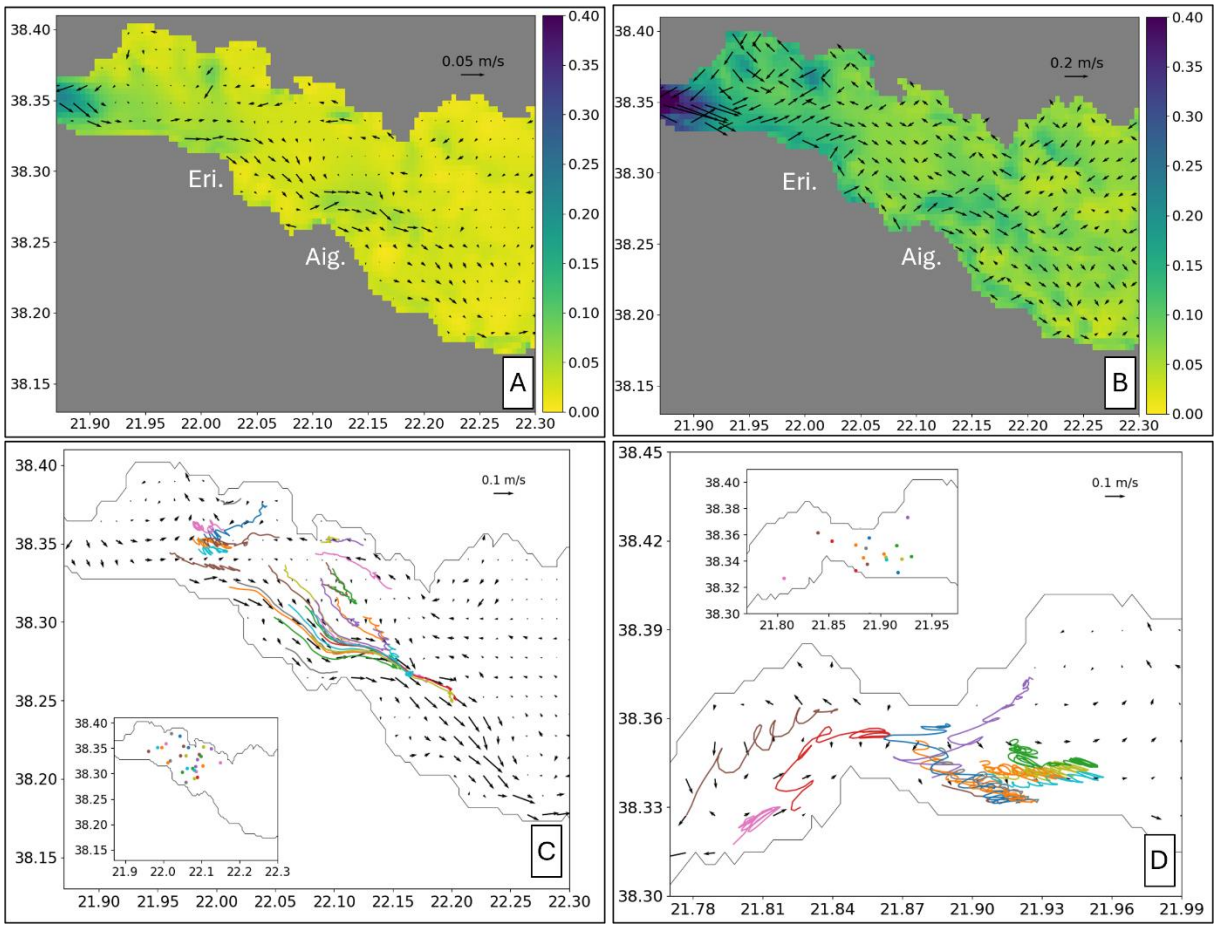

Figure 5.7: Zoom on the dynamics in the Western Corinth area. (A) Mean bottom velocities (m s^{-1}) for the month of May 2023. (B) Maximal velocities (m s^{-1}) for the month of May 2023. (A-B) Eri = Erineos Delta, Aig = Aigio Delta. (C) Track of simulated particles at the bottom of the Western Corinth area and their initial position. (D) Track of simulated particles at the bottom around the Mornos Delta and their initial position. Particles trajectories were simulated from 9 May 2023 to 14 May 2023.

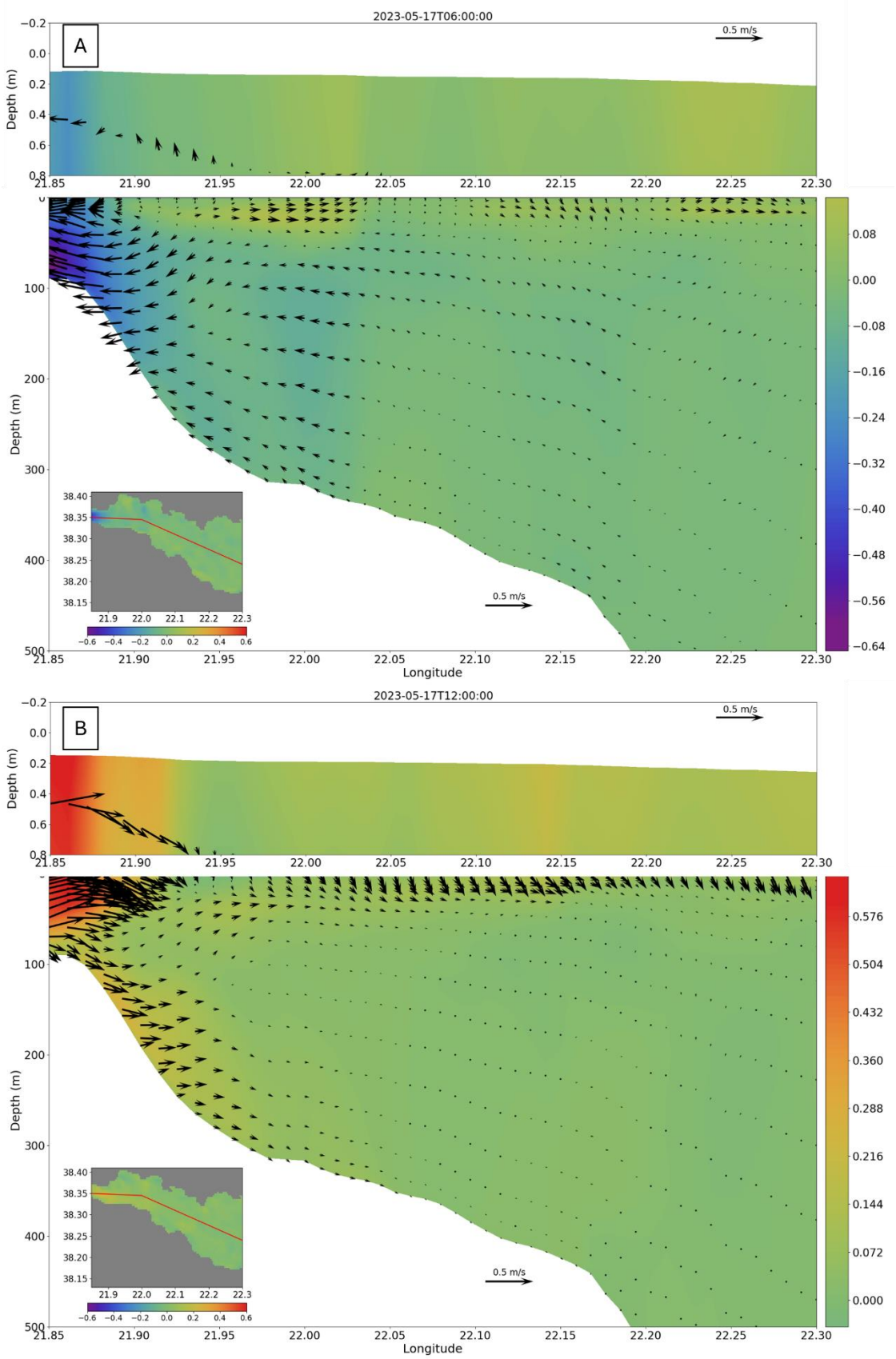

Figure 5.8: Sections of the modelled currents (m s^{-1}). The two timesteps represented evidence the ebb tide (A) and the flood tide (B) for the 17 May 2023. The Sea Surface Height (SSH) associated with tidal movements is represented in the top layer of each section. The color scales represent the eastward velocity

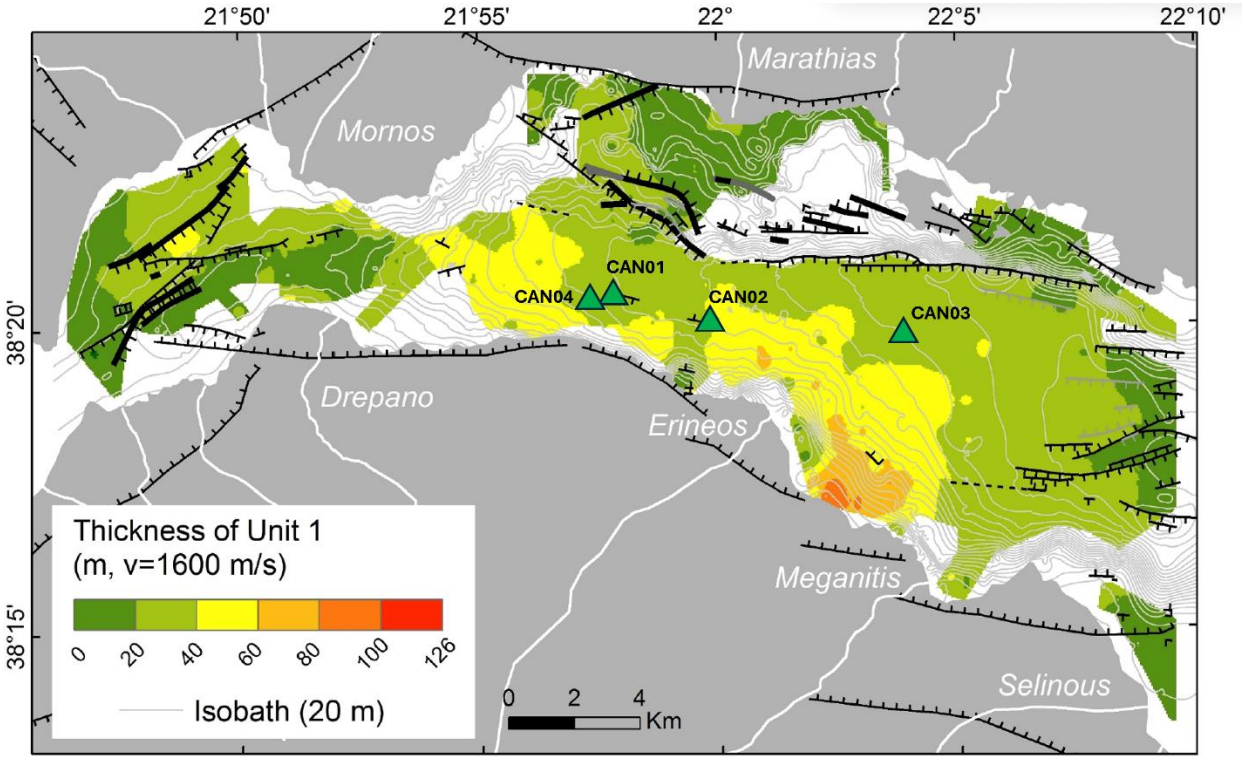

Figure 5.9: Thickness of the Holocene deposits in the Western Corinth area. The location of the core is presented by the green triangles. Modified from Beckers et al. (2016).

Further east (~22.22 °E), near the end of the Delphic Plateau (**Figure 5.1)** seismic line 39–40 provides evidence of strong bottom currents within the Aigio Canyon (**Figure 5.10**). The correspondence between the locations of maximal current velocities and the seismic line helps to interpret erosional patterns revealed in the sedimentary record. The central channel is clearly defined and coincides with maximal velocities of approximately 0.1 m s^{-1} at a depth of ~500 m. On the southern slope of the Gulf, two small U-shaped valleys (approximately 300 m wide and 30 m deep) are observed. These features were interpreted by Rubi (2018) as moats bounded by a sediment drift, sensu Hernández-Molina *et al.* (2008). Although the spatial resolution of the ROMS model does not allow a detailed characterization of the local processes, the presence of near-bottom currents reaching ~0.10 m s^{-1} in these valleys (**Figure 5.7**, **Figure 5.10**) supports the hypothesis that such currents contributed to the observed erosion.

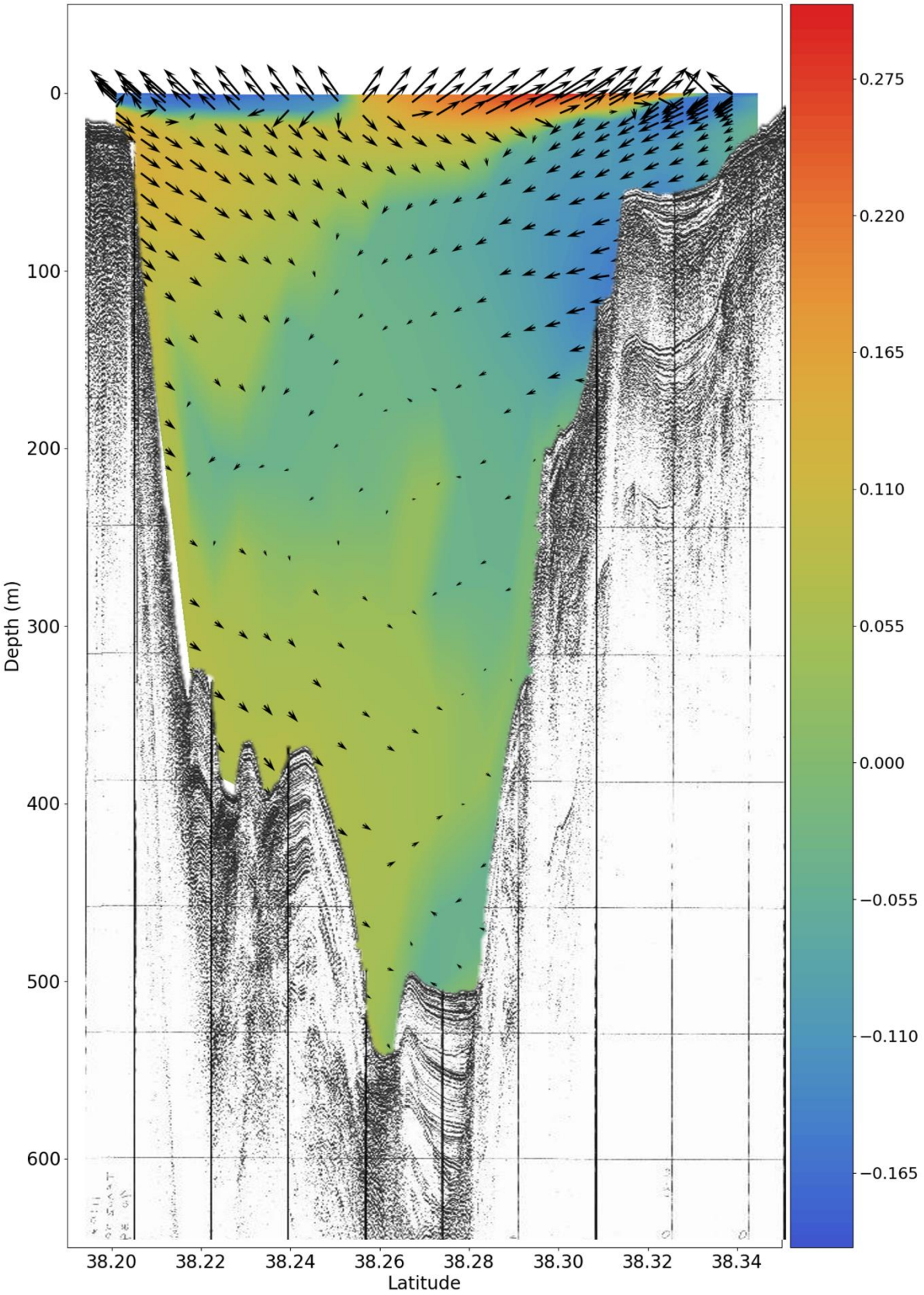

Figure 5.10: Cross-section through the Western Corinth area (39-40 on Figure 0.1) with modelled velocity above seismic data. The seismic section is modified from Rubi (2018). The colors represent the maximal current intensity, the arrows their direction. The eastward velocity (m s^{-1}) is represented (red = eastward, blue = westward).

4.2.2. CAN Cores

4.2.2.1. Sediment characteristics

Bioturbation dominates the sedimentary record, yet distinct layering remains well preserved, although strongly irregular (**Figure 5.11**). The deposits exhibit subparallel to crinkled laminae, wavy, and lenticular bedding, as well as wavy lamination. All cores display heterolithic facies, characterized by irregular alternations of sand or silt layers, 2–60 mm thick, and mud. These coarser-grained layers occur either isolated or stacked.

The sediment cores are in areas known to be affected by turbidity currents that have repeatedly broken submarine cables. Coarse-grained deposits are therefore likely associated with earthquake-triggered or shelf-break-related events. Beckers et al. (2017), in a short core collected near CAN2, identified the youngest coarse-grained deposit as the 1963 Erineos submarine landslide, linked to a shelf break. They also attributed a thicker coarse-grained unit to the 1861 earthquake (Mw ~6.5) that ruptured the onshore Helike Fault (Albini *et al*. 2017).

In all four sedimentary cores, we documented deposits corresponding to normally graded turbidites, with sharp horizontal bases and occasional internal laminations (**Figure 5.11**). All deposits show variable degrees of bioturbation, yet their internal structures remain clearly visible. The strongest bioturbation occurs at the tops of turbiditic beds. In CAN4, three deposits thicker than 6 mm are observed at 1.21 m, 1.6 m, and 1.8 m depth (**Figure 5.2**). The deepest shows soft-sediment deformation and contains terrestrial organic matter, dated by radiocarbon (**Figure 5.12**, **Table 5.4**). In CAN1, a single thick (10 cm) event occurs at 1.4 m, associated with organic matter and internal lamination. It represents the largest and coarsest event in that core. In CAN2, a stacked sequence of deformed turbidites occurs between 0.87 m and 1.25 m, with partially preserved erosive bases (**Figure 5.2**); several coarser units contain organic matter dated by radiocarbon (**Figure 5.13**, **Table 5.4**). In CAN3, three main turbidites are present: two thin stacked layers near the top (0.05–0.1 m) and a thicker, coarser one between 0.48 m and 0.59 m (**Figure 5.2**), also radiocarbon dated (**Figure 5.13**, **Table 5.4**). Magnetic susceptibility (MS) and XRF core logs show that these coarse-grained deposits consistently coincide with MS peaks and high Zr/Rb ratios, proxies for grain size (**Figure 5.12**, **Figure 5.13**).

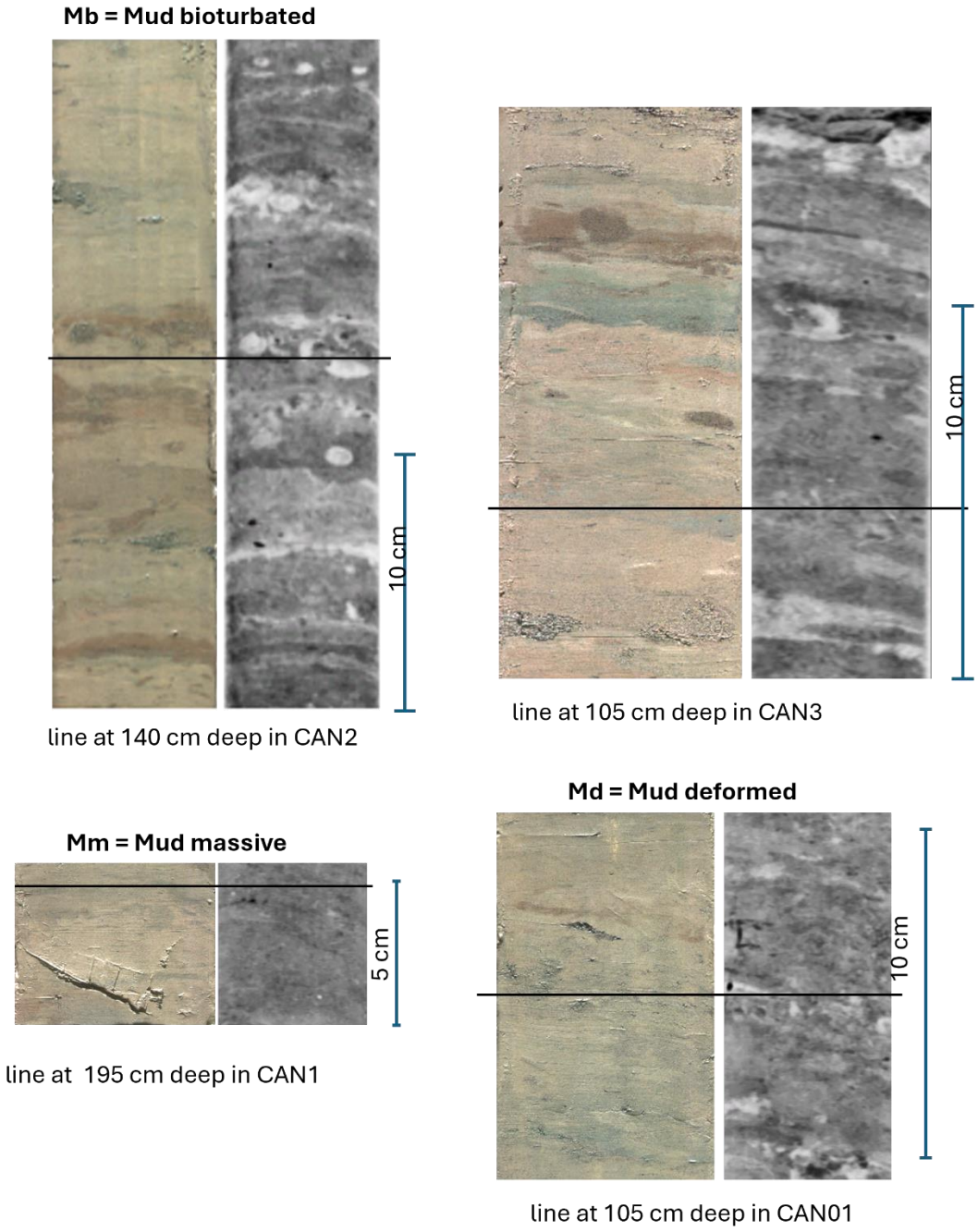

Figure 5.11: Characteristics of the different facies from the CAN Cores from CT scan and line scan images

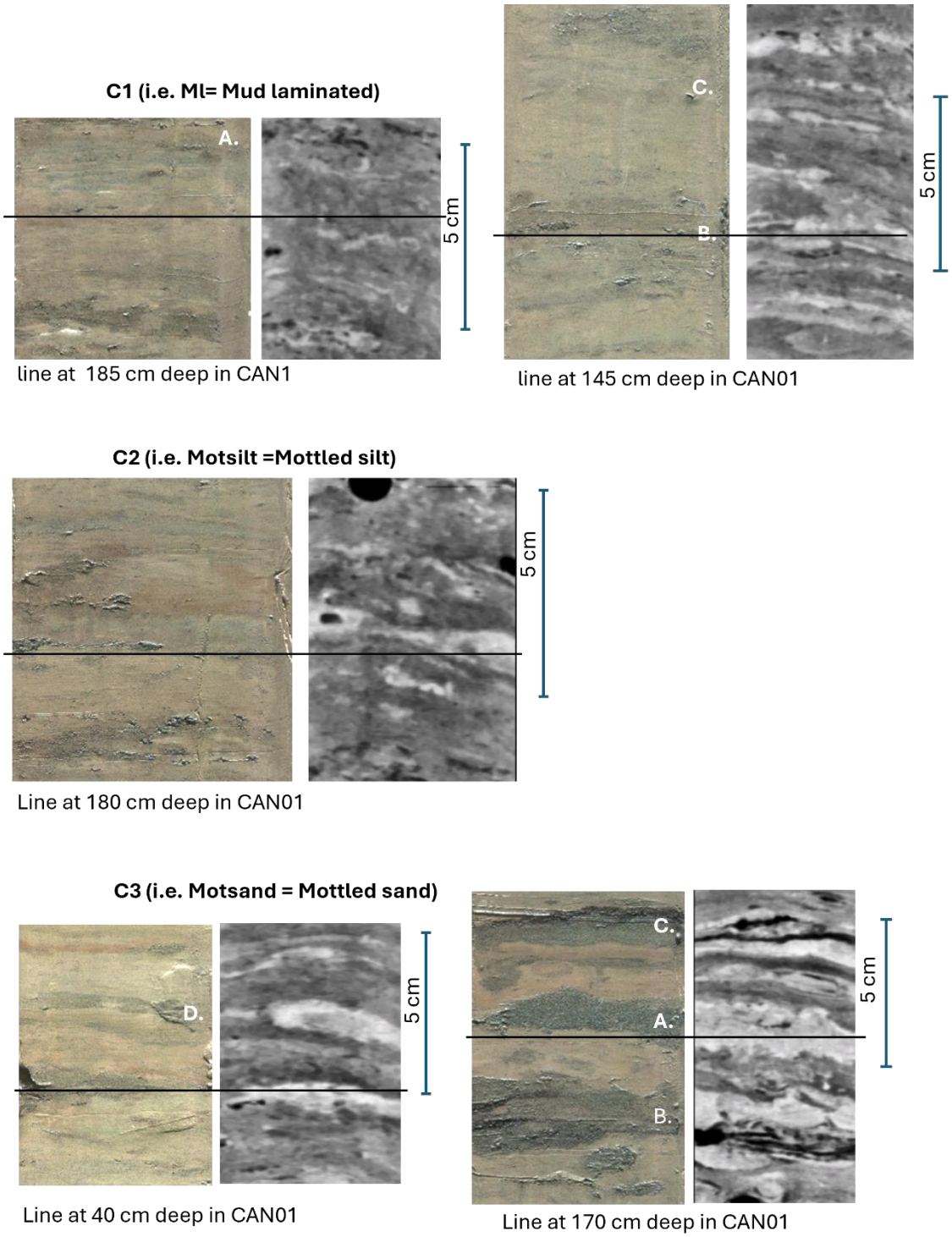

Figure 5.11 (continuing): Characteristics of the different facies from the CAN Cores from CT scan and line scan images

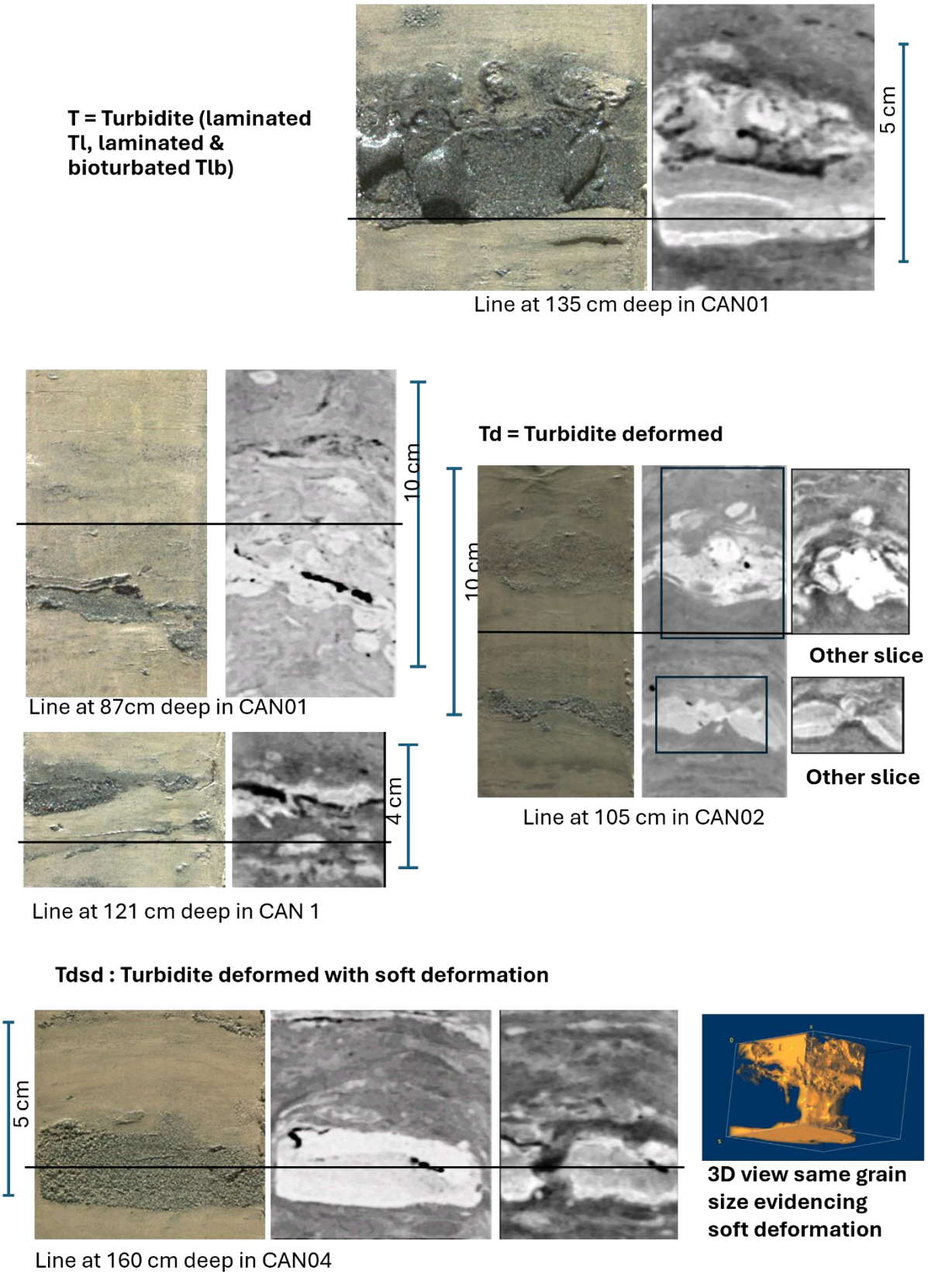

Figure 5.11 (continuing): Characteristics of the different facies from the CAN Cores from CT scan and line scan images

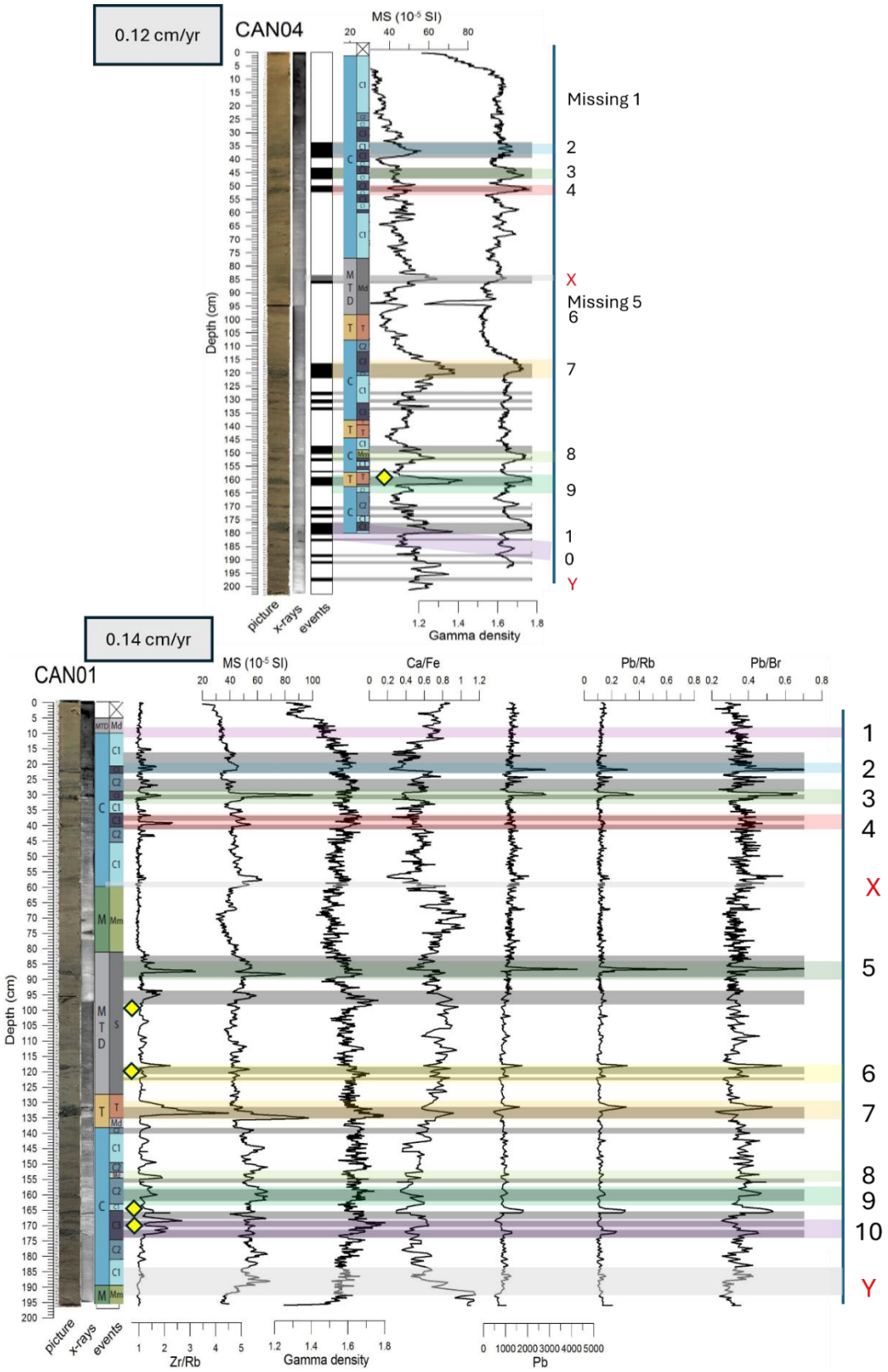

Figure 5.12: Detailed display of the cores CAN04 and CAN01 with from left to right, photo line scan, X-Ray, facies and facies associations, measurements of magnetic susceptibility and gamma density and XRF data. Gray lines show coarser-grained layers, and levels in pale colors are correlative ones between the sedimentary cores. Yellow diamonds indicate the locations of radiocarbon dating samples.

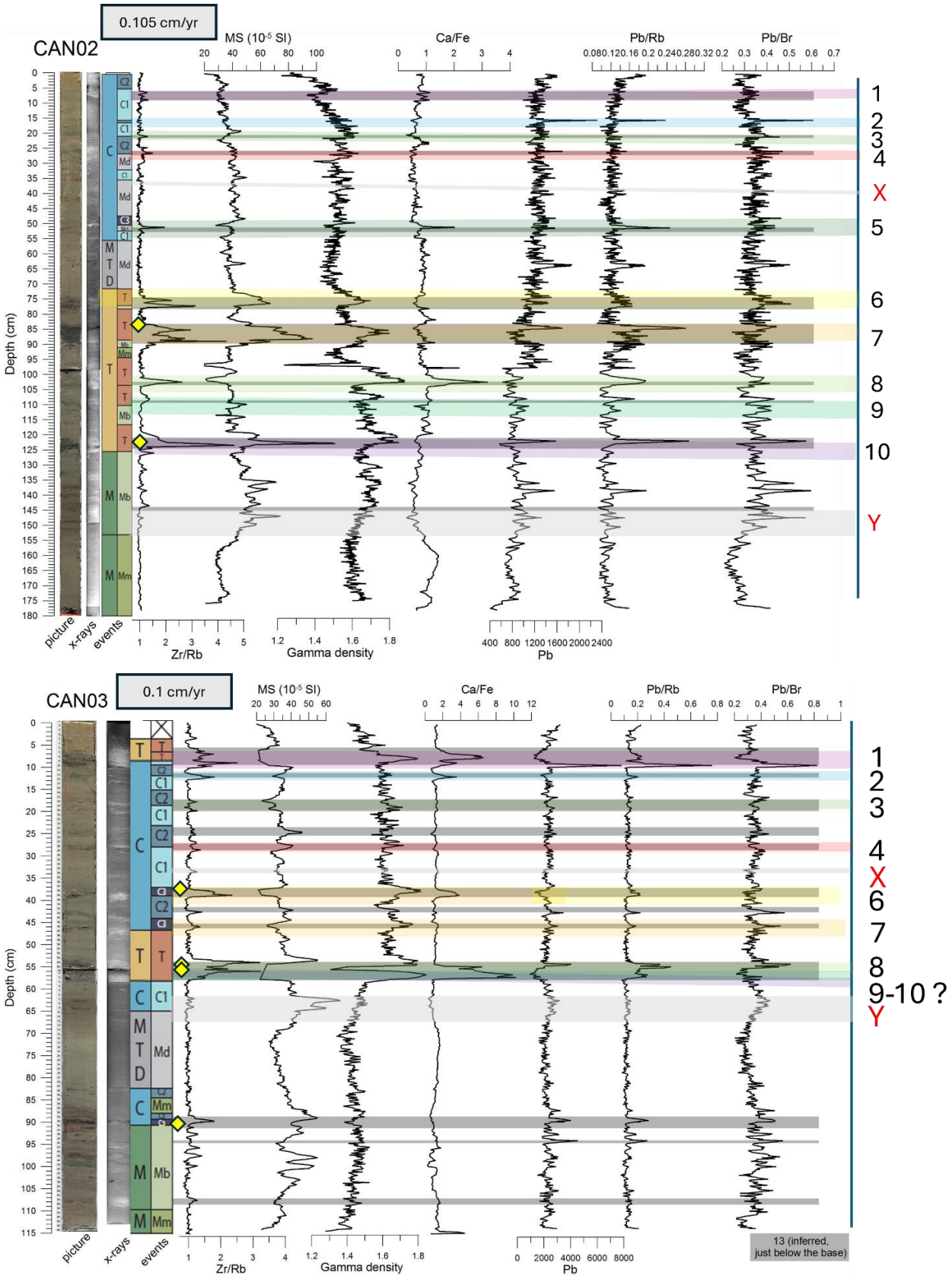

Figure 5.13: Detailed display of the cores CAN02 and CAN03 with from left to right, photo line scan, X-Ray, facies and facies associations, measurements of magnetic susceptibility and gamma density and XRF data. Gray lines show coarser-grained layers, and levels in pale colors are correlative ones between the sedimentary cores. Yellow diamonds indicate the locations of radiocarbon dating samples.

Other coarse-grained facies are completely mottled and lack normal grading (**Figure 5.11**). Although faint bedding may persist locally, it is systematically wavy. Based on grain size, two variants are distinguished: mottled sand (MotSand/C3) and mottled silt (MotSilt/C2).

Mottled sand deposits show significant variability: (1) massive homogeneous sandy beds with wavy tops; (2) heterogeneous sand lenses containing organic matter; (3) fining-upward sequences marked only by organic matter at the top; and (4) centimetric sand lenses interbedded within mud. This facies is most abundant in CAN4, where eleven intervals occur (up to 10 cm thick) (**Figure 5.2**). Its frequency decreases eastward: three deposits in CAN1, one in CAN2, and three thin layers in CAN3. Mottled sand layers exhibit MS and XRF signatures similar to the turbidites (**Figure 5.12**, **Figure 5.13**). Mottled silt deposits consist of irregular, wavy silt laminae and lenses; they are frequent in CAN4, less so in CAN1 and CAN2, but again frequent in CAN3. The third facies is similar but finer-grained (**Figure 5.11**). It consists of bioturbated laminated mud (Ml/C1) characterized by three different types of laminations: (1) discontinuous millimetric laminae, (2) continuous millimetric laminae that may be wavy, flat, or inclined, and (3) small millimetric lenses within a finely laminated background. This facies is very frequent in CAN4 and occurs in all other cores at lower frequency. Given its pervasive bioturbation and tractional structures, it is interpreted as a contouritic deposit as well as the other coarser deposits: mottled sand (MotSand) and mottled silt (MotSilt). These facies would correspond to the C1, C2, C3 contourite facies of Rebesco et al. (2014), and are labelled as such.

Other mud facies are also present (**Figure 5.11**). The massive, deformed mud (Md) facies consists of strongly bioturbated and deformed muds, locally containing disrupted sand or silt layers. This facies is observed in all cores: ~24 cm thick in CAN4; ~5 cm thick in CAN1 (possibly linked to the 1963 slope failure); and a thick (~50 cm) deformed interval at 1.275 m, correlating with the thick Md unit in CAN4 (**Figure 5.2**). In CAN2, Md occurs frequently in the upper 0.8 m, while in CAN3 there is one layer thicker than 15 cm. Thick Md units generally exhibit lower density and MS values than surrounding deposits. The massive mud (Mm) facies is homogeneous in color and grain size and lacks bioturbation (**Figure 5.11**). In CAN4, it occurs only as a minor layer, whereas in CAN1 it forms a 21 cm-thick deposit overlying the deformed mud and another >6 cm thick unit at the base (Figure 5.2). In CAN2 and CAN3, this facies mainly occupies the basal sections and is characterized by high Ca/Fe ratios and low density (**Figure 5.13**). Finally, the bioturbated mud (Mb) facies consists of very fine sediments with faint centimeter-scale horizontal color banding but without erosive features typical of tractional flow (unlike the MotSand/C3 facies) (Figure 10_2). It occurs only in CAN2 and CAN3, above Mm deposits (Figure 10_1). In CAN2, it forms a >25 cm unit overlying a >25 cm Mm layer near the core base; in CAN3, a similar 18 cm Mb layer overlies an Mm deposit. In both cases, MS values are variable (**Figure 5.13**).

Although all these facies are fine-grained, there is no evidence of slow, continuous hemipelagic sedimentation. Instead, they are interpreted as the product of reworking of previously deposited fine-grained sediments, originating for instance from the steep slopes of the Erineos or Mornos deltas. The Md–s facies, marked by strong deformation, is interpreted to corresponds to mass-transport deposits (MTDs) of fine-grained sediments. The Mm facies, massive and unbioturbated with low density and MS, likely results from a sudden influx of fine suspended sediment settling rapidly above a denser basal layer (not recovered in CAN2–CAN3 but correlating with the deformed deposit in CAN1) (**Figure 5.12, Figure 5.13**). It is a typical homogenized facies (A. Beckers *et al*. 2017). The rapid deposition would have prevented bioturbation. The Mb facies, found above Mm layers, is interpreted as the result of post-MTD settling of fine suspended material within months following a large mass-transport event, possibly earthquake-triggered, like what observed after the 2010 Haiti earthquake (McHugh *et al*. 2011).

The individual facies were grouped into four facies associations, each representing a dominant depositional process or environment in the western Gulf of Corinth. T (Turbidite facies association) includes sand–silt–mud successions showing normal grading, sharp or slightly erosive bases, and faint internal lamination. Although these deposits retain diagnostic features of turbidites, they are strongly bioturbated and partly reworked. Their textures and structures are thus interpreted to reflect a hybrid character between classical turbidites and contouritic flows (Stow & Smillie 2020; Rodrigues *et al*. 2022). C (Contouritic facies association): comprises the bioturbated laminated mud (Ml/C1) together with the mottled sand and silt facies (MotSand/C3 and MotSilt/C2). These facies are characterized by wavy or discontinuous laminae, local traction structures, and pervasive bioturbation and correspond to the different contourite end-members of Rebesco et al. (2014). They record continuous to intermittent reworking by weak bottom currents, in agreement with the bidirectional near-bottom flow regime simulated by hydrodynamic modelling. MTD (Mass-Transport Deposit association): includes deformed muds (Md) and associated mixed sand–silt lenses (s). These facies display soft-sediment deformation, chaotic structures, and local shear fabrics, indicating slope instability and downslope remobilization of previously deposited sediments. Such deposits can originate from on the Mornos and Erineos slopes, and more generally along the depocenter flanks, where locally high sedimentation rates and drift accumulation induced by bottom currents promote slope failure and sediment instability (A. Beckers *et al*. 2017). M (Massive mud association): groups homogeneous muds (Mm and Mb facies) with low density and faint internal structures. These layers are interpreted as rapid fine-grained fallout deposits, formed during and just after major mass-transport events or slope failures.

Together, these four facies associations summarize the main sedimentary processes operating at the western entrance of the Gulf of Corinth and provide a framework for

interpreting the interplay between gravity-driven deposition, bottom-current reworking, and mass-wasting processes in the following sections.

4.2.2.2. Sedimentation rate, dating and core correlation

Average fine-grained sedimentation rates were derived from radionuclide data in all four cores.

For CAN3, a sedimentation rate for the upper 6 cm was obtained using the Constant Initial Concentration (CIC) model. The calculated rate ranges between 1.52 mm yr^{-1} and 1.65 mm yr^{-1} (r^2 = 0.93 for the regression between excess ^{210}Pb activity and depth; see PhD thesis of A. Beckers). However, the ^{210}Pb profile is incomplete because of an event deposit at 6 cm. The $^{210}Pb_{xs}$ activity decreases linearly from the top of the core to the top of this event layer, but no excess activity is detected below (**Table 5.3**). Considering that the top of event E1 lies at 6 cm, this implies an age of 1975–1978 AD for this deposit. The ^{137}Cs profile shows a single broad peak between 1 and 5 cm, with only minor activity in E1 and none below. This large peak probably results from diffusion and/or post-depositional mixing of ^{137}Cs originating from the 1960s and 1986 fallout peaks. It suggests an age of ~1955–1960 AD for event E1—slightly older than the age inferred from $^{210}Pb_{xs}$. This yields an estimated sedimentation rate of ~1.1 mm yr^{-1}.

For the other cores, the derived rates are relatively similar: CAN2: 0.105 mm yr^{-1} (r^2 = 0.90), CAN1: 0.14 mm yr^{-1} (r^2 = 0.98), CAN4: 0.12 mm yr^{-1} (r^2 = 0.98). Overall, the fine-grained sedimentation rates in all cores are consistent, ranging between ~1.0 and 1.4 mm yr^{-1} (**Figure 5.14, Table 5.3**).

Radiocarbon dating provides additional chronological constraints (**Table 5.4**). Only the youngest ages were retained, as older apparent ages likely reflect reworked or terrestrial organic matter with long residence times in the catchment prior to deposition. Five consistent radiocarbon ages fall between 270 and 395 yr BP, forming the basis for initial inter-core correlation.

Figure 5.2 summarizes the proposed correlations integrating all available data. The short core PSP05, located within a few hundred meters of CAN2 and studied by Beckers et al. (2016), also provides ages for event deposits corresponding to those in CAN2.

A straightforward correlation can be established between CAN4 and CAN1 (**Figure 5.2**), which are spatially close and display similar sedimentation patterns. All coarse-grained deposits can be matched between the two, including a shared radiocarbon age of ~390 BP at 1.8 m in CAN4 and 1.75 m in CAN1. The correlation highlights the co-occurrence of turbidites at 1.2 m in CAN4 and 1.4 m in CAN1, overlain by a correlative mass-transport deposit (MTD) overlined by massive mud unit in CAN1. A comparable but thinner (~15 cm) MTD is identified in CAN2, whereas this layer is absent in CAN3. The correlation of CAN3 with the other cores is primarily based on a radiocarbon age of ~390 BP within a thick

turbidite at ~60 cm depth. Additionally, we propose correlating the MTD at 0.8 m in CAN3 with the massive muddy Mb/Mm facies at the base of CAN2 and CAN3, as these units exhibit similar geochemical (high Ca/Fe) and physical (low MS) signatures (**Figure 5.13**). These correlations form the stratigraphic framework used to interpret hydrodynamic control on sedimentation patterns in the next section.

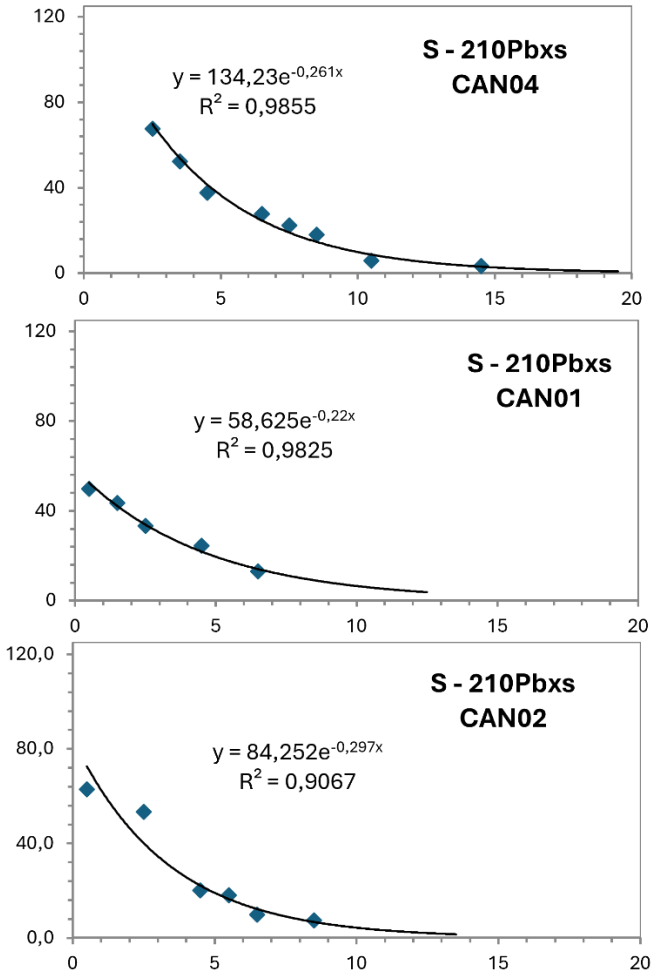

Figure 5.14 : Derived sedimentation rates from radionuclide measurements in CAN1, CAN2 and CAN4

4.2.2.3. Influence of bottom currents in the western Corinth depocenter

The overall sedimentation in the western Corinth depocenter is controlled by the interplay between gravity-driven processes and bottom-current reworking. Turbidity currents and mass-transport processes deliver and redistribute most of the fine-grained material, while near-bottom currents of variable intensity continuously reshape the upper sediment surface, forming contouritic structures and hybrid deposits.

The influence of bottom currents progressively decreases from west to east across the depocenter. In the westernmost part, at CAN4, sediment reworking by bottom currents is most intense. Here, mottled and bioturbated facies (C3) dominate, indicating persistent near-bottom flow activity. The alternation of reworked turbidites and contouritic layers

suggests frequent overprinting of gravity-flow deposits by current-induced winnowing and redistribution.

Eastward, at CAN2, the expression of bottom-current processes becomes much weaker. The sedimentary record is dominated by less reworked Md and Mm facies, showing reduced tractional structures and weaker hydrodynamic influence. CAN2 is in a quieter depositional zone where bottom currents have lost much of their energy (**Figure 5.7**), and sedimentation is mainly governed by gravity-driven accumulation. Further east, at CAN3, bottom-current influence becomes slightly stronger again. The reappearance of C1 and C2 facies (bioturbated laminated muds and mottled silts) indicates renewed near-bottom flow activity, consistent with hydrodynamic model results showing enhanced bottom-current velocities in this sector before the seafloor constriction at the western end of the Corinth Plateau (**Figure 5.7**). This pattern suggests a complex hydrodynamic configuration where local topography and alternating current cells related to the Rio–Antirio Strait control the intensity of sediment reworking.

The hydrodynamic modelling confirms that bottom currents in the western Gulf are predominantly bidirectional, driven by tidal exchanges through the Rio–Antirio Strait (**Figure 5.8**). Current velocities are highest near the strait and along the western depocenter margin, where alternating inflow and outflow pulses generate persistent near-bottom shear. This dynamic circulation explains the prevalence of reworked contouritic facies (C3 and C2) in CAN4. Eastward, current energy decreases sharply, allowing gravity-driven processes and MTD accumulation to dominate. Near CAN3, flow constriction and topographic steering enhance near-bottom velocities again, correlating with renewed contouritic structures.

Together, sedimentological and hydrodynamic evidence demonstrates that bottom-current variability exerts a first-order control on sediment preservation and facies distribution. Areas of stronger flow promote winnowing, bioturbation, and contouritic layering, whereas lower-energy zones favor the accumulation and deformation of fine-grained gravity-driven sediments. This interplay defines a spatial alternation of contouritic and gravitational domains, reflecting the dynamic coupling between sediment supply, slope morphology, and tidal circulation at the entrance of the Corinth Gulf.

4.3. Center of Corinth Gulf

Modelling shows that the seabed of the central Corinth Gulf is the slowest and quietest area of the basin. In this sector, bottom currents reach maximal velocities of 0.1 m s^{-1} near the margins and of 0.07 m s^{-1} in deeper waters (**Figure 5.15**). These values are consistent between the model mean fields and previously in situ measurements (Poulos *et al.* 1996). Local velocities maxima occur near the bathymetric gradients.

Regarding circulation, the model mean shows a large cyclonic gyre spanning most of the deep basin. On average, flow along the southern margin is directed eastward, whereas

flow in the basin center and along the northern continental slope is preferentially westward. The modelling also confirms the currents reversals reported by Poulos et al. (1996): the east-west shift recurs approximately every 2-3 days (**Figure 5.15**). Despite these reversals, current magnitude are so low that they generate only negligible bottom shear stress.

These low velocities explain the sediment accumulation in the basin center (Nixon *et al.* 2016; Shillington *et al.* 2019). At the IODP sites (**Figure 5.16**), the weak near-bottom circulation is reflected by deposits that show no evidence of bottom currents reworking (McNeill, Shillington, Carter, Everest, Le Ber, *et al.* 2019b; a). The central depocenter is therefore well expressed owing to the absence of stronger velocities such as those found in the western Corinth area.

The extent of this depocenter is limited to the eastern part of the central basin (in front of the Antikyra Bay). This is due to the sediment infill volumes in the west compared to the east (Watkins *et al.* 2019), but also to potentially the central Corinth hydrodynamics. The presence of an anticyclonic gyre in the western part of the basin may facilitate eastward sediment transfer (Caterina & Hubert-Ferrari 2025). In addition, eastward bottom current along the southern margins reach 0.05 m s^{-1} would also favor sediment export to the eastern part of the central basin where it is then deposited, which is consistent with the observed accumulation in that area (**Figure 5.16**) (Nixon *et al.* 2016; Rubi 2018).

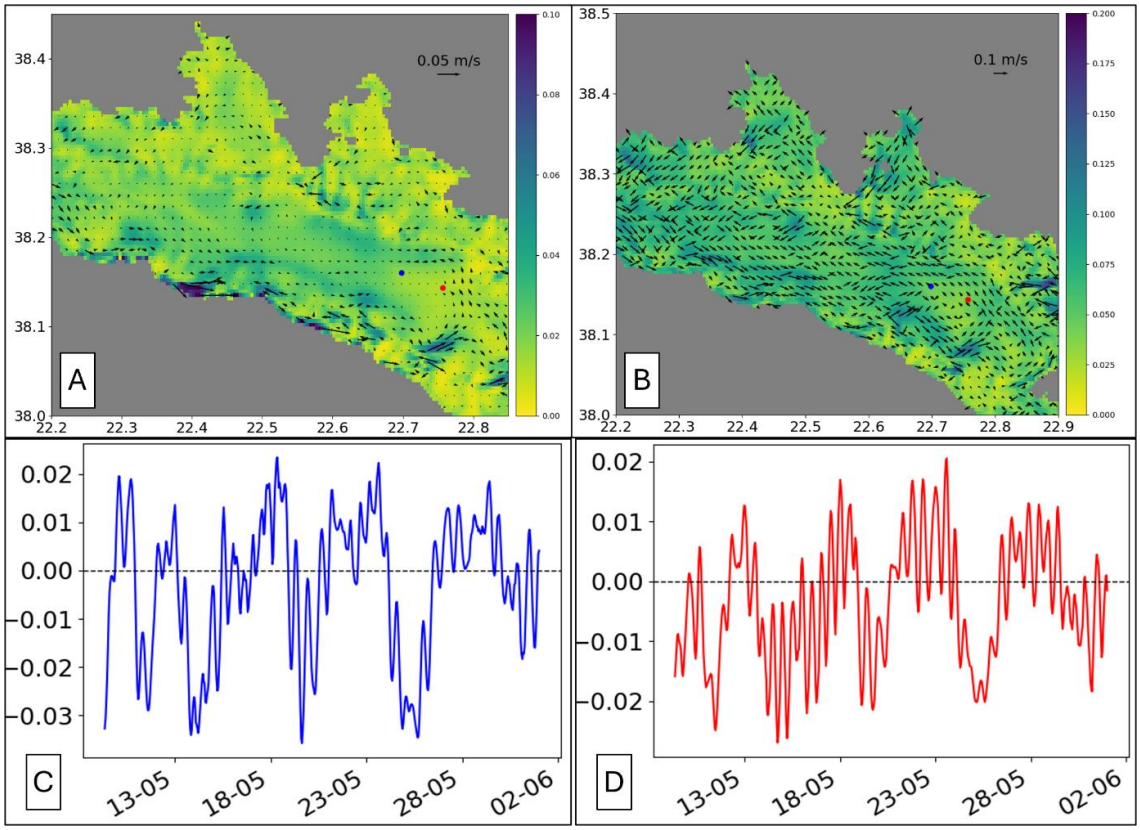

Figure 5.15: (A) Average bottom velocities (m s^{-1}) at the center of the Corinth Gulf. (B) Maximal bottom velocities at the center of the Corinth Gulf. The colored dots represent the position of the IODP cores

from McNeill et al. (2019a, 2019b). (C) Eastward velocity at the bottom at the site M0079 from the IODP expedition. (D) Eastward velocity at the bottom at the site M0078 from the IODP expedition.

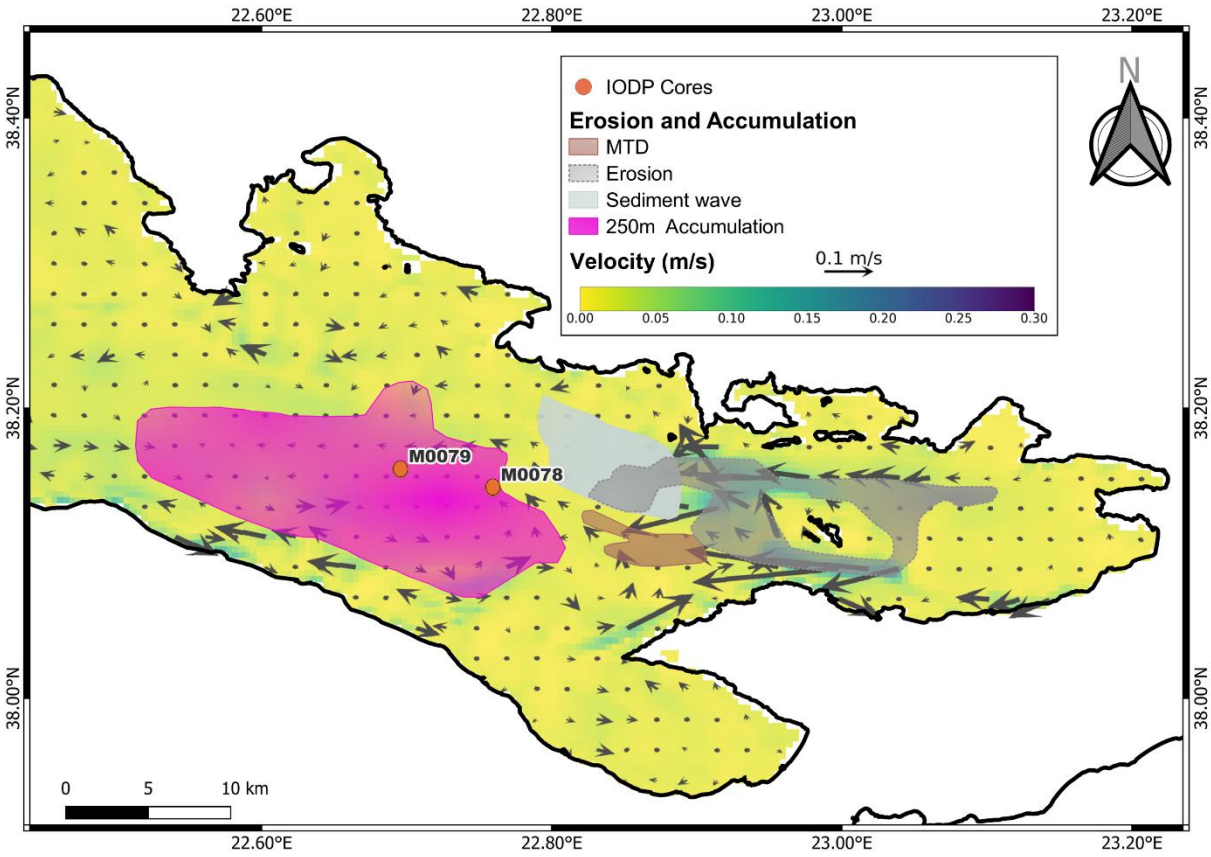

Figure 5.16: Eastern part of the Center of Corinth and of the Alkyonides Basin. The mean velocities of the bottom currents are from the ROMS modelling. The thickness of 0-130 kyr sediments and erosion are modified from (Rubi 2018) and (Nixon *et al.* 2016).

4.4. Alkyonides

The Alkyonides Gulf lies at the eastern extremity of the Gulf of Corinth and is approximately 13 km wide and 22 km long, with a maximum depth of ~360 m. It encloses three small Alkyonides Islands—Zoodochos, Daskalio, and Glaronisi—which form a shallow structural high bordered by canyons. These islands mark the transition between the main Corinth Basin and the eastern Alkyonides Basin, where local canyon systems and fault scarps strongly influence present-day bottom-current dynamics and sediment distribution (Leeder *et al.* 2005).

In the Alkyonides Gulf, bottom currents are generally weak on average, except within the canyons north and south of the Islands (**Figure 5.17**). The two high-velocity channels observed correspond to the main submarine canyons, with mean velocities reach ~0.2 m s^{-1} and peak values up to 0.4 m s^{-1}, whereas the basin-wide average is only ~0.05 m s^{-1}. Model results indicate that water masses from the Alkyonides are exported into the deeper parts of the Gulf of Corinth through these canyons (**Figure 5.18**). In contrast, the eastern sector of the Alkyonides Gulf is characterized by very low velocities and minimal near-bottom circulation, favoring sediment accumulation (**Figure 5.18**).

Because current velocities are relatively high in the canyons, no significant sediment accumulation occurs within them. The southern canyon is deeper and coincides with the highest modelled velocities (0.4 m s^{-1}) (**Figure 5.17**), indicating strong scouring of the seafloor. Sediment accumulation is instead observed along the flanks and in the eastern part of the Alkyonides Gulf, where current velocities are lower. Mapping of sediment accumulation and erosion highlights the influence of cascading currents on sediment transport and deposition (**Figure 5.16**) (Nixon *et al*. 2016; Rubi 2018). At the base of the canyon slopes, erosion is more pronounced in front of the northern canyon, whereas mass-transport deposits (MTDs) are documented in front of the southern one (**Figure 5.16**) Sediment waves and thin draping deposits occur downslope of the northern canyon, consistent with local reductions in current velocity and sediment remobilization during waning flow stages.

The erosion and impact of the high-velocity currents emerging from the canyons can also be observed on the high-resolution seismic line 95–96 (**Figure 5.1**, **Figure 5.19**). From south to north, the section highlights a bathymetric rise related to the coastal proximity near the end of Lechaio Bay. This bathymetric restriction is corroborated by the current velocity distribution (**Figure 5.19**). Farther north, the deep Corinth Basin is characterized by sediment accumulation, with deposits resulting from falling-down and/or axial transport, mass-transport deposits (MTDs), or sediment waves (**Figure 5.16**, **Figure 5.19**; Rubi 2018). At the foot of the northern slope, two waterways originating from the northern canyon of the Alkyonides area (**Figure 5.17**) shaped the bathymetry into narrow U-shaped valleys (**Figure 5.19**). In this area, the highest near-bottom current intensities of the section are recorded, reaching up to 0.15 m s^{-1} near the distal ends of the canyons.

Sediment accumulation within the Alkyonides Basin is highest in its easternmost part, where bottom-current velocities are minimal (max. ~0.05 m s^{-1}; **Figure 5.18**) (Collier *et al*. 2000). Collier et al. (2000) attributed this pattern primarily to climatic variations between the Holocene and Pleistocene, but our results suggest that hydrodynamic control also plays a major role. The strong bottom currents within the canyons are likely to promote sediment exportation from the western Alkyonides, preventing local accumulation near the canyon mouths. In contrast, the low-energy conditions prevailing in the southeastern sector allow suspended material to settle and build up thick fine-grained drapes (**Figure 5.18**).

The hydrodynamic modelling also reveals that the canyons act as preferential conduits for water and sediment exchange between the Alkyonides sub-basins and the deeper Corinth Gulf. These topographically controlled channels channelize downslope cascading flows, which can transport fine-grained suspended sediments toward the main basin. The strongest cascading and export activity is associated with the southern canyon, where bathymetric confinement enhances near-bottom acceleration and turbulence. This pattern indicates that the Alkyonides canyons not only shape the local

sedimentary architecture but also contribute to the regional sediment redistribution toward the deeper Corinth depocenter.

Overall, the Alkyonides region illustrates how canyon morphology and localized bottom-current acceleration combine to modulate sediment transport and deposition at the eastern termination of the Corinth Rift. The resulting pattern—erosion and sediment bypass within the canyons and enhanced fine-grained accumulation in the sheltered eastern basin—highlights the tight coupling between tectonic morphology, cascading flow dynamics, and sedimentary architecture in this sector of the Gulf.

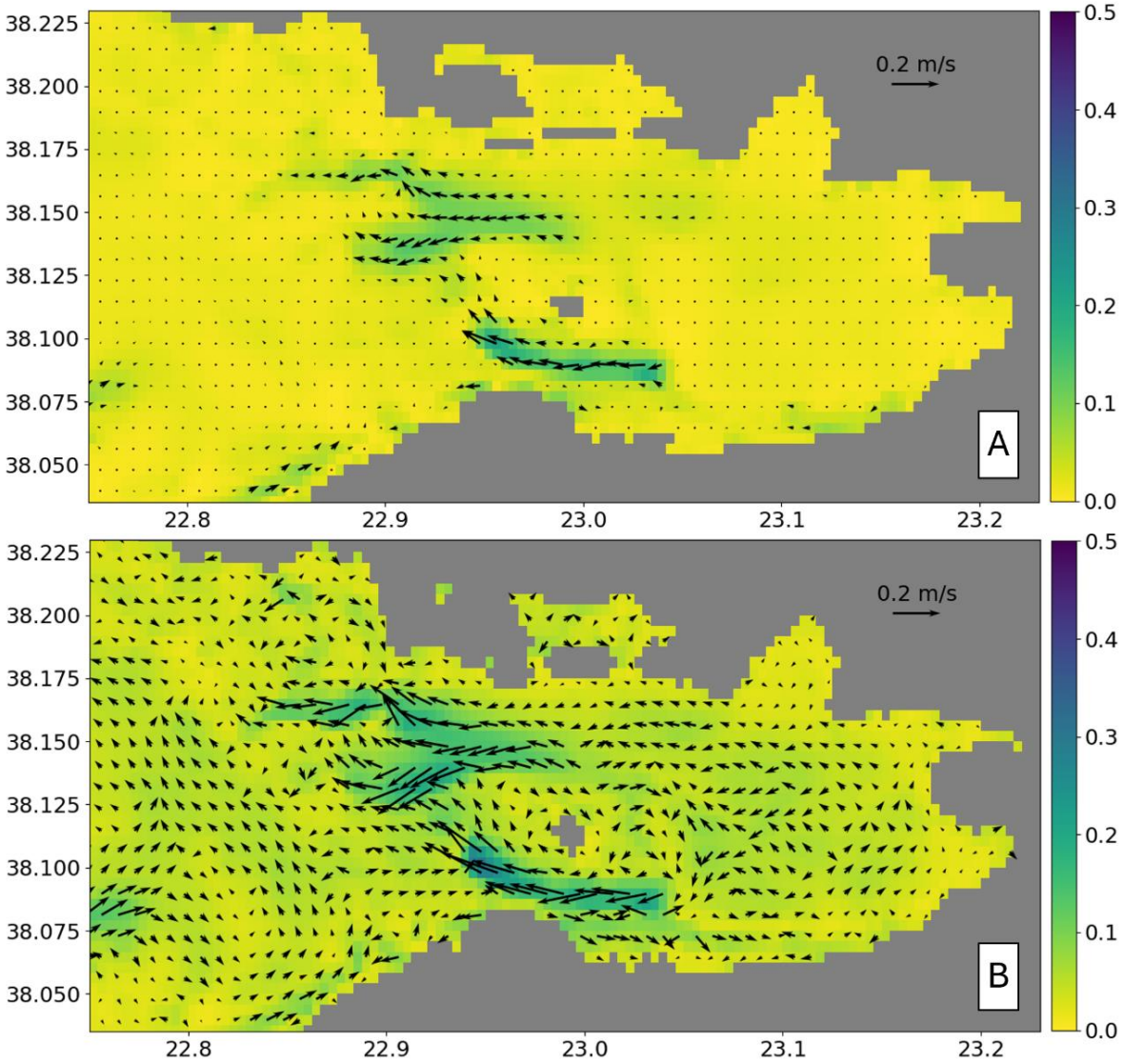

Figure 5.17: (A) Intensity (colors; m s^{-1}) and direction for the average bottom currents in the Alkyonides Gulf. (B) Intensity (m s^{-1}) and direction for the maximal bottom currents in the Alkyonides Gulf.

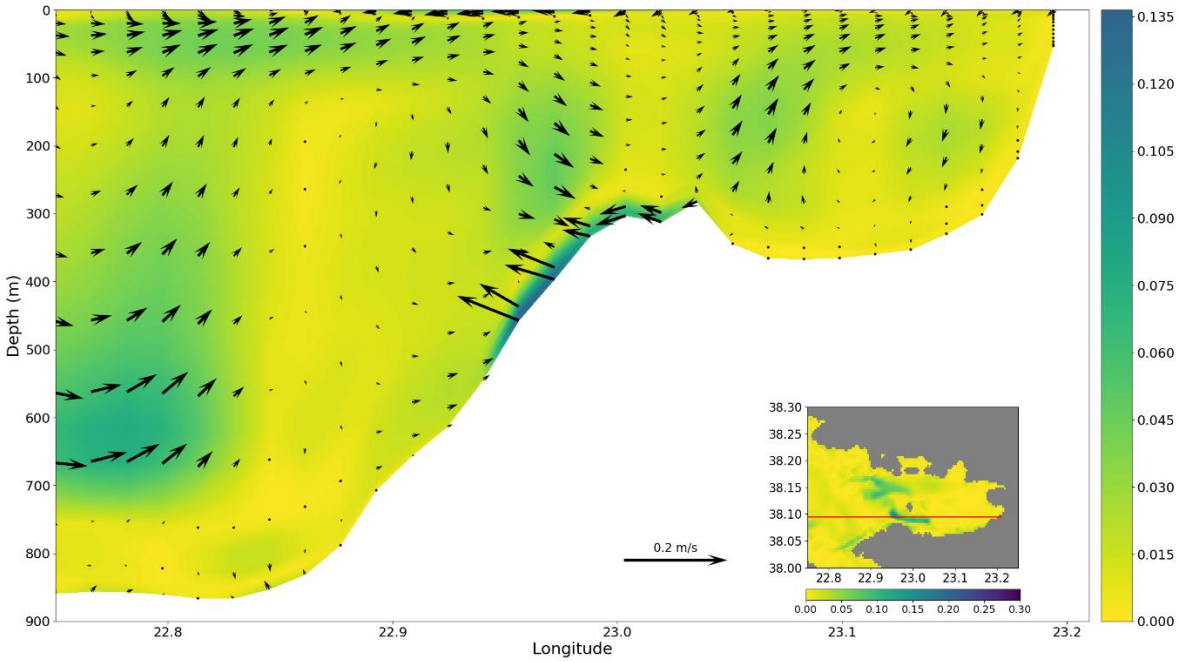

Figure 5.18: Section through the Alkyonides Gulf and the eastern part of the Corinth Gulf. Colors are for average current's intensity (m s^{-1}) and arrows for the current's average velocity and direction (m s^{-1}) along the section (red on the map).

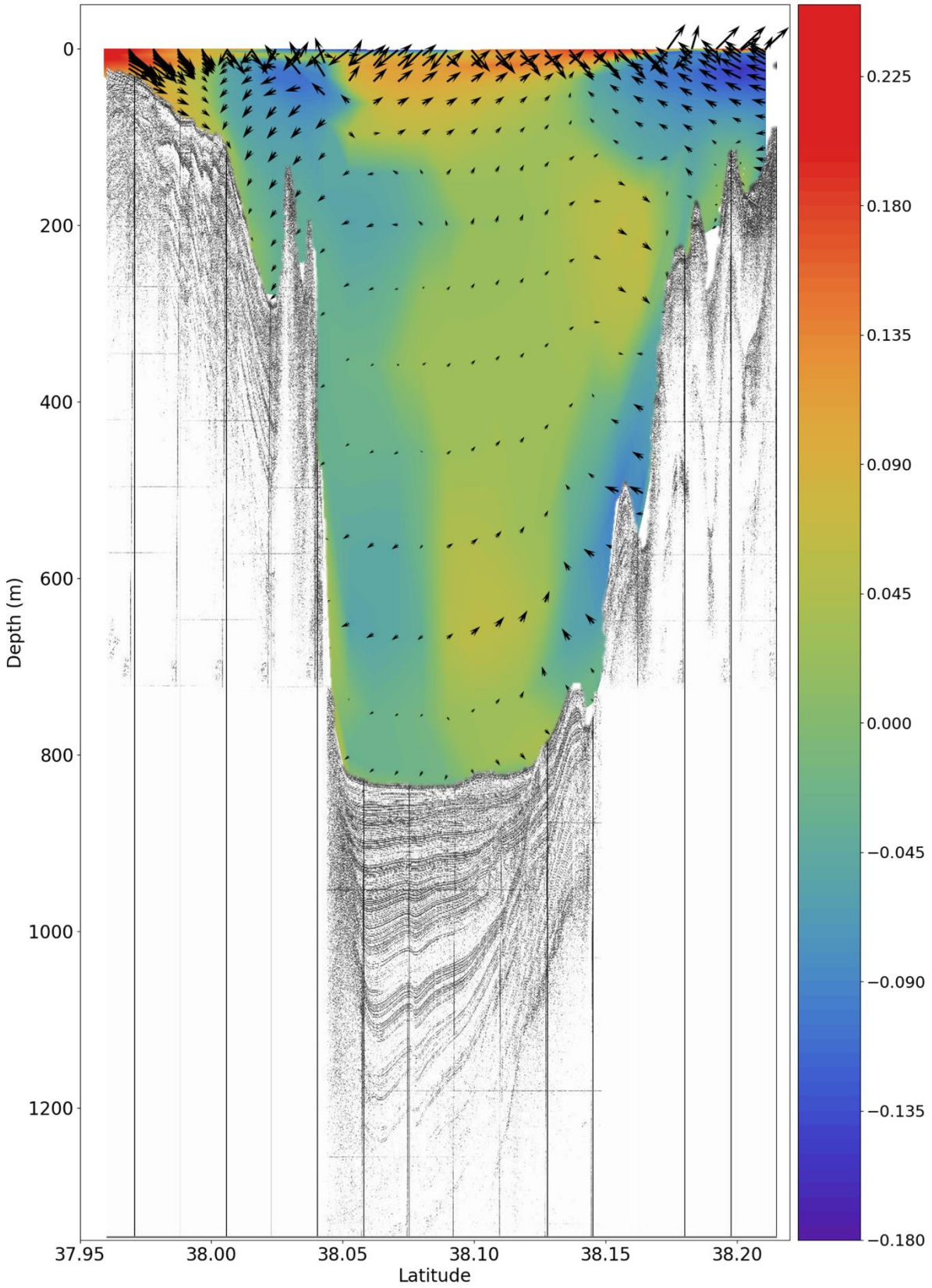

Figure 5.19: Cross-section through the boundary between the Deep Corinth Basin and the Alkyonides Gulf (95-96 on Figure 0.1). The seismic section is modified from Rubi (2018). The colors represent the maximal intensity of the currents, the arrows the direction when the currents are with maximal intensity according to the ROMS output for the month of May 2023. The eastward velocity (m s^{-1}) is represented (red = eastward, blue = westward).

5. Conclusions

This study demonstrates that present-day bottom currents exert a fundamental control on sedimentation and seabed morphology within the semi-enclosed Gulf of Corinth, challenging the traditional view that gravity-driven processes alone dominate sediment transfer in rift basins. Integrating hydrodynamic modelling, multibeam bathymetry, seismic profiling, and sediment core analyses reveals a dynamic interplay between tidal circulation, bottom shear stress, and sedimentary architectures throughout the basin.

The Rio–Antirio Strait emerges as the key hydrodynamic gateway connecting the Corinth and Patras Gulfs. Its shallow sill and constricted topography amplify tidal exchanges, producing alternating inflow and outflow jets that generate high bottom shear stress (up to 3 N m^{-2}). These currents erode the seabed and sculpt its characteristic morphologies while controlling where deposition can occur. Eastward of the sill, in Nafpaktos Bay and along the Drepano spit, gyre-induced turbulence and shear stress gradients govern the spatial distribution of contouritic drifts and erosional pools, confirming that bottom current activity is the dominant process shaping the strait's seafloor.

Downstream of the strait, the western Corinth depocenter records the sedimentary imprint of these near-bottom flows. Core and seismic data reveal four main facies associations—turbidites, contourites, MTD, and massive muds—reflecting a continuum between gravitational and current-controlled deposition. The occurrence of mottled sands, laminated muds, and bioturbated silt layers (C1–C3 facies) indicates persistent bottom current reworking and the development of hybrid contouritic/turbiditic systems. Hydrodynamic simulations confirm a bidirectional, tidally modulated regime that winnows fine material in high-energy zones while promoting sediment draping and drift formation in sheltered areas. Sedimentation rates of ~1 mm yr^{-1}, together with the stratigraphic correlations among cores, show that even weak, oscillatory currents can continuously reshape the depositional architecture.

Eastward, current intensity decreases across the central Corinth Basin, producing a quiescent depocenter characterized by fine-grained, undisturbed accumulation. In contrast, at the Alkyonides Gulf, local canyon systems accelerate near-bottom flows and induce strong erosion, while adjacent low-energy basins serve as traps for fine sediment. Together, these observations illustrate the tight coupling between bathymetry, hydrodynamics, and sedimentary processes in a tectonically active rift environment.

Overall, the Gulf of Corinth provides a clear example of how contouritic dynamics operate within a shallow, semi-enclosed basin. The Rio–Antirio Strait functions as the hydrodynamic engine of the system, driving a west–east gradient from high-energy erosional zones to low-energy depositional environments. The resulting sedimentary architecture reflects a mixed-energy regime in which bottom currents play an important role in shaping the modern seafloor and influencing long-term stratigraphic development.

Chapter 6: Paleogeographies of the Corinth Gulf: What Were the Possible Past Oceanographic Configurations?

This chapter focuses on the investigative component of the thesis, namely the implementation of oceanographic simulations over potential paleogeographic configurations of the Corinth Gulf. This step aims to address some of the unresolved questions concerning the Gulf's dynamics through geological time, as influenced by its paleo-configurations.

1. Introduction

Studying sediment deposition in a semi-enclosed, syn-rift marine basin can provide important insights into regional climate and sea-level changes (Gawthorpe & Leeder 2000; Sergiou *et al.* 2024). While erosion of the surrounding terrain supplies the primary sediments, the basin's hydrodynamics control their spatial distribution and accumulation. Understanding the interactions between sediments and bottom currents within a basin is therefore essential to reconstruct changes in sedimentation and basin evolution (Sergiou *et al.* 2024). Sedimentation in the Corinth Gulf reflects both climate-driven processes—such as river runoff, vegetation changes, and erosion rates—and tectonic processes associated with uplift and subsidence of the region (Bell *et al.* 2009; Watkins *et al.* 2019; Sergiou *et al.* 2024). Recent IODP drilling campaign (McNeill, Shillington, Carter, Everest, Le Ber, *et al.* 2019a; Shillington *et al.* 2019) and seismic reflection studies (Piper *et al.* 1980; Perissoratis *et al.* 2000; Bell *et al.* 2009; Nixon *et al.* 2016) indicate that the Corinth Gulf has alternated between marine and isolated environments over the last 700 ka (Sergiou *et al.* 2024).

Reconnections during highstands with the Mediterranean Sea occur through the Rio–Antirio Strait, which appears to have functioned in this role for at least the last ~400 ka (Gawthorpe *et al.* 2018; Sergiou *et al.* 2024). Present-day studies of Holocene sediments provide limited information regarding the hydrodynamics under past paleogeographic configurations of the Gulf (Poulos *et al.* 1996; Moretti *et al.* 2004; A. Beckers *et al.* 2016; Sergiou *et al.* 2024). Previous research has documented connections between the Corinth Gulf and the Aegean Sea via the Corinth Isthmus as well as an approach over the hydrodynamics they implied (Collier & Thompson 1991; de Gelder *et al.* 2019; Caterina *et al.* 2022). The Isthmus of Corinth, now intersected by the Corinth Canal, serves as a geological analogue of a tidal strait. Tidal strait structures preserved in the upper section of the Canal walls indicate past reconnections with the Aegean Sea (Caterina *et al.* 2022). A double opening has been proposed to account for tidal currents strong enough to generate asymmetrical herringbone structures (Tsimplis 1994; Caterina *et al.* 2022). Conversely, a single connection through the Corinth Isthmus, while the Rio–Antirio Strait

remained closed, likely represents an earlier stage in the Gulf's opening before the formation of a tidal strait (Collier 1990; Caterina *et al.* 2022).

The goal of this study is to simulate several paleoenvironmental scenarios to explore different paleogeographic configurations of the Corinth Gulf. This approach allows us to infer past hydrodynamics critical to sediment deposition. First, we simulate variations in sea level to assess the hydrodynamic influence of the Rio–Antirio Strait between lowstands and highstands over geological time (Gawthorpe *et al.* 2018; Sergiou *et al.* 2024). Second, we model the opening of the Corinth Isthmus to evaluate circulation dynamics when the Corinth Gulf was connected to the Aegean Sea (**Figure 6.1**).

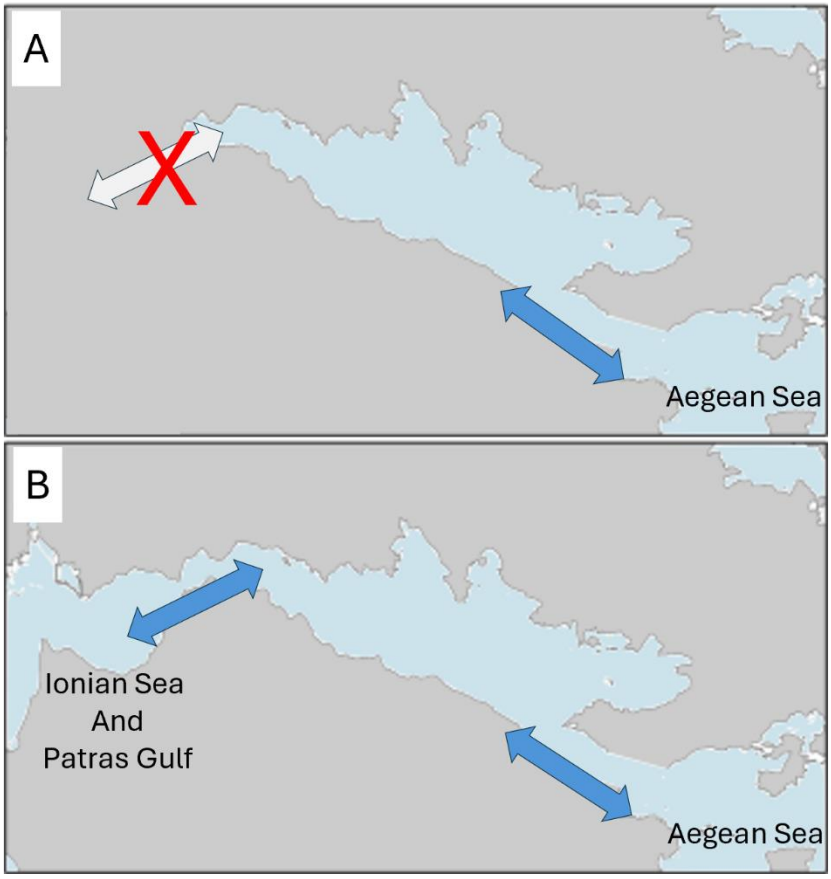

Figure 6.1: Schematic view of the configurations with the connection to the Aegean Sea. (A) Unique connection to the Aegean Sea. (B) Double opening scenario with connections through the Rio-Antirio Strait and the "Corinth" Strait.

2. Methodology

The paleogeographic reconstruction is based on the ROMS modeling of the Corinth Gulf detailed in Caterina *et al.* (2025). The approach to simulating paleogeographies involved varying the bathymetry, either globally across the domain or locally to create different configurations. By adding positive values to the seafloor depth, we simulated sea-level decreases that might have occurred during glacial periods and lowstands (Sergiou *et al.* 2024). The preparation of the first two simulations was straightforward, consisting of adding 10 m (first case) and 25 m (second case) to the entire bathymetry.

For the simulation representing the opening of the Aegean Sea, the bathymetry was modified around the Corinth Isthmus/Corinth Canal area. To achieve this, the ~450 m bathymetric dataset from GEBCO (GEBCO 2024) was used, and the Aegean Sea was not masked in this case. The modifications were as follows: (1) a polygon was defined around the Isthmus, with its dimensions determined by two factors: (a) the existing bathymetry and the delimitation provided by the surrounding mountain ranges, and (b) the tidal strait structures observed on the walls of the Corinth Canal (Caterina *et al*. 2022). (2) To create the opening and establish the Aegean connection, the bathymetry within this polygon was lowered by 140 m. This value ensured that the highest point of the Corinth Canal (~70–80 m) reached a maximum bathymetry of ~60–70 m, matching that of the present-day Rio–Antirio Strait. (3) Bathymetric smoothing was applied around the polygon to prevent sharp depth gradients. In addition to digital smoothing through interpolation, (4) manual corrections were performed on several pixels to maintain a topography consistent with plausible natural conditions.

In the case of a simple opening through the Corinth Isthmus, the Patras Gulf bathymetry up to the Rio sill (the minimum lateral extent of the Rio–Antirio Strait) was inverted to ensure the strait was properly closed. In the double-opening configuration, the Rio–Antirio Strait bathymetry remained unchanged from the dataset used in Caterina et al. (2025).

The initial forcings for May 2023 were retained for these simulations, as the experiment was based on geological evidence without available paleo-oceanographic models to constrain the forcings. This choice allowed the simulations to reproduce the May 2023 conditions, with only the bathymetry altered to represent the paleogeographic configurations.

Once the bathymetry files were finalized, each ROMS grid was generated using the May 2023 initial forcings. For the “sea-level variation” simulations, no modifications were made to the boundaries. Changes were introduced only for the simulations involving a connection to the Aegean Sea. In the ROMS configuration file, the southern and eastern boundaries were set as open under “RadNud” conditions for 3D velocity, temperature, and salinity (Shchepetkin & McWilliams 2005; Barth 2025). "RadNud" refers to radiation boundary condition with nudging (Shchepetkin & McWilliams 2005). For the simple opening case only, the western boundary was set as closed.

3. Results

3.1. “Sea Level” Changes

The variations applied to simulate sea-level changes do not affect the general surface circulation in the Gulf of Corinth (**Figure 6.2**). This is expected, as a 10 m change in the central basin represents only about 1% of the total depth (~2.5% for a 25 m change). The

surface gyres remain present, with similar intensity and positions to those observed today (Caterina & Hubert-Ferrari 2025; Caterina *et al.* 2025).

In the shallow areas (Patras Gulf, Rio–Antirio Strait, and the western part of Western Corinth), the effects are more pronounced. Increasing the bathymetry (i.e., lowering sea level) results in a narrower strait and affects the width of the Patras Gulf's connection with the Ionian Sea. One consequence of this narrowing is a reduction in the intensity of the surface gyre in the Patras Gulf (**Figure 6.2**). Another effect of the constriction is the increase in current velocity near the Mornos area and along the slope toward the central basin. On the opposite side of the Gulf, currents intensify around Zoodochos Island in the Alkyonides when the bathymetry is increased. This occurs due to the narrowing of nearby channels, particularly the one located south of the island. Overall, regarding surface circulation, only the geometry (position and size) of the main hydrodynamic features is affected, while their intensity remains comparable to the standard configuration.

On the seafloor, the dynamics appear stable and comparable between the modified and standard simulations (**Figure 6.3**). The only noticeable changes occur in the Rio–Antirio Strait region and at the entrances of both the Patras and Corinth Gulfs from the strait (**Figure 6.4**).

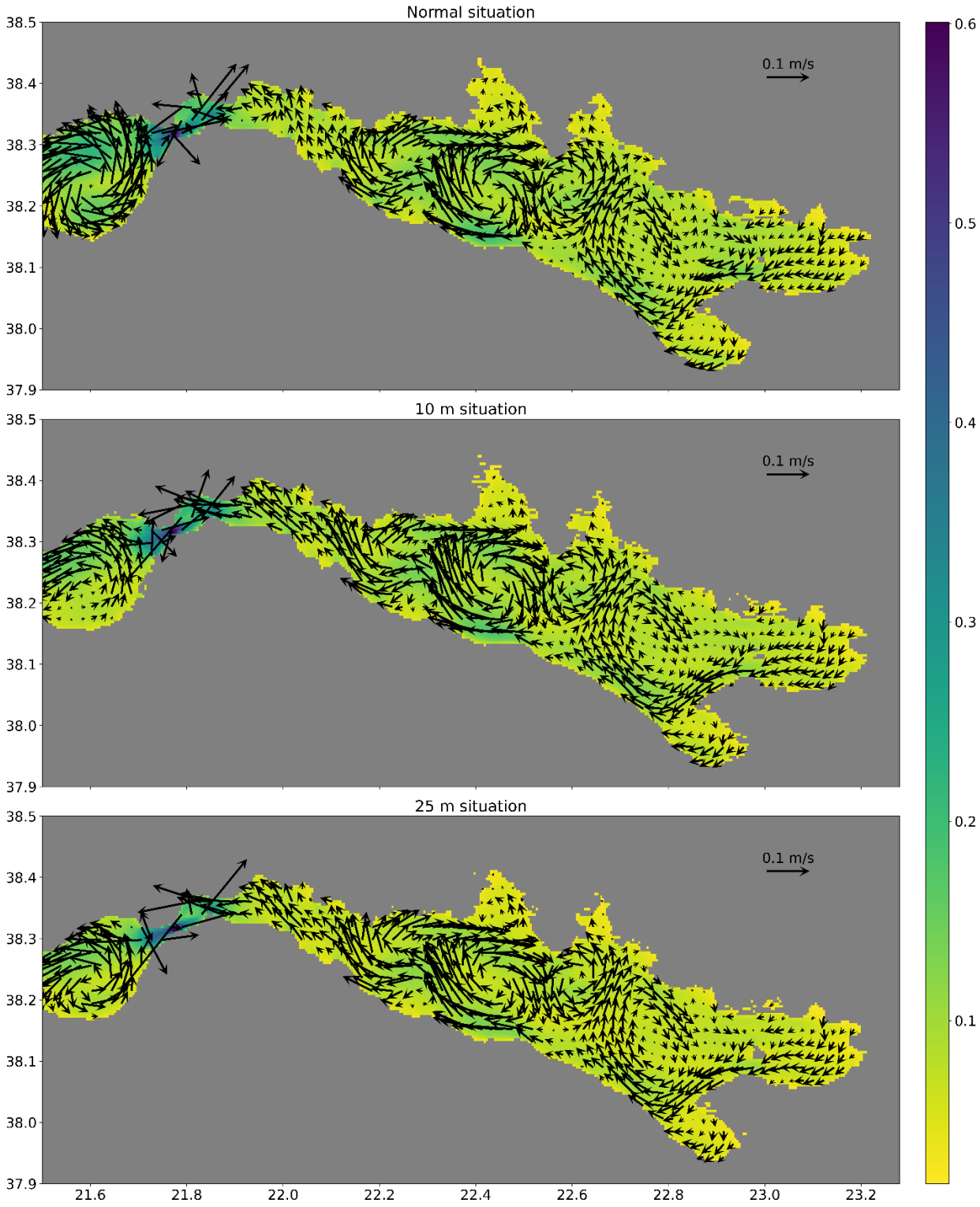

Figure 6.2: Average velocity maps at the surface for the actual situation, the 10 m increased bathymetry and the 25 m increased bathymetry. The colors are for the average intensity of the velocity and the arrows for the average directions.

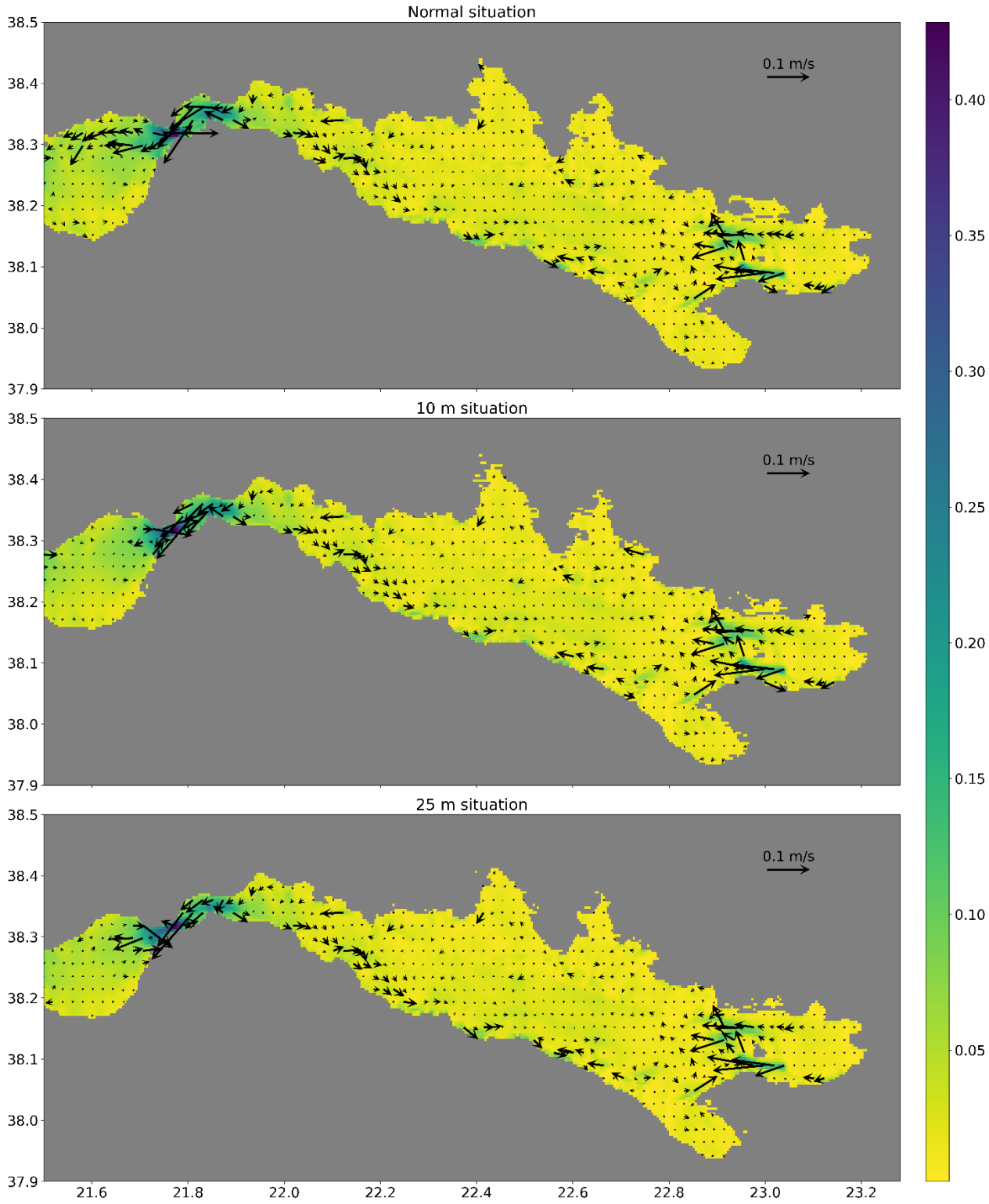

Figure 6.3: Average velocity maps at the bottom for the actual situation, the 10 m increased bathymetry and the 25 m increased bathymetry. The colors are for the average intensity of the velocity and the arrows for the average directions

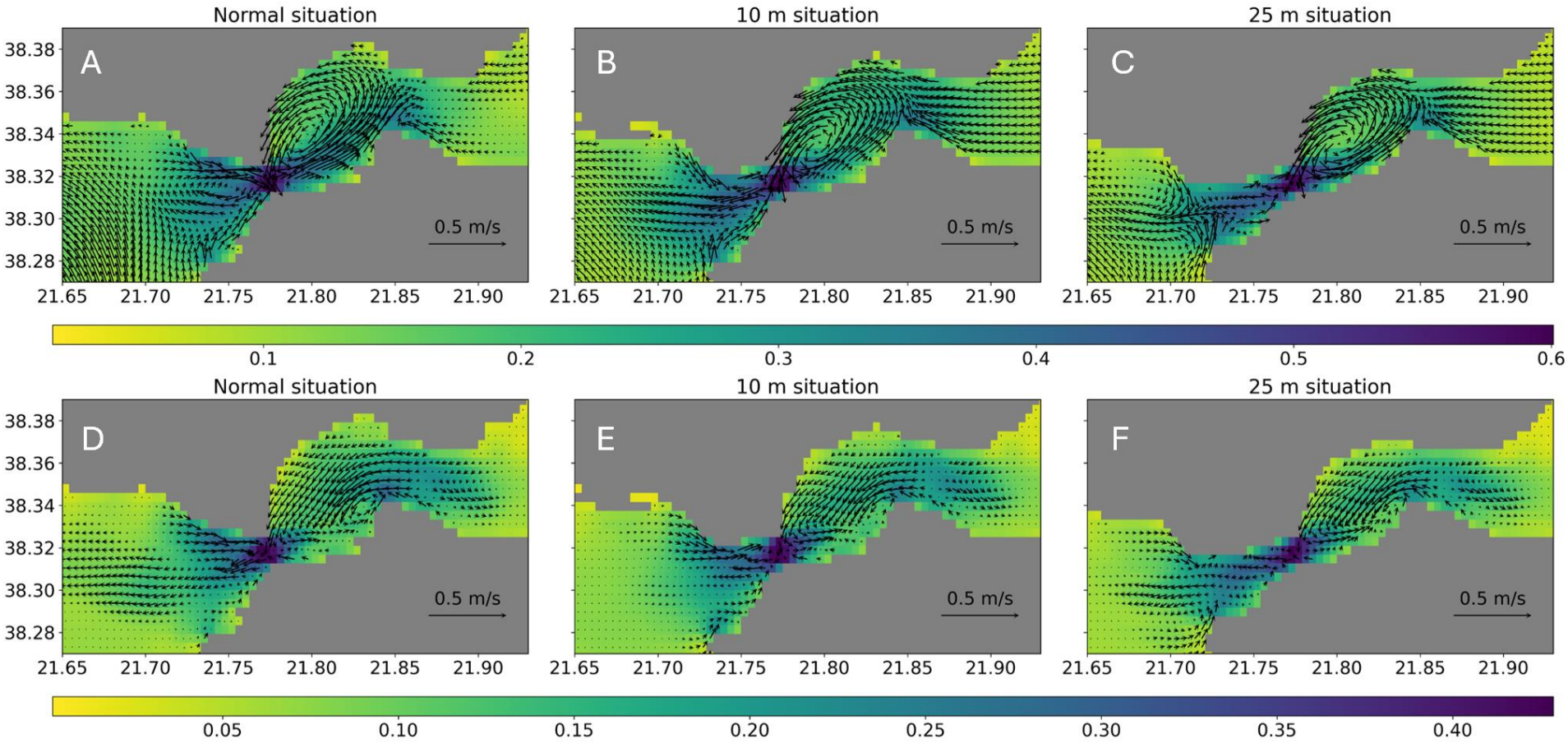

Figure 6.4: Zoom on the strait area of the average velocity maps, at the surface (A, B, C) and the bottom (D, E, F) for the actual situation (A, D), the 10 m increased bathymetry (B, E) and the 25 m increased bathymetry (C, F). The colors are for the average intensity of the velocity and the arrows for the average directions

Since the Rio–Antirio Strait is the narrowest and shallowest part of the Corinth Gulf, increasing the bathymetry (i.e., making it shallower) affects this area more significantly than the rest of the basin (a 10 m increase corresponds to ~15% shallowing, and a 25 m increase to ~28%). In addition to reducing the available water depth, the strait's width also becomes narrower. These modifications impact both surface and bottom circulation (**Figure 6.4**).

At the surface, the overall circulation patterns remain similar. The gyre in the Patras Gulf persists, but surface waters tend to move eastward (away from the strait) earlier and more rapidly on average in both sea-level change experiments. In the 10 m scenario, the narrowing of the strait entrance from the Patras Gulf remains sufficient to allow surface waters to flow toward Corinth along the northern and southern coasts (**Figure 6.4A, B**). In the 25 m scenario, however, the strait becomes too constricted, and the inflow toward Corinth diminishes considerably in intensity (**Figure 6.4**). Consequently, the main dynamics shift westward, with surface currents moving westward and extending farther into the Patras Gulf. In the eastern part of the strait, the Nafpaktos Gyre remains present regardless of water depth. The only noticeable change occurs in the average flow direction in front of the Mornos Delta, where waters tend to move westward more frequently.

At the bottom of the strait, sea-level lowering leads to the gradual disappearance of the near-seafloor gyre in Nafpaktos Bay (**Figure 6.4D, E, F**). Nevertheless, shear stress between the southern and northern water flows persists. The most significant changes occur along the southern coast, while the northern coast shows no notable variation in current intensity or direction, even in the 25 m case. In the Patras Gulf, bottom currents exhibit variations in both direction and intensity depending on sea level. In the 10 m scenario, there is a slight decrease in current intensity, and the mean flow direction becomes nearly null, indicating more oppositely directed currents (**Figure 6.4D, E**). In the 25 m scenario, stronger bottom currents extend farther into the Patras Gulf than in the standard configuration. Overall, the bottom-flow pattern near the Patras Gulf entrance resembles the surface circulation, though with reduced intensity.

Across the simulations, the main effect of sea-level lowering is an overall westward extension of the high-velocity field. This extension is most pronounced in the western part of the strait's central section, reaching progressively farther into the Patras Gulf entrance as the strait narrows. When comparing the maximum velocity differences between the 25 m and standard configurations (**Figure 6.5**), both the Patras entrance and the eastern part of the strait's center appear highly sensitive to sea-level lowering. The highest velocity intensities occur near the southern coast of the strait's western section. Conversely, along the northern coast of this same area, sea-level variations do not significantly affect the maximum velocity magnitude. In the Patras Gulf, sea-level lowering increases the maximum velocity at the strait's exit (**Figure 6.5**).

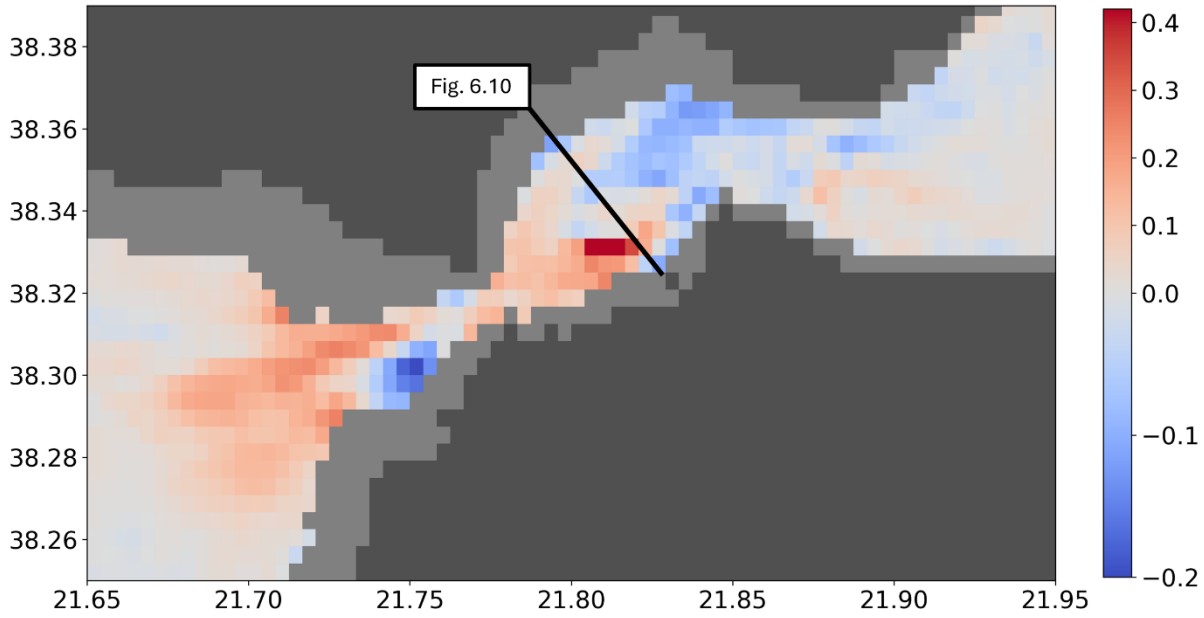

Figure 6.5: Map of the difference between maximal velocities in the 25 m situation and the maximal velocities in the Standard situation. The present-day strait borders are in dark gray, and the 25 m strait borders are in gray. The line represents the section for Figure 6.10.

3.2. Opening the Aegean Sea

3.2.1. Unique connection

By closing the Rio–Antirio Strait and opening the Corinth Isthmus, the only connection between the Corinth Gulf and the Mediterranean Sea occurs through the Aegean Sea. This connection is established via the "Corinth Strait," which is approximately 6 km wide at its narrowest point.

The average surface dynamics are characterized mainly by gulf-wide anticyclonic gyres (**Figure 6.6**). Compared with the previously established circulation patterns (**Figure 3.11**), the central Corinth gyres remain largely unchanged. In contrast, the surface current within the "Strait and Entrance Area" now flows westward across the entire width of the Gulf. These circulation patterns can be attributed to predominantly westward-directed winds (**Figure 3.8**). Even under this modified configuration, the Alkyonides Gulf retains its anticyclonic circulation, as previously described in **Chapter 4**. Within the Corinth Strait itself, the mean current is directed outward, flowing from the Gulf toward the Aegean Sea (**Figure 6.6**).

Near the seafloor, when the Isthmus is open, strong mean currents are observed only in the Alkyonides canyons (**Figure 6.6**). The western Corinth area appears largely quiescent on average, although some downward flow is observed within the canyon. The central part of the Gulf exhibits some of the strongest bottom currents within the basin. In the newly formed strait created by lowering the Corinth Isthmus bathymetry, the currents appear weaker than those in the Rio–Antirio Strait. This difference can be attributed to (1) the

Corinth Strait being approximately three times wider than the present-day Rio–Antirio Strait, and/or (2) the relatively weak tidal influence from the Aegean Sea.

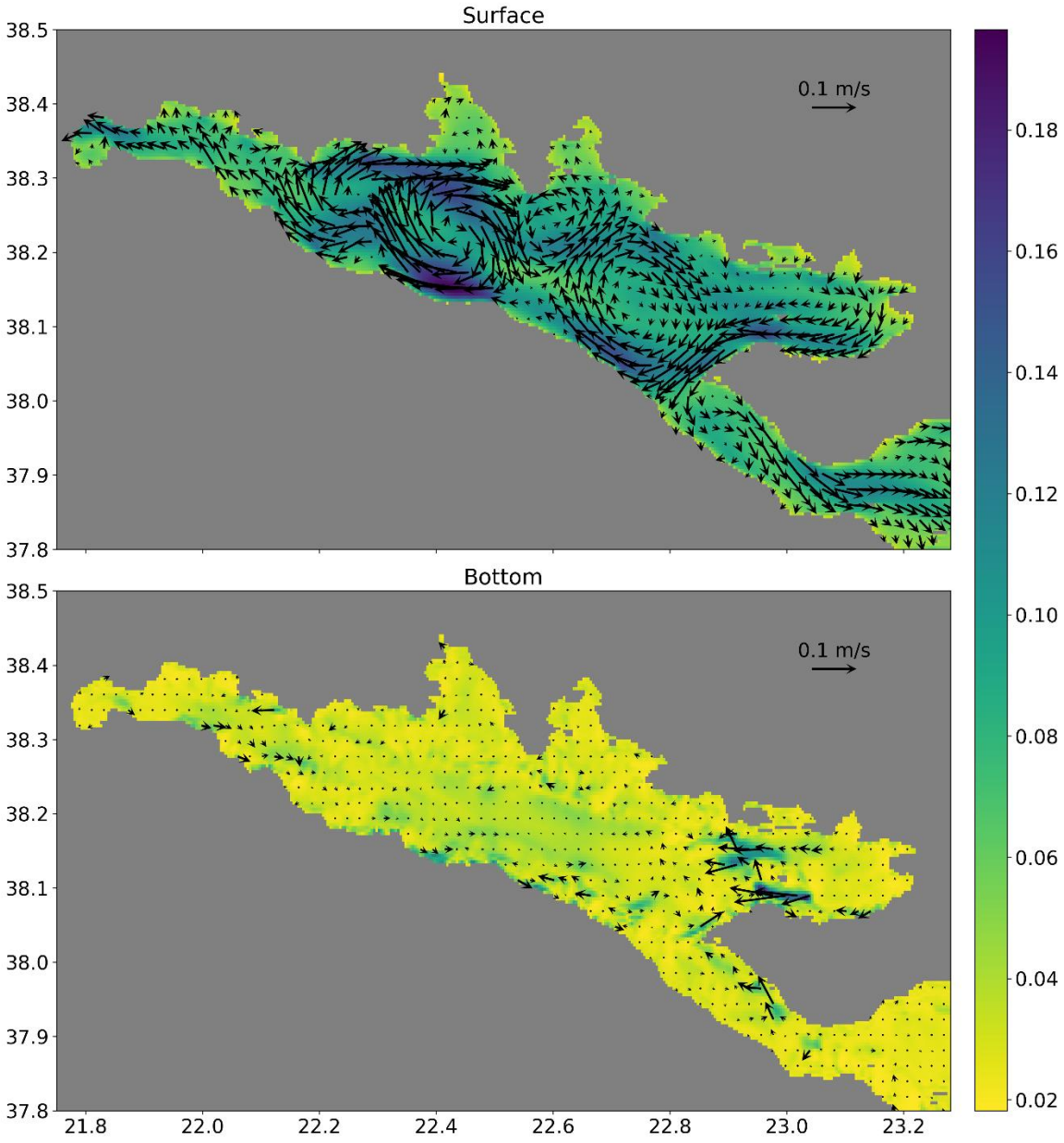

Figure 6.6: Average surface (top) and bottom (bottom) currents for the "month of May 2023" in the case where the Aegean Sea is connected to the Corinth Gulf via the Corinth Isthmus. The colors are for the intensity (m s^{-1}) and the arrows for the direction.

When considering the Aegean Sea connection through the Corinth Strait configuration, the cross-sections of the strait exhibit very low-velocity currents, with no clearly identifiable tidal-induced flow directions (**Figure 6.7**). Throughout most of the water column, current velocities remain close to 0 m s^{-1}, reaching up to approximately 0.15 m s^{-1} only near the surface or in localized areas close to the seafloor.

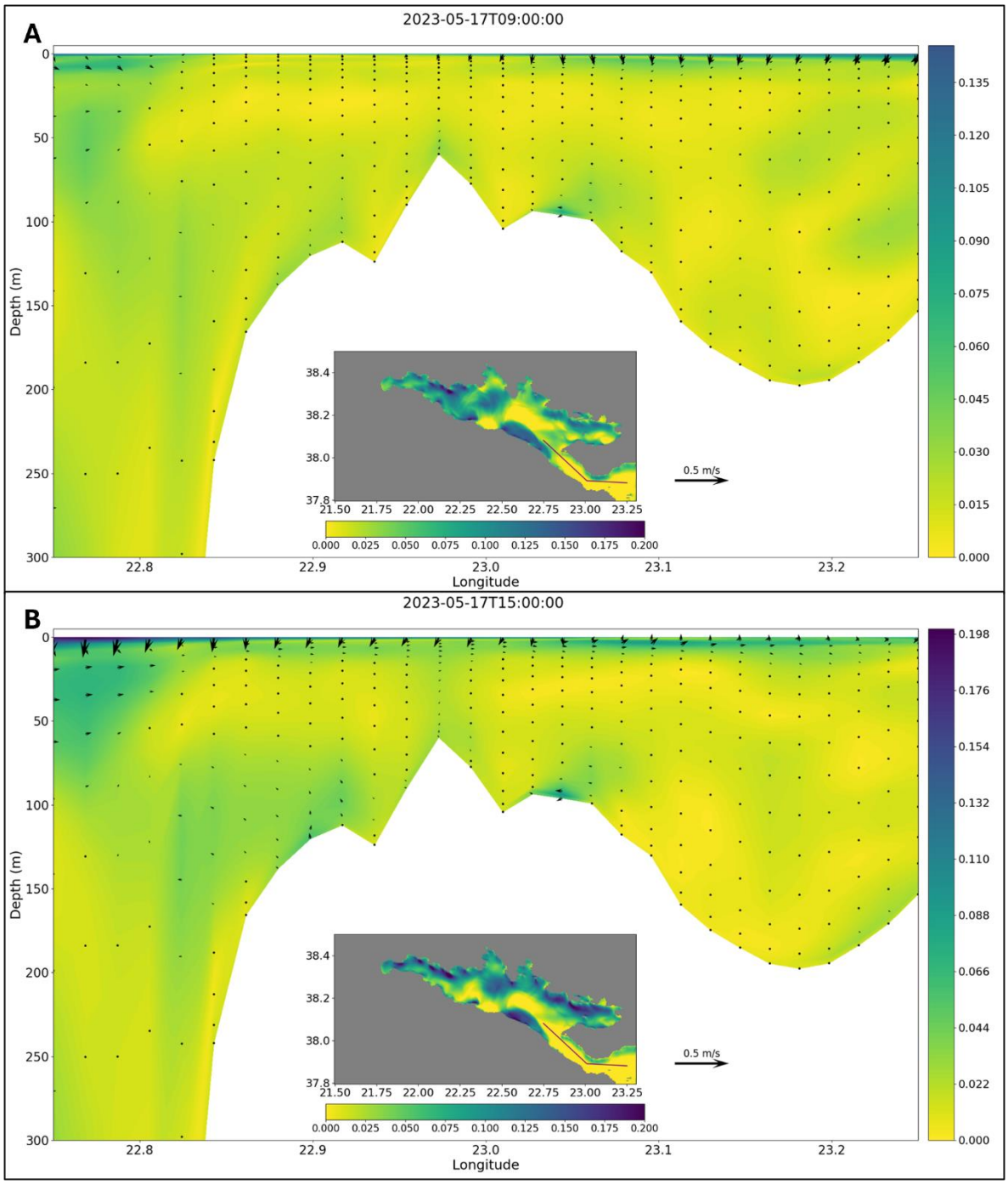

Figure 6.7: Section of the modelled Corinth Strait displaying the velocity's intensity (u and v combined, m s^{-1}) and the current direction (m s^{-1}, arrows) under two different tidal phases. (A) Section during the low tide and (B) Section during the high tide according to SSH and tidal gauge data.

3.2.2. Double opening

Having a double connection between the Corinth Gulf and the Mediterranean Sea results in surface circulation patterns that remain largely similar to the present-day situation (**Figure 6.8**, **Figure 4.5**). On average, at the surface, the current through the Corinth Strait flows into the Gulf rather than toward the Aegean Sea, as observed in the single-connection configuration (**Figure 6.6**). The presence of the Corinth Strait modifies the geometry and intensity of the anticyclonic gyre in front of Antikyra Bay, while also reducing

the size of the adjacent cyclonic gyre closer to the bay. The average surface dynamics near the Rio–Antirio Strait remain unchanged, supporting the hypothesis that the Rio–Antirio Strait exerts the primary control on the overall hydrodynamics of the Corinth Gulf.

At the seafloor, the Rio–Antirio Strait continues to exhibit the strongest mean currents, followed by the Alkyonides canyons and, subsequently, the Corinth Strait (**Figure 6.8**). The directions of the bottom currents are like those in the present configuration. In the Corinth Strait, current vectors approach 0 m s^{-1} in velocity, while peak intensities reach up to ~0.2 m s^{-1}. This suggests that the currents periodically shift direction depending on the tidal phase, as observed elsewhere in the Corinth Gulf. This alternating behavior is further illustrated by the cross-sections through the Corinth Strait (**Figure 6.9**).

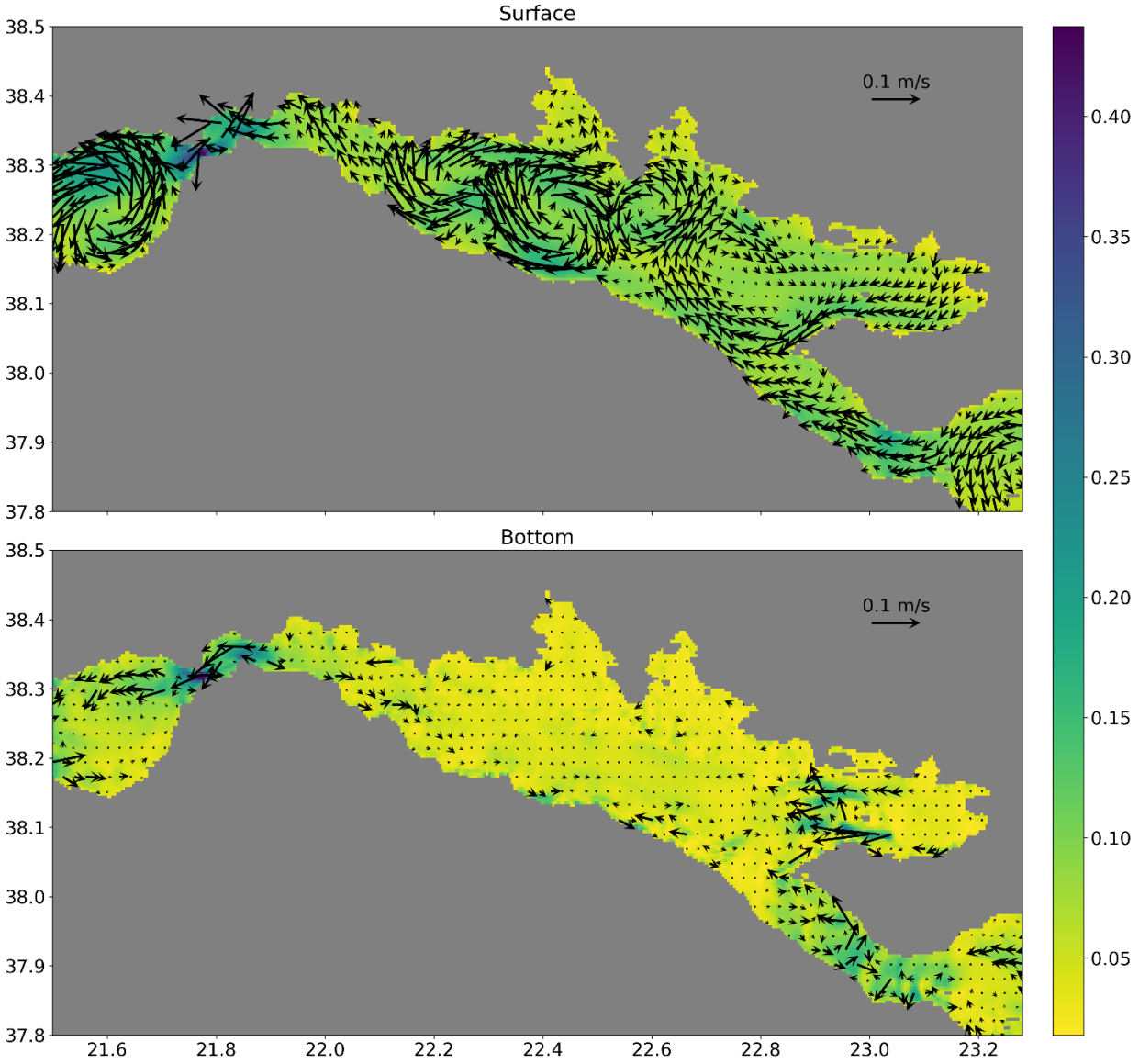

Figure 6.8: Average surface (top) and bottom (bottom) currents for the "month of May 2023" in the case where the Aegean Sea is connected to the Corinth Gulf via the Corinth Isthmus and the Rio-Antirio strait still open (double opening). The colors are for the intensity (m s^{-1}) and the arrows for the direction

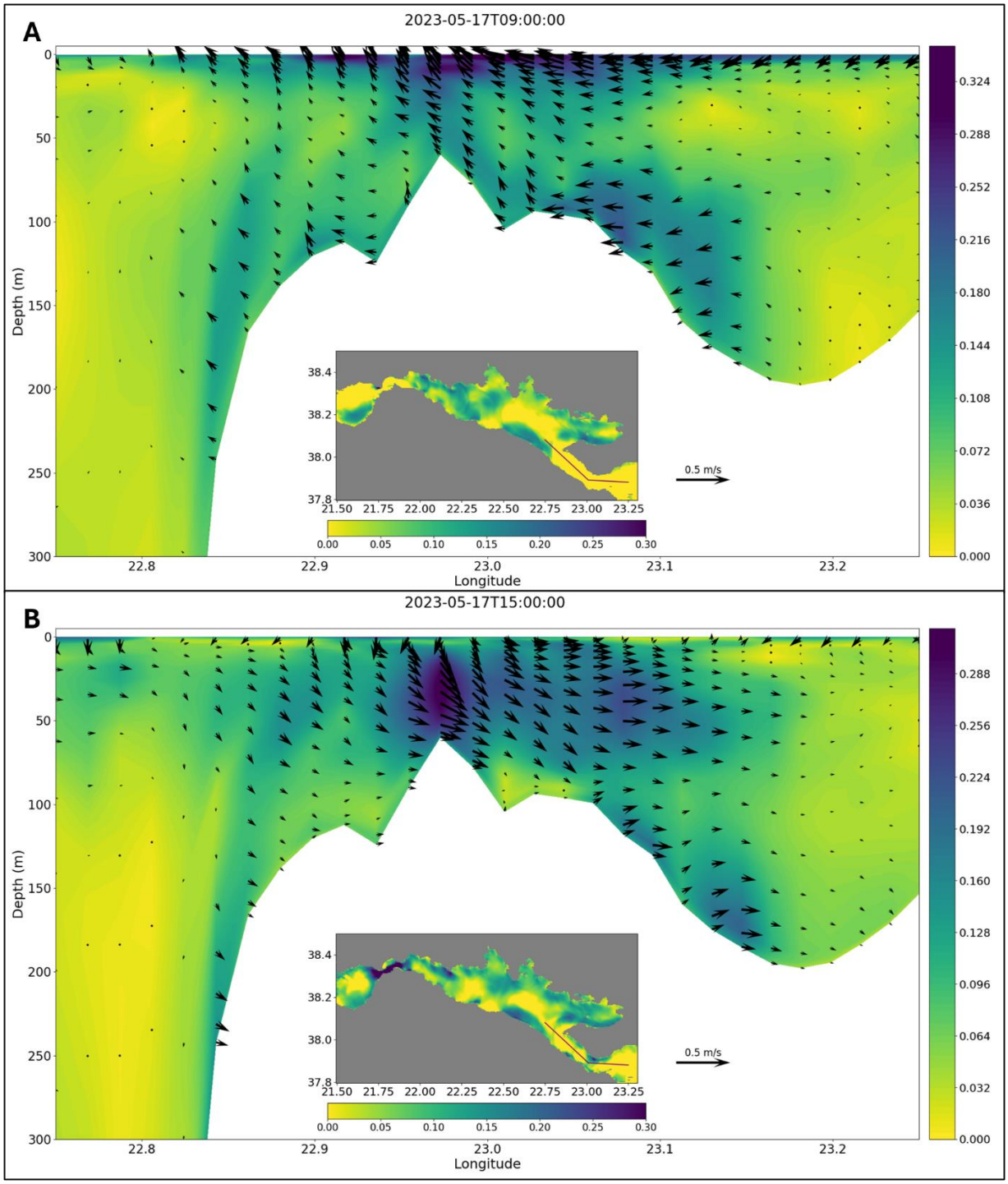

Figure 6.9: Section of the modelled Corinth Strait (in the double connection settings) displaying velocity's intensity (u and v combined, m s^{-1}) and the current direction (m s^{-1}, arrows) under two different tidal phases. (A) Section during the low tide and (B) Section during the high tide according to SSH and tidal gauge data.

In the cross-sections, under the influence of the double opening, tidal currents appear to dominate the dynamics within the Corinth Strait, similar to those in the Rio–Antirio Strait. The current directions alternate according to the tidal phase. However, the tidal flow in the Corinth Strait occurs in the opposite direction to that of the Rio–Antirio Strait. During

low tide in the Rio–Antirio Strait, currents in the Corinth Strait flow toward the Corinth Gulf rather than toward the open basin. Conversely, during high tide, currents flow toward the Aegean Sea instead of into the enclosed basin (**Figure 6.9**).

This behavior may result either from the ~1-hour time lag between high tides in the two straits (**Figure 6.10**) or from the absence of tidal forcing specific to a potential Corinth Strait in the present-day oceanographic inputs used for the ROMS simulations. The high-tide timing difference is explained by the distance separating the two straits and was previously documented through the position of amphidromic points in the Ionian and Aegean Seas (Tsimplis 1994). Nevertheless, when disregarding the tidal phase, the currents exhibit a clear tidal asymmetry: the flow toward the Corinth Gulf is slower than the flow toward the Aegean Sea (**Figure 6.9**).

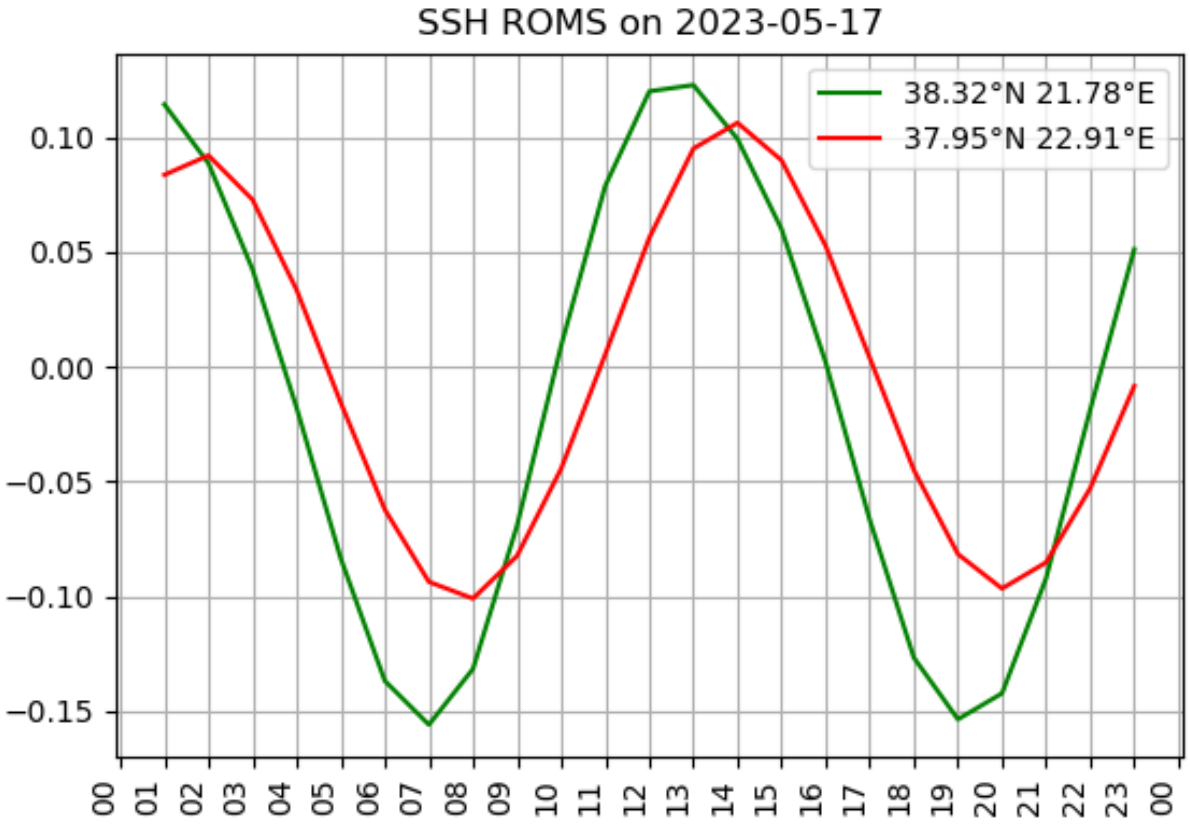

Figure 6.10: SSH from ROMS in the double opening simulation. The curves are from the points located in the center of each strait (green = Rio-Antirio, red = Corinth). The "lag" between the high/low tides is around 1h.

4. Discussion

4.1. "Sea Level" Changes

Increasing the bathymetry to simulate a 25 m sea-level drop has significant effects on the circulation of the Corinth Gulf. This configuration further isolates the Gulf, leaving only a ~40 m deep strait connecting it to the Ionian Sea through the very shallow Patras Basin. Under such conditions, the average surface flow within the strait and in front of the

Mornos area is directed toward the Ionian Sea (**Figure 6.2, Figure 6.4**). At the seafloor, the flow is oriented toward the Corinth Gulf, particularly within Western Corinth and along the canyon (**Figure 6.3, Figure 6.4**). This configuration could resemble conditions during the MIS 5a–MIS 4 transition, which led to the deposition of aragonite in the deep Corinth Basin (Sergiou *et al.* 2024).

Also associated with the 25 m configuration, the high-velocity bottom currents exiting the strait into the Patras Gulf (between ~21.70°E and 21.75°E; **Figure 6.4**, **Figure 6.5**) may have contributed to the formation of the giant depression observed in this area—the southwestern mini-basin shown in **Figure 2.6** (Rubi *et al.* 2022). The dynamics there, characterized by a westward central current flanked by eastward flows along the northern and southern coasts (**Figure 6.4E**), support the hypothesis of erosion occurring away from the strait's center. Such erosion, resulting from turbulent and quasi-circular motion, cannot be explained by present-day currents, but aligns well with the paleogeographic conditions of the 25 m configuration

Still related to these current dynamics, the currents along the northern coast near the Patras end of the Rio–Antirio Strait are stronger than those along the southern coast (**Figure** 6.4**C, D**). Since this pattern also occurs in both the 10 m and present-day configurations, it may explain the existence of the moat observed in the western part of the strait (**Figure 2.6**). Assuming the 10 m configuration represents an intermediate stage between the 25 m and present-day situations, this would also explain why the moat remains eroded, since the northern current intensity did not significantly decrease between configurations.

On the opposite side of the strait, the southern coast of Nafpaktos Bay is consistently swept by stronger bottom currents than the northern coast, regardless of the paleogeographic configuration (10 m or 25 m; **Figure 6.5**). This asymmetry in current intensity may therefore explain the presence of the two sediment drifts in the Nafpaktos area (A. Beckers *et al.* 2016), with the southern drift being younger than the northern one. Considering that the 25 m configuration likely corresponds to a "reconnection phase" with the Ionian Sea, the northern drift could have formed under lower current velocities that allowed sediment deposition. Meanwhile, intense bottom currents along the southern coast would have inhibited deposition there. Sedimentation could occur only once the water column deepened, and bottom velocities decreased. The presence of a giant depression in front of the Drepano spit within Nafpaktos Bay (**Figure 2.7**) further supports the occurrence of strong shear stress and/or intense gyre activity during these paleo-conditions.

In addition to the giant depression and the marginal sediment drifts, the buried channel identified in the central Nafpaktos area (**Figure 6.11**) also attests to past episodes of strong bottom currents (A. Beckers *et al.* 2016). Cross-sectional analysis shows that the location of this buried channel corresponds to areas of greatest difference between the

maximal currents in the 25 m configuration and those in the present-day situation (**Figure 6.5**). The presence of high-velocity bottom currents in the past likely caused substantial erosion of the seafloor, enabling channel formation. As local current velocities decreased between the 25 m and modern configurations, the channel was progressively infilled with sediments, eventually becoming buried.

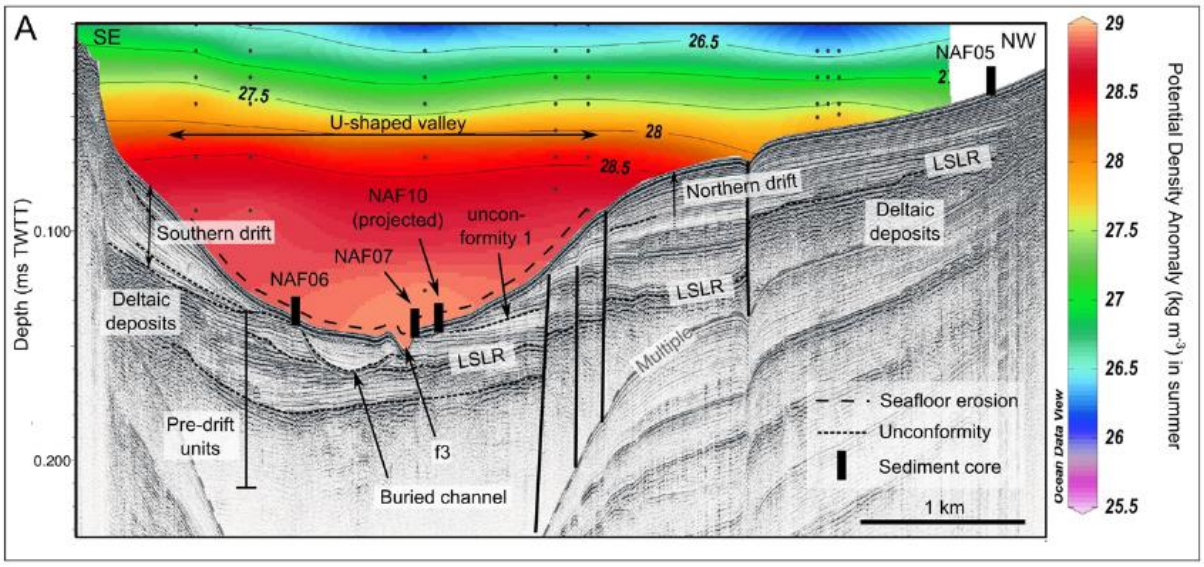

Figure 6.11: Sparker seismic profile showing depositional reliefs interpreted as sediment drifts in the Nafpaktos Bay. LSLR: last sea level rise. Colors represent the potential density anomaly in summer inferred from 6 temperature and salinity profiles (black dots) from the World Ocean Database (Boyer *et al.* 2018). Location of the profile in Figure 6.4. Modified from Beckers et al. (2016).

4.2. Aegean Connections

The case of a single connection through the Corinth Isthmus, via the "Corinth Strait," appears to represent a lacustrine-like setting, where the circulation is primarily wind-driven rather than tide-driven, as is currently the case. The circulation within the Alkyonides Basin remains like the one observed today, suggesting a time-consistent hydrodynamic regime in this sub-basin. The presence of an anticyclonic surface circulation (**Figure 6.6**) would promote sediment export toward the southeastern corner of the basin, leading to enhanced deposition in this area (Collier *et al.* 2000).

The main limitation of a configuration where the Corinth Gulf is connected solely to the Aegean Sea is the absence of strong tidal currents within the Corinth Strait (**Figure 6.7**). Under such conditions, the Corinth Strait could not be classified as a tidal strait. This type of connection likely corresponds to transgressive episodes, when the environment transitions from lacustrine to marine conditions. Such a shift in paleoenvironment is recorded in the geological sequence of the Corinth Canal (Sequence 1 in Figure 2.11; Caterina *et al.* 2022).

Conversely, a double opening of the Corinth Gulf would generate significantly stronger tidal currents within the Corinth Strait. These currents could reach velocities of up to 0.6 m s^{-1} (with an average of ~0.2 m s^{-1}; **Figure 6.8**) sufficient to produce tidal-stratified

sedimentary structures (Stow *et al.* 2009; Longhitano 2013). Moreover, the tidal asymmetry observed in the Corinth Strait (**Figure 6.9**) aligns well with the geological features identified in the tidal dunes (**Figure 2.12**; Caterina *et al.* 2022). The first-order herringbone cross-stratification observed in the Corinth Canal corresponds closely to the intensity and direction of the modeled tidal currents in the double-opening scenario. The larger, lower sets oriented towards the northwest are consistent with the stronger currents flowing in that direction. Faster near-bottom currents would have favored the deposition of larger and flatter foresets. During the opposite tidal phase, weaker near-bottom currents directed toward the southeast (**Figure 6.9**) would have produced smaller sets preserved on top of the herringbone cross-bedding (Caterina *et al.* 2022).

While the connection with the Aegean Sea could have existed as a single waterway at the Corinth Isthmus, the formation of the tidal dune structures observed in the Corinth Canal requires a double opening. In such a configuration, the timing of the connections may have varied, but it is more plausible that the Aegean connection predated the Rio–Antirio connection. According to Caterina et al. (2022), the Aegean connection was established during MIS 9c, whereas the Rio–Antirio Strait connected the Corinth Gulf to the Ionian Sea only since MIS 7e and MIS 5e. Earlier episodes of double connection may have occurred, as the tidal strait deposits are dated to approximately 300 ka (MIS 9–MIS 8; Collier 1990; Caterina *et al.* 2022). In any case, during the early stages of the Corinth Rift—prior to the uplift of the Isthmus—the first marine connection was most likely with the Aegean Sea, followed later by the opening to the Ionian Sea.

5. Conclusions

Modeling paleo-conditions, including both paleogeography and paleo-oceanography, relies on hypotheses that are difficult to verify. In our study, the proposed paleogeographies for the Corinth Gulf were consistent with both its morphological features and the observed sedimentary structures. By increasing the bathymetry, we were able to simulate sea-level decreases that may have occurred during past climatic changes in the region. Despite using present-day oceanographic conditions as forcings, the evidence of stronger bottom currents in the paleo-configurations corresponds well with the erosional features observed near the Rio–Antirio Strait.

Creating a hypothetical waterway through the Corinth Isthmus, based on geological and geomorphological evidence, allowed us to test the Aegean Sea connection hypothesis. A single connection through the Corinth Strait does not generate significant tidal currents and corresponds to a lake-like system intermittently reconnected to the sea. In contrast, tidal currents consistent with the tidal-stratified structures observed in the Corinth Canal can only occur when the Corinth Gulf is first connected to the Aegean Sea, followed later by a connection through the Rio–Antirio Strait.

Chapter 7: General Discussion and Conclusions

1. Rio-Antirio: A Tidal Strait

Across the range of analyses conducted in this thesis, it is evident that the Rio-Antirio Strait is the key factor controlling both the hydrodynamics and sedimentation of the entire Corinth Gulf. Due to its shallower bathymetry compared to the deep Corinth basin, it acts as the bathymetric threshold, or bathymetric sill, controlling the circulation in the area. Its classification as a tidal strait is unequivocal when considering its hydrodynamic behavior, though less apparent from the sedimentary record (Longhitano & Chiarella 2020; Rubi *et al.* 2022). The strong tidal dynamics within the strait influence the circulation of the Corinth Gulf well beyond its immediate boundaries. Numerical modeling further supports this interpretation: when the tidal component is removed, the strait no longer exhibits the same dynamic impact observed under real conditions (Caterina *et al.* 2025).

The Rio-Antirio Strait, as part of the Corinth Gulf system—and therefore the Mediterranean Sea—exists within a microtidal regime (Tsimplis 1994; Horsch & Fourniotis 2017; Rubi *et al.* 2022; Aspioti & Fourniotis 2024; Fourniotis 2024). This microtidal context is characterized by a low surface tidal amplitude of approximately 0.2 m. Despite this small surface expression, the strait's complex bathymetry facilitates the development of an internal tide (Rubi *et al.* 2022; Fourniotis 2024; Caterina *et al.* 2025), which generates currents reaching up to 1.3 m s^{-1} and exerts a maximum shear stress of about 3 N m^{-2} on the seafloor (**Figure 5.3**). These strong currents produce pronounced erosional features in and around the strait (Rubi *et al.* 2022).

Bathymetric analyses of the Gulf reveal pools and crest morphologies, some at large scale, reflect persistent erosional activity. Such features are sustained by near-bottom flow dynamics that prevent sediment deposition within the strait. While the presence of strong tidal currents alone supports the classification of the Rio-Antirio as a tidal strait, a second criterion is typically the occurrence of tidal dunes deposited in its vicinity (Longhitano 2013). In the case of the Rio-Antirio Strait, the dominance of tidal forcing has now been demonstrated (Caterina *et al.* 2025); thus, the lack of depositional features and the prevalence of erosional structures should not preclude its classification as a tidal strait.

Modeling results and sedimentary facies analyses from coring indicate that the only significant deposits occur farther east, beyond the strait's center; beginning in the Nafpaktos Bay, where the internal tide's effects are weaker and asymmetrical, particularly along the northern margin. East of Nafpaktos Bay, the Mornos Delta area is also influenced by the tidal currents and internal tide, as reflected in sediment transport

trajectories that either converge toward the strait or are redirected toward the Aigio Canyon and the central Corinth Basin (**Figure 5.7**).

The spatial extent of the Rio-Antirio internal tide can thus be delineated from the entrance of the Patras Gulf in the west to the Aigio Delta and Aigio Canyon in the east (Caterina *et al*. 2025). Even though the internal tide dissipates throughout the full water column (~900 m) in the deep Corinth Basin, its influence on the basin-scale circulation remains significant. Indeed, the upwelling of deep Corinth waters driven by this internal tide is a key process controlling the overall circulation within the Gulf (Caterina & Hubert-Ferrari 2025).

2. General circulation: A Mini Mediterranea Sea

The overall circulation pattern of the Corinth Gulf was summarized in **Figure 3.11**). In the Patras Gulf, a persistent cyclonic gyre develops under the combined influence of local winds and the inflow of upwelled, cold deep waters from the Corinth Basin entering the strait. In the Strait & Entrance Region, when these deep Corinth waters reach the surface but do not cross the strait, they flow back into the Gulf along the steep, fault-bounded southern margin. This "reflected flow" originates from the amplification of internal waves over the shallow bathymetry of the strait (Caterina & Hubert-Ferrari 2025; Caterina *et al*. 2025). As these colder waters move eastward, they reach the central part of the Gulf, where they may become trapped within the West Corinth anticyclonic gyre or continue along the coast toward the East Corinth region. In this area, the flow interacts with the East Corinth cyclonic gyre in front of Antikyra Bay. The largest gyres form in front of these two bays, largely due to the wider available space and the influence of dominant winds (Koletsis *et al*. 2014; Caterina & Hubert-Ferrari 2025). The observations through satellite data also evidenced an increase of the Corinth Gulf's SST of ~1.4°C over 14 years (~0.097°C yr^{-1}. An increase of the SST trend is also observed in the Mediterranean Sea (Skliris *et al*. 2012; García-Monteiro *et al*. 2022) but with three times less intensity (~0.026°C yr^{-1} to 0.042°C yr^{-1}), the Corinth Gulf being smaller and thus more sensitive to climate change.

In terms of general circulation, the Corinth Gulf can be viewed as a smaller-scale analogue of the Mediterranean Sea, with the Rio-Antirio Strait acting as its counterpart to the Strait of Gibraltar. Similar to the Mediterranean system, the Corinth Gulf exhibits a pronounced west–east temperature gradient (Caterina & Hubert-Ferrari 2025). Moreover, dominant northwesterly winds (Pinardi & Masetti 2000; Koletsis *et al*. 2014) drive surface waters toward the closed eastern end of the basin, while deeper waters flow in the opposite direction (Pinardi & Masetti 2000; Rubi *et al*. 2022). Model results indicate that a clear large-scale "return flow" of deep waters toward the strait is not consistently observed. However, localized bottom currents flowing westward toward the strait are present in certain areas, such as the Western Corinth area and the Alkyonides Gulf. These return flows occur primarily in shallower or more enclosed sub-basins. In the Western

Corinth area, westward bottom currents are likely driven by tidal forcing, whereas in the Alkyonides Basin, downslope cascading through the canyons results from the confined geometry of this smaller sub-basin (Caterina *et al*. 2025).

A final, robust parallel between the Mediterranean Sea and the Corinth Gulf lies in the control exerted by their respective tidal straits on basin-scale circulation. Both the Strait of Gibraltar and the Rio-Antirio Strait regulate exchanges between a relatively open basin (the Atlantic Ocean and Ionian Sea, respectively) and a relatively enclosed one (the Mediterranean Sea and Corinth Gulf, respectively). The two straits share similar morphologies and bathymetric characteristics, including steep bathymetric gradients and narrowing geometries at the transition between basins (Tsimplis & Bryden 2000; Luján *et al*. 2011; González-Castillo *et al*. 2015; Rubi *et al*. 2022; Caterina *et al*. 2025). Furthermore, both straits exhibit strong vertical stratification, and their bathymetry enhances the generation of internal tides that amplify local currents and water-mass exchanges (Tsimplis & Bryden 2000; Morozov *et al*. 2002; Rubi *et al*. 2022; Fourniotis 2024; Caterina *et al*. 2025). Consequently, a significant part of the present-day dynamics within these enclosed basins is driven by the circulation processes controlled by their tidal straits, particularly the tidal components.

3. Sediments under tidally-induced bottom currents

In the Rio-Antirio strait, the sedimentation is null. Only erosion is observed, at small and large scale and persistent through time (and diverse paleogeographies). The “first” sedimentation evidence in the Corinth Gulf when coming from the strait lies in the western Corinth depocenter. There the deposition is controlled by the interplay between gravity-driven processes and bottom-current reworking. Near-bottom currents of variable intensity and direction continuously reshape the upper sediment surface, forming contouritic structures and hybrid deposits.

The influence of bottom currents, going away from the strait, progressively decreases from west to east across the depocenter. In the westernmost part, at CAN4, sediment reworking by bottom currents is the most intense, evidenced by mottled and bioturbated facies (C3) indicating persistent near-bottom flow activity. Eastward, at CAN2, the expression of bottom-current processes becomes much weaker. The sedimentary record is dominated by less reworked Md and Mm facies, showing reduced tractional structures and weaker hydrodynamic influence. CAN2 is in a quieter depositional zone and sedimentation is mainly governed by gravity-driven accumulation. Further east, at CAN3, bottom-current influence becomes slightly stronger again. The reappearance of C1 and C2 facies (bioturbated laminated muds and mottled silts) indicates renewed near-bottom flow activity, consistent with hydrodynamic model results showing enhanced bottom-current velocities. This pattern suggests a strongly influenced hydrodynamic by the currents related to the Rio–Antirio Strait which control the intensity of sediment reworking.

The strong dynamic circulation near the strait explains the prevalence of reworked contouritic facies (C3 and C2) in CAN4. Eastward, current energy decreases sharply, allowing gravity-driven processes and MTD accumulation to dominate. Near CAN3, flow constriction and topographic steering enhance near-bottom velocities again, correlating with renewed contouritic structures. Together, sedimentological and hydrodynamic evidence demonstrates that bottom-current variability exerts a first-order control on sediment preservation and facies distribution. Areas of stronger flow promote winnowing, bioturbation, and contouritic layering, whereas lower-energy zones favor the accumulation and deformation of fine-grained gravity-driven sediments. This interplay defines a spatial alternation of contouritic and gravitational domains, reflecting the dynamic coupling between sediment supply, slope morphology, and tidal circulation at the entrance of the Corinth Gulf.

4. Tidal Dynamics in Paleogeographies

The present-day Rio-Antirio Strait is dominated by tidal dynamics. When the tidal component is removed from the model, no significant water movement is observed within the strait (Figure 4.12; Caterina *et al*. 2025). This observation is as valid today as it likely was when the Rio-Antirio Strait was closed and the Corinth Gulf was instead connected to the sea via a “Corinth Strait” linking it to the Aegean Sea. If a single connection through the Corinth Isthmus is considered, its width would be too large to amplify microtidal dynamics, resulting in a bottom circulation that appears nearly stagnant. Nevertheless, the Corinth Isthmus has been identified as a geological analogue for tidal straits, as the deposits exposed along the Corinth Canal display well-developed tidal dunes (Caterina *et al*. 2022).

Even if a strait connecting the Corinth Gulf to the Aegean Sea existed, the simulated bottom current velocities alone would be insufficient to generate the sedimentary structures observed in the Canal. The presence of tidal forcing therefore appears to be the key controlling factor under any paleogeographic configuration of the Corinth Gulf. To reproduce the strong alternating bottom currents necessary to form the characteristic herringbone structures, the Rio-Antirio Strait must have been open. Numerical modelling based on present-day oceanographic conditions, coupled with geological evidence, supports the hypothesis that a connection between the Corinth Gulf and the Aegean Sea could have coexisted with an active Rio-Antirio Strait.

If only a single connection existed, the Corinth Gulf would have exhibited low hydrodynamic energy, with circulation primarily driven by wind forcing and characteristics resembling those of a semi-enclosed lake with limited marine influence. In contrast, a double opening—linking the Gulf both to the Ionian Sea through the Rio-Antirio Strait and to the Aegean Sea through the Corinth Isthmus—would allow for the development of a tidal strait within the Isthmus. Paleogeographic simulations further demonstrate that even in a scenario where the Rio-Antirio Strait was positioned at a higher elevation, its

dynamics would still display strong tidal signatures, justifying its classification as a tidal strait across most of its likely configurations.

5. Perspectives

This work highlights how to play around the persistent lack of real-time and in-situ oceanographic data for the Corinth Gulf. While this gap can be partially addressed using satellite observations for surface dynamics or numerical modelling for the entire water column, the absence of direct measurements remains a limitation. Even with the limited dataset collected both externally and within this study, the numerical analyses conducted here have proven to be robust and validated. However, given that the investigated processes often occur at small spatial scales, the resolution constraints of both models and satellite data can limit the precision of the results and the interpretation of local dynamics. Publicly accessible results from dedicated marine campaigns focusing on the oceanography of this key Greek gulf would therefore be invaluable for future research. Such data would enable a more accurate characterization of present-day oceanographic conditions in the Corinth Gulf and, consequently, a refined understanding of its past configurations. Improving the reconstruction of paleogeographies would, in turn, allow for more precise assessments of sedimentological hypotheses related to specific paleo-configurations of the Gulf.

Despite the lack of in-situ data, the Gulf-scale analysis of its hydrodynamics presented in this study provides a strong and reliable foundation for future oceanographically oriented research in the region. The satellite-based assessment of surface dynamics and sea surface temperature (SST) offers an updated perspective on the general circulation, while the present-day numerical modelling can serve as a valuable reference for studies investigating processes throughout the entire water column at the scale of the Gulf.

Simulating various bathymetric scenarios under present-day oceanographic forcing has proven to be both relevant and reasonably accurate for the objectives of this study. Nevertheless, higher precision could be achieved by developing paleo-oceanographic forcings to drive the ROMS model. Such work would be challenging, as it would require integrating extensive geological analyses beyond the Corinth Gulf to reconstruct past oceanographic currents and wind regimes. Furthermore, the paleogeographic reconstructions in this study relied on a limited number of geological constraints to determine the timing and feasibility of different configurations. Consequently, the results presented here provide a foundation for future efforts to refine the geological chronology of the Corinth Gulf's connections to the open sea and to better constrain its past oceanographic conditions.

References

Albini, P., Rovida, A., Scotti, O. & Lyon-Caen, H., 2017. Large Eighteenth–Nineteenth Century Earthquakes in Western Gulf of Corinth with Reappraised Size and Location. *Bull. Seismol. Soc. Am.* doi:10.1785/0120160181

Alford, M.H., MacKinnon, J.A., Nash, J.D., Simmons, H., Pickering, A., Klymak, J.M., Pinkel, R., *et al.*, 2011. Energy Flux and Dissipation in Luzon Strait: Two Tales of Two Ridges. *J. Phys. Oceanogr.*, **41**, 2211–2222. doi:10.1175/JPO-D-11-073.1

Allen, P.A., 2017. *Sediment Routing Systems: The Fate of Sediment from Source to Sink*, Cambridge University Press.

Alvera-Azcárate, A., Barth, A., Sirjacobs, D. & Beckers, J.-M., 2009. Enhancing temporal correlations in EOF expansions for the reconstruction of missing data using DINEOF. *Ocean Sci.*, **5**, 475–485. doi:10.5194/os-5-475-2009

Anderson, J.J. & Carmack, E.C., 1973. Some physical and chemical properties of the Gulf of Corinth. *Estuar. Coast. Mar. Sci.*, **1**, 195–202. doi:10.1016/0302-3524(73)90034-0

Androulidakis, Y., Kolovoyiannis, V., Makris, C. & Krestenitis, Y., 2024. Evidence of 2024 Summer as the Warmest During the Last Four Decades in the Aegean, Ionian, and Cretan Seas. *J. Mar. Sci. Eng.*, **12**, 2020. doi:10.3390/jmse12112020

Appleby, P.G. & Oldfield, F., 1978. The calculation of lead-210 dates assuming a constant rate of supply of unsupported 210Pb to the sediment. *CATENA*, **5**, 1–8. doi:10.1016/S0341-8162(78)80002-2

Appleby, P.G. & Oldfield, F., 1983. The assessment of 210Pb data from sites with varying sediment accumulation rates. *Hydrobiologia*, **103**, 29–35. doi:10.1007/BF00028424

Armijo, R., Meyer, B., King, G.C.P., Rigo, A. & Papanastassiou, D., 1996. Quaternary evolution of the Corinth Rift and its implications for the Late Cenozoic evolution of the Aegean. *Geophys. J. Int.*, **126**, 11–53. doi:10.1111/j.1365-246X.1996.tb05264.x

Ashley, G.M., 1990. Classification of large-scale subaqueous bedforms: a new look at an old problem; SEPM bedforms and bedding structures. *J. Sediment. Petrol.*, **60**, 160–172. doi:10.1306/212f9138-2b24-11d7-8648000102c1865d

Aspioti, A.G. & Fourniotis, N.T., 2024. A Brief Review of Hydrodynamic Circulation in the Mediterranean Gulfs. *Dynamics*, **4**, 873–888. doi:10.3390/dynamics4040045

Aspioti, A.G. & Fourniotis, N.T., 2025. Numerical Study of Barotropic Circulation in the Gulfs of Patras and Corinth System. *Oceans*, **6**, 10. doi:10.3390/oceans6010010

Baines, P.G. & Garnek, H., 1990. Hydraulic models of deep stratified flows over topography. in *The Physical Oceanography of Sea Straits*, p. 318, ed. Pratt, L.J., Springer Netherlands. doi:10.1007/978-94-009-0677-8

Barnard, P.L., Hanes, D.M., Rubin, D.M. & Kvitek, R.G., 2006. Giant sand waves at the mouth of San Francisco Bay. *Eos (Washington. DC).*, **87**, 285–289. doi:10.1029/2006eo290003

Barth, A., 2024. NCDatasets.jl: a Julia package for manipulating netCDF data sets. *J. Open Source Softw.*, **9**, 6504. doi:10.21105/joss.06504

Barth, A., 2025. ROMS.jl. Retrieved March 18, 2025, from https://alexander-

barth.github.io/ROMS.jl/dev/

Bearzi, G., Bonizzoni, S., Santostasi, N.L., Furey, N.B., Eddy, L., Valavanis, V.D. & Gimenez, O., 2016. Dolphins in a Scaled-Down Mediterranean: The Gulf of Corinth's Odontocetes, pp. 297–331. doi:10.1016/bs.amb.2016.07.003

Bearzi, Giovanni, Bonizzoni, S. & Gonzalvo, J., 2011. Mid-distance movements of common bottlenose dolphins in the coastal waters of Greece. *J. Ethol.*, **29**, 369–374. doi:10.1007/s10164-010-0245-x

Beckers, A., Beck, C., Hubert-Ferrari, A., Reyss, J.-L., Mortier, C., Albini, P., Rovida, A., *et al.*, 2017. Sedimentary impacts of recent moderate earthquakes from the shelves to the basin floor in the western Gulf of Corinth. *Mar. Geol.*, **384**, 81–102. doi:10.1016/j.margeo.2016.10.018

Beckers, A., Beck, C., Hubert-Ferrari, A., Tripsanas, E., Crouzet, C., Sakellariou, D., Papatheodorou, G., *et al.*, 2016. Influence of bottom currents on the sedimentary processes at the western tip of the Gulf of Corinth, Greece. *Mar. Geol.*, **378**, 312–332, Elsevier B.V. doi:10.1016/j.margeo.2016.03.001

Beckers, A., Hubert-Ferrari, A., Beck, C., Bodeux, S., Tripsanas, E., Sakellariou, D. & Batist, M. De, 2015. Active faulting at the western tip of the Gulf of Corinth, Greece, from high-resolution seismic data. *Mar. Geol.*, **360**, 55–69, Elsevier B.V. doi:10.1016/j.margeo.2014.12.003

Beckers, J.-M., Barth, A. & Alvera-Azcárate, A., 2006. DINEOF reconstruction of clouded images including error maps – application to the Sea-Surface Temperature around Corsican Island. *Ocean Sci.*, **2**, 183–199. doi:10.5194/os-2-183-2006

Belgacem, M., Schroeder, K., Barth, A., Troupin, C., Pavoni, B., Raimbault, P., Garcia, N., *et al.*, 2021. Climatological distribution of dissolved inorganic nutrients in the western Mediterranean Sea (1981–2017). *Earth Syst. Sci. Data*, **13**, 5915–5949. doi:10.5194/essd-13-5915-2021

Bell, R.E., McNeill, L.C., Bull, J.M. & Henstock, T.J., 2008. Evolution of the offshore western Gulf of Corinth. *Geol. Soc. Am. Bull.*, **120**, 156–178. doi:10.1130/B26212.1

Bell, R.E., McNeill, L.C., Bull, J.M., Henstock, T.J., Collier, R.E.L. & Leeder, M.R., 2009. Fault architecture, basin structure and evolution of the Gulf of Corinth Rift, central Greece. *Basin Res.*, **21**, 824–855. doi:10.1111/j.1365-2117.2009.00401.x

Binford, M.W., Kahl, J.S. & Norton, S.A., 1993. Interpretation of210Pb profiles and verification of the CRS dating model in PIRLA project lake sediment cores. *J. Paleolimnol.*, **9**, 275–296. doi:10.1007/BF00677218

Bouilloux, A., Valet, J.-P., Bassinot, F., Joron, J.-L., Dewilde, F., Blanc-Valleron, M.-M. & Moreno, E., 2013. Influence of seawater exchanges across the Bab-el-Mandeb Strait on sedimentation in the Southern Red Sea during the last 60 ka. *Paleoceanography*, **28**, 675–687. doi:10.1002/2013PA002544

Boyer, T.P., Baranova, O.K., Coleman, C., Garcia, H.E., Grodsky, A., Locarnini, R.A., Mishonov, A. V, *et al.*, 2018. World Ocean Database 2018, 1–207. Retrieved from http://www.nodc.noaa.gov/

Briole, P., Ganas, A., Elias, P. & Dimitrov, D., 2021. The GPS velocity field of the Aegean. New observations, contribution of the earthquakes, crustal blocks model. *Geophys. J. Int.*, **226**, 468–492. doi:10.1093/gji/ggab089

Briole, P., Rigo, A., Lyon-Caen, H., Ruegg, J.C., Papazissi, K., Mitsakaki, C., Balodimou, A., *et al.*,

2000. Active deformation of the Corinth rift, Greece: Results from repeated Global Positioning System surveys between 1990 and 1995. *J. Geophys. Res. Solid Earth*, **105**, 25605–25625. doi:10.1029/2000JB900148

Brooks, M. & Ferentinos, G., 1984. Tectonics and sedimentation in the Gulf of Corinth and the Zakynthos and Kefallinia channels, Western Greece. *Tectonophysics*, **101**, 25–54. doi:10.1016/0040-1951(84)90040-4

Bryden, H.L. & Nurser, A.J.G., 2003. Effects of Strait Mixing on Ocean Stratification. *J. Phys. Oceanogr.*, **33**, 1870–1872. doi:10.1175/1520-0485(2003)033<1870:EOSMOO>2.0.CO;2

Buongiorno Nardelli, B., Tronconi, C., Pisano, A. & Santoleri, R., 2013. High and Ultra-High resolution processing of satellite Sea Surface Temperature data over Southern European Seas in the framework of MyOcean project. *Remote Sens. Environ.*, **129**, 1–16. doi:10.1016/j.rse.2012.10.012

Canals, M., Puig, P., Madron, X.D. de, Heussner, S., Palanques, A. & Fabres, J., 2006. Flushing submarine canyons. *Nature*, **444**, 354–357. doi:10.1038/nature05271

Cartigny, M.J.B., Ventra, D., Postma, G. & Berg, J.H. van Den, 2014. Morphodynamics and sedimentary structures of bedforms under supercritical-flow conditions: New insights from flume experiments. (J. Venditti, Ed.)*Sedimentology*, **61**, 712–748. doi:10.1111/sed.12076

Caterina, B. & Hubert-Ferrari, A., 2025. Using 14 Years of Satellite Data to Describe the Hydrodynamic Circulation of the Patras and Corinth Gulfs. *J. Mar. Sci. Eng.*, **13**, 623. doi:10.3390/jmse13030623

Caterina, B., Hubert-Ferrari, A., Barth, A. & Beckers, J.-M., 2025. Modelling of the Present Oceanographic Situation of the Gulfs of Patras and Corinth. *J. Mar. Sci. Eng.*, **13**, 1827. doi:doi.org/10.3390/jmse13091827

Caterina, B., Rubi, R. & Hubert-Ferrari, A., 2022. Stratigraphic architecture, sedimentology and structure of the middle Pleistocene Corinth canal (Greece). *Geol. Soc. London, Spec. Publ.*, **523**, 279–304. doi:10.1144/SP523-2021-143

CMEMS, 2025. Mediterranean Sea - High Resolution and Ultra High Resolution L3S Sea Surface Temperature. doi:https://doi.org/10.48670/moi-00171

Cnudde, V., Masschaele, B., Dierick, M., Vlassenbroeck, J., Hoorebeke, L. Van & Jacobs, P., 2006. Recent progress in X-ray CT as a geosciences tool. *Appl. Geochemistry*, **21**, 826–832. doi:10.1016/j.apgeochem.2006.02.010

Colella, S., Falcini, F., Rinaldi, E., Sammartino, M. & Santoleri, R., 2016. Mediterranean Ocean Colour Chlorophyll Trends. (F. G. Schmitt, Ed.)*PLoS One*, **11**, e0155756. doi:10.1371/journal.pone.0155756

Collier, R., 1990. Eustatic and Tectonic controlsupon Quaternary coastal sedimentation in the Corinth Basin, Greece. *J. Geol. Soc. London.*, **147**, 301–314.

Collier, R. & Dart, C.J., 1991. Neogene to Quaternary rifting, sedimentation and uplift in the Corinth Basin, Greece. *J. Geol. Soc. London.*, **148**, 1049–1065. doi:10.1144/gsjgs.148.6.1049

Collier, R., Leeder, M., Rowe, P. & Atkinson, T., 1992. Rates of tectonic uplift in yhe Corinth and Megara basins, Central Greece, **11**, 1159–1167.

Collier, R., Leeder, M.R., Trout, M., Ferentinos, G., Lyberis, E. & Papatheodorou, G., 2000. High sediment yields and cool, wet winters: Test of last glacial paleoclimates in the northern

Mediterranean. *Geology*, **28**, 999. doi:10.1130/0091-7613(2000)28<999:HSYACW>2.0.CO;2

Collier, R. & Thompson, J., 1991. Transvers and linear dunes in a Upper Pleistocene marine sequence, Corinth Basin, Greece.

Cooper, C., Forristall, G.Z. & Joyce, T.M., 1990. Velocity and hydrographic structure of two Gulf of Mexico warm-core rings. *J. Geophys. Res. Ocean.*, **95**, 1663–1679. doi:10.1029/JC095iC02p01663

Copernicus Marine Service, 2025. Mediterranean Sea, Bio-Geo-Chemical, L3, daily Satellite Observations (1997-ongoing). doi:doi.org/10.48670/moi-00299

Costello, W.R. & Southard, J.B., 1981. Flume experiment on lower-flow-regime bed forms in coarse sand, **51**, 849–864.

D'Ortenzio, F. & Ribera d'Alcalà, M., 2009. On the trophic regimes of the Mediterranean Sea: a satellite analysis. *Biogeosciences*, **6**, 139–148. doi:10.5194/bg-6-139-2009

Dalrymple, R.W., 1992. Tidal Deposition Systems. in *Facies Models: response to sea level changes*, p. 407, eds. Walker, R.G. & James, N.P., Geological Association of Canada.

Dalrymple, R.W., 2023. A review of the morphology, physical processes and deposits of modern straits. *Geol. Soc. London, Spec. Publ.*, **523**, 17–83. doi:10.1144/SP523-2021-76

Defant, A., 1958. *Ebb and flow; the tides of earth, air and water*. Retrieved from https://ui.adsabs.harvard.edu/abs/1958efte.book.....D

Deleersnijder, E.L., 1989. Upwelling and upsloping in three-dimensional marine models. *Appl. Math. Model.*, **13**, 462–467. doi:10.1016/0307-904X(89)90094-2

Dey, S., 1999. Sediment threshold. *Appl. Math. Model.*, **23**, 399–417. doi:10.1016/S0307-904X(98)10081-1

Donald R. Lowe, 1982. Sediment Gravity Flows: II Depositional Models with Special Reference to the Deposits of High-Density Turbidity Currents. *SEPM J. Sediment. Res.*, **Vol. 52**. doi:10.1306/212F7F31-2B24-11D7-8648000102C1865D

ECMWF, 2018. MARS - the ECMWF meteorological archive. *Softw. Comput. Serv.*, ECMWF. Retrieved from https://www.ecmwf.int/node/18124

Egbert, G.D., Bennett, A.F. & Foreman, M.G.G., 1994. TOPEX/POSEIDON tides estimated using a global inverse model. *J. Geophys. Res. Ocean.*, **99**, 24821–24852. doi:10.1029/94JC01894

Egbert, G.D. & Erofeeva, S.Y., 2002. Efficient Inverse Modeling of Barotropic Ocean Tides. *J. Atmos. Ocean. Technol.*, **19**, 183–204. doi:10.1175/1520-0426(2002)019<0183:EIMOBO>2.0.CO;2

Fakiris, E., Blondel, P., Papatheodorou, G., Christodoulou, D., Dimas, X., Georgiou, N., Kordella, S., *et al.*, 2019. Multi-Frequency, Multi-Sonar Mapping of Shallow Habitats—Efficacy and Management Implications in the National Marine Park of Zakynthos, Greece. *Remote Sens.*, **11**, 461. doi:10.3390/rs11040461

Faugères, J.-C. & Stow, D.A.V., 2008. Contourite drifts: nature, evolution and controls., pp. 257–288. doi:10.1016/S0070-4571(08)10014-0

Ferentinos, G., Brooks, M. & Doutsos, T., 1985. Quaternary tectonics in the Gulf of Patras, western Greece. *J. Struct. Geol.*, **7**, 713–717. doi:10.1016/0191-8141(85)90146-4

Ferentinos, G., Papatheodorou, G. & Collins, M.B., 1988. Sediment Transport processes on an

active submarine fault escarpment: Gulf of Corinth, Greece. *Mar. Geol.*, **83**, 43–61. doi:10.1016/0025-3227(88)90051-5

Fernández-Blanco, D., Gelder, G. de, Lacassin, R. & Armijo, R., 2020. Geometry of Flexural Uplift by Continental Rifting in Corinth, Greece. *Tectonics*, **39**. doi:10.1029/2019TC005685

Flanders Marine Institute (VLIZ), 2025. Sea level station monitoring facility. *Intergov. Oceanogr. Comm.* doi:10.14284/482

Flood, R.D., 1983. Classification of sedimentary furrows and a model for furrow initiation and evolution. *Geol. Soc. Am. Bull.*, **94**, 630. doi:10.1130/0016-7606(1983)94<630:COSFAA>2.0.CO;2

Ford, M., Hemelsdaël, R., Mancini, M. & Palyvos, N., 2017. Rift migration and lateral propagation: evolution of normal faults and sediment-routing systems of the western Corinth rift (Greece). *Geol. Soc. London, Spec. Publ.*, **439**, 131–168. doi:10.1144/SP439.15

Ford, M., Rohais, S., Williams, E.A., Bourlange, S., Jousselin, D., Backert, N. & Malartre, F., 2013. Tectono-sedimentary evolution of the western Corinth rift (Central Greece). *Basin Res.*, **25**, 3–25. doi:10.1111/j.1365-2117.2012.00550.x

Fourniotis, N.T., 2024. Effect of Internal Waves on the Hydrodynamics of a Mediterranean Sea Strait. *J. Mar. Sci. Eng.*, **12**, 532. doi:10.3390/jmse12040532

Fourniotis, N.T. & Horsch, G.M., 2010. Three-dimensional numerical simulation of wind-induced barotropic circulation in the Gulf of Patras. *Ocean Eng.*, **37**, 355–364, Elsevier. doi:10.1016/j.oceaneng.2010.01.002

Fourniotis, N.T. & Horsch, G.M., 2015. Baroclinic circulation in the Gulf of Patras (Greece). *Ocean Eng.*, **104**, 238–248. doi:10.1016/j.oceaneng.2015.04.080

Friglios, N., Theocharis, A. & Georgopoulos, D., 1985. Preliminary chemical and physical observations during summer 1980 on a silled embayment in the Ionian Sea. *Vie Milieu*, **35**, 115–125.

Frydas, D., 1987. Calcareous nannoplankton from the Neogene of the NW-Peloponnes, Greece. *Neues Jahrb. für Geol. und Paläontologie - Monatshefte*, **1987**, 274–286. doi:10.1127/njgpm/1987/1987/274

García-Monteiro, S., Sobrino, J.A., Julien, Y., Sòria, G. & Skokovic, D., 2022. Surface Temperature trends in the Mediterranean Sea from MODIS data during years 2003–2019. *Reg. Stud. Mar. Sci.*, **49**, 102086. doi:10.1016/j.rsma.2021.102086

García, M., Hernández-Molina, F.J., Llave, E., Stow, D.A.V., León, R., Fernández-Puga, M.C., Diaz del Río, V., *et al.*, 2009. Contourite erosive features caused by the Mediterranean Outflow Water in the Gulf of Cadiz: Quaternary tectonic and oceanographic implications. *Mar. Geol.*, **257**, 24–40. doi:10.1016/j.margeo.2008.10.009

Gawthorpe, R.L., Fabregas, N., Pechlivanidou, S., Ford, M., Collier, R.E.L., Carter, G.D.O., McNeill, L.C., *et al.*, 2022. Late Quaternary mud-dominated, basin-floor sedimentation of the Gulf of Corinth, Greece: Implications for deep-water depositional processes and controls on syn-rift sedimentation. *Basin Res.*, **34**, 1567–1600. doi:10.1111/bre.12671

Gawthorpe, R.L. & Leeder, M.R., 2000. Tectono-sedimentary evolution of active extensional basins. *Basin Res.*, **12**, 195–218. doi:10.1111/j.1365-2117.2000.00121.x

Gawthorpe, R.L., Leeder, M.R., Kranis, H., Skourtsos, E., Andrews, J.E., Henstra, G.A., Mack, G.H., *et al.*, 2018. Tectono-sedimentary evolution of the Plio-Pleistocene Corinth rift, Greece.

Basin Res., **30**, 448–479. doi:10.1111/bre.12260

GEBCO, 2024. GEBCO Gridded Bathymetry Data Download. Retrieved March 11, 2025, from https://download.gebco.net/

Gelder, G. De, Doan, M.L., Beck, C., Carlut, J., Seibert, C., Feuillet, N., Carter, G.D.O., *et al.*, 2022. Multi-scale and multi-parametric analysis of Late Quaternary event deposits within the active Corinth Rift (Greece). (A. McArthur, Ed.)*Sedimentology*, **69**, 1573–1598. doi:10.1111/sed.12964

Gelder, G. de, Fernández-Blanco, D., Melnick, D., Duclaux, G., Bell, R.E., Jara-Muñoz, J., Armijo, R., *et al.*, 2019. Lithospheric flexure and rheology determined by climate cycle markers in the Corinth Rift. *Sci. Rep.*, **9**, 4260. doi:10.1038/s41598-018-36377-1

Gibbard, P.L., 1995. The formation of the Strait of Dover. *Geol. Soc. London, Spec. Publ.*, **96**, 15–26. doi:10.1144/GSL.SP.1995.096.01.03

González-Castillo, L., Junge, A., Galindo-Zaldívar, J. & Löwer, A., 2015. Influence of a narrow strait connecting a large ocean and a small sea on magnetotelluric data: Gibraltar Strait. *J. Appl. Geophys.*, **122**, 103–110. doi:10.1016/j.jappgeo.2015.09.007

Gupta, S., Collier, J.S., Garcia-Moreno, D., Oggioni, F., Trentesaux, A., Vanneste, K., Batist, M. De, *et al.*, 2017. Two-stage opening of the Dover Strait and the origin of island Britain. *Nat. Commun.*, **8**, 15101. doi:10.1038/ncomms15101

Harms, J.C., Southard, J.B. & Walker, R.G., 1982. Structures and sequences in clastic rocks. *Soc. Econ. Paleontol. Mineral. Short Course*, **9**.

Hayward, C.L., 1996. High-resolution provenance determination of construction-stone: A preliminary study of Corinthian oolitic limestone quarries at Examilia. *Geoarchaeology*, **11**, 215–234. doi:10.1002/(SICI)1520-6548(199605)11:3<215::AID-GEA2>3.0.CO;2-6

Heezen, B.C., Hollister, C.D. & Ruddiman, W.F., 1966. Shaping of the Continental Rise by Deep Geostrophic Contour Currents. *Science (80-.).*, **152**, 502–508. doi:10.1126/science.152.3721.502

Hergarten, S., Robl, J. & Stüwe, K., 2014. Extracting topographic swath profiles across curved geomorphic features. *Earth Surf. Dyn.*, **2**, 97–104. doi:10.5194/esurf-2-97-2014

Hernández-Molina, F.J., Llave, E. & Stow, D.A.V., 2008. Chapter 19 Continental Slope Contourites, pp. 379–408. doi:10.1016/S0070-4571(08)10019-X

Horsch, G.M. & Fourniotis, N.T., 2017. Wintertime Tidal Hydrodynamics in the Gulf of Patras, Greece. *J. Coast. Res.*, **33**, 1305–1314. doi:10.2112/JCOASTRES-D-16-00133.1

Hutchison, C.S., 2005. Miri Zone. in *Geology of North-West Borneo*, pp. 77–134, Elsevier. doi:10.1016/B978-044451998-6/50008-9

Iatrou, M., 2013. *The Study of the Dispersion of the Red Mud Slurry in the Central Corinth Gulf Using Geophysical, Sedimentological and Geochemical Approaches*, University of Patras. Retrieved from http://www.didaktorika.gr/eadd/readonline?%0Ahandle=10442/37557

Iatrou, M., Papatheodorou, G., Geraga, M. & Ferentinos, G., 2010. THE STUDY OF HEAVY METAL CONCENTRATIONS IN THE RED MUD DEPOSITS AT THE GULF OF CORINTH, USING MULTIVARIATE TECHNIQUES. *Bull. Geol. Soc. Greece*, **43**, 1018. doi:10.12681/bgsg.11267

Issaris, Y., Katsanevakis, S., Pantazi, M., Vassilopoulou, V., Panayotidis, P., Kavadas, S., Kokkali, A., *et al.*, 2012. Ecological mapping and data quality assessment for the needs of

ecosystem-based marine spatial management: case study Greek Ionian Sea and the adjacent gulfs. *Mediterr. Mar. Sci.*, **13**, 297. doi:10.12681/mms.312

Keller, G.H. & Richards, A.F., 1967. Sediments of the Malacca Strait, Southeast Asia. *J. Sediment. Petrol.*, **37**, 102–127.

Kelletat, D., Kowalczyk, G., Schröder, B. & Winter, K.-P., 1976. A Synoptic View on the Neotectonic Development of the Peloponnesian Coastal Regions. *Zeitschrift der Dtsch. Geol. Gesellschaft*, **127**, 447–465. doi:10.1127/zdgg/127/1976/447

Koletsis, I., Kotroni, V. & Lagouvardos, K., 2014. A model-based study of the wind regime over the Corinthian Gulf. *Nat. Hazards Earth Syst. Sci.*, **14**, 459–472. doi:10.5194/nhess-14-459-2014

Koutsodendris, A., Papatheodorou, G., Kougiourouki, O. & Georgiadis, M., 2008. Benthic marine litter in four Gulfs in Greece, Eastern Mediterranean; abundance, composition and source identification. *Estuar. Coast. Shelf Sci.*, **77**, 501–512. doi:10.1016/j.ecss.2007.10.011

Kubin, E., Menna, M., Mauri, E., Notarstefano, G., Mieruch, S. & Poulain, P.-M., 2023. Heat content and temperature trends in the Mediterranean Sea as derived from Argo float data. *Front. Mar. Sci.*, **10**. doi:10.3389/fmars.2023.1271638

Lamarche, G., Lurton, X., Verdier, A.-L. & Augustin, J.-M., 2011. Quantitative characterisation of seafloor substrate and bedforms using advanced processing of multibeam backscatter—Application to Cook Strait, New Zealand. *Cont. Shelf Res.*, **31**, S93--S109. doi:10.1016/j.csr.2010.06.001

Lascaratos, A., Salusti, E. & Papageorgaki, G., 1989. Wind-induced upwellings and currents in the gulfs of Patras, Nafpaktos and Korinthos, western Greece. *Oceanol. Acta*, **12**, 159–164.

Leeder, M.R., Gray, T.E. & Alexander, J., 2005. Sediment suspension dynamics and a new criterion for the maintenance of turbulent suspensions. *Sedimentology*, **52**, 683–691. doi:10.1111/j.1365-3091.2005.00720.x

Longhitano, S.G., 2013. A facies-based depositional model for ancient and modern, tectonically-confined tidal straits. *Terra Nov.*, **25**, 446–452. doi:10.1111/ter.12055

Longhitano, S.G., 2018. Between Scylla and Charybdis (part 1): the sedimentary dynamics of the modern Messina Strait (central Mediterranean) as analogue to interpret the past. *Earth-Science Rev.*, **185**, 259–287, Elsevier. doi:10.1016/j.earscirev.2018.06.008

Longhitano, S.G. & Chiarella, D., 2020. *Tidal straits: basic criteria for recognizing ancient systems from the rock record*. *Reg. Geol. Tectonics Princ. Geol. Anal.*, BV. doi:10.1016/b978-0-444-64134-2.00014-6

Longhitano, S.G. & Colella, A., 2007. Geomorphology, sedimentology and recent evolution of the anthropogenically modified Simeto River delta system (eastern Sicily, Italy). *Sediment. Geol.*, **194**, 195–221. doi:10.1016/j.sedgeo.2006.06.004

Longhitano, S.G. & Nemec, W., 2005. Statistical analysis of bed-thickness variation in a Tortonian succession of biocalcarenitic tidal dunes, Amantea Basin, Calabria, southern Italy. *Sediment. Geol.*, **179**, 195–224. doi:10.1016/j.sedgeo.2005.05.006

Luján, M., Crespo-Blanc, A. & Comas, M., 2011. Morphology and structure of the Camarinal Sill from high-resolution bathymetry: evidence of fault zones in the Gibraltar Strait. *Geo-Marine Lett.*, **31**, 163–174. doi:10.1007/s00367-010-0222-y

Lykousis, V., Sakellariou, D., Moretti, I. & Kaberi, H., 2007. Late Quaternary basin evolution of the Gulf of Corinth: Sequence stratigraphy, sedimentation, fault–slip and subsidence rates.

Tectonophysics, **440**, 29–51. doi:10.1016/j.tecto.2006.11.007

Martín, J.M., Braga, J.C., Aguirre, J. & Puga-Bernabéu, Á., 2009. History and evolution of the North-Betic Strait (Prebetic Zone, Betic Cordillera): A narrow, early Tortonian, tidal-dominated, Atlantic–Mediterranean marine passage. *Sediment. Geol.*, **216**, 80–90. doi:10.1016/j.sedgeo.2009.01.005

Martín, J.M., Braga, J.C. & Betzler, C., 2001. The messinian guadalhorce corridor: The last Northern, atlantic-mediterranean gateway. *Terra Nov.*, **13**, 418–424. doi:10.1046/j.1365-3121.2001.00376.x

Martín, J.M., Puga Bernabéu, Á., Aguirre Rodríguez, J. & Braga Alarcón, J., 2014. Miocene Atlantic-Mediterranean seaways in the Betic Cordillera (southern Spain). *Rev. la Soc. Geológica España*, **27**, 175–186.

Martorelli, E., Falcini, F., Salusti, E. & Chiocci, F.L., 2010. Analysis and modeling of contourite drifts and contour currents off promontories in the Italian Seas (Mediterranean Sea). *Mar. Geol.*, **278**, 19–30. doi:10.1016/j.margeo.2010.08.007

Masson, D.G., Wynn, R.B. & Bett, B.J., 2004. Sedimentary environment of the Faroe-Shetland and Faroe Bank Channels, north-east Atlantic, and the use of bedforms as indicators of bottom current velocity in the deep ocean. *Sedimentology*, **51**, 1207–1241. doi:10.1111/j.1365-3091.2004.00668.x

McHugh, C.M., Seeber, L., Braudy, N., Cormier, M.-H., Davis, M.B., Diebold, J.B., Dieudonne, N., *et al.*, 2011. Offshore sedimentary effects of the 12 January 2010 Haiti earthquake. *Geology*, **39**, 723–726. doi:10.1130/G31815.1

McNeill, L.C., Shillington, D.J., Carter, G.D.O., Everest, J.D., Ber, E. Le, Collier, R.E., Cvetkoska, A., *et al.*, 2019. Site M0078. *Proc. Int. Ocean Discov. Progr.*, **381**. doi:10.14379/iodp.proc.381.104.2019

McNeill, L.C., Shillington, D.J., Carter, G.D.O., Everest, J.D., Ber, E. Le, Collier, R.E., Cvetkoska, A., *et al.*, 2019. Site M0079. *Proc. Int. Ocean Discov. Progr.*, **381**. doi:10.14379/iodp.proc.381.105.2019

McNeill, L.C., Shillington, D.J., Carter, G.D.O., Everest, J.D., Gawthorpe, R.L., Miller, C., Phillips, M.P., *et al.*, 2019. High-resolution record reveals climate-driven environmental and sedimentary changes in an active rift. *Sci. Rep.*, **9**. doi:10.1038/s41598-019-40022-w

Miall, A.D., 2006. *The Geology of Fluvial Deposits*. *Geol. Fluv. Depos.* doi:10.1007/978-3-662-03237-4

Miramontes, E., Garreau, P., Caillaud, M., Jouet, G., Pellen, R., Hernández-Molina, F.J., Clare, M.A., *et al.*, 2019. Contourite distribution and bottom currents in the NW Mediterranean Sea: Coupling seafloor geomorphology and hydrodynamic modelling. *Geomorphology*, **333**, 43–60. doi:10.1016/j.geomorph.2019.02.030

Moore, A.M., Arango, H.G., Broquet, G., Powell, B.S., Weaver, A.T. & Zavala-Garay, J., 2011. The Regional Ocean Modeling System (ROMS) 4-dimensional variational data assimilation systems. *Prog. Oceanogr.*, **91**, 34–49. doi:10.1016/j.pocean.2011.05.004

Moretti, I., Lykousis, V., Sakellariou, D., Reynaud, J.-Y., Benziane, B. & Prinzhoffer, A., 2004. Sedimentation and subsidence rate in the Gulf of Corinth: what we learn from the Marion Dufresne's long-piston coring. *Comptes Rendus Geosci.*, **336**, 291–299. doi:10.1016/j.crte.2003.11.011

Morozov, E.G., Kozlov, I.E., Shchuka, S.A. & Frey, D.I., 2017. Internal tide in the Kara Gates Strait. *Oceanology*, **57**, 8–18. doi:10.1134/S0001437017010106

Morozov, E.G., Trulsen, K., Velarde, M.G. & Vlasenko, V.I., 2002. Internal Tides in the Strait of Gibraltar. *J. Phys. Oceanogr.*, **32**, 3193–3206. doi:10.1175/1520-0485(2002)032<3193:ITITSO>2.0.CO;2

Mujiasih, S., Beckers, J.-M. & Barth, A., 2021, March 3. Implementation and Validating of the Regional Ocean Model System (ROMS) for the Sunda Strait connecting the Java Sea to the Indian Ocean. doi:10.5194/egusphere-egu21-3457

Mutti, E. & Normark, W.R., 1987. Comparing Examples of Modern and Ancient Turbidite Systems: Problems and Concepts. in *Marine Clastic Sedimentology*, pp. 1–38, Springer Netherlands. doi:10.1007/978-94-009-3241-8_1

Myrianthis, M.L., 1984. Graben formation and associated seismicity in the Gulf of Korinth (Central Greece). *Geol. Soc. London, Spec. Publ.*, **17**, 701–707. doi:10.1144/GSL.SP.1984.017.01.56

Nagy, H., Lorenzo, E. Di & El-Gindy, A., 2019. The impact of climate change on circulation patterns in the Eastern Mediterranean Sea upper layer using Med-ROMS model. *Prog. Oceanogr.*, **175**, 226–244. doi:10.1016/j.pocean.2019.04.012

Nemec, W., 2009. Deltas-Remarks on Terminology and Classification. *Coarse-Grained Deltas*, 3–12. doi:10.1002/9781444303858.ch1

Nixon, C.W., McNeill, L.C., Bull, J.M., Bell, R.E., Gawthorpe, R.L., Henstock, T.J., Christodoulou, D., *et al.*, 2016. Rapid spatiotemporal variations in rift structure during development of the Corinth Rift, central Greece. *Tectonics*, **35**, 1225–1248. doi:10.1002/2015TC004026

Nugraha, H.D., Jackson, C.A.-L., Johnson, H.D. & Hodgson, D.M., 2020. Lateral variability in strain along the toewall of a mass transport deposit: a case study from the Makassar Strait, offshore Indonesia. *J. Geol. Soc. London.*, **177**, 1261–1279. doi:10.1144/jgs2020-071

Oceanus-Lab, 2025. Oceanus-Lab. Retrieved March 24, 2025, from https://oceanus-lab.upatras.gr/

Ori, G.G., 1989. Geologic history of the extensional basin of the Gulf of Corinth (?Miocene-Pleistocene), Greece. *Geology*, **17**, 918–921. doi:10.1130/0091-7613(1989)017<0918:GHOTEB>2.3.CO;2

Pallikarakis, A.E., 2018. *Quaternary multi-proxy analysis of the paleoenvironment , paleogeography and active tectonics of the Corinth Isthmus*, Agricultural University of Athens.

Papanikolaou, I.D., Triantaphyllou, M., Pallikarakis, A. & Migiros, G., 2015. Active faulting at the Corinth Canal based on surface observations, borehole data and paleoenvironmental interpretations. Passive rupture during the 1981 earthquake sequence? *Geomorphology*, **237**, 65–78. doi:10.1016/j.geomorph.2014.10.036

Papatheodorou, G., Lyberis, E. & Ferentinos, G., 1999. Use of Factor Analysis to Study the Distribution of Metalliferous Bauxitic Tailings in the Seabed of the Gulf of Corinth, Greece. *Nat. Resour. Res.*, **8**, 277–286. doi:10.1023/A:1021654300171

Paramana, T., Karditsa, A., Petrakis, S., Milatou, N., Megalofonou, P., Dassenakis, M. & Poulos, S., 2023. Ecosystem-Based Blue Growth: The Case of the Semi-Enclosed Embayment of the Inner NE Ionian Sea and Adjacent Gulfs. *Water*, **15**, 2892. doi:10.3390/w15162892

Perissoratis, C., Mitropoulos, D. & Angelopoulos, I., 1984. The role of earthquakes in inducing

sediment mass movements in the eastern Korinthiakos Gulf. An example from the February 24–March 4, 1981 activity. *Mar. Geol.*, **55**, 35–45. doi:10.1016/0025-3227(84)90131-2

Perissoratis, C., Piper, D.J.W. & Lykousis, V., 2000. Alternating marine and lacustrine sedimentation during late Quaternary in the Gulf of Corinth rift basin, central Greece. *Mar. Geol.*, **167**, 391–411. doi:10.1016/S0025-3227(00)00038-4

Peterson, E.L., 1999. Benthic shear stress and sediment condition. *Aquac. Eng.*, **21**, 85–111. doi:10.1016/S0144-8609(99)00025-4

Petruncio, E.T., Rosenfeld, L.K. & Paduan, J.D., 1998. Observations of the Internal Tide in Monterey Canyon. *J. Phys. Oceanogr.*, **28**, 1873–1903. doi:10.1175/1520-0485(1998)028<1873:OOTITI>2.0.CO;2

Pinardi, N. & Masetti, E., 2000. Variability of the large scale general circulation of the Mediterranean Sea from observations and modelling: a review. *Palaeogeogr. Palaeoclimatol. Palaeoecol.*, **158**, 153–173. doi:10.1016/S0031-0182(00)00048-1

Piper, D.J.W., Kontopoulos, N., Anagnostou, C., Chronis, G. & Panagos, A.G., 1990. Modern fan deltas in the western Gulf of Corinth, Greece. *Geo-Marine Lett.*, **10**, 5–12. doi:10.1007/BF02431016

Piper, D.J.W., Kontopoulos, N. & Panagos, A.G., 1980. Deltaic, coastal and shallow marine sediments of the western Gulf of Corinth. *Thalassographica*, **3**, 5–14.

Piper, D.J.W. & Panagos, A., 1979. Marine Geology of the Gulf of Patras. *Thalassographica*, **3**, 5–20.

Poulos, S.E., Collins, M.B., Pattiaratchi, C., Cramp, A., Gull, W., Tsimplis, M. & Papatheodorou, G., 1996. Oceanography and sedimentation in the semi-enclosed, deep-water Gulf of Corinth (Greece). *Mar. Geol.*, **134**, 213–235. doi:10.1016/0025-3227(96)00028-X

Rebesco, M., Camerlenghi, A. & Loon, A.J. Van, 2008. Chapter 1 Contourite Research, pp. 1–10. doi:10.1016/S0070-4571(08)10001-2

Rebesco, M., Hernández-Molina, F.J., Rooij, D. Van & Wåhlin, A., 2014. Contourites and associated sediments controlled by deep-water circulation processes: State-of-the-art and future considerations. *Mar. Geol.*, **352**, 111–154. doi:10.1016/j.margeo.2014.03.011

Reynaud, J.-Y. & Dalrymple, R.W., 2012. Shallow-Marine Tidal Deposits. in *Principles of Tidal Sedimentology*, pp. 335–369, Springer Netherlands. doi:10.1007/978-94-007-0123-6_13

Robinson, A.R., Leslie, W.G., Theocharis, A. & Lascaratos, A., 2001. Mediterranean Sea Circulation. in *Encyclopedia of Ocean Sciences*, pp. 1689–1705, Elsevier. doi:10.1006/rwos.2001.0376

Rodrigues, S., Hernández-Molina, F.J., Fonnesu, M., Miramontes, E., Rebesco, M. & Campbell, D.C., 2022. A new classification system for mixed (turbidite-contourite) depositional systems: Examples, conceptual models and diagnostic criteria for modern and ancient records. *Earth-Science Rev.*, **230**, 104030. doi:10.1016/j.earscirev.2022.104030

Rohais, S., Eschard, R., Ford, M., Guillocheau, F. & Moretti, I., 2007. Stratigraphic architecture of the Plio-Pleistocene infill of the Corinth Rift: Implications for its structural evolution. *Tectonophysics*, **440**, 5–28. doi:10.1016/j.tecto.2006.11.006

Rohais, S., Eschard, R. & Guillocheau, F., 2008. Depositional model and stratigraphic architecture of rift climax Gilbert-type fan deltas (Gulf of Corinth, Greece). *Sediment. Geol.*, **210**, 132–145. doi:10.1016/j.sedgeo.2008.08.001

Rohais, S. & Moretti, I., 2017. Structural and Stratigraphic Architecture of the Corinth Rift (Greece): An Integrated Onshore to Offshore Basin-Scale Synthesis, pp. 89–120. doi:10.1007/978-3-319-44726-1_5

Rubi, R., 2018. *Caractérisation des systèmes sédimentaires profonds en contexte de rift actif – Etude intégrée des affleurements Plio-Pléistocène et des données sismiques du Golfe de Corinthe, Grèce*, Université de Rennes.

Rubi, R., Hubert-Ferrari, A., Fakiris, E., Christodoulou, D., Dimas, X., Geraga, M., Papatheodorou, G., *et al.*, 2022. Hydrodynamics and sedimentary processes in the modern Rion strait (Greece): Interplay between tidal currents and internal tides. *Mar. Geol.*, **446**, 106771. doi:10.1016/j.margeo.2022.106771

Rubi, R., Rohais, S., Bourquin, S., Moretti, I. & Desaubliaux, G., 2018. Processes and typology in Gilbert-type delta bottomset deposits based on outcrop examples in the Corinth Rift. *Mar. Pet. Geol.*, **92**, 193–212. doi:10.1016/j.marpetgeo.2018.02.014

Rubin, D.M. & Carter, C.L., 1987. *Cross-bedding, Bedforms and Paleocurrents*.

Sakellariou, D., Lykousis, V. & Papanikolaou, I.D., 2001. Active faulting in the Gulf of Corinth, Greece. *36th CIESM Congr. Proc.*, p. 43.

Santoro, V.C., Amore, E., Cavallaro, L., Cozzo, G. & Foti, E., 2002. Sand Waves in the Messina Strait, Italy. *J. Coast. Res.*, **36**, 640–653. doi:10.2112/1551-5036-36.sp1.640

Schlager, W., 1993. Accommodation and supply—a dual control on stratigraphic sequences. *Sediment. Geol.*, **86**, 111–136. doi:10.1016/0037-0738(93)90136-S

Schlitzer, R., 2021. Ocean Data View. Retrieved from https://odv.awi.de

Schmitz, J., Deschamps, R., Joseph, P., Lerat, O., Doligez, B. & Jardin, A., 2014. From 3D photogrammetric outcrop models to reservoir models: an integrated modelling workflow, 143.

Schroeder, K., Garcìa-Lafuente, J., Josey, S.A., Artale, V., Nardelli, B.B., Carrillo, A., Gačić, M., *et al.*, 2012. Circulation of the Mediterranean Sea and its Variability. in *The Climate of the Mediterranean Region*, pp. 187–256, Elsevier. doi:10.1016/B978-0-12-416042-2.00003-3

Sergiou, S., Geraga, M., Pechlivanidou, S., Gawthorpe, R.L., Ninnemann, U., Meckler, A.-N., Modestou, S., *et al.*, 2024. Stratigraphic and paleoceanographic alternations within a Mediterranean semi-enclosed, syn-rift basin during Marine Isotope Stage 5: The Gulf of Corinth, Greece. *Mar. Geol.*, **474**, 107340. doi:10.1016/j.margeo.2024.107340

Shanmugam, G., 2008. Chapter 5 Deep-water Bottom Currents and their Deposits, pp. 59–81. doi:10.1016/S0070-4571(08)10005-X

Shanmugam, G., 2013. Modem internal waves and internal tides along oceanic pycnoclines: Challenges and implications for ancient deep-marine baroclinic sands. *Am. Assoc. Pet. Geol. Bull.*, **97**, 799–843. doi:10.1306/10171212101

Shchepetkin, A.F. & McWilliams, J.C., 2005. The regional oceanic modeling system (ROMS): a split-explicit, free-surface, topography-following-coordinate oceanic model. *Ocean Model.*, **9**, 347–404. doi:10.1016/j.ocemod.2004.08.002

Shchepetkin, A.F. & McWilliams, J.C., 2009. Correction and commentary for “Ocean forecasting in terrain-following coordinates: Formulation and skill assessment of the regional ocean modeling system” by Haidvogel et al., J. Comp. Phys. 227, pp. 3595–3624. *J. Comput. Phys.*, **228**, 8985–9000. doi:10.1016/j.jcp.2009.09.002

Shillington, D.J., McNeill, L.C. & Carter, G.D.O., 2019. *Expedition 381 Preliminary Report: Corinth Active Rift Development*. *Integr. Ocean Drill. Progr. Prelim. Reports* International Ocean Discovery Program Preliminary Report, Vol. 381, International Ocean Discovery Program. doi:10.14379/iodp.pr.381.2019

Siokou-Frangou, I., Bianchi, M., Christaki, U., Christou, E.., Giannakourou, A., Gotsis, O., Ignatiades, L., *et al.*, 2002. Carbon flow in the planktonic food web along a gradient of oligotrophy in the Aegean Sea (Mediterranean Sea). *J. Mar. Syst.*, **33–34**, 335–353. doi:10.1016/S0924-7963(02)00065-9

Skliris, N., Sofianos, S., Gkanasos, A., Mantziafou, A., Vervatis, V., Axaopoulos, P. & Lascaratos, A., 2012. Decadal scale variability of sea surface temperature in the Mediterranean Sea in relation to atmospheric variability. *Ocean Dyn.*, **62**, 13–30. doi:10.1007/s10236-011-0493-5

Stathopoulou, A., Papatheodorou, G., Tripsanas, E., Hubert Ferrari, A., Rubi, R., Geraga, M., Kokkalas, S., *et al.*, 2023. Evolution of the Low-Stand Acheloos Fluvial-Dominated Delta Complex in Western Greece, through 3D Seismic Stratigraphy. *Fourth EAGE East. Mediterr. Work.*, pp. 1–3, European Association of Geoscientists & Engineers. doi:10.3997/2214-4609.202330016

Stefatos, A., Charalampakis, M., Papatheodorou, G. & Ferentinos, G., 1999. Marine Debris on the Seafloor of the Mediterranean Sea: Examples from Two Enclosed Gulfs in Western Greece. *Mar. Pollut. Bull.*, **38**, 389–393. doi:10.1016/S0025-326X(98)00141-6

Stefatos, A., Papatheodorou, G., Ferentinos, G., Leeder, M. & Collier, R., 2002. Seismic reflection imaging of active offshore faults in the Gulf of Corinth: their seismotectonic significance. *Basin Res.*, **14**, 487–502. doi:10.1046/j.1365-2117.2002.00176.x

Stow, D., Hernández-Molina, F.J., Llave, E., Sayago-Gil, M., Díaz del Río, V. & Branson, A., 2009. Bedform-velocity matrix: The estimation of bottom current velocity from bedform observations. *Geology*, **37**, 327–330. doi:10.1130/G25259A.1

Stow, D. & Smillie, Z., 2020. Distinguishing between Deep-Water Sediment Facies: Turbidites, Contourites and Hemipelagites. *Geosciences*, **10**, 68. doi:10.3390/geosciences10020068

Taylor, B., Weiss, J.R., Goodliffe, A.M., Sachpazi, M., Laigle, M. & Hirn, A., 2011. The structures, stratigraphy and evolution of the Gulf of Corinth rift, Greece. *Geophys. J. Int.*, **185**, 1189–1219. doi:10.1111/j.1365-246X.2011.05014.x

Tideschart, 2025. Rio tide times. Retrieved September 11, 2025, from https://www.tideschart.com/Greece/West-Greece/Nomos-Achaias/Rio/

Titri, L., Hubert-Ferrari, A., Caterina, B., Gerovasileiou, V., Christodoulou, D., Fakiris, E., Dimas, X., *et al.*, 2025. Cold-Water Corals in High-Energy Environments after a large anthropic impact: Discoveries from the Rion-Antirion Strait, Greece. *Front. Mar. Sci.*

Trincardi, F., Verdicchio, G. & Miserocchi, S., 2007. Seafloor evidence for the interaction between cascading and along-slope bottom water masses. *J. Geophys. Res. Earth Surf.*, **112**. doi:10.1029/2006JF000620

Tsimplis, M.N., 1994. Tidal Oscillations in the Aegean and Ionian Seas. *Estuar. Coast. Shelf Sci.* doi:10.1006/ecss.1994.1058

Tsimplis, M.N. & Bryden, H.L., 2000. Estimation of the transports through the Strait of Gibraltar. *Deep Sea Res. Part I Oceanogr. Res. Pap.*, **47**, 2219–2242. doi:10.1016/S0967-0637(00)00024-8

Turley, C., Bianchi, M., Christaki, U., Conan, P., Harris, J., Psarra, S., Ruddy, G., *et al.*, 2000. Relationship between primary producers and bacteria in an oligotrophic sea-the Mediterranean and biogeochemical implications. *Mar. Ecol. Prog. Ser.*, **193**, 11–18. doi:10.3354/meps193011

Venditti, J.G., Church, M. & Bennett, S.J., 2005. Morphodynamics of small-scale superimposed sand waves over migrating dune bed forms. *Water Resour. Res.*, **41**. doi:10.1029/2004WR003461

Viana, A. & Rebesco, M., 2007. *Economic and palaeoceanographic significance of contourite deposits*. (A. Viana & M. Rebesco, Eds.), Geological Society of London.

Watkins, S.E., Whittaker, A.C., Bell, R.E., McNeill, L.C., Gawthorpe, R.L., Brooke, S.A.S. & Nixon, C.W., 2019. Are landscapes buffered to high-frequency climate change? A comparison of sediment fluxes and depositional volumes in the Corinth Rift, central Greece, over the past 130 k.y. *GSA Bull.*, **131**, 372–388. doi:10.1130/B31953.1

WikiROMS, 2019. Vertical S-coordinate. *WikiROMS*. Retrieved from https://www.myroms.org/wiki/Vertical_S-coordinate

Wynn, R.B. & Stow, D.A.V., 2002. Classification and characterisation of deep-water sediment waves. *Mar. Geol.*, **192**, 7–22. doi:10.1016/S0025-3227(02)00547-9

Wynn, R.B., Weaver, P.P.E., Masson, D.G. & Stow, D.A. V., 2002. Turbidite depositional architecture across three interconnected deep-water basins on the north-west African margin. *Sedimentology*, **49**, 669–695. doi:10.1046/j.1365-3091.2002.00471.x

Zelilidis, A., Koukouvelas, I. & Doutsos, T., 1988. Neogene paleostress changes behind the forearc fold belt in the Patraikos Gulf area, western Greece. *Neues Jahrb. für Geol. und Paläontologie - Monatshefte*, **1988**, 311–325. doi:10.1127/njgpm/1988/1988/311

Appendix A: Julia Code – SST Maps (Chapter 3)

SST Observations

1) Load data

```
using Pkg
using NCDatasets
using PyPlot
using Missings
using Dates
using Statistics
using Polynomials
using CSV
using Tables
using DataFrames
using DelimitedFiles
```

```
#read the initial (cloudy) data, land-sea mask, time, latitude and
longitude
ds =
Dataset("SST_MED_SST_L3S_NRT_OBSERVATIONS_010_012_b_1642686414862.nc");
```

```
#load data locally
lat = nomissing(ds["lat"][:], NaN);
lon = nomissing(ds["lon"][:], NaN);
sstK = nomissing(ds["sea_surface_temperature"][:,:,:], NaN);
temps = nomissing(ds["time"][:], NaN);
sst = sstK.-273.15;
sst[205:end,1:31,:].= NaN;
sst[250:end,:,:].= NaN; #Negating Aegean Sea
```

Mean and verification

```
function nanmean(x,dim)
    m = isnan.(x)
    x2 = copy(x)
    x2[m] .= 0
    return sum(x2,dims=dim) ./ sum(.!m,dims=dim)
end
```

```
sst1 = nanmean(sst,1);
sst2 = nanmean(sst1,2);
fig = figure()
plot(sst2[1,1,:])
title("Mean SST - Patras and Corinth Gulf")
```

2) Masks and cleaning data

```
#transform time variable (in miliseconds) into year-day
mdate = Dates.value.(temps - DateTime(1981,1,1))/1000/60/60/24;
```

```
#create a first land-sea mask. This mask will be "refined" by eliminating
pixels that are
# covered more than 98% of the time and images that are covered more than
98% in space
mask = nanmean(sst,3);
mask[.!isnan.(mask)].=1;
mask[isnan.(mask)].=0;

covT = coverage(sst,mask,"tm"); #calculate average % of missing data in
time

#Visualise % of missing data in time
plot(covT)
```

```
#several images has no data: these should be eliminated
i=findall(covT.<95); #identify images with more than 95% of missing data
sstb = sst[:,:,i]; #remove those images
mdateb = mdate[i]; #remove those dates from the time vector
tempsb = temps[i]
```

```
#new temporal size of the SST matrix: 81 out of 90 images have been
retained
@show size(sstb)
maskb = nanmean(sstb,3); #new mask with the new matrix
maskb[.!isnan.(maskb)].=1; #non-missing data to sea
maskb[isnan.(maskb)].=0; #missing data to land
#maskb[205:end,1:31,:].=0;
@show size(maskb)
covS = coverage(sstb,maskb,"sp");  #calculate average % of missing data in
space
```

```
#Visualise the % of missing data in space
#pcolor(lon',lat,covS'),clim(50,100),colorbar();
pcolor(covS'),clim(50,100),colorbar();
covS[covS.>=95].=0; #if a pixel is missing more than 95% we set that to
land
@show extrema(covS)
#the map showing % of missing data will be transformed in the final land-
sea mask
covS[covS.==0].=NaN;
covS[.!isnan.(covS)].=1; #non-missing data to sea
covS[isnan.(covS)].=0; #missing data to land
PyPlot.contourf(lon',lat,covS',levels = [0., 0.5],colors =[[.5,.5,.5]])
#pcolor(lon',lat,sstb[:,:,10]',cmap="RdYlBu_r");clim(21,28);colorbar()
pcolor(lon',lat,sstb[:,:,1]',cmap="RdYlBu_r");colorbar()
#pcolor(lon',lat,copy(covS')),colorbar();
```

Clean mean SST

```
sst3 = nanmean(sstb,1);
sst4 = nanmean(sst3,2);
fig = figure()
plot(tempsb, sst4[1,1,:]')
ylabel("Temperature (°C)")
xlabel("Time")
```

```
using Polynomials
# Dates into decimal years
function datetime_to_year(dt::DateTime)
    year = Dates.year(dt)
    start_of_year = DateTime(year)
    end_of_year = DateTime(year + 1)
    frac = (dt - start_of_year) / (end_of_year - start_of_year)
    return year + frac
end
x_dates = tempsb
x = datetime_to_year.(x_dates)  # Années décimales
y = y = collect(sst4[1,1,:])                # Température
# Linear Regression
p = fit(x, y, 1)
y_fit = p.(x)
# Slope
pente = p.coeffs[2]
intercept = p.coeffs[1]
text_slope = "Trend = $(round(pente, digits=4)) °C/an"
@show(text_slope)
# Plot
fig = figure()
figure(figsize = (9,6))
plot(x_dates, y, label="SST")
plot(x_dates, y_fit, "r--", label="Trend")
xlabel("Time (years)")
ylabel("Temperature (°C)")
legend()
grid(true)
# Equation
println("Équation de la droite : y = $(round(p.coeffs[2], digits=4)) * x +
$(round(p.coeffs[1], digits=4))")
```

3) Mapping all the dates

```
for n = 1:size(sstb,3)
    fig=figure()
    clf()

    xlim(21.45,23.3)
    ylim(37.8,38.5)
    pcolormesh(lon',lat,sstb[:,:,n]',cmap="RdYlBu_r"),#=clim(15,21),=#
colorbar(orientation="horizontal")
    contourf(lon',lat,covS',levels = [0., 0.5],colors =[[.5,.5,.5]])
    title("SST \n $(tempsb[n])", fontsize = 14)
    aspect_ratio=1/cos(pi*mean(lat)/180);
    gca().set_aspect(aspect_ratio);

    IJulia.clear_output(true)
    display(fig)
    sleep(0.2)
    savefig("SST_Global_$n.png");
   clf()
end
```

4) DINEOF File Creation

```
#write down the results into a new netCDF file
output = Dataset("sst_L3_Corinthe_15y.nc","c");
defDim(output,"lon",size(maskb,1))
defDim(output,"lat",size(maskb,2))
defDim(output,"time",size(sstb,3))
ncSST = defVar(output,"SST",Float32,("lon","lat","time");fillvalue=-
9999.f0);
sstb[isnan.(sstb)].=-9999.;
ncSST[:] = sstb;
ncTime = defVar(output,"time",Float32,("time",));
ncTime[:] = mdateb;
ncMask = defVar(output,"mask",Float32,("lon","lat"));
ncMask[:] = covS;
ncLat = defVar(output,"lat",Float32,("lat",));
ncLat[:] = lat;
ncLon = defVar(output,"lon",Float32,("lon",));
ncLon[:] = lon;
close(output)
```

Appendix B: Julia Code - ROMS Sections (Chapters 4, 5 & 6)

Packages & Functions

```
using LinearAlgebra
using Statistics
using PyPlot
using NCDatasets
using Pkg
using Interpolations
using Dates
using ROMS
using GeoDatasets
using ColorSchemes
```

```
function nanmean(x,dim)
    m = isnan.(x)
    x2 = copy(x)
    x2[m] .= 0
    return sum(x2,dims=dim) ./ sum(.!m,dims=dim)
end
```

Bathymetry

```
ds_grid =
NCDataset("C:/Users/basil/Desktop/ROMS_datasets/Corinth_Mai_2023.nc");
lon = ds_grid["lon_rho"][:,:];
lat = ds_grid["lat_rho"][:,:];
h = ds_grid["h"][:,:];
mask_rho = ds_grid["mask_rho"][:,:];
mask_rho[139,138] = 0;
mask_rho[272,139] = 0;
mask_rho[287,134] = 0;
mask_rho[355,41] = 0;
mask_rho[1,137] = 0;
mask_rho[2,137] = 0;
clf();
figure(figsize = (17,9))
hmask = copy(h)
hmask[mask_rho .== 0] .= NaN;
pcolormesh(lon, lat, hmask);
grid()
colorbar()
gca().set_aspect(1/cosd(mean(lat)))
title("smoothed bathymetry [m]");
```

Dataset

```
ds = NCDataset("C:/Users/basil/Desktop/ROMS_datasets/roms_his_Mai2023.nc")
# instance to plot
n = 393
temp = nomissing(ds["temp"][:,:,32,n],NaN);
```

```
#mask_rho[64:66,47:50,:,:] .= 0;
temp[mask_rho .== 0] .= NaN;
```

SST

```
tt = ds["ocean_time"][200:end];
clf();
pcolormesh(lon,lat,temp, cmap="RdYlBu_r"), clim(16.5, 21),
gca().set_aspect(1/cosd(mean(lat)))
colorbar(orientation ="horizontal");
title("sea surface temperature [°C] \n $(tt[n-199])")
```

Surface elevation

```
for n = 386:408
x = 1
zeta = nomissing(ds["zeta"][:,:,n],NaN)
u = nomissing(ds["u"][:,:,x,n],NaN);
v = nomissing(ds["v"][:,:,x,n],NaN);
mask_u = ds_grid["mask_u"][:,:];
mask_v = ds_grid["mask_v"][:,:];
u[mask_u .== 0] .= NaN;
v[mask_v .== 0] .= NaN;
zeta[mask_rho .== 0] .= NaN;
# ROMS uses an Arakawa C grid
u_r = cat(u[1:1,:], (u[2:end,:] .+ u[1:end-1,:])/2, u[end:end,:], dims=1);
v_r = cat(v[:,1:1], (v[:,2:end] .+ v[:,1:end-1])/2, v[:,end:end], dims=2);
# all sizes should be the same
size(u_r), size(v_r), size(mask_rho);
clf();
figure(figsize = (10,10))
cmap = ColorMap(ColorSchemes.coolwarm.colors)
    cmap.set_bad("gray")
pcolormesh(lon,lat,zeta, cmap=cmap), clim(-0.2,0.2)
cb = colorbar(orientation ="vertical",shrink=0.75,pad=0.03,);
cb.ax.tick_params(labelsize=18);
xticks(fontsize=14)
yticks(fontsize=14)
title("$(tt[n]) \n");
gca().set_aspect(1/cosd(mean(lat)))
savefig("C:/Users/basil/Desktop/Analyse_models/Images/SSH/Corinthe_$n.png")
end
```

Sections

```
opt = (
    Tcline = 50,    # m
    theta_s = 5,    # surface refinement
    theta_b = 4, # bottom refinement
    nlevels = 32,  # number of vertical levels
    Vtransform  = 2,
    Vstretching = 4,
);

hmin = minimum(h);
hc = min(hmin,opt.Tcline);
z_r = -ROMS.set_depth(opt.Vtransform, opt.Vstretching,
```

```
                    opt.theta_s, opt.theta_b, hc, opt.nlevels,
                    1, h,);
#Horizontal section
tempi = ROMS.model_interp3(lon,lat,z_r,temp,lon,lat,[-30])
mlon,mlat,mdata = GeoDatasets.landseamask(resolution='f', grid=1.25)

clf();
pcolormesh(lon,lat,tempi[:,:,1])
colorbar();
ax = axis()
contourf(mlon,mlat,mdata',[0.5, 3],colors=["gray"])
axis(ax)
gca().set_aspect(1/cosd(mean(lat)))
title("temperature at -30 m [°C]")
```

```
## Free section
opt = (
    Tcline = 50,    # m
    theta_s = 5,    # surface refinement
    theta_b = 4, # bottom refinement
    nlevels = 32,   # number of vertical levels
    Vtransform  = 2,
    Vstretching = 4,
);

hmin = minimum(h);
hc = min(hmin,opt.Tcline);
z_r = -ROMS.set_depth(opt.Vtransform, opt.Vstretching,
                    opt.theta_s, opt.theta_b, hc, opt.nlevels,
                    1, h,);
section_lon2 = vcat(LinRange(21.66, 21.844,20),LinRange(21.844,21.98,20));
section_lat2 = vcat(LinRange(38.27, 38.352,20),LinRange(38.352,38.352,20));

zeta = nomissing(ds["zeta"][:,:,:],NaN);

using Interpolations

function section_interp2(v)
    itp2 = interpolate((lon[:,1],lat[1,:]),v,Gridded(Linear()))
    return itp2.(section_lon2,section_lat2)
end

for n = 386:408

    z_r = -ROMS.set_depth(opt.Vtransform, opt.Vstretching,
                    opt.theta_s, opt.theta_b, hc, opt.nlevels,
                    1, h, zeta=zeta[:,:,n]);

temp = nomissing(ds["temp"][:,:,:,n],NaN);
temp[mask3 .== 0] .= NaN;

u = nomissing(ds["u"][:,:,:,n],NaN);
v = nomissing(ds["v"][:,:,:,n],NaN);
    # ROMS uses an Arakawa C grid
u_r = cat(u[1:1,:,:,:], (u[2:end,:,:,:] .+ u[1:end-1,:,:,:])/2,
u[end:end,:,:,:], dims=1);
```

```
v_r = cat(v[:,1:1,:,:], (v[:,2:end,:,:] .+ v[:,1:end-1,:,:])/2,
v[:,end:end,:,:], dims=2);


section_temp2 = mapslices(section_interp2,temp,dims=(1,2))
section_u2 = mapslices(section_interp2,u_r[:,:,1:2:end,:],dims=(1,2))
section_v2 = mapslices(section_interp2,v_r[:,:,1:2:end,:],dims=(1,2))
    section_zt = mapslices(section_interp2,z_r,dims=(1,2))
section_z2 = mapslices(section_interp2,z_r[:,:,1:2:end,:],dims=(1,2))

section_xt = repeat(section_lon2,inner=(1,size(temp,3)))
section_x2 = repeat(section_lon2,inner=(1,16))

clf()
    figure(figsize = (30,15))
    cmap = ColorMap((ColorSchemes.thermal.colors))
    cmap.set_bad("gray")
    contourf(section_xt,section_zt[:,1,:],section_temp2[:,1,:],100, cmap =
cmap, vmin=14, vmax=19)#, clim(14,18.5)
    tick_params(labelsize=20)
ylim(0,300)
     gca().invert_yaxis()
cb = colorbar(orientation="vertical", shrink=1, pad=0.01)
cb.ax.tick_params(labelsize=18)    # Agrandir les labels de la colorbar

    q =
quiver(section_x2,section_z2[:,1,:],section_u2[:,1,:],section_v2[:,1,:],sca
le=8, headwidth = 4, headlength = 7)
qk = quiverkey(q,0.75,0.15,0.5,"0.5 m/s",coordinates="axes")
 qk.text.set_fontsize(16)
xlabel("Longitude", fontsize = 22)
ylabel("Depth (m)", fontsize = 22)
title("$(tt[n]) \n", fontsize = 24);


ax2 = gcf().add_axes([0.16,0.13,0.3,0.3])

    pc = ax2.pcolormesh(lon,lat,temp[:,:,31], cmap=cmap, vmin=14,
vmax=19)#, clim(18,20),

    cb2 = colorbar(pc, orientation ="horizontal",shrink=0.8,pad=0.10,)
    cb2.ax.tick_params(labelsize=16)
axis("on")
ax2.set_aspect(1/cosd(mean(lat)))
ax2.plot(section_lon2,section_lat2,"g")
    ax2.tick_params(labelsize=18)

savefig("C:/Users/basil/Desktop/Analyse_models/Tides/Sections_Strait_$n.png
");
end
```

```
### Avec les maximums
u = nomissing(ds["u"][:,:,:,200:end],NaN);
v = nomissing(ds["v"][:,:,:,200:end],NaN);
    # ROMS uses an Arakawa C grid
u_r = cat(u[1:1,:,:,:], (u[2:end,:,:,:] .+ u[1:end-1,:,:,:])/2,
u[end:end,:,:,:], dims=1);
```

```
v_r = cat(v[:,1:1,:,:], (v[:,2:end,:,:] .+ v[:,1:end-1,:,:])/2,
v[:,end:end,:,:], dims=2);
```

```
function max_abs_signed(arr, dim)
    sz = size(arr)
    # keep all dims
    new_sz = ntuple(i -> i == dim ? 1 : sz[i], 4)
    result = similar(arr, new_sz)  # matrice résultat

    # On boucle seulement sur les autres dimensions
    for i in 1:sz[1], j in 1:sz[2], k in 1:sz[3]
        slice = arr[i,j,k,:]          # slice along 4th dims
        idx = argmax(abs.(slice))     # indice du max absolu
        result[i,j,k,1] = slice[idx]  # good sign
    end
    return dropdims(result, dims=dim)  # remove 4th dims
end

u_max = max_abs_signed(u_r, 4);
v_max = max_abs_signed(v_r, 4);
zeta = nomissing(ds["zeta"][:,:,:],NaN);
zetaM = max_abs_signed(zeta,4);
maxvit2 = sqrt.((u_max) .^2 .+(v_max) .^2);
```

```
section_lon2 = vcat(LinRange(22.834,22.843,30));
section_lat2 = vcat(LinRange(37.95, 38.22,30));

using Interpolations

function section_interp2(v)
    itp2 = interpolate((lon[:,1],lat[1,:]),v,Gridded(Linear()))
    return itp2.(section_lon2,section_lat2)
end

      z_r = -ROMS.set_depth(opt.Vtransform, opt.Vstretching,
                  opt.theta_s, opt.theta_b, hc, opt.nlevels,
                  1, h, zeta=zetaM[:,:]);

section_temp2 = mapslices(section_interp2,maxvit2,dims=(1,2))
section_u2 = mapslices(section_interp2,u_max[:,:,1:2:end,:],dims=(1,2))
section_v2 = mapslices(section_interp2,v_max[:,:,1:2:end,:],dims=(1,2))
    section_zt = mapslices(section_interp2,z_r,dims=(1,2))
section_z2 = mapslices(section_interp2,z_r[:,:,1:2:end,:],dims=(1,2))

section_xt = repeat(section_lat2,inner=(1,size(u_r,3)))
section_x2 = repeat(section_lat2,inner=(1,16))

clf()
    figure(figsize = (17,25))
cmap=ColorMap(ColorSchemes.rainbow.colors)
    #cmap = get_cmap("viridis_r")
    cmap.set_bad("none")
    contourf(section_x2,section_z2[:,1,:],section_u2[:,1,:],100, cmap =
cmap, vmin=-0.2, vmax=0.2)
    tick_params(labelsize=20)
ylim(-50,1350)
     gca().invert_yaxis()
```

```
cb = colorbar(orientation="vertical", shrink=1, pad=0.01)
cb.ax.tick_params(labelsize=18)


    q =
quiver(section_x2,section_z2[:,1,:],section_u2[:,1,:],section_v2[:,1,:],sca
le=5, headwidth = 4, headlength = 7)

xlabel("Latitude", fontsize = 20)
ylabel("Depth (m)", fontsize = 20)
title("Currents (m/s) section \n", fontsize = 20);

savefig("C:/Users/basil/Desktop/Analyse_models/Images/Sismique/Ligne95-
96_CURRENTS_v2.png");
```

```
#h-points
section_lon = vcat(LinRange(21.50,
21.844,60),LinRange(21.844,21.98,40),LinRange(21.98,22.87,210),LinRange(22.
87,23.20,50));
section_lat = vcat(LinRange(38.17,
38.352,60),LinRange(38.352,38.352,40),LinRange(38.352,38.09,210),LinRange(3
8.09,38.1,50));

section_lon2 = vcat(LinRange(21.66, 21.844,20),LinRange(21.844,21.98,20));
section_lat2 = vcat(LinRange(38.27, 38.352,20),LinRange(38.352,38.352,20));

using Interpolations

function section_interp(v)
    itp = interpolate((lon[:,1],lat[1,:]),v,Gridded(Linear()))
    return itp.(section_lon,section_lat)
end

function section_interp2(v)
    itp = interpolate((lon[:,1],lat[1,:]),v,Gridded(Linear()))
    return itp.(section_lon2,section_lat2)
end

for n = 393

temp = nomissing(ds["temp"][:,:,:,n],NaN);
temp[mask3 .== 0] .= NaN;

u = nomissing(ds["u"][:,:,:,n],NaN);
v = nomissing(ds["v"][:,:,:,n],NaN);
    # ROMS uses an Arakawa C grid
u_r = cat(u[1:1,:,:,:], (u[2:end,:,:,:] .+ u[1:end-1,:,:,:])/2,
u[end:end,:,:,:], dims=1);
v_r = cat(v[:,1:1,:,:], (v[:,2:end,:,:] .+ v[:,1:end-1,:,:])/2,
v[:,end:end,:,:], dims=2);


section_temp = mapslices(section_interp,temp,dims=(1,2))
section_u = mapslices(section_interp,u_r,dims=(1,2))
section_v = mapslices(section_interp,v_r,dims=(1,2))
section_z = mapslices(section_interp,z_r,dims=(1,2))
```

```
    section_z2 = mapslices(section_interp2,z_r,dims=(1,2))
    section_x2 = repeat(section_lon2,inner=(1,size(temp,3)))

section_x = repeat(section_lon,inner=(1,size(temp,3)))

clf()
    figure(figsize = (17,9))
    scatter(section_x,section_z[:,1,:],marker=".")
ylim(0,900)
     gca().invert_yaxis()


xlabel("Longitude", fontsize = 15)
ylabel("Depth (m)", fontsize = 15)
#Title("Vertical repartition of the computing points", size = "xx-large");
xticks(fontsize=13)
yticks(fontsize=13)

ax2 = gcf().add_axes([0.17,0.17,0.25,0.34])
    ax2.scatter(section_x2,section_z2[:,1,:],marker=".")
    ylim(0,300)
    gca().invert_yaxis()
axis("on")
xlabel("Longitude")
ylabel("Depth (m)")


ax3 = gcf().add_axes([0.768,0.12,0.13,0.16])
    # Create the colormap and set the 'bad' (NaN) color to light blue
cmap = get_cmap("viridis_r")
cmap.set_bad("gray")
    ax3.pcolormesh(lon, lat, hmask, cmap=cmap)
axis("on")
ax3.set_aspect(1/cosd(mean(lat)))
ax3.plot(section_lon,section_lat,"m")

#savefig("Corinth_vsection_avecstrait_$n.png");
end
```

```
## ADCP section
section_lon = vcat(LinRange(21.728,
21.727,50))#,LinRange(21.844,21.98,50));
section_lat = vcat(LinRange(38.277,
38.327,50))#,LinRange(38.352,38.352,50));

using Interpolations

function section_interp(v)
    itp = interpolate((lon[:,1],lat[1,:]),v,Gridded(Linear()))
    return itp.(section_lon,section_lat)
end

for n = 389:413

temp = nomissing(ds["temp"][:,:,:,n],NaN);
#temp[64:66,47:50,:,:] .= NaN;
```

```
u = nomissing(ds["u"][:,:,:,n],NaN);
v = nomissing(ds["v"][:,:,:,n],NaN);
    # ROMS uses an Arakawa C grid
u_r = cat(u[1:1,:,:,:], (u[2:end,:,:,:] .+ u[1:end-1,:,:,:])/2,
u[end:end,:,:,:], dims=1);
v_r = cat(v[:,1:1,:,:], (v[:,2:end,:,:] .+ v[:,1:end-1,:,:])/2,
v[:,end:end,:,:], dims=2);

section_temp = mapslices(section_interp,temp,dims=(1,2))
section_u = mapslices(section_interp,u_r,dims=(1,2))
section_v = mapslices(section_interp,v_r,dims=(1,2))
section_z = mapslices(section_interp,z_r,dims=(1,2))

section_x = repeat(section_lon,inner=(1,size(temp,3)))
section_y = repeat(section_lat,inner=(1,size(temp,3)))

clf()
    figure()
    figure(figsize = (7,5))
    contourf(section_y,section_z[:,1,:],-section_u[:,1,:],50,
cmap=ColorMap(ColorSchemes.rainbow.colors))

ylim(0,70)
    gca().invert_yaxis()

colorbar()
    clim(-0.5,0.75)
r = 3;
i = 1:r:size(lon,1);
j = 1:r:size(lon,2);
#q =
quiver(section_x,section_z[:,1,:],section_u[:,1,:],section_v[:,1,:],scale=1
2, headwidth = 4, headlength = 7)
#quiverkey(q,0.55,0.15,1,"1 m/s",coordinates="axes",color="r")
xlabel("Latitude")
ylabel("Depth (m)")
title("Westward currents (m/s) section \n at 21.728°E \n ROMS Modelling on
$(time[n])");

savefig("Corinthe_west_curr_ADCP_$n.png");
end
```